Wastewater re-use in agriculture:
Modelling contaminant transport and impact on soil structure

Pavan Cornelissen

Propositions

1. The risks of wastewater irrigation are uncertain as long as the harmful effects of emerging contaminants are poorly known.
   (this thesis)

2. The sodium adsorption ratio is a more reliable measure of soil sodicity problems than the exchangeable sodium percentage.
   (this thesis)

3. The pressure that PhD candidates face to finish their own thesis inhibits collaboration and integration with other research projects.

4. Numerical models can provide valuable data that cannot be measured in experiments.

5. Moving university facilities from the city centre to a campus outside the city will negatively impact the public trust in science.

6. The ticket price of short-distance flights should never be lower than less environmentally damaging alternative methods of transport.

Propositions belonging to the thesis, entitled:

'Wastewater re-use in agriculture: modelling contaminant transport and impact on soil structure'

Pavan Cornelissen

Wageningen, 1 April 2022

Wastewater re-use in agriculture: modelling contaminant transport and impact on soil structure

Pavan Cornelissen

Thesis committee

Promotor:
Prof. Dr S.E.A.T.M. van der Zee
Emeritus Personal Chair Ecohydrology
Wageningen University & Research

Co-promotors:
Prof. Dr A. Leijnse
Emeritus Professor Groundwater Quality
Wageningen University & Research

Dr V. Niasar
Reader, School of Chemical Engineering
The University of Manchester, United Kingdom

Other members:
Prof. Dr J. van der Gucht, Wageningen University & Research
Prof. Dr M.Th. van Genuchten, Federal University of Rio de Janeiro, Brazil
Prof. Dr S.C. Dekker, Utrecht University
Dr M. Heinen, Wageningen University & Research

This research was conducted under the auspices of the Research School for Socio-Economic and Natural Sciences of the Environment (SENSE)

Wastewater re-use in agriculture: modelling contaminant transport and impact on soil structure

Pavan Cornelissen

Thesis
submitted in fulfilment of the requirements for the degree of doctor
at Wageningen University
by the authority of the Rector Magnificus
Prof. Dr A.P.J. Mol,
in the presence of the
Thesis Committee appointed by the Academic Board
to be defended in public
on Friday 1 April 2022
at 11 a.m. in the Aula.

Pavan Cornelissen
Wastewater re-use in agriculture: modelling contaminant transport and impact on soil structure, 178 pages.

PhD thesis, Wageningen University, Wageningen, the Netherlands (2022)
With references, with summary in English

ISBN: 978-94-6447-023-9
DOI: https://doi.org/10.18174/556803

Table of contents

Chapter 1

General introduction

1.1 Context

Water is a vital resource for humans and our civilization. Not only is the accessibility of clean water necessary for drinking and sanitation purposes to prevent public health risks, but it is also an important resource for food production and industrial processes. However, freshwater scarcity is a major problem in the world. Currently, 1.8 billion people live under water-stressed conditions for 6 months per year, and over 4 billion people experience water stress at least one month a year (Mekonnen and Hoekstra, 2016). In the future, this number is expected to increase even further due to climate change, urbanization, and population growth (Vörösmarty et al., 2000; Sarhadi et al., 2016; Ali et al., 2017). Traditional water resources such as surface- and groundwater are already under pressure due to increased withdrawal rates (Famiglietti, 2014). Therefore, alternative water sources need to be considered.

Most freshwater is used for agriculture, which is responsible for 70% of all water withdrawals in the world (UNESCO-WWAP, 2003). In comparison, industrial and domestic use are responsible for 19% and 11% of water withdrawals, respectively (FAO, 2010). Thus, significant amounts of freshwater may be saved when using alternative water sources for agricultural purposes. If water is of insufficient quality for drinking water, it may still be of sufficient quality for irrigating crops. For example, it is possible to irrigate crops with marginal water sources, such as wastewater and return flows. This wastewater or effluent can be of either industrial or municipal origin. In this thesis, we will use 'wastewater' as a general term for all these types of marginal water.

Wastewater irrigation has been practiced for many years, particularly in arid and semi-arid regions. In the Middle-East, wastewater irrigation is particularly widespread due to the combination of large population and extreme water scarcity (Hamilton et al., 2007). Wastewater irrigation is prominent in countries such as Israel (Lawhon and Schwartz, 2001), Kuwait, and Iran (Radcliffe, 2004). Other arid regions where wastewater irrigation is prominent include North-Africa (Bahri, 1998; USEPA, 2004), Australia (Radcliffe, 2004), and the United States (Hamilton et al., 2007). Wastewater irrigation in the United States is most common in California, which already started re-using wastewater for irrigation purposes back in 1890 (Recycled Water Taskforce, 2003).

However, wastewater irrigation is not limited to arid climates. In recent years, wastewater irrigation has received more attention in temperate climates (Bixio et al., 2006). The interest in wastewater irrigation stems from two reasons. First, weather patterns are becoming more extreme due to climate change. For example, the Netherlands have experienced severe droughts in the years 2018, 2019, and 2020, which led to local restrictions on water use and decreased crop yields. Therefore, wastewater irrigation has received increased attention as a possible water source during future droughts. The second reason is that wastewater irrigation may potentially be more environmentally

friendly than current practices. Currently, treated wastewater is discharged directly into surface waters in many countries, which may lead to environmental problems. The idea is that the soil acts as a filter and prevents contaminants from entering the surface- or groundwater (Hamilton et al., 2007). Irrigation may therefore be a more sustainable way of disposing wastewater.

Despite the aforementioned advantages, wastewater irrigation also poses risks. The large number of contaminants that may be present in wastewater can harm the public health and the environment. Common contaminants seen in wastewater include salts (Jalali et al., 2008; Muyen et al., 2011), heavy metals (Mapanda et al., 2005; Rezapour et al., 2011; Farahat and Linderholm, 2015), organic chemicals (Chen et al., 2014; Woodward et al., 2014; Wang et al., 2015), and pathogens (Toze, 2006). The nutrients contained in wastewater may reduce the need for fertilizers (Al-Nakshabandi et al., 1997), which is an important advantage in developing countries where regular fertilizers may not be economically feasible (Hamilton et al., 2007). However, these nutrients can also harm crops and the environment when they are present in excess quantities (Tang et al., 2004).

The exact composition of the wastewater depends on its source, and the treatment it underwent before re-use. While wastewater is generally treated before re-use, this may not always be the case in developing countries where wastewater treatment is not economically feasible. Additionally, current wastewater treatment plants are optimised for removal of 'traditional' contaminants, such as heavy metals. However, wastewater treatment plants do not target relatively 'new' contaminants, such as contaminants of emerging concern. The removal rate of contaminants in treatment plants may therefore vary from 2 to 99 percent, depending on the type of contaminant (Petrović et al., 2003; Kim et al., 2018). Thus, even treated wastewater may pose a risk to the public health and the environment.

To ascertain that no harm is done to the public health and the environment, the risks associated with the contaminants present in wastewater have to be investigated carefully. In this thesis, various concerns related to wastewater irrigation will be investigated through modelling. The large number of contaminants that may be present in wastewater makes it impossible to do an in-depth analysis of each contaminant. Therefore, we start with general problems which are applicable to a large number of contaminants instead. Besides the general part, we will also focus on sodium as a contaminant in wastewater and its adverse impact on soil structure.

1.2 The sustainability of wastewater irrigation

Since wastewater irrigation has a long history in some countries, there already exist guidelines for irrigation water quality. For example, there are guidelines proposed by the

World Health Organization (WHO, 2006), the United States Environmental Protection Agency (USEPA, 2012), and the European Union (European Council, 2019). Several other countries have adopted their own irrigation water standards based on these guidelines. These guidelines encompass quality standards for several contaminant groups such as heavy metals, nutrients, and microbes, as well as some chemo-physical properties such as the electric conductivity and pH of the irrigation water. However, quality standards for many chemical hazards are missing (Rizzo et al., 2018). This includes contaminants of emerging concern (CECs), whose long-term toxicological effects and environmental behaviour are still unknown. This group contains compounds such as (veterinary-) pharmaceuticals, personal care products, and surfactants.

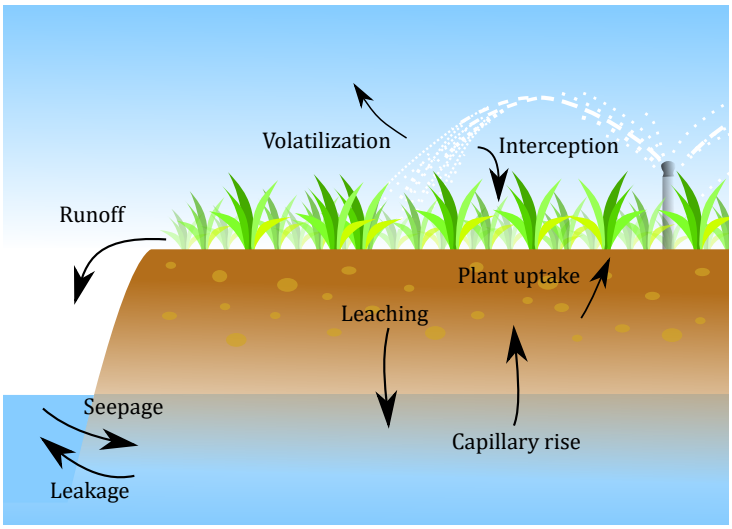

Figure 1.1: A schematic representation of an agricultural field which is irrigated with wastewater. The figure shows the various contaminant pathways between the environment environmental compartments.

Therefore, the question arises whether wastewater irrigation is sustainable. By sustainability, we mean that no harmful effects are expected for the public health and the environment, on both short and long timescales. First, it is necessary to determine how to assess sustainability of a wastewater irrigation practice. This task is complicated by the large number of contaminants present in wastewater. Each contaminant may differ in toxicity and behaviour in the environment. Additionally, there are many pathways through which a contaminant may travel through the environment, each which their own risks to the public health or the environment. Contaminants may be exchanged between numerous environmental compartments (Figure 1.1), such as the soil (Qian and Mecham, 2005; Virto et al., 2006; Xu et al., 2010; Rezapour and Samadi, 2011; Razzaghi et al., 2016), groundwater (Gallegos et al., 1999; Candela et al., 2007; Paruch, 2014), surface water (Pedersen et al., 2005), crops (Chiou et al., 2001; Jjemba, 2002; Pedrero and Alarcón, 2009), and air (Jury et al., 1990; Weber et al., 2006). Each environmental compartment may be associated with various risks. For example, the presence of contaminants may

not only inhibit crop growth, but may also pose a risk to the public health when the contaminants end up in food crops. Naturally, all risks need to be considered to assess the sustainability of wastewater irrigation.

Until now, the concept of sustainability is often considered only for separate environmental compartments. However, the various environmental compartments are coupled. For example, the contaminant mass that ends up in the groundwater, is also dependent on the contaminant uptake by crops, and vice versa. This means that each environmental compartment needs to be considered simultaneously to get an accurate prediction of a contaminant's environmental fate. Additionally, the concept of sustainability should hold for all compartments simultaneously. For example, a situation is not sustainable when the crop quality is sufficient, but the groundwater quality is threatened. Therefore, it is necessary to consider all compartments in an integrated fashion. However, a framework for such an integrated sustainability assessment is still missing.

1.3 Adsorption and degradation of contaminants

As mentioned earlier, the numerous contaminants present in wastewater may each show different behaviour in the environment. However, many contaminants experience adsorption and degradation to a certain degree. This group includes many contaminants of emerging concern, such as pharmaceuticals. The processes of adsorption and degradation are often simplified. Contaminant adsorption is often assumed to be linear with regard to the contaminant concentration in the pore water. However, adsorption isotherms are often nonlinear in reality. The specific effects that occur under nonlinear adsorption may strongly affect the transport and fate of contaminants in the subsurface (Cirkel et al., 2015; van Duijn and van der Zee, 2018).

With regards to degradation of contaminants, there is often debate on whether or not adsorption of contaminants affects their bioavailability. In other words, it is uncertain whether a contaminant degrades while it is adsorbed to the soil. For example, Mrozik and Stefanńska (2014) showed that for certain pharmaceuticals, degradation is prevented due to adsorption, while Park et al. (2003) found that adsorbed contaminants were degraded significantly. Thus, both options are possible. Whether or not an adsorbed contaminant degrades may differ per contaminant and is also influenced by external factors such as the soil type. Nevertheless, these degradation concepts are important for the role that adsorption plays in the environmental fate of a contaminant.

For steady water flow conditions, Beltman et al. (2008) showed that whether or not a contaminant is degraded in the adsorbed phase determines the role of adsorption on the fate of contaminants. When adsorbed contaminants are not degraded, adsorption only affects the time it takes for contaminants to reach the groundwater table. Adsorption does not affect the total contaminant mass which is leached to the groundwater. However,

steady flow conditions are not applicable to irrigated fields. Instead, these fields are exposed to transient water flow conditions due to temporal variations in atmospheric driving forces, such as daily and seasonal fluctuations in rainfall and evapotranspiration demand. These transient conditions complicate the subsurface transport of contaminants. It is not known if the conclusions found by Beltman et al. (2008) regarding the role of adsorption are also applicable to the transient conditions typical for wastewater irrigation.

1.4 Sodium in wastewater

In addition to the general analyses mentioned in the previous sections, the effect sodium on soil structure will also be considered in this thesis. High sodium concentrations are often seen in wastewater of both municipal and industrial origin (Menneer et al., 2001). Long-term irrigation with such water therefore risks sodification of loamy and clayey soils (Rengasamy and Olsson, 1993; Schacht and Marschner, 2015). As the name suggests, a sodic soil contains a relatively high concentration of adsorbed sodium in the cation exchange complex (Bresler et al., 1982). When such a sodic soil comes into contact with low salinity water (e.g., rainwater or good quality irrigation water), the soil may swell significantly. Dense sodic layers develop which drastically impede water flow and aeration, and hinder plant root growth (Shainberg and Letey, 1984). This change in soil structure makes soils unsuitable for agriculture. Once sodic soils are degraded, remediation is difficult, time-consuming, and expensive (Lebron et al., 2002). Therefore, the focus should be on anticipation and prevention instead of remediation. To predict the degradation of sodic soils, a thorough understanding of the underlying processes is required.

The processes leading to soil structure damage occur at the microscopic scale. Clay particles are shaped like thin sheets termed platelets. The clays which are sensitive to sodicity are so-called 2:1 clays, referring to their structure of one octahedral hydroxide sheet sandwiched between two tetrahedral silicate sheets. A prime example is montmorillonite, which is the clay mineral most associated with sodicity problems. The ions in the crystal lattice of these sheets may be substituted by ions of lesser valence by a process called isomorphous substitution. For example, silicon (Si^{4+}) may be substituted by aluminium (Al^{3+}) in the tetrahedral sheets, and aluminium may be substituted by magnesium (Mg^{2+}) in the octahedral sheets. This substitution by ions of lesser valence leads to a charge deficit within the crystal lattice. The clay platelets therefore have a net negative charge which is more or less evenly distributed across the face of the clay particle (van Olphen, 1977). The magnitude of the negative charge differs for each clay mineral, as it depends on its structure. The negative charge of clay platelets is of great importance for the stability of clay soils.

Due to the negative charge of the clay platelets, cations are attracted the clay surface, while anions are repelled. The electrostatic attraction and repulsion are opposed by

thermal motion, as the ions tend to diffuse in the direction of lower ion concentration. The equilibrium situation in the so-called diffuse double layer shows an exponential increase of the cation concentration towards the clay surface, and an exponential decrease of the anion concentration (Bresler et al., 1982), as shown in Figure 1.2. The surplus of cations in the double layer screens off the negative charge of the clay platelet. Monovalent cations such as sodium are much less efficient at screening the negative charge than divalent cations such as calcium. Additionally, screening is less effective at low salt concentrations, when fewer cations are present. Therefore, the thickness of the double layer is inversely related to the ionic strength of the pore water.

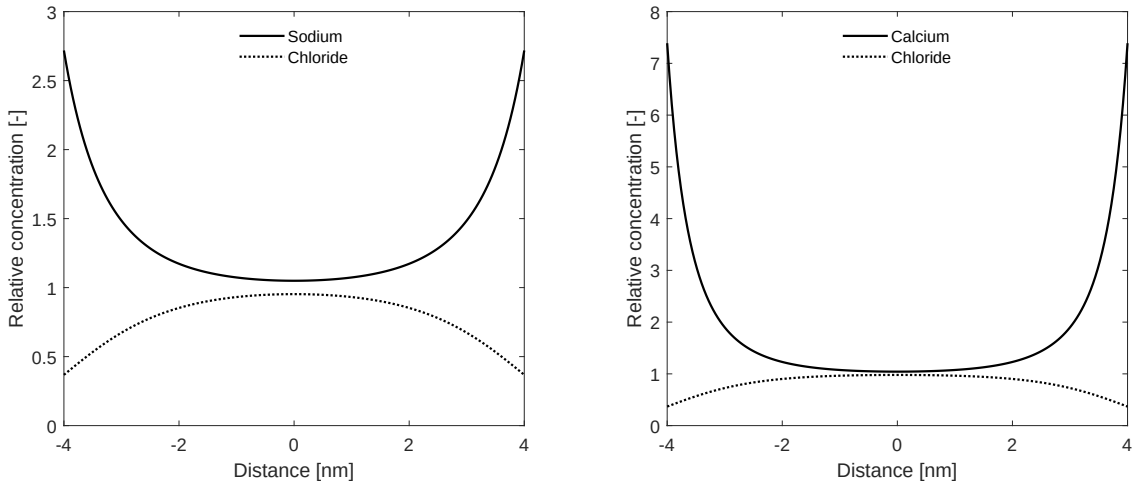

Figure 1.2: Example of the ion concentration profiles between two clay particles, for a sodium-chloride solution (NaCl) and calcium-chloride solution ($CaCl_2$). The ionic concentrations are given to their concentration in the bulk solution, unaffected by electric fields. The chloride concentration in the bulk solution is the same for both figures. The cation concentration increases towards the clay surface, while the anion concentration decreases. Note that the double layers overlap for the sodium-chloride solution, but not the calcium-chloride solution.

When the thickness of the double layer is large compared to the distance between two clay platelets, the double layers of two adjacent clay particles will overlap. When this occurs, a repulsive force known as the disjoining pressure develops between the clay particles (Derjaguin et al., 1987). The disjoining pressure pushes the adjacent clay particles apart, causing the clay to swell. Since the double layer overlap is strongest in the smallest pores, the disjoining pressure is the largest in these pores, while the disjoining pressure in the largest pores will be negligible in comparison. Therefore, the small pores grow at the expense of the larger pores (Musso et al., 2013). This shift in the pore size distribution significantly affects the soil hydraulic properties.

The shrinking of macropores causes the saturated hydraulic conductivity to decrease (Quirk and Schofield, 1955; McNeal and Coleman, 1966; Shainberg and Caiserman, 1971),

which leads to reduced water flow in soils. The soil water retention curve is also affected (Russo and Bresler, 1977; Siyag et al., 1983; Malik et al., 1992), which makes it more difficult for plants to take up water. The pore water chemistry is thus an essential parameter affecting the soil hydraulic properties. Nevertheless, this coupling is often neglected in soil-water models.

The UNSATCHEM module of Hydrus (Šimůnek et al., 2012) does include reduction of the hydraulic conductivity in response to the pore water chemistry. However, their reduction function is based on the limited empirical data from McNeal and Coleman (1966). The problem with their data is that is their reduction function is discontinuous. This yields unphysical results where small changes in sodium content can lead to large changes in the reduction function. Additionally, the effect of swelling on the soil water retention curve is neglected in UNSATCHEM. The alternative is upscaling the microscopic processes using theoretical models. Several studies attempted to scale up the effects of swelling on the saturated and unsaturated soil hydraulic properties (e.g., Russo (1988); Moyne and Murad (2002); Tuller and Or (2003); Moyne and Murad (2006); Murad and Moyne (2008)). However, these studies are limited in two ways. First, heterogeneity at the microscopic scale is often neglected. Secondly, simplified models were used to calculate the disjoining pressure between clay particles.

Many models exist for describing the disjoining pressure in the electrical double layer, with varying level of complexity. The Gouy-Chapman model is frequently used to describe the diffuse part of the double layer, which uses the Poisson-Boltzmann equation. Within this theory, ions are treated as infinitely small point charges. The Gouy-Chapman model is known to give good results for monovalent electrolyte solutions, such as sodium-chloride. However, poor matches with experiments are obtained when divalent ions such as calcium are considered. From both experimental observations (Ebeling et al., 2011) and molecular Monte Carlo simulations (Segad et al., 2010), it is known that an attractive force persists between adjacent clay particles under certain conditions in calcium-rich clays. This attractive force is not predicted by Poisson-Boltzmann theory, which only predicts repulsive forces. The Poisson-Boltzmann equation is still frequently used despite this discrepancy between experimental observations and theoretical predictions.

However, more advanced theories which includes ions of a finite size are able to predict the attractive force in calcium clays. This requires the inclusion of statistical mechanics in the model, using frameworks such as the hypernetted-chain approximation (HNC) or density functional theory (DFT). These theories are much more complex and more difficult to solve than Poisson-Boltzmann theory, which explains why these advanced theories are not used frequently. For the case of a constant surface potential, the HNC approach has been used by Kjellander et al. (1988) to explain the stability of calcium clays. Further advancements have recently been made by Le et al. (2015) for the case of a constant surface charge density, which is more realistic for clays which owe their negative charge

to isomorphous substitution Tournassat et al. (2011). These advanced models have not yet been applied to the topic of soil sodicity.

In theoretical upscaling methods, the microscopic scale is often assumed to be homogeneous. However, since the magnitude of the disjoining pressure is strongly correlated to the pore size, heterogeneity of pores at the microscopic scale is expected to significantly impact deformation, in addition to microscopic salt transport and water flow. Upscaling water flow and salt transport in such heterogeneous systems can be done with pore-network models. Within these models, the pore space is simplified and discretized in pore bodies (nodes) and pore throats (bonds). The geometry of the pores is simplified. For example, often spherical or cubic shapes are assigned to the pore bodies, and rectangular or cylindrical shapes to the pore throats. This allows for analytical solutions for water flow and salt transport at the scale of an individual pore. This makes pore-network models a computationally efficient tool. Macroscopic parameters can be obtained from pore-networks by averaging over a large number of pores. Pore-network models were first used by Fatt (1956) for multiphase flow. In recent years, the application of these models has been extended to topics such as upscaling solute transport (Acharya et al., 2005) and electrokinetics in porous media (Joekar-Niasar et al., 2013). Pore-network models may also be applied to scale up effects related to sodicity.

Upscaling sodicity effects is not limited to the disjoining pressure. The negative charge of clay particles give rise to several other phenomena which are not seen in uncharged porous media. Clay behaves like a semi-permeable membrane due to its negative charge. Therefore, gradients in salt concentration and electric potential may drive water flow through chemico- and electro-osmosis, respectively. Under certain conditions, these additional water fluxes may considerably alter the fluid pressure inside the micropores, leading to additional swelling or shrinking of soils (Barbour and Fredlund, 1989). Gradients in electric potential also affect salt transport through electromigration. Clay soils are thus a complex system, where the fluid pressure, salt concentration, and electric potential are all linked to the degradation of sodic soils. Thus, all these processes need to be included in the pore-network model for upscaling sodicity effects.

1.5 Research objectives and outline

In the previous sections, several knowledge gaps related to the impact of wastewater irrigation in agriculture were identified. Based on this, multiple research questions are defined which will be answered in this thesis.

Under steady flow conditions, it is known that the effect of adsorption on contaminant fate is determined by whether or not adsorbed contaminants are available for biodegradation. However, wastewater irrigation is characterized by transient conditions, where each irrigation event causes an input pulse of contaminants. Thus, the first research question

is:

- What is the role of adsorption for degrading contaminants under transient flow conditions?

The analysis of degradation concepts under transient flow conditions is presented in Chapter 2. Additionally, we investigate how transient conditions affect the contaminant concentration and fluxes in the root zone, concerning both the long-term average and its fluctuations in time.

Whether wastewater irrigation is sustainable depends on many factors, such as the irrigation water quality, but also the crops, climate, irrigation management, and soil type. The sustainability of each wastewater has to be determined for each individual case. Therefore, a framework is required on how to assess whether a certain wastewater irrigation practice is sustainable. The second research question is then:

- How can the sustainability of wastewater be assessed in an integrated manner?

We develop such a framework for the integrated sustainability assessment of wastewater irrigation in Chapter 3.

Next, we zoom in on sodium and its adverse effects on soil structure. The heterogeneity of pore sizes is often neglected when scaling up the microscopic process such as water flow, salt transport, and the swelling pressure. Therefore, the third research question is:

- What is the effect of pore size heterogeneity on coupled salt transport and the disjoining pressure in charged porous media?

We develop a pore-network model which is extended to include these electrokinetics in Chapter 4. This model is used to scale up salt transport in charged porous media such as clay with heterogeneous pore sizes.

Often, simplified theories are used to compute swelling at the microscopic scale. Advanced theories which include ion-ion correlations, such as density functional theory, have not been applied to the topic of soil sodicity. Hence, the final research question is:

- Can changes in hydraulic parameters of sodic soils be predicted with density functional theory?

In Chapter 5, we compute swelling at the microscopic scale using density functional theory, and relate this to changes in the macroscopic soil hydraulic parameters using a pore-network model.

Finally, the main findings of this thesis are summarized in Chapter 6. The results and their implications are discussed, and recommendations for further research directions are given.

Chapter 2

Role of degradation concepts for adsorbing contaminants in wastewater irrigation

This chapter is based on:

Cornelissen, P., van der Zee, S. E. A. T. M., Leijnse, A., (2020). Role of degradation concepts for adsorbing contaminants in context of wastewater irrigation. *Vadose Zone Journal, 19*, e20064.

Abstract

Marginal water, like treated effluent or other types of wastewater, induce contaminant accumulation in different environmental compartments such as soil and groundwater. With a root zone model and daily rainfall data as input, accumulation in case of two different degradation concepts was modelled: (i) the solute degrades only in the solution phase, and (ii) the solute degrades in both the solution and the adsorption phase. For linear adsorption, both degradation concepts not only yield similar results but also adsorption does not affect the long-term concentration. This can be readily explained with the governing equations. For nonlinear adsorption, the degradation concept does affect the concentration and fluxes. When the first concept is valid, the long-term concentration is not affected by adsorption, while the short-term and fluctuations are. For the second degradation concept, the long-term average concentration and fluxes are also affected by adsorption. A correction factor was derived to correct the analytical solution of the time-dependent concentration of nonlinearly adsorbing solutes. For all scenarios, reasonable estimates of the long-term concentration could be obtained with analytical models for most parameter combinations, which can be used to identify contaminant species that should be prioritized for further research.

2.1 Introduction

Wastewater irrigation is practiced to comply with increasing freshwater scarcity due to the growing world population and climate change (UNDP, 2006). While wastewater irrigation is currently more widespread in arid and semi-arid regions (Shetty, 2004; Lawhon and Schwartz, 2001; Hamilton et al., 2005), it has also received increasing attention recently in temperate climates to decrease the pressure on existing freshwater sources (Bixio et al., 2006). However, re-using wastewater for irrigation also introduces contaminants to the subsurface. A wide range of contaminant species can be found in wastewater, depending on its source and treatment, such as salts (Feigin et al., 1978), heavy metals (Bradl, 2004), organic compounds (Walter et al., 2000), and emerging contaminants such as pharmaceuticals (Drillia et al., 2005; Mrozik and Stefanńska, 2014; Geissen et al., 2015). These contaminant species might undergo adsorption and/or degradation in various degrees. Predicting the environmental fate of such contaminants is crucial to assess the long-term impact of wastewater irrigation on soil, crop, and groundwater quality.

Simplifications concerning degradation and adsorption are common. The debate regarding degradation has concentrated for years on whether or not adsorbed contaminant can be degraded. Ogram et al. (1985) showed that this may not be the case for a pesticide, and also regarding other degradable contaminants, the bio-availability/bio-accessibility issue has been debated. Beltman et al. (2008) showed that the impact of adsorption on leaching and on the long-term fate of solutes for single solute applications under steady flow conditions depends on whether degradation of adsorbed contaminants occurs. Contrary to the scenario considered by Beltman et al. (2008), wastewater irrigation is characterized by multiple contaminant input pulses and unsteady flow conditions, and it is thus uncertain if these conclusions are relevant for the sustainability assessment of wastewater irrigation. Additionally, adsorption is often assumed to be linear with regard to the concentration in solution, while in general it is a nonlinear process and this can induce significant differences with respect to transport (Cirkel et al., 2015; van Duijn and van der Zee, 2018).

For contaminants with small retardation factors, significant fluctuations in concentration may occur in response to daily and seasonal variations in rainfall and irrigation. The effect of erratic atmospheric forcing was investigated using a stochastic approach for soil moisture (Rodgriguez-Iturbe et al., 1999; Laio et al., 2001) and solute transport, such as salt (Suweis et al., 2010; Shah et al., 2011) and nutrients (Botter et al., 2008; Manzoni and Porporato, 2009). Analytical solutions are feasible when assuming that daily rainfall follows a Poisson distribution, but seasonal variations in precipitation cannot be accommodated then (van der Zee et al., 2014).

In this paper, we investigate the importance of degradation concepts on the environmental fate of contaminants in the context of wastewater irrigation. We therefore distinguish two

degradation concepts: one where the solute is degraded only in the solution phase, and one where the solute is degraded in both the solution and the adsorbed phase. This analysis is carried out for both linearly and nonlinearly adsorbing solutes to identify the complexities that may arise because of nonlinearity. We consider erratic weather with seasonal rainfall patterns to determine its importance for the long-term fate of contaminants. Analytical approximations are developed for average water fluxes to address the dominant features of contaminant redistribution.

2.2 Root zone model

We developed a numerical model to calculate the solute concentration under erratic atmospheric forcing. Root zone models have been used to predict soil moisture and solute concentration dynamics (Rodgriguez-Iturbe et al., 1999). Such models consider a perfectly mixed zero-dimensional root zone, and thus only consider the average moisture content and solute concentration. Adhering to previous studies by Vervoort and van der Zee (2008) and Shah et al. (2011), we consider a root zone of thickness Z_r [cm], that may be assumed homogeneous in view of annual ploughing. In the case of heterogeneous soil profiles, effective parameters can still be used to accurately model water flow and solute transport (van der Zee and Boesten, 1991; Wildenschild and Jensen, 1999). The groundwater table is located at a fixed depth Z [cm] below the root zone. The governing equations are the water and solute mass balance equations. Figure 2.1 shows a schematic representation of the root zone and the water fluxes.

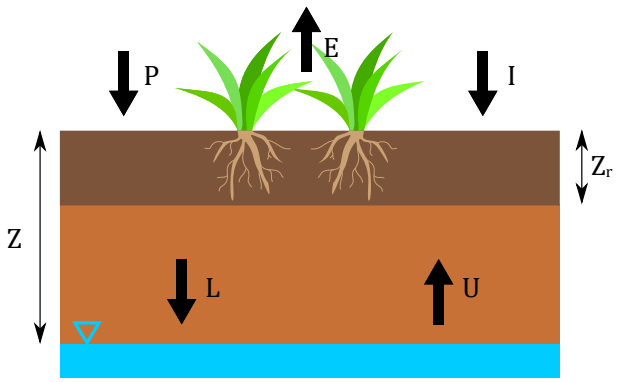

Figure 2.1: Schematic representation of the root zone at the soil surface, the underlying unsaturated zone, and saturated groundwater, as well as the water fluxes.

2.2.1 Water balance

The incoming water fluxes in the root zone are the rates of precipitation, irrigation, and capillary rise from the groundwater, respectively. The outgoing water fluxes are the rates of drainage towards the groundwater, evapotranspiration, and runoff. The water mass

balance is therefore

$$\phi Z_r \frac{ds}{dt} = P + I + U - L - E - R_o \tag{2.1}$$

where ϕ is the porosity [-], s is the soil saturation [-], P is precipitation [cm/d], I is irrigation [cm/d], U is capillary rise [cm/d], L is drainage to the groundwater [cm/d], E is evapotranspiration [cm/d], and R_o is runoff [cm/d]. The soil saturation varies between 0 and 1, denoting completely dry and fully saturated conditions, respectively.

Erratic rainfall events were assumed to be Poisson distributed in previous studies (Rodriguez-Iturbe and Porporato, 2005). While this allows for analytical expressions for the probability density function of the soil moisture content, seasonal variations in precipitation cannot be accommodated for, despite being important in many climatic regions. We therefore consider daily rainfall records from two locations with different precipitation patterns instead. The first location is Wageningen, The Netherlands (WAG), using data from the Royal Netherlands Meteorological Institute (KNMI, 2019). There are no strong seasonal variations in precipitation throughout the year, but dry periods can occur sporadically (Figure 2.2). The second location is Tennant Creek Airport, Australia (TCA). The rainfall records from the Australian Bureau of Meteorology (BOM, 2019) reveal a strong seasonal variation in precipitation (Figure 2.2), with a dry season from April to September, and a wet season from October to March. The chosen rainfall records concern a period of 30 years, spanning from April 1st, 1989 to March 31st, 2019 for both locations. The annual cumulative rainfall can vary strongly between years. These rainfall records were analysed to determine if the Poisson assumption was valid for these locations by means of a chi-square test. This was found to be unlikely for both locations, as both p-values were close to zero. All precipitation was assumed to be rain. The amount of precipitation that infiltrates into the soil is dependent on the current storage capacity of the root zone. We assume that excess water can leave the system as runoff when the storage capacity of the soil is exceeded, but this was found to be negligible in our case.

All water fluxes other than precipitation are functions of the saturation, using expressions as derived by Vervoort and van der Zee (2008). The water balance has three saturation thresholds. The first threshold is the wilting point s_w, below which plants cannot take up water. The second threshold is s_*, below which the transpiration rate of plants is less than the potential transpiration rate. The third threshold is the field capacity s_{fc}, above which water drains to the groundwater. Capillary rise is governed by evapotranspiration demand and can therefore not exceed the evapotranspiration flux. If the maximum possible capillary rise exceeds the evapotranspiration flux, we set the actual capillary flux equal to the evapotranspiration flux. The capillary rise flux, as derived by Vervoort

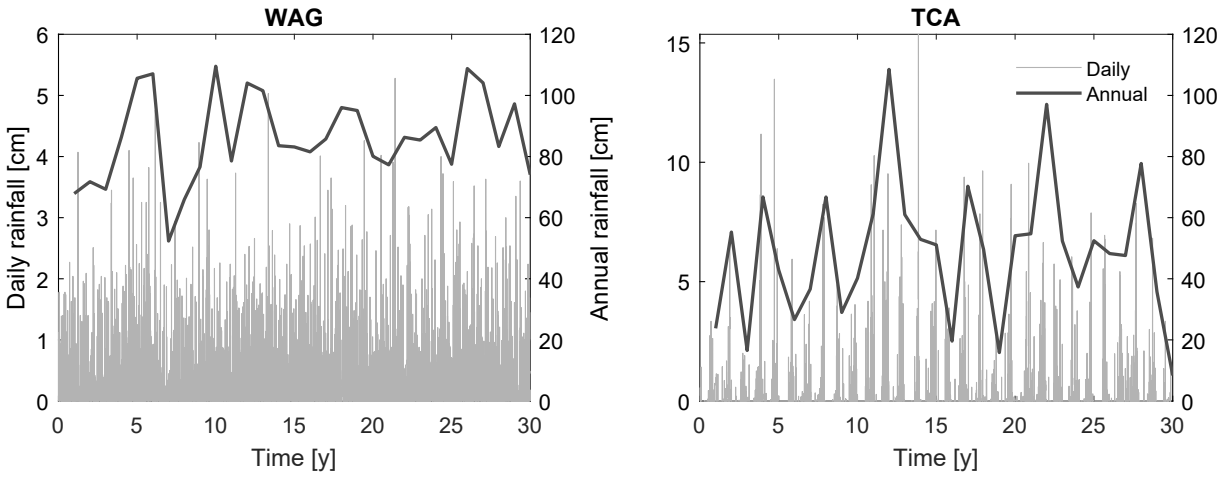

Figure 2.2: Daily and annual cumulative rainfall for both locations from April 1st, 1989 to March 31st, 2019 (KNMI, 2019; BOM, 2019).

and van der Zee (2008) is then given by

$$U = \begin{cases} 0 & s \leq s_w \\ m_2 & s_w < s \leq s_* \\ m_1(1 - \exp(\beta(s - s_{fc}))) & s_* < s < s_{fc} \\ 0 & s_{fc} \leq s \leq 1 \end{cases} \tag{2.2}$$

where $m_2 = (K_s G)/(\phi Z_r)$, with K_s the saturated hydraulic conductivity of the soil and $G = \alpha_e (h_b/Z)^{2+3/b}$ is a dimensionless parameter, h_b as the bubbling pressure [cm], the hydraulic shape parameter $\alpha_e = 1 + 3/[2(1 + 3/b)]$ [-], and the soil hydraulic shape parameter b [-] (Eagleson, 1978). Additionally, $m_1 = K_s G/(\phi Z_r 1 - \exp[\beta(s_* - s_{fc})])$, and β is a parameter to fit the hydraulic conductivity function to the exponential model (Rodriguez-Iturbe and Porporato, 2005). Drainage only occurs when the saturation is above the field capacity

$$L = \begin{cases} 0 & s < s_{fc} \\ m(\exp(\beta(s - s_{fc})) - 1) & s_{fc} \leq s \leq 1 \end{cases} \tag{2.3}$$

where $m = K_s/(\phi Z_r \exp(\beta(1 - s_{fc}) - 1))$ The field capacity is defined as $s_{fc} = (Z/h_b)^{-1/b}$, and is thus a function of the soil properties and the depth of the groundwater table. According to Teuling and Troch (2005), evapotranspiration can be expressed as

$$E = f_R \beta_T (1 - \exp(-c_T f_{LAI})) E_p \tag{2.4}$$

where f_R is the volumetric root fraction [-], β_T is a soil moisture stress function [-], c_T is a light use efficiency parameter [-], f_{LAI} is the leaf area index [-], and E_p is the potential evapotranspiration rate [cm/d], that is the evapotranspiration rate when water is not a limiting factor. The parameter β_T equals zero below the wilting point, as transpiration

cannot occur. When the saturation exceeds s_*, the evapotranspiration is equal to its maximum. In between these two saturation points, evapotranspiration is assumed to be a linear function of the saturation. The expression for β_T then yield

$$\beta_T = \begin{cases} 0 & s \leq s_w \\ \frac{s-s_w}{s_*-s_w} & s_w < s \leq s_* \\ 1 & s > s_* \end{cases} \tag{2.5}$$

These fluxes are shown in Figure 2.3 as a function of the saturation. Irrigation was not included in the work of Vervoort and van der Zee (2008) nor in the work of Shah et al. (2011). In this model, we included irrigation in a simplistic manner. When the soil water content drops below a specified threshold s_1^{irr}, and no precipitation occurs that day, a certain amount of irrigation water is applied to bring the saturation to the specified value s_2^{irr}. The duration of irrigation is spread out over one day. The saturation thresholds for irrigation are defined as

$$s_1^{irr} = s_w + I_a(s_* - s_w) \tag{2.6a}$$

$$s_2^{irr} = s_{fc} + I_b(1 - s_{fc}) \tag{2.6b}$$

Both parameters I_a [-] and I_b [-] can vary between 0 and 1. Irrigation starts when the saturation drops below a certain value between the wilting point and the point below which transpiration becomes limited. The saturation is then brought to a point between field capacity and full saturation.

2.2.2 Solute mass balance

We can write a general mass balance for solutes (contaminants) that allows for adsorption and degradation of solutes. While groundwater can be a source of solutes, we disregard this and assume groundwater capillary rise will only dilute rootzone water. For a negligible contaminant concentration in rainwater and groundwater, the solute mass balance equation is given by

$$\frac{dM}{dt} = IC_i - LC - Q - T \tag{2.7}$$

where M is the solute mass [g/cm^2], C_i is the solute concentration in the irrigation water [g/cm^3], C is the solute concentration in the root zone [g/cm^3], Q is the removal by degradation [g/cm^2/d], and T is the removal by plant uptake [g/cm^2/d].

The total solute mass is the sum of the mass in solution and the mass adsorbed to the solid phase: $M = Z_r(\phi sC + \rho_b q)$, where ρ_b is the soil dry bulk density [g/cm^3], and q is the adsorbed mass fraction [-]. We assume that adsorption can be described by the Freundlich isotherm, which relates the adsorbed mass to the solute concentration in solution: $q = K_F C^n$, where K_F [cm^{3n}/g^n] and n [-] are empirical constants. This reduces to linear adsorption when $n = 1$.

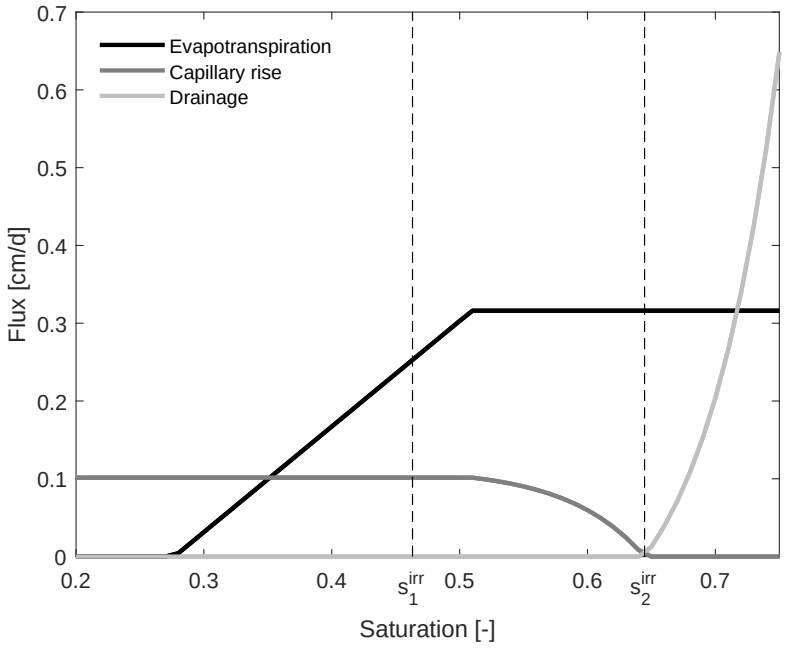

Figure 2.3: Illustration of water fluxes as a function of the soil saturation, for a sandy clay loam soil, grass vegetation, and a groundwater depth of 200 cm. The two dotted lines indicate the irrigation thresholds with $I_a = 0.8$ and $I_b = 0$.

The description of the degradation rate is crucial for this study. There is ongoing debate on the bioavailability of adsorbed contaminants. Bioavailability is generally defined as the amount of solute which is readily available and accessible for uptake by organisms (Riding et al., 2013). Bacteria may be unable to take up solute from the adsorbed phase, and thus adsorption may reduce the bioavailability of the solute. This was found to be the case for some pesticide species (Ogram et al., 1985; Guo et al., 2000) and pharmaceuticals (Mrozik and Stefanńska, 2014), which were degraded only in the solution phase. However, significant degradation in the adsorption phase can occur (Park et al., 2003). Whether degradation occurs in the adsorbed phase was found to significantly affect the role adsorption plays for the environmental fate of the solute (Beltman et al., 2008). This distinction is often not made, despite significantly impacting the environmental fate of contaminants. We extend the analysis of Beltman et al. (2008) to transient flow conditions, as is characteristic for wastewater irrigation. Therefore, we consider two scenarios: (I) one where the solute degrades only in the solution phase, and (II) one where degradation occurs in both the solution and adsorbed phase with equal degradation rate constants in both phases. When concept I is valid instead, the degradation rate is a linear function of only the mass in the solution phase

$$Q = \mu \phi s Z_r C \tag{2.8}$$

where μ is the degradation rate constant [1/d] under concept I. When concept II is valid,

the degradation rate is expressed as a linear function of the total solute mass:

$$Q = \lambda M = \lambda Z_r(\phi s C + \rho_b K_F C^n) \tag{2.9}$$

with λ the degradation rate constant [1/d] under concept II. To compare both degradation concepts, we modify the degradation rate constant such that the total degradation rates in both concepts are equal. For linear adsorption, this yields

$$\lambda = \frac{\phi\langle s\rangle}{\phi\langle s\rangle + \rho_b K_F}\mu = \frac{\mu}{R} \tag{2.10}$$

where $\langle s\rangle$ is the saturation averaged over the whole simulation period, and R is the average linear retardation factor

$$R = 1 + \frac{\rho_b K_F}{\phi\langle s\rangle} \tag{2.11}$$

Thus, the degradation rate constant under concept II is smaller than in concept I, yet compensated by the additional degradation in the adsorbed phase. For nonlinearly adsorbing solutes, the retardation factor is a function of the concentration. A rate constant scaled by the retardation factor similar to Equation 2.10 cannot be derived for the nonlinear case, as it would only be valid for a single concentration. Therefore, we use the same expression as for the linear case.

Finally, we require an expression for the plant uptake rate. This is assumed to be a linear function of a rate constant and the evapotranspiration rate, as most of the contaminants under consideration are not nutrients (Dietz and Schnoor, 2001; Mathur, 2004). We assume that plants only remove contaminants from the solution phase. Thus, we obtain $T = \alpha E C$, where α is the uptake rate constant [-].

Substituting the above expressions for mass, degradation rate, and uptake rate into the solute mass balance equation and rearranging yields

$$\phi s Z_r R_c \frac{dC}{dt} = IC_i - \left(L + \lambda\phi s Z_r + \alpha E + \phi Z_r \frac{ds}{dt}\right) C - \lambda\rho_b Z_r K_F C^n \tag{2.12}$$

where

$$R_c = 1 + \frac{\rho_b K_F}{\phi s} n C^{n-1} \tag{2.13}$$

is the concentration-dependent retardation factor [-].

2.2.3 Analytical solutions

If we disregard the complexity of erratic weather and fast fluctuations of the concentration, we can focus on the main features of the mode such as the average solute concentration and fluxes. The solute mass balance equation then becomes analytically tractable. While it is already known that this yields reasonable results for most field conditions (Kuntz and Grathwohl, 2009), this may not be the case for extreme infiltration events, such as

during irrigation or the seasonal rainfall of the TCA climate. We rewrite Equation 2.12 with average water fluxes and saturation. Thus

$$\bar{R}_c \frac{dC}{dt} = \langle I \rangle C_i - \left(\langle L \rangle + \lambda \phi Z_r \langle s \rangle + \alpha \langle E \rangle \right) C - \lambda \rho_b Z_r K_F C^n \tag{2.14}$$

where $\bar{R}_c = 1 + \rho_b K_F n C^{n-1} / (\phi \langle s \rangle)$ is the average nonlinear retardation factor, and the $\langle \cdot \rangle$ operator denotes the time-average over the entire simulation period of 30 years. We rewrite Equation 2.14 using the dimensionless variables $\hat{t} = t \langle L \rangle / (\phi \langle s \rangle Z_r)$, $\hat{C} = \langle L \rangle C / (\langle I \rangle C_i)$ and the Damköhler numbers $Da_{sol} = \lambda \phi \langle s \rangle Z_r / \langle L \rangle$, $Da_{plant} = \alpha \langle E \rangle / \langle L \rangle$, and $Da_{ads} = \lambda \rho_b Z_r K_F \langle I \rangle^{n-1} C_i^{n-1} / \langle L \rangle^n$, yielding

$$\bar{R}_c \frac{d\hat{C}}{d\hat{t}} = 1 - (1 + Da_{sol} + Da_{plant}) \hat{C} - Da_{ads} \hat{C}^n \tag{2.15}$$

The Damköhler numbers can be used to quickly identify the important transport processes, since they indicate the relative importance of the fluxes compared to leaching. Degradation in the solution phase is reflected by Da_{sol}, plant uptake by Da_{plant}, and degradation in the adsorbed phase by Da_{ads}. It should be noted the Damköhler numbers only indicate the average importance of the transport processes over the whole simulation period. Strong variations of the actual importance of each flux may occur through time. Equation 2.15 also suggests the concentration at steady state is independent of adsorption when there is no degradation in the adsorbed phase (i.e., $Da_{ads} = 0$). For linearly adsorbing solutes, Equation 2.15 can be readily solved for the concentration

$$\hat{C}(\hat{t}) = \frac{1}{1 + Da_{sol} + Da_{plant} + Da_{ads}} - \left(\hat{C}_0 - \frac{1}{1 + Da_{sol} + Da_{plant} + Da_{ads}} \right) \exp\left(- \frac{(1 + Da_{sol} + Da_{plant} + Da_{ads}) \hat{t}}{R} \right) \tag{2.16}$$

where $\hat{C}_0$ is the dimensionless initial concentration and R is the average linear retardation factor, as defined earlier. Contrarily to the nonlinear retardation factor, the linear retardation factor is not a function of the solute concentration. A general analytical solution for Equation 2.15 is not available for the case of nonlinear adsorption, except for special cases when $n = 0.5$ and the solute mass in the solution phase is negligible. This is a reasonable approximation for large retardation factors. Equation 2.14 can then be rewritten as

$$\frac{dM}{dt} = A - \gamma M - B M^2 \tag{2.17}$$

where A is the input rate [g/cm^2/d]. For a solute which degrades in both the solution phase and the adsorbed phase, $B = (\langle L \rangle + \alpha \langle E \rangle) / ((Z_r \rho_b K_F)^{1/n})$ is a coefficient for the combined effect of leaching and plant uptake and $\gamma = \lambda$ is the degradation rate constant. For a solute which degrades only in the solution phase, $B = (\langle L \rangle + \alpha \langle sE \rangle \phi Z_r + \lambda \langle s \rangle \phi Z_r) / ((Z_r \rho_b K_F)^2)$

and $\gamma = 0$. Equation 2.17 is easily integrated (Boekhold and van der Zee, 1991), yielding

$$M(t) = \frac{2A(e^{Dt} - 1) - (\gamma - D)M_0 e^{Dt} + (\gamma + D)M_0}{2BM_0(e^{Dt} - 1) - (\gamma - D) + (\gamma + D)e^{Dt}} \tag{2.18}$$

where $D = (\gamma^2 + 4AB)^{1/2}$. Approximating the solute mass as before, we have for the solute concentration

$$C(t) = \left(\frac{M(t)}{Z_r \rho_b K_F}\right)^2 \tag{2.19}$$

When degradation in the solution phase is significant, Equation 2.19 must be multiplied by a correction factor to obtain the correct concentration at steady state. The derivation of the correction factor is shown in Appendix 2A, and is defined as

$$\begin{aligned} f = \Bigg[& 2(1 + Da_{plant})^2 \Big(Da_{ads}^2 + 2(1 + Da_{sol} + Da_{plant}) \\ & - \sqrt{4(1 + Da_{sol} + Da_{plant}) Da_{ads}^2 + Da_{ads}^4} \Big) \Bigg] \Big/ \Bigg[2(1 + Da_{sol} + Da_{plant})^2 \\ & \times \left(Da_{ads}^2 + 2(1 + Da_{plant} - \sqrt{4(1 + Da_{plant}) Da_{ads}^2 + Da_{ads}^4} \right) \Bigg] \end{aligned} \tag{2.20}$$

This correction factor is applied to Equation 2.19 at every time step, even though it is derived for the steady state situation. All results for the nonlinearly adsorbing solute presented further on are the corrected concentrations.

2.2.4 Model parameters

The parameter values used in the numerical model are presented in Table 2.1. The soil properties are based on a sandy clay loam soil from Shah et al. (2011), based on standard Australian soils in Neurotheta (Minasny and McBratney, 2002). The vegetation properties are based on grass (Porporato et al., 2001; Whitehead and Beadle, 2004). The dry bulk density of the soil is calculated as $(1 - \phi)\rho_s$, where ρ_s is the density of the solid phase [g/cm^3]. The groundwater table is located 200 cm below the root zone, which is representative for large parts of The Netherlands (van Duijvenbooden et al., 1987) and other delta areas. We consider three irrigation scenarios with different saturation thresholds when irrigation starts. The irrigation threshold for the start of irrigation $I_a = 0.8$, meaning the crops are under occasional drought stress, but the evapotranspiration rate is mostly optimal. The threshold I_b is chosen as 0, because there is already sufficient drainage due to rainfall without having drainage after irrigation events. The minimum leaching fractions are 22 and 44% for TCA and WAG, respectively. The water fluxes and saturation required for the analytical model have been obtained by averaging the numerical results. The initial concentration cannot be set to zero, as the retardation factor is inversely related to the solute concentration. Therefore, we chose an arbitrary small

initial concentration. The value for the plant uptake coefficient was chosen such that plant uptake flux is of similar magnitude as the leaching flux. The degradation rate constant varies between 0 and 12.5 [1/y], corresponding to solute half-lives of infinity to 20 days, such that the wide range of degradation rates found in soils is represented (Stamatelatou et al., 2003; Zhang et al., 2013). The adsorption coefficient ranges from 0 to 1.1781, such that the average linear retardation factor ranges from 1 to 10. For nonlinearly adsorbing solutes, the retardation factor is a function of the solute concentration and thus highly variable. The solute concentration in the irrigation water is constant at 0.1 g/cm^3.

Table 2.1: Soil, vegetation and solute properties used in the model.

Symbol	Parameter	Value
ϕ	Porosity [-]	0.367
K_s	Saturated hydraulic conductivity [cm/d]	52.08
b	Pore size distribution number [-]	6.4069
ρ_s	Density of solid phase [g/cm^3]	2.6
ρ_b	Dry bulk density [g/cm^3]	1.6458
Z	Depth of groundwater table [cm]	400
Z_r	Root zone depth [cm]	40
s_w	Saturation at wilting point [-]	0.2768
s_*	Saturation at limited transpiration [-]	0.5097
E_p	Potential evapotranspiration rate [cm/d]	0.5
f_{LAI}	Leaf area index [-]	2.5
c_T	Light use efficiency coefficient [-]	0.4
f_R	Root fraction [-]	1.0
C_0	Initial solute concentration [g/cm^3]	10^{-5}
C_i	Solute concentration in irrigation water [g/cm^3]	0.1
K_F	Freundlich adsorption constant [cm^{3n}/g^n]	0-1.1781
n	Freundlich adsorption exponent [-]	0.5, 1
λ	Degradation rate constant [1/y]	0-12.5
α	Plant uptake rate constant [-]	0.15

2.3 Results and discussion

2.3.1 Saturation and water fluxes

Before discussing the role of the degradation concept on solute transport, we first consider the water fluxes. The average saturation and water fluxes are shown in Table 2.2 for both climates. The soil saturation is held above a certain threshold by irrigation. Therefore, the average saturation and several of the water fluxes are similar under both climates. However, their change over time is significantly different. Therefore, we show the water

fluxes over time during the final five years of the simulation (Figure 2.4). At TCA, both the saturation and its variation are much smaller during the dry season than during the wet season. This causes the average saturation to be slightly lower at TCA than at WAG. The dry season also requires frequent irrigation to prevent the saturation to drop to critical levels. The amount of irrigation is the same per event for both climates, but the higher irrigation frequency at TCA results in larger annual irrigation rates than at WAG. The magnitude of the capillary fluxes from the groundwater is limited by the saturation range induced by irrigation. Therefore, the capillary fluxes do not vary strongly between both climates. However, the capillary flux is generally larger at TCA because of the drier conditions. The drainage events are relatively spread out throughout time at WAG, because there is no distinct seasonality in rainfall. At TCA, however, the drainage events are concentrated in the wet season. The drainage rate per event is generally much larger at TCA, since all the rainfall is concentrated in a small timeframe. Surprisingly, the average annual drainage rate is similar for both climates. This means that these two opposing effects cancel each other out in this particular case. The minimum and maximum evapotranspiration rates are equal between both climates, since the saturation is kept within a certain range and equal potential evapotranspiration rates are used. However, the evapotranspiration rate is generally lower at TCA than at WAG, because the crops experience drought stress during the dry seasons. On average, the annual evapotranspiration rates are similar between both climates. The differences in water fluxes of both climates significantly affects the change of the solute concentration in the root zone, which is expanded upon in the appendix (Figure 2C.1).

Table 2.2: Average saturation and water fluxes over the whole simulation period of 30 years, for a groundwater depth of 200 cm and irrigation parameters $I_a = 0.8$ and $I_b = 0$.

Climate	**s [-]**	**I [cm/y]**	**U [cm/y]**	**L [cm/y]**	**E [cm/y]**
WAG	0.587	22.12	21.47	16.29	113.41
TCA	0.556	57.59	27.76	16.61	111.27

2.3.2 Nonreactive solute transport

First, we consider the transport of tracers to see how the climate affects solute transport. Thus, we consider a solute which does not adsorb, does not degrade, and is not taken up by plants. The concentration over time is shown in Figure 2.5 for both climates. Generally, the concentration is higher for the TCA climate. This is no surprise, because the irrigation rate is much higher, while the drainage flux is similar to that of WAG. Since irrigation is the only contaminant source in our model, this results in higher concentrations at TCA. The concentration also follows a seasonal pattern at TCA. The concentration rises during the dry season when there is frequent irrigation and the soil water content is lower, and the concentration drops during the wet season, where there is significant drainage. Nevertheless, the minimum and maximum concentrations show strong variation per year,

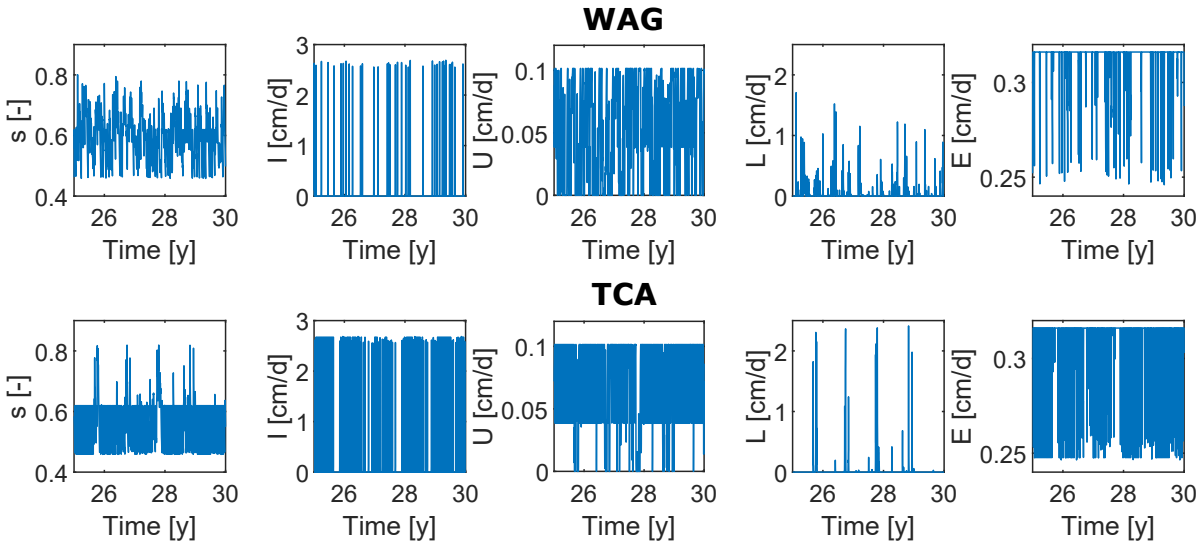

Figure 2.4: Impression of the saturation and water fluxes for both climates during the final five years of the simulation.

because of interannual differences in rainfall. Under the WAG climate, the concentration is much lower, because not as much irrigation is required. Strong fluctuations of the concentration are observed here due to occasional dry or wet periods, but they do not follow a seasonal pattern.

2.3.3 Role of the degradation concept

As mentioned before, we distinguish two degradation concepts: (I) a solute which only degrades in the solution phase, and (II) a solute which degrades in both the solution phase and the adsorbed phase. We can then define scenarios L-I and II-L for linearly adsorbing solutes, and I-NL and II-NL for nonlinearly adsorbing solutes. Non-adsorbing solutes can then be considered as a special case of either linear and nonlinear adsorption with K_F=0. To illustrate the effect of the degradation concept, the concentration over time for a non-adsorbing, linearly adsorbing, and nonlinearly adsorbing solute is shown under both degradation concepts in Figure 2.6, for select realisations out of the parameter range mentioned earlier. The probability density functions of the concentration of these solutes are shown in Figure 2D.1.

For linearly adsorbing solutes, the concentration over time is nearly identical under both degradation concepts. While there is additional degradation in the adsorbed phase in concept II, we used a lower degradation rate constant such that the total degradation rate is equal to that in concept I on average. The degradation rates thus may not be equal in both concepts at specific points in time. As a result, there are minor differences of up to 3% between both degradation concepts. The degradation concept thus does

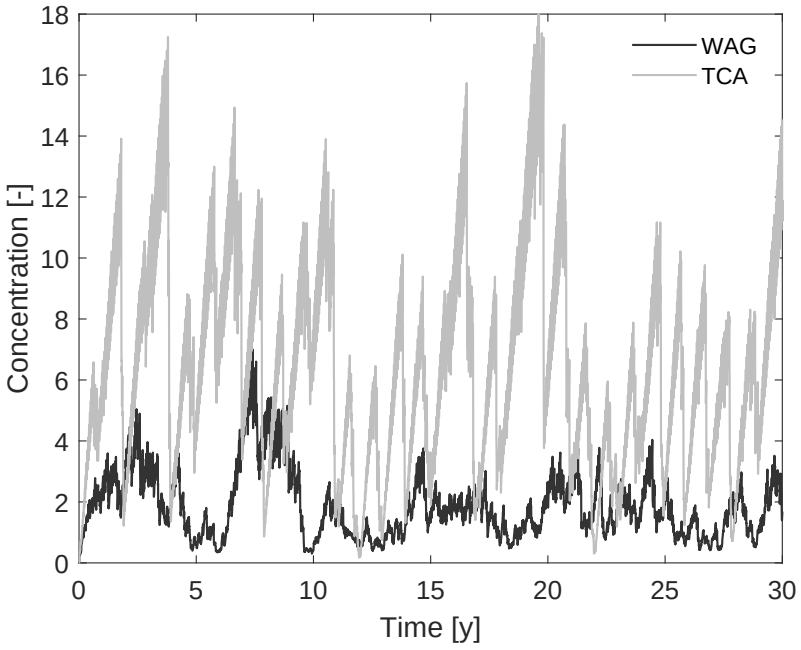

Figure 2.5: Dimensionless concentration C/C_i as a function of time for both climates, for a non-degrading and non-adsorbing solute.

not impact the fate of linearly adsorbing solutes as long as the total degradation rates are equal between both concepts. However, the concentration of nonlinearly adsorbing solutes differs strongly between the two degradation concepts. Significantly smaller concentrations occur under concept II, despite that we used a lower degradation rate constant to account for the additional degradation in the adsorbed phase. The solute mass is also lower for nonlinear adsorption under concept II (Figure 2D.2). However, the reduction of the degradation rate constant according to Equation 2.10 is based on linearly adsorbing solutes, since an analytical expression for nonlinear adsorption could not be derived. An even smaller degradation rate constant is required to obtain similar results to concept I. This suggests that the retardation factor of the nonlinearly adsorbing solute is larger than that of the linearly adsorbing solute.

Indeed, the retardation factor of nonlinearly adsorbing solutes is larger than that of linearly adsorbing solutes (Figure 2.7). The linear retardation factor is equal to 5 on average, and only varies slightly because the fluctuating soil water content (Equation 2.11). Therefore, the linear retardation factor is similar for both climates, which is why only the result of TCA is presented for the linear case. In contrast, the nonlinear retardation factor is also inversely related to the solute concentration (Equation 2.13), which causes the nonlinear retardation factor to be larger than the linear retardation factor. Additionally, lower solute concentrations lead to larger retardation factors. The concentrations are higher in TCA, since more irrigation is required to prevent the soil from drying out. Therefore, the retardation factors at TCA are lower than at WAG. Likewise,

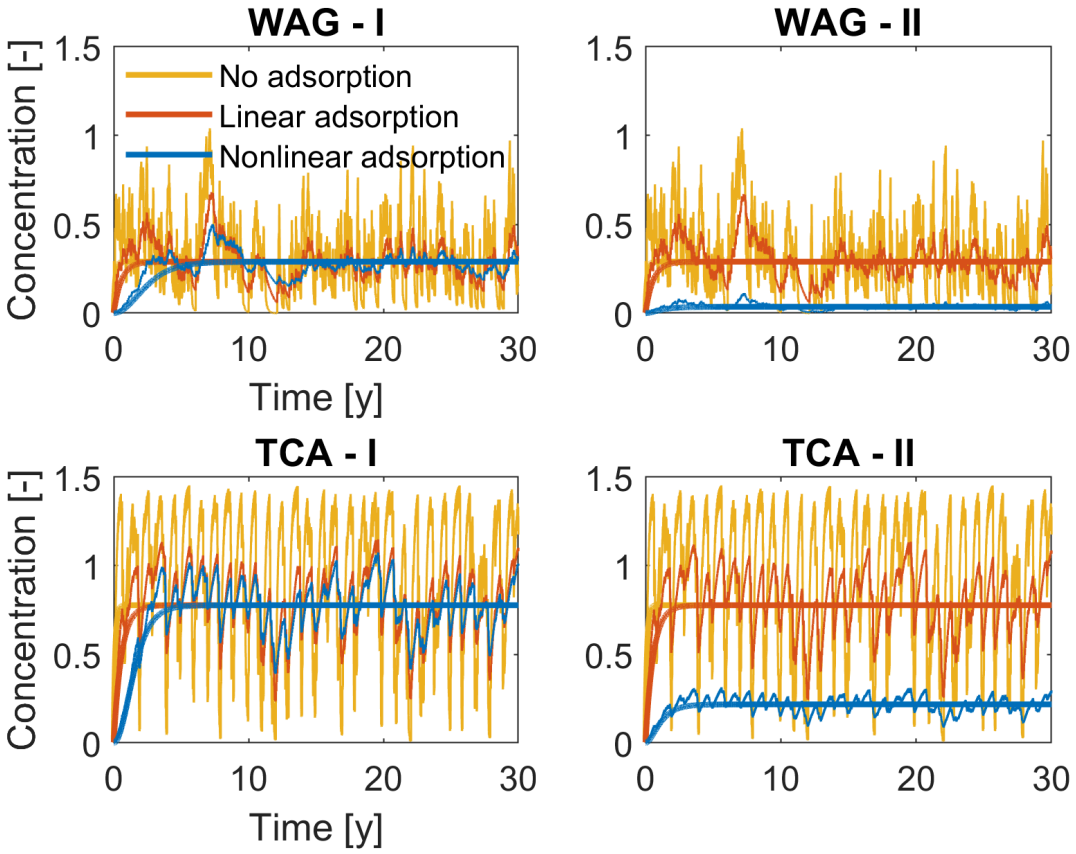

Figure 2.6: The daily average dimensionless concentration C/C_i over time as calculated by the numerical model (fluctuating lines) and analytical model (smooth lines) for non-adsorbing, linearly adsorbing, and nonlinearly adsorbing solutes. These simulations used a solute half-life of 50 days and adsorption coefficient of 0.5, giving the average linear retardation factor of 5.

the concentration is lower under degradation concept II, because of the additional degradation in the adsorbed phase. Therefore, the retardation factors are higher under concept II than under concept I. At low concentrations, the retardation factor is also more sensitive to changes in the concentration. This is seen especially under concept II, where the fluctuations of the retardation factor compared to its mean value are larger at WAG than at TCA.

Despite the differences in retardation factor, Figure 2.6 shows that the long-term average concentration is independent of the adsorption isotherm under degradation concept I. Additionally, the long-term average concentration was also found to be insensitive to the adsorption coefficient (Appendix C). We can see from Equation 2.14 that when there is no degradation in the adsorbed phase, the retardation factor only occurs in the time-derivative term. This means that at steady state, when the time-derivative term equals zero, the solute concentration and fluxes are independent of the retardation factor.

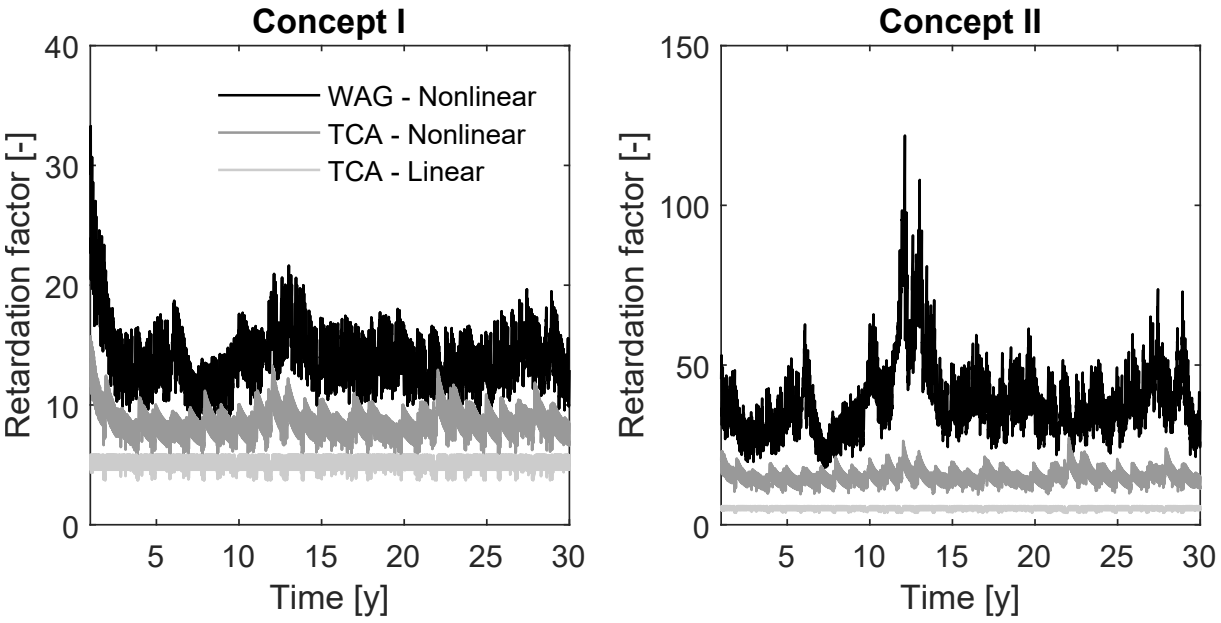

Figure 2.7: Retardation factor over time under both degradation concepts corresponding to the simulations of Figure 2.6. The results of linearly adsorbing solutes at WAG are omitted, since they are not significantly different from those of TCA. Note the difference scales on the y-axis between both concepts: the retardation factor for linear adsorption is the same for both concepts.

However, Equation 2.14 considers the simplified case with average water fluxes. Our results confirm this also applies to transient water flow conditions. Similar results were presented by Beltman et al. (2008), who found that the leached mass fraction of single solute applications was insensitive to adsorption under steady flow conditions. As we have shown, this also applies to multiple input pulses and transient flow conditions, and not only the leached mass fraction, but also the long-term average solute concentration in the root zone is insensitive to the adsorption coefficient and nonlinearity.

Likewise, the long-term solute fluxes are also insensitive to adsorption under degradation concept I. The effect of the degradation concepts and adsorption isotherms on the leached solute mass is shown in Figure 2E.1. The magnitude of the solute fluxes during the final ten years relative to the solute input are presented in Figure 2.8 as a function of the degradation rate constant. The results of scenario II-L are omitted, since they are identical to scenario I-L. The plant uptake rate and leaching rate are similar in all scenarios because of the chosen value of the plant uptake coefficient. The fluxes in scenarios I-L and I-NL are very similar, with only minor differences caused by the difference in retardation factor. The fluxes in scenario II-NL are significantly different. The lower concentrations here enhance adsorption and create a positive feedback loop that promotes degradation in the adsorbed phase, while the importance of leaching and plant uptake is diminished. For high degradation rate constants, up to 97% of the incoming solute mass is degraded

in scenario II-NL, compared to 75-78% in scenarios I-L and I-NL.

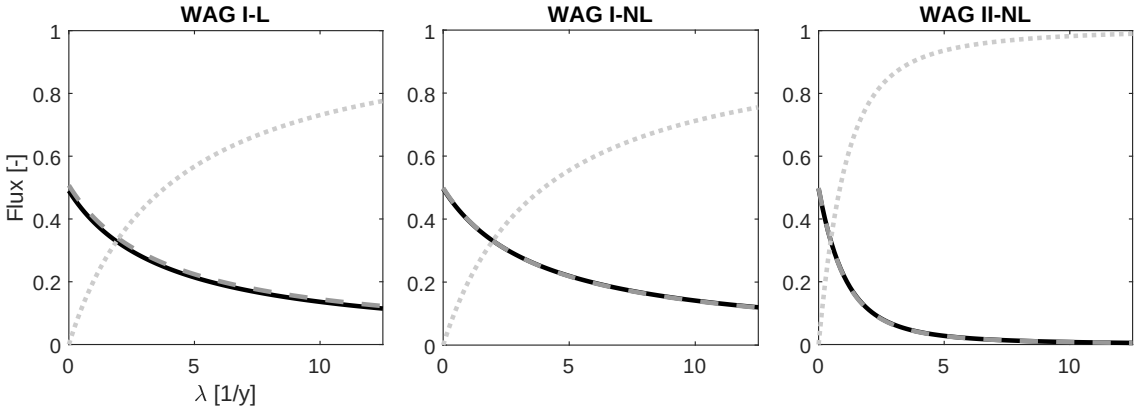

Figure 2.8: Solute fluxes relative to the contaminant input averaged over the final ten years of the simulation as a function of the degradation rate constant at WAG. The results of TCA are omitted since they are similar. The adsorption coefficient is set such that the linear retardation factor $R = 5$.

Despite adsorption having little effect on the long-term average concentration and fluxes, Figure 2.6 shows that adsorption does affect the time it takes to reach the long-term concentration. Since the annual rainfall varies per year, a true steady state is never reached. Instead, the long-term concentration fluctuates around an average value, which we consider the steady state concentration for this case. The time it takes to reach steady state is shown as a function of the degradation rate constant and the adsorption coefficient for the aforementioned scenarios in Figure 2.9. For linear adsorption, the adsorption coefficient can be converted to the retardation factor. However, for nonlinear adsorption this cannot be done, since the retardation factor is also a function of the solute concentration. Generally, it takes more time to reach the equilibrium situation for higher adsorption coefficients. For linear adsorption, equilibrium is reached faster for large degradation rate constants. For nonlinear adsorption, this does not need to be the case, as lower concentrations increase the retardation factor. Since the retardation factor of nonlinearly adsorbing solutes is larger than that of linearly adsorbing solutes, it takes more time to reach steady state for nonlinearly adsorbing solutes. There are no differences between scenarios I-L and II-L, which is why scenario II-L is omitted. For nonlinear adsorption, it generally takes more time to reach steady state in scenario I-NL than in II-NL. Although the retardation factor is larger for II-NL, the equilibrium situation is reached faster due to the larger degradation rate compared to I-NL.

Additionally, adsorption also affects the amplitude of high frequency fluctuations. The magnitude of the fluctuations with respect to the average concentration may be quantified by the normalized range wherein 90% of the concentration observations fall: $(C_{95} - C_5)/\langle C \rangle$, with C_5 and C_{95} as the 5th and 95th percentiles, respectively. This concentration

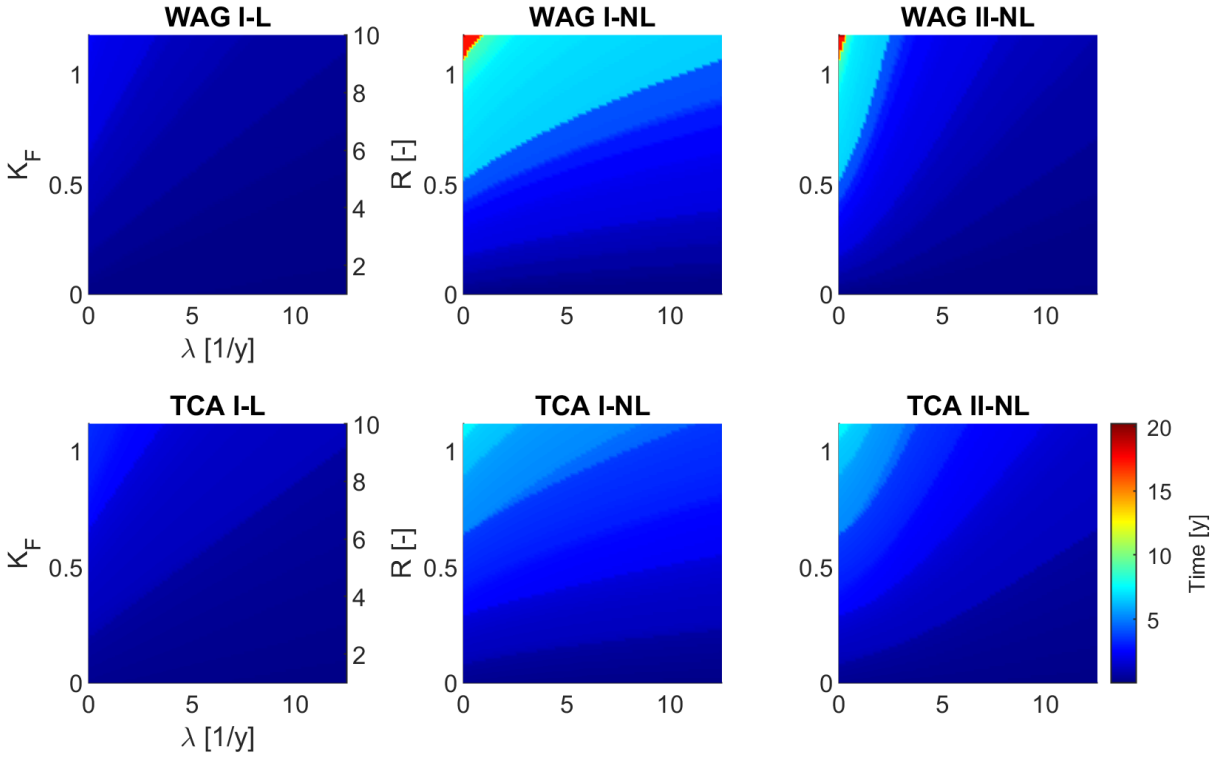

Figure 2.9: Time it takes to reach the average long-term concentration for the degradation scenarios for both climates. The results of scenario II-L have been omitted, since they are similar to scenario I-L.

range is shown as a function of the degradation rate constant and adsorption coefficient in Figure 2.10 for the different scenarios. The dashed lines in Figure 2.10 indicate where the concentration range equals 1, which means that the fluctuations are equal to the mean value. The results of scenario II-L are again omitted due to their similarity to the results of scenario I-L. In general, larger adsorption coefficients reduce the magnitude of the fluctuations due to the buffering effect of adsorption, while larger degradation rate constants increase the magnitude of the fluctuations. The concentration range is smaller in scenario I-NL compared to scenario I-L, since the retardation factor of nonlinearly adsorbing solutes is larger. In scenario II-NL, the fluctuations are larger than in the other scenarios. Rapid degradation in combination with small average concentrations result in large normalized concentration ranges. This indicates that strong deviations from the average concentration occur due to the erratic weather conditions, which may affect the environmental risk of wastewater re-use practices. Fluctuations in concentration also affect the variability of solute fluxes, such as the leached solute mass (Table 2E.1 in the Appendix).

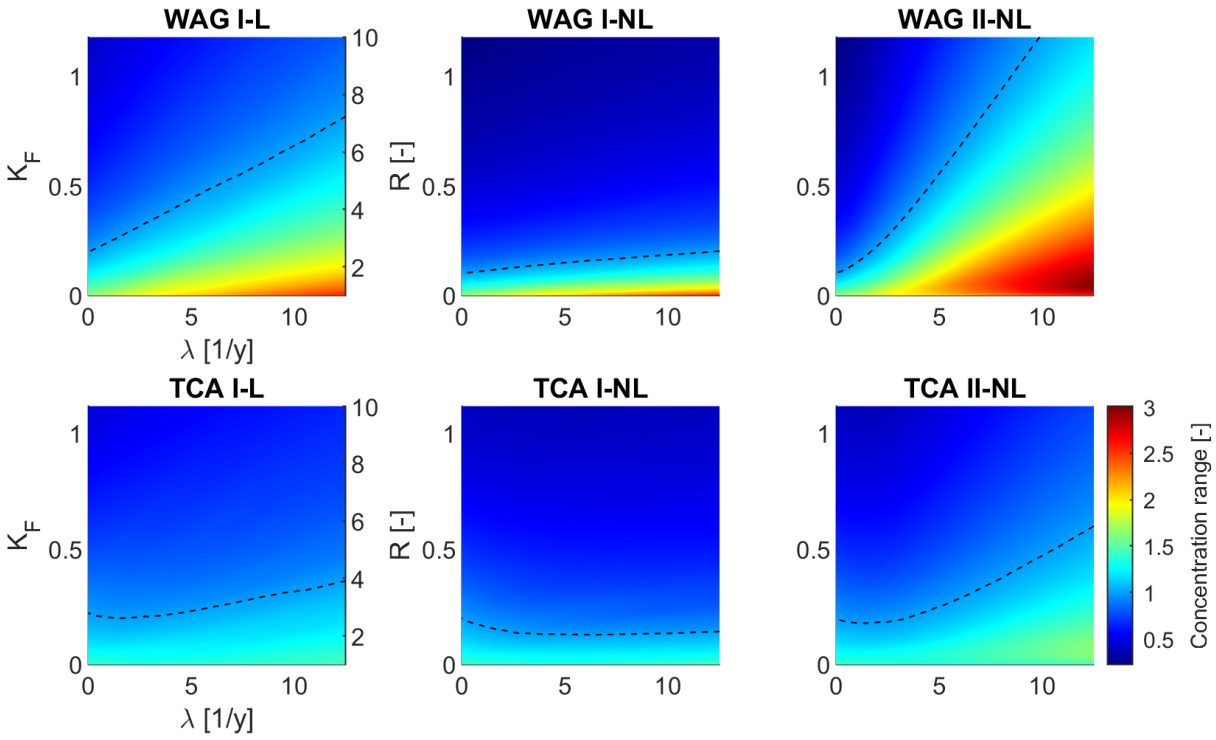

Figure 2.10: Concentration range normalized by the numerical average concentration, defined as $(C_{95} - C_5)/\langle C \rangle$, during the final ten years of the simulation, as a function of the adsorption coefficient and the degradation rate constant in Wageningen. The units of K_F are cm^3/g for linear adsorption and $\mathrm{cm}^{1.5}/\mathrm{g}^{0.5}$ for nonlinear adsorption. The realisations from Figure 2.6 correspond to $K_F = 0.5$ and $\lambda = 5$.

2.3.4 Approximation by analytical solutions

Figure 2.6 shows that the short-term concentration is approximated well for TCA for all degradation concepts and adsorption isotherms. However, the concentration at early time is underestimated by the analytical model compared to the numerical results. Similar results have been found for the whole range of degradation rate constants and adsorption coefficients. At WAG, the precipitation rate is low during the first five years compared to the 30-year average annual precipitation. Therefore, more irrigation is required during this period, which leads to a quick rise of the concentration. However, the analytical model uses the 30-year annual average fluxes. Extreme situations such as these initial dry years are therefore smoothed out. Time series of irrigation (as in this study) that differ significantly in the first years compared with the entire period, may therefore bias the prediction accuracy with simple models.

For the long-term concentration, we indicate the agreement between both models by the ratio of the analytical and numerical solutions C_{an}/C_{num}. The approximation of the long-term concentration is presented as a function of the degradation rate constant and adsorption coefficient in Figure 2.11. The results of II-L are omitted since they

are comparable to I-L. For I-L and II-L, the analytical approximation of the long-term average concentrations lies within 10% of the numerical result for WAG, and 22% for TCA. The poorest approximations are made for non-adsorbing and non-degrading solutes. For such solutes, the concentration fluctuations are larger since they are not attenuated by adsorption. These fluctuations in concentration affect the average concentration as calculated by the numerical model. However, the fluctuations are not included in the analytical model, which causes the discrepancy between the numerical and analytical models. Similar results are seen for I-NL, but the approximations are slightly worse compared to linear adsorption. For II-NL, the error is up to 20% at both WAG and TCA, but within 10% for most parameter combinations. At WAG, the poorest approximations are seen for large degradation rate constants but small adsorption coefficients. Under such conditions, the concentration fluctuations are large (Figure 2.10), since there is strong degradation and little attenuation by adsorption. However, the concentration cannot drop below zero, and thus the concentration distribution becomes truncated (Figure 2D.1). This results in the average concentration to be larger in the numerical model than in the analytical model, which yields the larger discrepancies between both models. This effect is not seen at TCA, since the higher irrigation rate there yields a larger concentration, and the concentration distribution therefore does not become truncated.

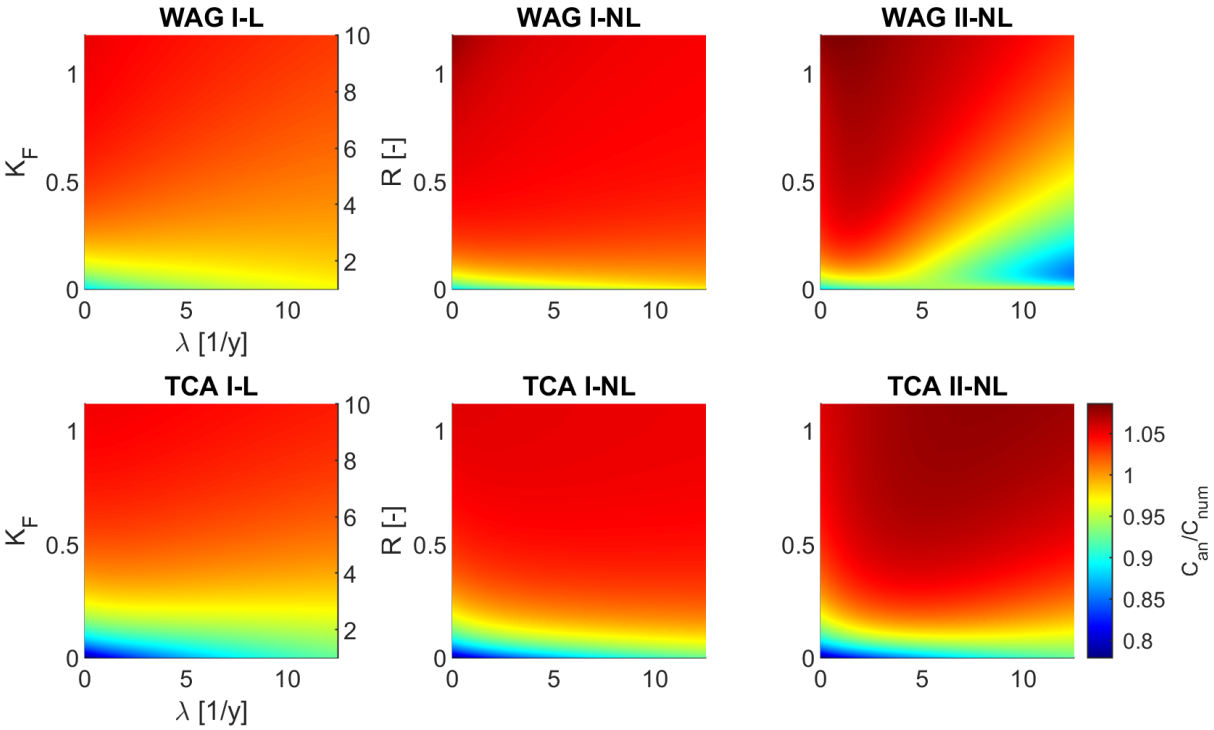

Figure 2.11: Ratio of the analytical and numerical solutions as a function of the degradation rate constant and the adsorption coefficient. The units of K_F are cm^3/g for linear adsorption and $cm^{1.5}/g^{0.5}$ for nonlinear adsorption.

The long-term leaching and plant uptake solute fluxes were also approximated by the

analytical model. The approximation of the leached mass fraction is much poorer than that of the concentration (Figure 2.12). At WAG, the leached mass fraction is predicted well only for non-adsorbing and non-degrading solutes. The error of the approximation is up to 14% for I-L, II-L, and I-NL, while for II-NL the error is up to 35%. The approximation is considerably poorer for TCA for strongly degrading but weakly adsorbing solutes, with errors up to 327%, whereas strongly adsorbing but weakly degrading solutes are still approximated within 10%. Leaching occurs sporadically in the numerical model, resulting in strong peaks during drainage events, while there is no leaching otherwise. In the analytical model, the drainage flux is smoothed out over time, resulting in continuous leaching. The leaching peaks are thus averaged out in the analytical model, which causes a large discrepancy between the numerical and analytical results for TCA. The approximation is poorer at TCA because drainage events only occur during the wet season, while drainage events are distributed more evenly at WAG. Leaching is therefore strongly seasonal, which is averaged out by the analytical model. Better results may be obtained with more complex analytical models, such as the periodical leaching model of van der Zee et al. (2010a), but requires more detailed knowledge of the water balance. The approximation of the plant uptake mass fraction is similar to that of the solute concentration (Figure 2.11), and these contour plots are therefore not repeated here. The analytical model thus predicts plant uptake within 10% of the numerical result for most parameter combinations. The plant uptake fraction is approximated well compared to the leached mass fraction, since it is more constant throughout time.

While the analytical model yields reasonable approximations for most parameter combinations, it does not account for temporal fluctuations in the concentration, despite being significant under certain conditions. Furthermore, the leached contaminant mass to the groundwater was poorly predicted for weakly adsorbing solutes. Thus, not all environmental risks of contaminant species can be identified from the analytical model. Nevertheless, the analytical model proves useful for obtaining estimates of the long-term situation, which can be used to identify contaminant species that are likely to cause problems with regard to environmental quality standards. Such information can be used to prioritize contaminant species for more detailed investigation, since the list of contaminant species that are present in wastewater is often extensive.

2.4 Conclusions

When re-using marginal water, such as treated effluent, for irrigation, it is important to have guidelines for assessing whether this is also sustainable. Therefore, we investigated this for adsorbing and degrading contaminants. In view of the debate in the literature regarding how much of contaminants in soil is biologically available (or accessible) for micro-organism mediated degradation, we explicitly addressed two degradation concepts

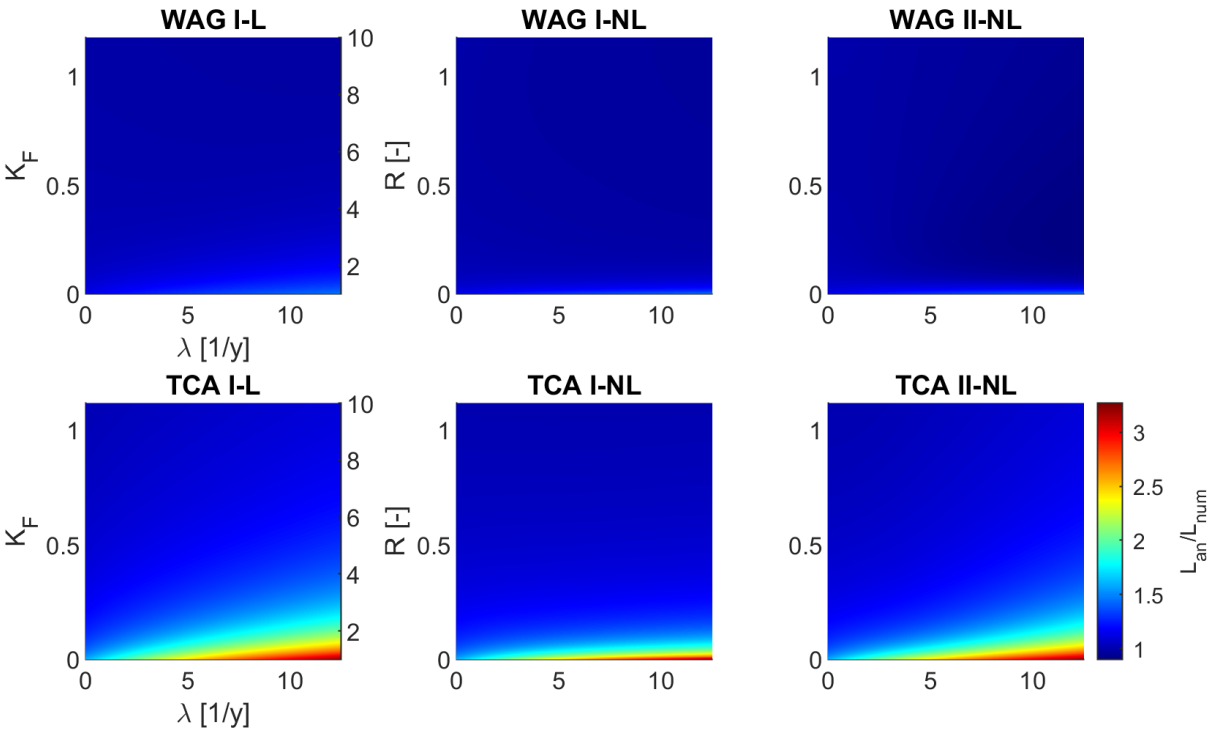

Figure 2.12: Approximation of the leached mass fraction during the last ten years of the simulation, as a function of the degradation rate constant and the adsorption coefficient. The units of K_F are cm^3/g for linear adsorption and $cm^{1.5}/g^{0.5}$ for nonlinear adsorption.

on the environmental fate of contaminants. These two degradation concepts are (i) the contaminant degrades only in the solution phase, and (ii) it degrades in both the solution and the adsorption phase. In reality, an intermediate scenario is the most probable. Daily rainfall records were used from The Netherlands and Australia to consider climates with either little or distinct seasonality, as well as some high frequency variability of rainfall. We made numerical calculations of the water and solute mass balances, and compared them with analytical approximations for average water fluxes. When degradation occurs only in the solution phase, the long-term average solute concentration and fluxes are insensitive to both the extent and the (non)linearity of adsorption. However, adsorption still influences the time to reach periodical steady state and the magnitude of the concentration fluctuations. When adsorbed contaminant can also degrade and adsorption is linear, this does not affect the fate of contaminants compared with the first degradation concept. However, this is different for solutes that adsorb nonlinearly, as then both the concentration and the fluxes of nonlinearly adsorbing solutes change significantly. When degradation also occurs in the adsorbed phase, lower solute concentrations are observed due to more contaminant removal by degradation, at the expense of plant uptake and leaching to the groundwater, which are reduced. These results indicate that the degradation concept of nonlinearly adsorbing solutes is an important property which should be determined in experimental research.

The analytical models could approximate the long-term average concentration and solute fluxes within 10% of the numerical result for most parameter combinations. While these models do not consider complexities such as the concentration fluctuations that might occur due to erratic weather, they may give a sufficiently good idea of which contaminant species are likely to cause problems with regard to environmental quality standards, e.g. depending on their adsorption coefficient and half-life. The large number of contaminants often found in wastewater as well as limited knowledge regarding their behaviour in the environment make sustainability analyses of wastewater irrigation challenging. Such analyses, integrated for soil, crop and groundwater quality, can be done with the relatively simple-to-use approaches advocated here, particularly the analytical model. This is also useful to identify which contaminant species should receive priority for more detailed analyses.

Appendix

2A Correction factor for analytical solution with nonlinear adsorption

The time-dependent solution of the nonlinear solute mass balance equation (Equation 2.18) is based on the assumption that most of the mass resides in the adsorbed phase. This can lead to incorrect solutions at steady state when this approximation is not valid. Therefore, a correction factor is required to obtain the correct analytical solution. We start with the steady state version of the approximate mass balance equation (Equation 2.17). This can be written in dimensionless variables as:

$$1 - (1 + Da_{plant})\hat{C} - Da_{ads}\hat{C}^{1/2} = 0 \tag{2A.1}$$

This has the following analytical solution for the dimensionless concentration at steady state:

$$\hat{C} = \frac{Da_{ads}^2 + 2(1 + Da_{plant}) - \sqrt{4(1 + Da_{plant})Da_{ads}^2 + Da_{ads}^4}}{2(1 + Da_{plant})^2} \tag{2A.2}$$

We now derive the true steady state solution to Equation 2.15. The full solute mass balance at steady state for a nonlinearly adsorbing solute can be written as:

$$1 - (1 + Da_{sol} + Da_{plant})\hat{C} - Da_{ads}\hat{C}^{1/2} \tag{2A.3}$$

The difference with Equation 2A.1 is thus the addition of the Da_{sol}-term, representing degradation in the solution phase. The analytical model overestimates the solute concentration at steady state when degradation in the solution phase is significant. Thus, we need a correction factor to correct the analytical solution. We solve Equation 2A.3 to

obtain the correct solution for $\hat{C}$:

$$\hat{C} = \frac{Da_{ads}^2 + 2(1 + Da_{sol} + Da_{plant}) - \sqrt{4(1 + Da_{sol} + Da_{plant})Da_{ads}^2 + Da_{ads}^4}}{2(1 + Da_{sol} + Da_{plant})^2} \quad \text{(2A.4)}$$

The correction factor f is obtained by dividing Equation 2A.4 by Equation 2A.2, such that the approximate solution multiplied by the correction factor returns the same solution as Equation 2A.4 at steady state. This yields the expression for the correction factor as stated in Equation 2.20. This correction factor is applied to the time-dependent solution (Equation 2.18). For the steady state solution, Equation 2A.4 can be used directly.

2B Average long-term concentration

The average concentration during the final ten years is shown in Figure 2B.1. The shape of the contours is similar between WAG and TCA. However, the concentration is much higher at TCA because there is more frequent irrigation. The contours are mostly controlled by the degradation rate constant. For scenarios L-I and I-NL, adsorption has little effect on the long-term average concentration. These results agree with the findings of Beltman et al. (2008). For II-NL, the adsorption coefficient does affect the concentration because of degradation in the adsorption phase.

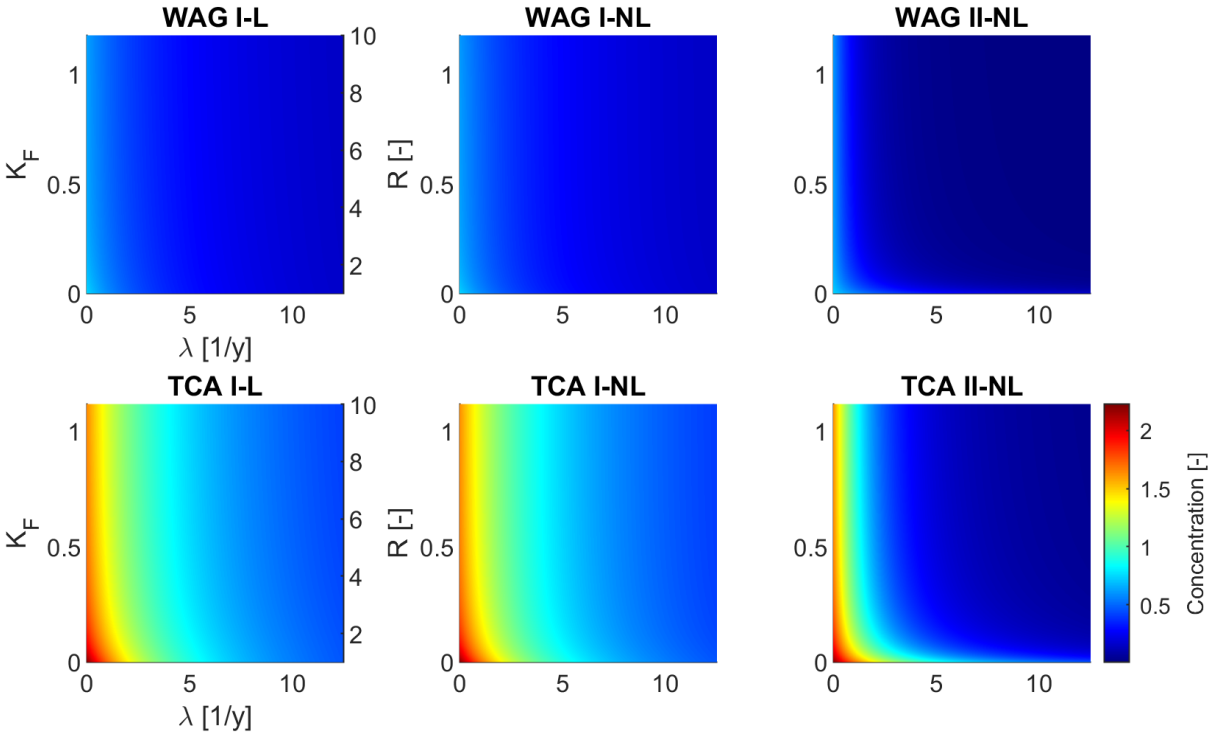

Figure 2B.1: Average solute concentration C/C_i during the final ten years of the simulation.

2C Probability density of soil saturation and water fluxes

The variation of the soil saturation and water fluxes can be captured by their probability density functions (Figure 2C.1), that give a different perspective on differences between the WAG and TCA climates. The saturation is generally lower at TCA than at WAG, because of more distinct dry periods. While there is frequent irrigation during these periods, the irrigation management is such that the saturation does not become too high. Still, the probability density of high saturations (larger than 80%) are more frequent at TCA than at WAG, because of the high saturations that may occur during the wet season. At WAG, the rainfall is more evenly spread, i.e., with less extreme values.

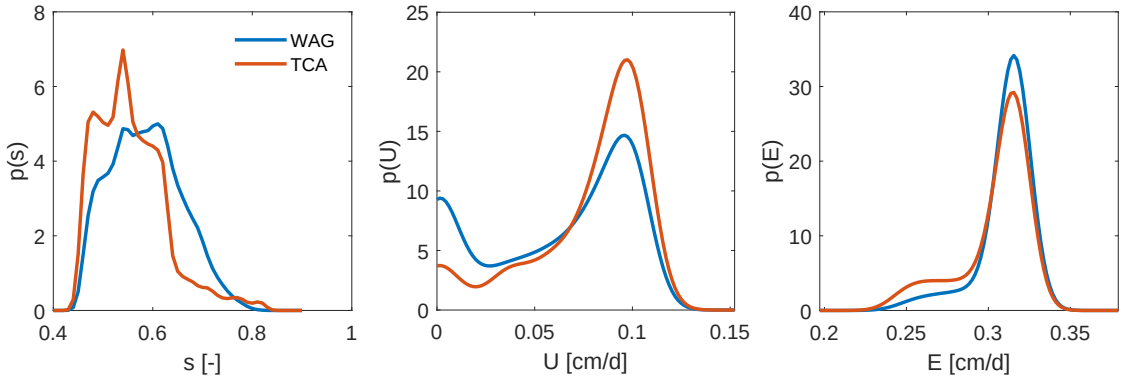

Figure 2C.1: Probability density functions of the soil saturation, capillary rise, and evapotranspiration rate for both the WAG and TCA climate.

The maximum capillary rise is a function of the soil properties and depth to the groundwater, which is equal for both climates. For these soil and climate conditions, the maximum capillary rise rate is reached at a saturation of 52% and lower (Figure 2.3 of the main manuscript). Since the saturation peaks around 54%, the maximum probability density of the capillary rise is generally near its maximum value. Therefore, the probability density function of the capillary rise flux p(U) shows similar peaks for both the WAG and TCA climate near the maximum value. The peak of the probability density is much larger for the TCA climate, since TCA experiences significant capillary rise during seasonal dry periods. Consequently, the probability density for the TCA climate is smaller for capillary fluxes close to zero.

Similarly, the maximum evapotranspiration rate is only a function of the vegetation type, which is the same for both locations. Since there is little drought stress due to irrigation, the peak of the probability density function is around its maximum value. There is a higher probability for lower evapotranspiration rates at TCA, where more drought stress is experienced in the dry season.

2D Probability density of solute concentration and mass

Figure 2D.1 shows the probability density function of the solute concentration, p(C), for the two degradation concepts mentioned in the main manuscript and various adsorption isotherms. These simulations were for a degradation rate constant λ of 5 [1/d] and an adsorption coefficient K_F such that the linear retardation factor R equals 5, which is similar to Figure 2.6 of the main article.

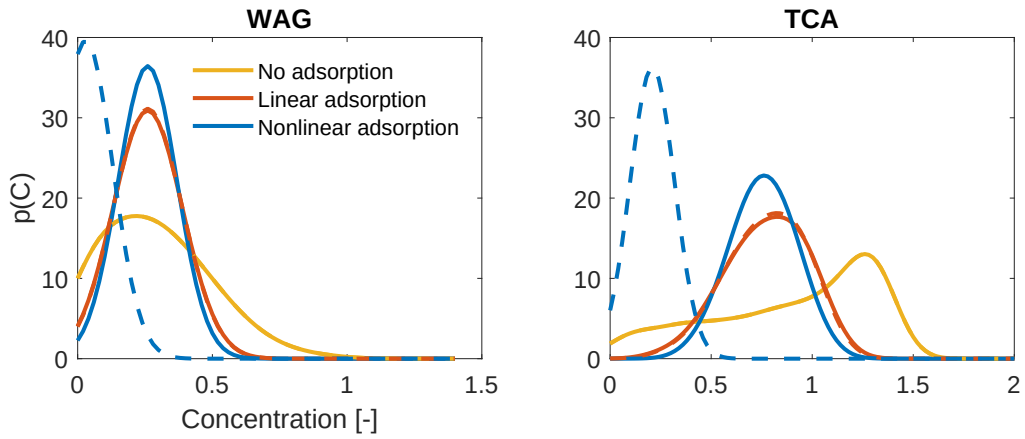

Figure 2D.1: Probability density functions of the dimensionless solute concentration C/C_i during the final 20 years of the simulation period, for various sorption isotherms and degradation concept I (solid lines) and concept II (dashed lines).

For the WAG climate under concept I, the effect of the adsorption isotherm can be seen clearly. The distributions have peaks at the same value, but the width of the distributions differs. The distribution is widest for non-adsorbing solutes, while the distribution is narrowest for nonlinearly adsorbing solutes, which were shown to have the highest retardation factors. This is expected, as temporal fluctuations of the solute concentration are attenuated when there is significant adsorption. Under concept II, we see that the probability density functions for the non-adsorbing and linearly adsorbing solutes remain virtually unchanged. However, the concentration of the nonlinearly adsorbing solutes is now much lower. The probability density function of the nonlinearly adsorbing solute is also strongly truncated. This supports our statements in the main manuscript on why the analytical solution gives worse results for this scenario.

For the TCA climate, the same effect of the degradation concept is seen for nonlinearly adsorbing solutes. However, the truncation of the probability density function is less significant, because the concentrations are higher due to frequent irrigation at TCA. Additionally, the distribution of the non-adsorbing solute strongly deviates from the bell shape and is much wider. These properties are caused by the strong seasonality of this

climate. As a consequence, the probability density of the concentration is much more equally distributed here.

For the same simulations as shown in Figure 2D.1, we show the probability density of the solute mass, p(M) in Figure 2E.1. While the solute concentration is centred around the same point under concept I, this is not the case for the solute mass. The solute mass is higher for the adsorbing solutes, with the nonlinearly adsorbing solute being the highest, because there is now also solute in the adsorbed phase in addition to solute in the solution phase. Similar to the probability density of the concentration, the effect of the degradation concept is negligible for linear adsorption, but significant for nonlinear adsorption.

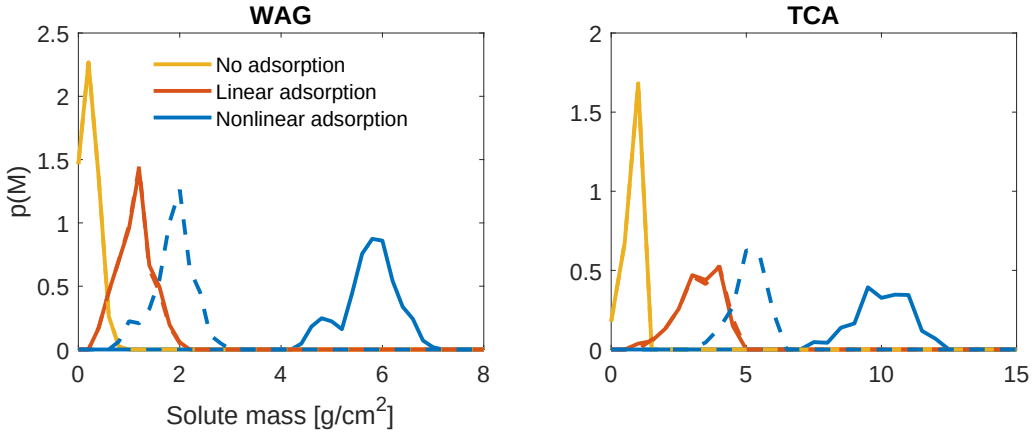

Figure 2D.2: Probability density function of solute mass during the final 20 years of the simulation period, which captures the 'steady state' situation. The figure shows the comparison between degradation concept I (solid lines), degradation concept II (dashed lines), and the analytical solution for solute mass at steady state (dotted vertical lines) for various sorption isotherms.

2E Solute leaching flux

The solute mass to the groundwater is also an important factor for the sustainability of wastewater irrigation practices. Figure 2E.1 shows the cumulative leached solute mass as a function of time, for the two degradation concepts and various adsorption isotherms. What may seem counterintuitive is that under concept I, more mass is leached to the groundwater for the adsorbing solutes compared to the non-adsorbing solute. Leaching occurs sporadically, when the soil becomes sufficiently wet after rainfall events. In our model, no leaching occurs during irrigation. At the start of a leaching event, the solute concentration is generally higher for non-adsorbing solutes, as seen by the concentration peaks in Figure 2.6 of the main manuscript. However, the concentration drops fast for non-adsorbing solutes due to leaching, degradation, and plant uptake. Therefore, there

is little leaching during the later part of the leaching event. Leaching, degradation, and plant uptake are slowed down when the solute does adsorb. Therefore, the concentration does not drop as fast, and there is more solute available for leaching during the later part of the leaching event. The net result is that more solute leaches to the groundwater for adsorbing solutes.

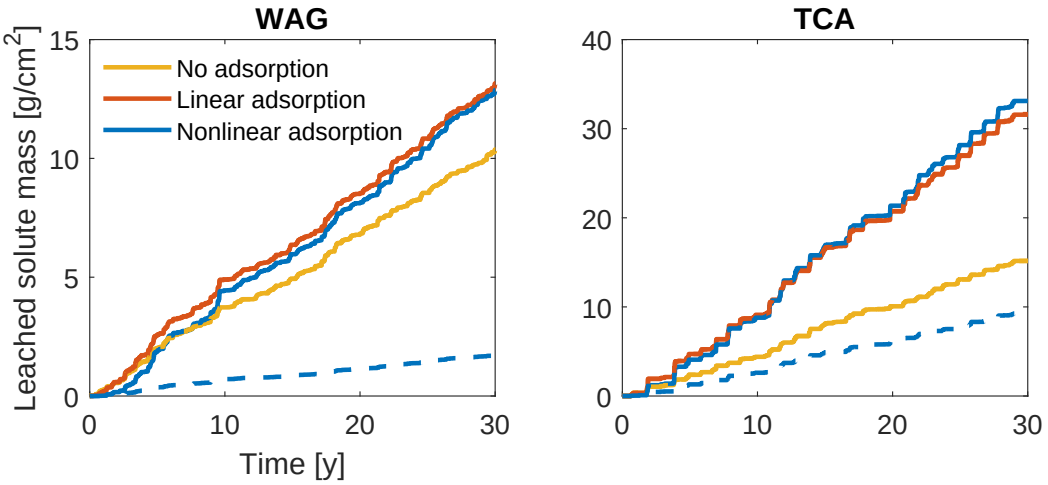

Figure 2E.1: Cumulative leached solute mass as a function of time, for degradation concept I (solid lines) and concept II (dashed lines).

The effect of the degradation concept can also be seen. There is no difference for the leached solute mass between the degradation concepts for linearly adsorbing solutes. However, for nonlinearly adsorbing solutes, the cumulative leached mass is much lower under degradation concept II. Under concept II, there is significant degradation in the adsorbed phase, and thus less solute is leached to the groundwater.

Table 2E.1: Coefficient of variation of the solute leaching flux for both climates and degradation concepts.

WAG	Concept I	Concept II
Non-adsorbing	3.60	3.60
Linear adsorption	3.39	3.39
Nonlinear adsorption	3.42	3.54
TCA	Concept I	Concept II
Non-adsorbing	5.61	5.61
Linear adsorption	5.32	5.31
Nonlinear adsorption	5.33	5.34

Solute leaching is a function of both the solute concentration and the drainage rate. However, the variability of the solute leaching flux is controlled more by the variability of the drainage rate than by the concentration. For the aforementioned simulations, the

coefficient of variation ranges of the concentration from 0.23-0.69, while it ranges between 3.29-5.32 and 3.39-5.61 for the drainage and leaching fluxes, respectively. The coefficients of variation of the solute leaching flux are shown in Table 2E.1 for the considered scenarios. The coefficients of variation show little variation with the degradation concept and adsorption isotherm. However, the differences between the two climates is much more significant. This further reinforces that it is the variation of the drainage flux which dominates the variability of the leaching flux.

2F Nomenclature

Table 2F.1: Nomenclature.

Symbol	Definition [units]
A	Mass input rate [g/cm^2/d]
a	Coefficient for mass input [g/cm^3/d]
B	Leaching coefficient for nonlinear adsorption [g$^{(n-1)/n}$/cm$^{2(n-1)/n}$/d]
b	Hydraulic shape parameter [-]
C	Solute concentration [g/cm^3]
C_{an}	Analytical solution concentration at steady state [g/cm^3]
C_i	Solute concentration in irrigation water [g/cm^3]
C_{num}	Numerically determined average concentration [g/cm^3]
C_0	Solute concentration at initial time [g/cm^3]
C_5	5^{th} percentile of concentration [g/cm^3]
C_{95}	95^{th} percentile of concentration [g/cm^3]
c_T	Light use efficiency parameter [-]
D	Coefficient for analytical solution with nonlinear adsorption [1/d^2]
Da_{ads}	Damköhler number for degradation in adsorbed phase [-]
Da_{plant}	Damköhler number for plant uptake [-]
Da_{sol}	Damköhler number for degradation in solution phase [-]
E	Actual evapotranspiration rate [cm/d]
E_p	Potential evapotranspiration rate [cm/d]
f	Correction factor analytical solution [-]
f_{LAI}	Leaf area index [-]
f_R	Volumetric root fraction [-]
G	Parameter for water flow [-]
h_b	Bubbling pressure head [cm]
I	Irrigation rate [cm/d]
I_a	Coefficient for irrigation management [-]
I_b	Coefficient for irrigation management [-]

Table 2F.1: Nomenclature (continued).

Symbol	Definition [units]
K_F	Freundlich adsorption coefficient [cm^{3n}/g^n]
K_s	Saturated hydraulic conductivity [cm/d]
L	Drainage rate [cm/d]
M	Total solute mass [g/cm^2]
M_0	Solute mass at initial time [g/cm^2]
m	Parameter for water flow [-]
m_1	Parameter for water flow [-]
m_2	Parameter for water flow [-]
n	Freundlich adsorption exponent [-]
P	Precipitation [cm/d]
Q	Degradation rate [$g/cm^2/d$]
q	Adsorbed mass fraction [-]
R	Average retardation factor [-]
R_c	Retardation factor [-]
R_o	Runoff [cm/d]
s	Saturation [-]
s_{fc}	Saturation at field capacity [-]
s_w	Saturation at wilting point [-]
s_1^{irr}	Saturation threshold for start of irrigation [-]
s_2^{irr}	Saturation threshold for end of irrigation [-]
s_*	Saturation below which evapotranspiration is limited [-]
T	Plant uptake rate [$g/cm^2/d$]
U	Capillary rise [cm/d]
Z	Depth to groundwater table [cm]
Z_r	Root zone depth [cm]
α	Plant uptake rate constant [-]
α_e	Hydraulic shape parameter [-]
β	Hydraulic shape parameter [-]
β_T	Soil moisture stress function [-]
γ	Degradation coefficient for nonlinear adsorption [1/d]
θ	Volumetric soil water content [-]
λ	Degradation rate constant [1/d]
ρ_b	Soil dry bulk density [g/cm^3]
ρ_s	Soil solid phase density [g/cm^3]
τ	Time step size [d]
ϕ	Porosity [-]

Chapter 3

Framework for the integrated sustainability assessment of wastewater irrigation

This chapter is based on:

Cornelissen, P., van der Zee, S. E. A. T. M., Leijnse, A. (2021). Framework for the integrated sustainability assessment of irrigation with marginal water. *Water, 13*, 1168.

Abstract

The re-use of wastewater for irrigation can reduce the pressure on existing freshwater resources. However, this can cause contaminants to accumulate in compartments such as the soil, crop, air, surface- and groundwater, which may harm the public health and the environment. Environmental quality standards for these compartments are generally considered separately. However, the compartments are related to each other by the fluxes between them, and the concept of sustainability should hold for all compartments simultaneously. An integrated approach is therefore required for the sustainability assessment of wastewater irrigation. Since such an approach has not been provided yet, we develop an integrated framework in this study. We provide sustainability indicators by comparing the long-term contaminant concentration and fluxes with quality standards for each environmental compartment. These indicators give comprehensible information on which contaminants will cause problems, which environmental compartments are threatened, and on what timescale this will occur. This allows for the prioritization of mitigation and preventive measures for better sustainability management. We illustrate the use of the framework by means of a case study.

3.1 Introduction

Freshwater scarcity is a growing global problem due to population growth, urbanization, and climate change (Sarhadi et al., 2016; Ali et al., 2017). The population in water-stressed regions was estimated at 700 million in 2006, and growing (UNDP, 2006). Alternative water resources are needed to reduce the pressure on existing freshwater resources. Using reclaimed wastewater or effluent for irrigation is such an alternative. As a comprehensive general term, we will use wastewater in this study to denote water resources that have quality issues, such as domestic and industrial effluent, or return flows. Since agriculture is responsible for 70% of freshwater use (UNESCO-WWAP, 2003), irrigating with wastewater significantly reduces the pressure on freshwater sources. Besides agriculture, wastewater is also re-used for irrigating urban greens, such as parks and sport fields (Hamilton et al., 2007). Wastewater irrigation is common practice in arid and semi-arid areas around the world where freshwater is scarce, including the Middle East, Australia, Mexico, and southern Europe (Hamilton et al., 2007). However, wastewater irrigation has recently also received increased attention in temperate climates to mitigate future water stress due to climate change (Bixio et al., 2006).

While freshwater scarcity is the main driving force for wastewater irrigation, there are additional benefits. First, irrigation with wastewater may prevent pollution of coastal and riverine systems, as wastewater is otherwise often discharged directly into surface waters (Toze, 2006; Hamilton et al., 2007). Secondly, the presence of nutrients and organic matter in wastewater is reported to improve crop yields (Al-Nakshabandi et al., 1997), which is particularly a benefit in developing countries where fertilizers are not always an economically feasible option (Hamilton et al., 2007).

However, wastewater poses a risk to human health and the environment due to the contaminants it contains. The composition of wastewater depends on its source and treatment before re-use, and therefore varies from case to case. Current treatment technologies are not designed to remove contaminants of emerging concern (CECs) (Metcalf et al., 2004). The removal efficiency of wastewater treatment systems therefore strongly depends on the contaminant, ranging from 2 to 99% for different contaminants (Petrović et al., 2003; Kim et al., 2018). Additionally, wastewater is applied directly without treatment in some regions. Commonly found contaminants in wastewater include heavy metals (Mapanda et al., 2005; Rezapour et al., 2011; Farahat and Linderholm, 2015), alkali and earth alkali salts (Jalali et al., 2008; Muyen et al., 2011; Tunc and Sahin, 2015), nutrients (Tang et al., 2004; Pereira et al., 2012; Paruch, 2014), organic chemicals (Chen et al., 2014; Woodward et al., 2014; Wang et al., 2015), and pathogens Toze (2006). The presence of these contaminants makes it unclear whether long-term wastewater irrigation is sustainable. In this paper, we consider a practice sustainable if it will not lead to violation of appropriately defined quality standards for the environment (e.g., for soil, crop, water). Quality standards for irrigation water are required for this purpose.

Quality standards for wastewater irrigation have already been developed for some contaminants such as heavy metals, nutrients, and microbes, as well as chemo-physical properties such as the electric conductivity and pH. The most commonly used standards are those proposed by the Word Health Organization (WHO, 2006), the United States Environmental Protection Agency (USEPA, 2012), and the European Union (European Council, 2019), which are used in many countries. However, regulations for many chemical hazards, including CECs, are still missing (Rizzo et al., 2018).

Regulations for contaminants in wastewater should be based on all potential risks to human health and the environment. In an attempt to devise irrigation water quality standards, risk assessment methodologies were proposed for chemical hazards in the context of wastewater irrigation (Weber et al., 2006; Troldborg et al., 2017). However, these studies neglected several exposure pathways, such as pollution of the groundwater. This highlights the issue that quality standards for the various environmental compartments (e.g., soil, crop, groundwater) are generally considered independently from each other. However, the contaminant fluxes between the different compartments are obviously coupled. Thus, neglecting one or more compartments might lead to erroneous predictions of the contaminant concentration, fluxes, and potential problems. Furthermore, the concept of sustainability should hold for all compartments simultaneously: that the quality standard of one compartment may not be exceeded, does not ascertain that the quality standards of other compartments will not be exceeded. Therefore, there is need of a tool that considers all threatened environmental compartments in an integrated manner.

Current frameworks to assess the sustainability of wastewater irrigation are lacking, as not all environmental pathways and contaminants are considered. We will therefore develop such a framework which can account for all threatened environmental compartments and potential risks to the public health on the farm level in an integrated manner. To our knowledge, a framework which integrates these pathways has not yet been provided. We develop sustainability indicators to translate the complex processes that occur in the soil into comprehensible and manageable information. The framework is applied to a case study in the Netherlands for illustration.

3.2 Methods

3.2.1 Contaminant balance

Wastewater often contains a large number of contaminants which show great diversity in behaviour, adverse effects, and fate in the environment (Hamilton et al., 2007). To assess if such water can be used for irrigation on longer time scales requires an approach that is valid for a large range of contaminants. For our integrated approach, we need to identify how humans and the environment are exposed to contaminants, in this case focused on

contaminants introduced by irrigation water. Contaminants can threaten the soil quality (Qian and Mecham, 2005; Virto et al., 2006; Xu et al., 2010; Rezapour and Samadi, 2011; Razzaghi et al., 2016), crop quality (Chiou et al., 2001; Jjemba, 2002; Pedrero and Alarcón, 2009), groundwater quality (Gallegos et al., 1999; Candela et al., 2007; Paruch, 2014), surface water quality (Pedersen et al., 2005), and air quality (Jury et al., 1990; Weber et al., 2006). The most important environmental compartments and contaminant pathways are summarized in Figure 3.1.

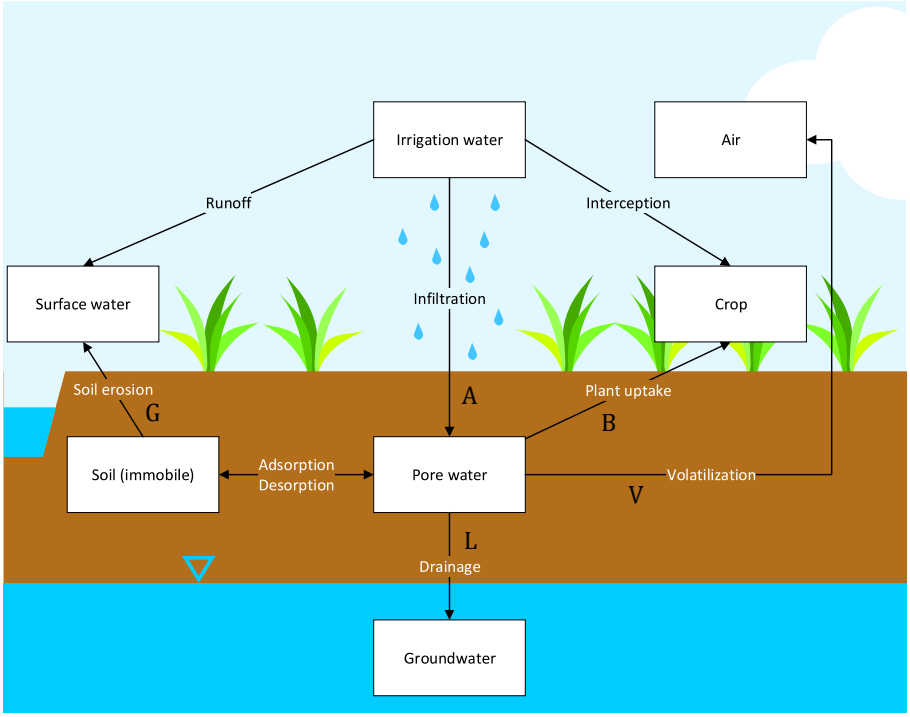

Figure 3.1: A schematic representation of various environmental compartments relevant to irrigation with wastewater, indicating the possible contaminant pathways between compartments. Accumulation of contaminants in each end compartment can cause risks for public health and the environment.

As Figure 3.1 illustrates, many processes and pathways of contaminants complicate the soil system. To provide an integrated tool for assessment of the sustainability of using wastewater irrigation, we make the assumption that this irrigation water is the sole source of contaminant. In that case, the contaminant mass balance for soil is given by the difference of input by irrigation water and removal via other processes given in Figure 3.1, or

$$\frac{dM}{dt} = A - L - D - B - G - V \tag{3.1}$$

where M is the total contaminant mass in the root zone [µg/cm^2], A is contaminant mass input [µg/cm^2/y], L is loss by leaching to the groundwater [µg/cm^2/y], D is loss by degradation [µg/cm^2/y], B is loss by plant uptake [µg/cm^2/y], G is loss by soil erosion

[µg/cm^2/y], and V is loss by volatilization [µg/cm^2/y]. The contaminant input A is a combination of various contaminant sources. Naturally, this includes poor quality irrigation water, but this may not be the only source of contaminants. For example, in regions with shallow groundwater tables and poor groundwater quality, capillary rise may also transport contaminants from the groundwater towards the root zone. However, in this paper we will consider irrigation as the only contaminant source. This also includes surface runoff that infiltrates into the soil. Note that interception does not introduce contaminants to the soil, and is therefore not included in this mass balance. The contaminant input A thus denotes only the soil input, not the total input.

This mass balance can be considered in various levels of detail, and we focus on longer time and non-acute contamination. For acute contamination problems, sustainability is less an issue, as those situations are often recognized immediately to involve unacceptable risks. Instead, we consider situations where contaminants may pose environmental risks, but which risks are of real concern and at which time scales is not apparent. For contamination problems of our interest, we may regard the top soil as a perfectly mixed reservoir, in view of regular soil tillage (Wildenschild and Jensen, 1999), by which high frequency (daily, weekly) variation of boundary conditions (rainfall, irrigation water quality) will be filtered out (Cornelissen et al., 2020).

Many CECs in wastewater exhibit linear adsorption to the solid phase (Boivin et al., 2005; Kodešová et al., 2015). We therefore consider only linear adsorption within this framework, although other adsorption expressions are feasible as well (Moolenaar et al., 1997; Cornelissen et al., 2020). In our case, all removal processes are first-order rates with respect to concentration in solution, and Equation (3.1) can be written as

$$\underbrace{\theta Z R \frac{dC}{dt}}_{\text{accumulation}} = \underbrace{IC_i}_{\text{input}} - \underbrace{qC}_{\text{leaching}} - \underbrace{\lambda \theta Z R C}_{\text{degradation}} - \underbrace{\alpha T C}_{\text{plant uptake}} - \underbrace{EkC}_{\text{soil erosion}} - \underbrace{\beta \theta Z C}_{\text{volatilization}} \tag{3.2}$$

where $R = 1 + (\rho_b k)/\theta$ is the retardation factor [-], with ρ_b being the soil dry bulk density [g/cm^3], k the adsorption coefficient [cm^3/g], θ is the soil water content [-], C is the contaminant concentration in the pore water [µg/cm^3], I is the effective irrigation rate [cm/y], Z is the root zone depth [cm], C_i is the contaminant concentration in the irrigation water [µg/cm^3], q is the drainage rate [cm/y], λ is the degradation rate constant [1/y], α is the plant uptake coefficient [-], T is the evapotranspiration rate [cm/y], E is the soil erosion rate [g/cm^2/y], and β is the first-order removal coefficient for volatilization [1/y]. The first term on the right-hand side describes input through irrigation, the second term describes leaching to the groundwater, the third is removal by (bio)degradation, the fourth is plant uptake, the fifth is removal by soil erosion, and the last term is loss by volatilization and all right-hand side terms are proportional with C. Therefore, making the substitutions

$$a = \frac{IC_i}{\theta Z} \tag{3.3a}$$

$$b = \frac{q + \alpha T + Ek}{\theta Z} + \lambda R + \beta \tag{3.3b}$$

the contaminant mass balance equation can be simplified to

$$R\frac{dC}{dt} = a - bC \tag{3.4}$$

This equation is linear in C, which enables a systems analysis approach. Integration yields for the contaminant concentration as a function of time

$$C(t) = \frac{a}{b} + \left(C_0 - \frac{a}{b}\right) \exp\left(-\frac{bt}{R}\right) \tag{3.5}$$

where C_0 is the initial concentration. If the irrigation regime and water quality are known, the most severe violation of environmental quality standards (if any) occurs at steady state, i.e., if this regime is continued for a long time. The steady state concentration is obtained by taking the limit of time to infinity in Equation (3.5), or by setting the time-derivative term equal to zero in Equation (3.2), yielding

$$C_{ss} = \frac{a}{b} \tag{3.6}$$

where C_{ss} is the contaminant concentration at steady state [µg/cm^3]. The different contaminant fluxes can also be calculated at steady state, by using Equation (3.6) and the expressions from Equation (3.2).

3.2.2 Sustainability indices

Quality standards have been developed in many countries to constrain concentrations of contaminants in various environmental compartments (e.g., air, soil, water, crop) or serve as a reference for perceived risks (European Council, 2006). These standards may or may not be based on e.g., (eco)toxicological risk assessments, as the proper functioning of the ecosystem apart from toxic effects is also of concern; an example is soil structure deterioration in case of soil sodicity (van de Craats et al., 2020). Seldomly, standards have been developed from the perspective of internal consistency for all environmental compartments. In fact, for many substances, standards may be lacking, despite being suspect as is the case for CECs. If standards are lacking for some of the environmental compartments, application of our framework is biased. As we show later, this may in some cases be a lesser bias, but in some cases be profound, for instance if the pathway without quality standards is of great concern.

A systems analysis approach, based on Equations (3.2)–(3.6) enables us to assess the sustainability in an integrated way. For this purpose, we modify the sustainability indices as proposed earlier by Moolenaar et al. (1997). Their framework was derived for the accumulation of heavy metals in agro-ecosystems, and was was founded on the work of Boekhold and van der Zee (1991). The behaviour of heavy metals in soils is characterized

by strong adsorption and persistence, which allows for certain simplifications in the mass balance equations, which may not be valid for all contaminants present in wastewater. In this paper, we generalize their analysis, by deriving expressions which are not limited to strongly adsorbing contaminants, and by including additional contaminant pathways or removal rates, namely biodegradation, volatilization, and runoff to surface water. These indices are designed to give comprehensible information for a particular irrigation regime and irrigation water quality concerning whether or not existing quality standards will be exceeded, on what timescale this occurs, and which environmental compartments are at risk.

Critical sustainability factor

Our system's analysis approach enables us to address several important issues of contamination. Besides recognizing which contaminants will cause violation of environmental standards and which of these will do so the most, we can also straightforwardly identify which environmental compartments are at risk. For this purpose, we compare the quality standards of each of the environmental compartments with the 'steady state' predicted contaminant concentrations and fluxes. We divide the predicted contaminant fluxes by the maximum allowed contaminant flux for each compartment. In the case of the soil quality, we divide the contaminant mass in the root zone by the maximum allowed contaminant mass in the soil. Within this first approach, we only look at the total crop uptake. We disregard where in the crop the contaminant accumulates (i.e., within edible or non-edible parts of the crop), although in a second-tier assessment this may be necessary. This results in (coupled) sustainability factors for soil (F_s), crop (F_p), groundwater (F_{gw}), surface water (F_{sw}), and air quality (F_a). The environmental compartment that is threatened the most will have the largest sustainability factor, and for this reason, we define the critical sustainability factor F_c as the largest sustainability factor of all considered environmental compartments

$$F_c = \max\left(F_s, F_p, F_{gw}, F_{sw}, F_a\right) = \max\left(\frac{M_{ss}}{M_c}, \frac{B_{ss}}{B_c}, \frac{L_{ss}}{L_c}, \frac{G_{ss}}{G_c}, \frac{V_{ss}}{V_c}\right) \tag{3.7}$$

where the subscript ss denotes the anticipated steady state value of the respective contaminant fluxes and the subscript c denotes the critical value of the contaminant flux as defined by the quality standards. The other symbols have already been defined in the contaminant mass balance (Equation (3.1)). Note that the term B_{ss} here only considers contaminant accumulation in the internal parts of the crop. Contaminant accumulation on the external surfaces of crops may be included by considering the intercepted water volume. We would then have $F_p = \frac{B_{ss}+WC_i}{B_c}$, where W is annual intercepted water depth [cm/y]. The critical sustainability factor is thus an integrated index which tells us for which environmental compartment the quality standards are exceeded and actually ranks how severe the five risks are. The critical sustainability factor may be different for each contaminant, as it is strongly influenced by the transport and persistence properties of

the contaminant. It is possible that not all transport parameters or even the quality standards are well available or defined. In that case, some fluxes or factors cannot be calculated. Since all fluxes are coupled, this implies a bias in predictions of the sustainability. However, the error in the mass balance itself will be small provided the unknown fluxes are much smaller than the others.

Critical sustainability time

As illustrative calculations by Boekhold and van der Zee (1991) revealed, time scales for heavy metals can be quite large (i.e., hundreds of years). This implies ample time to recognize that some standards may become violated and for mitigation measures to be developed. However, this may not be the case for the contaminant groups that we consider in the present framework. For these contaminants, standards may be violated within short time periods, yet not so short to qualify as acute problems (i.e., months, years). In such situations, it is more urgent to recognize when quality standards are exceeded to develop mitigation or adaptation strategies. The timescale at which the quality standards are exceeded is therefore relevant. We can estimate how much time it takes to exceed the quality standards for each environmental compartment, if exceeded at all. By rearranging Equation (3.5), we obtain the following expression for the time it takes to exceed the soil quality standard

$$t_s = \frac{R}{b} \ln \left(\frac{C_0 - \frac{a}{b}}{\frac{M_c}{\theta Z R} - \frac{a}{b}} \right) \tag{3.8}$$

The term $\frac{M_c}{\theta Z R}$ in Equation (3.8) needs to be replaced by $\frac{B_c}{\alpha T}$, $\frac{L_c}{q}$, $\frac{G_c}{Ek}$, and $\frac{V_c}{\beta \theta Z C}$ for the sustainability times for the crop, groundwater, surface water, and air compartments, respectively. The critical sustainability time t_c is then defined as the smallest value of all considered environmental compartments:

$$t_c = \min \left(t_s, t_p, t_{gw}, t_{sw}, t_a \right) \tag{3.9}$$

where t_s, t_p, t_{gw}, t_{sw}, t_a are the times it takes to exceed the quality standards for soil, crop, ground- and surface water, and air, respectively [y]. This factor tells us both which quality standard is exceeded first and how long this takes. Since we only consider linear adsorption and therefore have a linear systems analysis situation, the environmental compartment with the largest sustainability factor will also have the smallest sustainability time. For nonlinearly adsorbing solutes, however, this is not necessarily the case (Moolenaar et al., 1997).

Discrepancy factor

A third sustainability index was proposed by Moolenaar et al. (1997), namely the discrepancy factor. At steady state, the input rate of contaminants via irrigation water equals the removal rate by definition. The input of contaminant can be compared with

the removal that would be in agreement with the existing quality standards, and this we call the discrepancy factor

$$F_d = \frac{A - D}{B_c + L_c + E_c + V_c} \tag{3.10}$$

Equation (3.10) is modified from the expression given by Moolenaar et al. (1997), who disregarded biodegradation, erosion, and volatilization. When the discrepancy factor exceeds 1, one or several of the quality standards will be exceeded. Otherwise, no standard violation will occur, and there is no 'discrepancy'.

In the work of Moolenaar et al. (1997), this discrepancy factor served as a preliminary assessment of potential problems, stating that mitigation measures could be prioritized by comparing the discrepancy factors of different contaminants. However, here we argue that rather the discrepancy factor is a coarse indicator of potential problems. There are situations imaginable where the discrepancy factor is smaller than the critical threshold of 1, despite one or more quality standards being exceeded. This may occur when the quality standard of one compartment is exceeded slightly, but other compartments are not threatened. When the maximum output rate for one compartment is small compared to the maximum output rates of the other compartments, this is more likely to occur. Thus, the discrepancy factor only indicates when one or more quality standards are severely exceeded, especially for compartments whose maximum output rates are relatively large. Furthermore, the soil quality standard is not included in the discrepancy factor, as it is based on fluxes, while the soil quality standard is based on the concentration. These shortcomings are highlighted in the case study. Since its usefulness is limited, we disregard this index in our framework.

3.3 Example: The sustainability of onion farming in the Netherlands using wastewater irrigation

We illustrate the application of the sustainability indices through an example. We assess the sustainability of wastewater irrigation for onion farming in the Netherlands. The change of the contaminant concentration and fluxes in the subsurface over time are calculated using Equations (3.2) and (3.5). For such an assessment, we require site-specific information, like the soil properties and average annual water fluxes. Additionally, we require information on the irrigation water quality, including which contaminants are present in the irrigation water, in what quantities they are present, their transport properties, and their environmental quality standards.

As this case study only serves to illustrate the sustainability framework, we only consider a few contaminants. We recognize that wastewater such as treated sewage effluent may contain many contaminants and that water composition may differ from case to case

(Jaramillo and Restrepo, 2017). For actual assessments, a larger selection of contaminants may therefore have to be considered.

3.3.1 Input parameters

The soil and water parameters are listed in Table 3.1. The average root zone depth for onions was obtained from the Food and Agricultural Organization of the United Nations (Allen et al., 1998). The porosity was estimated using Neurotheta pedotransfer functions for a sandy clay loam soil (Minasny and McBratney, 2002). The average soil moisture content follows from an average soil saturation of 50%. The dry bulk density of the soil was chosen such that the density is ideal for plant growth (USDA, 2014). Information on the annual water fluxes depends on the local climate and irrigation management. For this example, the average irrigation rate was derived from annual irrigation data in the Netherlands (van der Meer, 2020). The drainage flux was based on a leaching fraction of 30% of the irrigated quantity. We averaged the reference crop evapotranspiration estimated at De Bilt, The Netherlands (KNMI, 2020) over the period 2010–2019 to obtain the average annual evapotranspiration rate. The reference crop evapotranspiration is also realistic for the evapotranspiration rate of onions (Allen et al., 1998). A subsurface irrigation system is considered, such that interception is negligible.

Table 3.1: Average annual water and sediment fluxes and soil parameters typical of the study area.

Parameter	**Symbol**	**Value**
Field area [cm^2]	A_f	10^8
Irrigation [cm/y]	I	26.5 (van der Meer, 2020)
Crop evapotranspiration [cm/y]	T	60.1 (KNMI, 2020)
Drainage [cm/y]	q	7.95
Soil erosion [g/cm^2/y]	E	0.2031 (Kwaad, 1991)
Root zone depth [cm]	Z	45 (Allen et al., 1998)
Soil porosity [-]	ϕ	0.367 (Minasny and McBratney, 2002)
Soil moisture content [-]	θ	0.18
Soil dry bulk density [g/cm^3]	ρ_b	1.3

We use yearly averaged fluxes and a homogeneous root zone for the present illustration. We thus neglect temporal fluctuations in water fluxes and contaminant input, for example due to erratic weather or seasonality. Cornelissen et al. (2020) found that the long-term average concentration could be predicted well with such relatively simple models for a large number of parameter values. However, the agreement between analytical and more complex models decreases when temporal variation in the water fluxes increases, for example in strongly seasonal climates. Also, sporadic events such as contaminant

leaching were overestimated with analytical models. Since we are interested in the long-term sustainability of wastewater irrigation, short-term fluctuations and aspects such as the irrigation frequency and vegetation growth period, are of lesser importance. This framework then serves as a first indicator of potential problems, which helps prioritize contaminants which should be analysed further in more detail.

We consider eight different contaminants from the list of priority contaminants of the European Union (European Council, 2006) to illustrate the sustainability framework. These are the pesticides diuron and isoproturon, the polycyclic aromatic hydrocarbon naphthalene, the nutrient phosphate, the heavy metals cadmium and lead, and the pharmaceuticals diclofenac and metoprolol. The contaminant parameters are summarized in Table 3.2. The concentration in the irrigation water of each contaminant is taken from typical concentrations in effluent (Muñoz et al., 2009). The Henry constant K_H is used to calculate the first-order rate constant for volatilization losses according to the European Commission (European Commission, 2015) (their Equation 57). The octanol-water partition coefficient K_{ow} is used to estimate the plant uptake coefficient α using the empirical relationship found by Briggs et al. (1982). Both the Henry constant and the octanol-water partition coefficient can be obtained from public databases (Kim et al., 2019). We assume that initially these contaminants are not present in the environmental compartments, although this is not a requirement for the framework. This assumption does not affect whether quality standards will be exceeded, but it does affect the time it takes to exceed quality standards.

The environmental quality standards are obtained from the Dutch National Institute for Public Health and the Environment (RIVM, 2020), or from the European Commission (European Commission, 2011). For some environmental compartments, such as ground- and surface water, constraints have been formulated as maximum concentrations instead of fluxes. In that case, fluxes that correspond with quality standards are calculated from the flux-concentration relationships in Equation (3.2). Inherent to this choice is the assumption that the effect of dilution in the surface- and groundwater is negligible, which is justified since we are interested in the long-term effects of persistent irrigation water applications. The maximum plant uptake rate was calculated by multiplying the average onion yield per hectare (VTA, 2019) with the maximum allowed concentrations in onions (European Council, 2005). Since the naphthalene air emission standard in the Netherlands is prescribed as total emission per company or farm, we assumed a certain field area of one hectare to convert the standard to flux per area. It should be noted that almost no quality standards exist for the emerging contaminants (the pharmaceuticals), while standards are available for most environmental compartments for the more traditional contaminants (e.g., pesticides, heavy metals). Crop quality standards were not available for naphthalene, diclofenac, and metoprolol, and therefore we assumed the same values as for diuron and isoproturon. The negative effect of excess nutrients on crop growth is already included in the soil quality standard, and therefore no crop

Table 3.2: Properties of the contaminants considered in this example: the contaminant concentration in the irrigation water C_i, the soil quality standard M_c, the groundwater quality standard L_c, the surface water quality standard G_c, the air quality standard V_c, the crop quality standard B_c, the soil adsorption coefficient k, the degradation rate constant λ, the Henry's constant K_H, and the octanol-water partition coefficient K_{ow}. Data marked with an asterisk (*) denote that no crop quality standard was available for this contaminant, and thus the values of diuron are used instead as a rough estimate.

Parameter	**Diuron**	**Isoproturon**	**Naphthalene**	**Phosphate**
C_i [µg/cm^3]	[a]4.00×10^{-4}	[a]3.20×10^{-4}	[a]1.00×10^{-4}	[b]2.2
M_c [µg/cm^3]	[c]1.04×10^{-4}	[c]6.5×10^{-5}	[c]1.3×10^{-6}	[d]10
L_c [µg/cm^2/y]	[c]3.20×10^{-5}	[c]2.40×10^{-5}	[c]8.00×10^{-5}	[c]15.9
G_c [µg/cm^2/y]	[c]1.34×10^{-3}	[c]3.00×10^{-4}	[c]2.56×10^{-2}	[e]1.53×10^{-1}
V_c [µg/cm^2/y]	-	-	[c]1.00×10^{-6}	-
B_c [µg/cm^2/y]	[f]5.96×10^{-3}	[f]5.96×10^{-3}	*5.96×10^{-3}	-
k [cm^3/g]	[g]33	[h]5	[i]62.9	[j]5.01
λ [1/y]	[k]6.84	[l]8.38	[m]4.44	0
K_H [-]	[n]2.0×10^{-8}	[n]5.0×10^{-9}	[n]0.019	0
$\log K_{ow}$ [-]	[o]2.68	[o]2.87	[o]3.30	-
Parameter	**Cadmium**	**Lead**	**Diclofenac**	**Metoprolol**
C_i [µg/cm^3]	[a]1.75×10^{-4}	[a]7.55×10^{-3}	[a]6.80×10^{-4}	[a]8.00×10^{-5}
M_c [µg/cm^3]	[c]16.9	[c]65	[c]1.17×10^{-5}	[c]1.17×10^{-5}
L_c [µg/cm^2/y]	[c]2.78×10^{-3}	[c]5.88×10^{-2}	[c]5.96×10^{-2}	[c]7.79×10^{-2}
G_c [µg/cm^2/y]	[c]1.32×10^{-2}	[c]5.61×10^{-2}	[e]2.10×10^{-5}	[c]2.17×10^{-1}
V_c [µg/cm^2/y]	-	-	-	-
B_c [µg/cm^2/y]	[p]5.96×10^{-2}	[p]1.79×10^{-1}	*5.96×10^{-3}	*5.96×10^{-3}
k [cm^3/g]	[q]810	[r]230	[s]1.03	[t]17.2
λ [1/y]	0	0	[s]82.40	[u]3.19
K_H [-]	0	0	[o]1.93×10^{-10}	[n]8.6×10^{-10}
$\log K_{ow}$ [-]	[v] -0.07	[v] -0.57	[o]4.51	[o]1.88

[a]Muñoz et al. (2009), [b]Pereira et al. (2012), [c]RIVM (2020), [d]Bouwer and Idelovitch (1987), [e]European Commission (2011), [f]European Council (2005), [g]Liu et al. (2010), [h]Boivin et al. (2005), [i]Carmo et al. (2000), [j]Debicka et al. (2016), [k]Rouchaud et al. (2000), [l]Walker et al. (2001), [m]Thiele-Bruhn and Brümmer (2005), [n]Sander (2015), [o]Kim et al. (2019), [p]NVWA (1999), [q]Lee et al. (1996), [r]Lee et al. (1998), [s]Xu et al. (2009), [t]Kodešová et al. (2015), [u]Kodešová et al. (2016), [v]USEPA (2014)

quality standard is stated here. No soil quality standards are currently available for the pharmaceuticals considered here. Therefore, we used the standard for permethrin, one of the few pharmaceuticals for which a soil quality standard is available in the Netherlands. Quality standards may also not exist if accumulation in that particular compartment is assumed to be of negligible concern for the public health and the environment. For example, an air quality standard is only available for naphthalene, which is a rather volatile contaminant in our example, as indicated by its relatively large Henry coefficient.

There may be significant uncertainty in some of the input parameters, such as the adsorption coefficient and degradation rate constant. Therefore, it is appropriate to investigate the sensitivity for these parameters to assess their influence on the sustainability indices. We use the values stated in Tables 3.1 and 3.2 as a reference scenario. To assess the sensitivity, we alter selected input parameters by a relative amount (e.g., an increase or decrease of 10% compared to the reference scenario) and recalculate the sustainability indices. These are then compared to the output of the reference scenario.

3.3.2 Results

Sustainability indices

First, we consider the individual sustainability factors of each environmental compartment. There is a large difference in the time it takes to reach the concentration plateau (i.e., the steady state situation). Figure 3.2 shows the change in sustainability factors on the short term (i.e., one year). It can be observed that the plateau, is reached within a year for most contaminants. This means that if any violation of quality standards will occur for these contaminants, this will happen within a year. However, it takes over 20 years to reach the steady state situation for phosphate, since phosphate removal in the root zone is slow. The heavy metals cadmium and lead adsorb very strongly to the soil. For these contaminants, it takes centuries to reach the steady state situation, as can be seen from Figure 3.3, which shows the change of the sustainability factors over 150 years.

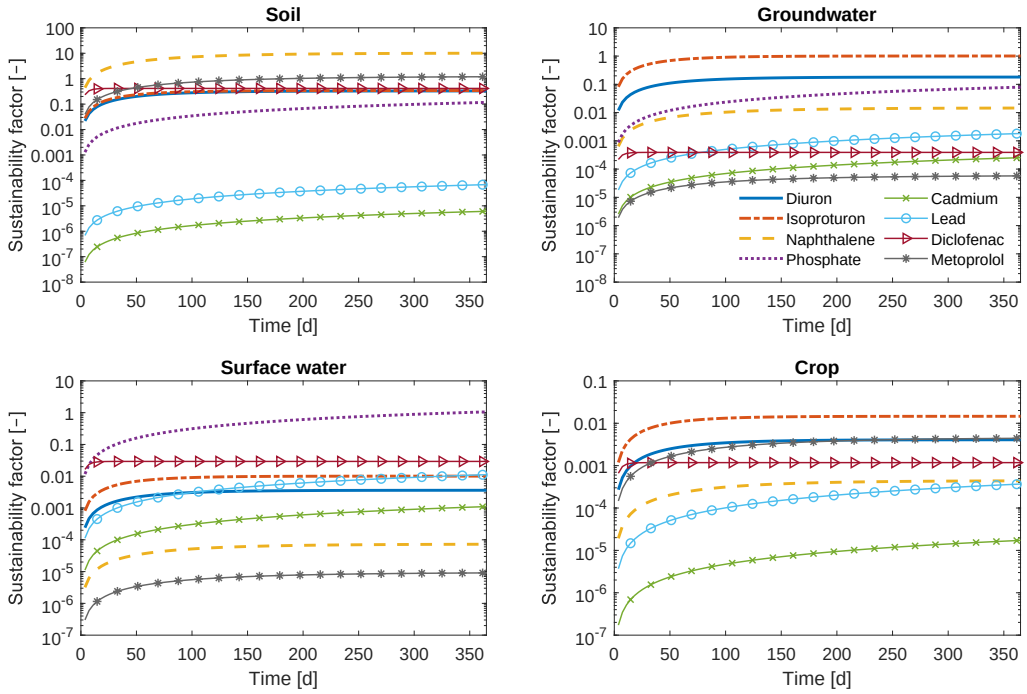

Figure 3.2: The short-term change of the sustainability factors over time, plotted for each contaminant and environmental compartment. Note the logarithmic scale of the y-axis.

The soil quality standard is exceeded severely for naphthalene, and less severe for metoprolol. Both of these contaminants tend to accumulate in the soil, because of their relatively large adsorption coefficient (the largest of all the contaminants considered here) in combination with a relatively large half-life. The soil quality standard for naphthalene is exceeded within several days, while it takes over 150 days to that quality standard for metoprolol.

Only the groundwater quality standard of isoproturon is exceeded, which takes about 100 days. This contaminant has a relatively low adsorption coefficient, and is therefore very mobile and prone to leaching. Additionally, the groundwater quality standard for isoproturon is relatively small compared to the quality standards of the other contaminants considered here. Diclofenac has an even lower adsorption coefficient, but its half-life is much shorter, and thus most of it is removed by biodegradation instead of leaching.

From Figure 3.2, the exceedance of the surface water quality standard is not apparent for lead, and may not seem severe when looking at the short timescale of Figure 3.2, since the steady state situation is not yet reached within this timeframe. However, from Figure 3.3, we observe that the surface water quality standards are exceeded severely for lead and phosphate by a factor of 2.8 and 5.6, respectively.

Quality standards for crop and air are not exceeded by any of the contaminants. The air compartment is omitted from Figure 3.2, since the air quality standard is only defined for

naphthalene. Naphthalene does not pose a risk to the air quality, as the sustainability factor for air equals 1.92×10^{-5} at steady state.

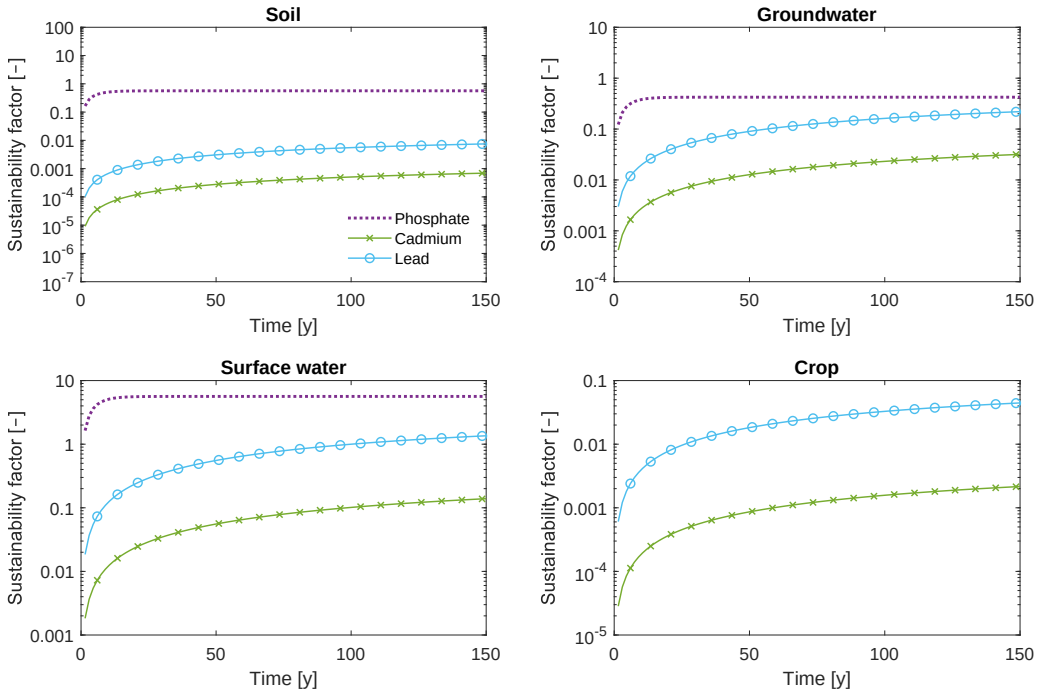

Figure 3.3: The long-term change of the sustainability factors over time in each environmental compartment, plotted for the persistent contaminants phosphate, cadmium, and lead. Note the logarithmic scale of the y-axis.

The information of each sustainability factor is integrated into the sustainability indices, which are shown in Table 3.3 for all the contaminants. The critical sustainability factors of isoproturon, naphthalene, phosphate, lead, and metoprolol are all larger than 1, ranging from 1.10 to 10.17. This indicates that quality standards are exceeded for these contaminants. In contrast, the critical sustainability factors of the other contaminants are smaller than 1, which indicates that no problems are expected to occur for these contaminants. The time it takes to exceed the quality standards depends on factors such as the input and output rates, the quality standard, and adsorption. Therefore, the critical sustainability time differs greatly between the different contaminants. For naphthalene, the soil quality standard is already exceeded within 9 days, while it takes several months to up to one year to exceed quality standards for isoproturon, metoprolol, and phosphate. However, for lead, which adsorbs strongly to the soil and does not degrade, the critical sustainability time exceeds 100 years. These differences are indicative of the differences in urgency regarding mitigation interventions.

Aside from phosphate, the discrepancy factor is smaller than 1 for all contaminants, which would indicate that no problems are expected to occur. However, the critical sustainability factors of both isoproturon and naphthalene exceed 1, which indicates that

at least one quality standard of these contaminants is exceeded. As we mentioned earlier, the discrepancy factor identifies mostly if quality standards are exceeded severely; it is not a good indicator if such standards are violated slightly, such as for isoproturon in this example. Hence, a discrepancy factor larger than 1 indicates that problems will definitely occur, but a value lower than 1 does not mean the opposite. Additionally, the definition of the discrepancy factor does not consider accumulation in the soil. The potential risks of contaminants, such as the strongly adsorbing contaminants naphthalene and metoprolol in our example, are therefore not recognized. For these reasons, we do not recommend the use of the discrepancy factor as the only indicator of sustainability.

Table 3.3: The sustainability indices for each contaminant, showing the discrepancy factor F_d, the critical sustainability factor F_c, and the critical sustainability time t_c. The latter is only defined for contaminants whose quality standards are exceeded.

	F_d [-]	F_c [-]	t_c [d]
Diuron	5.24×10^{-3}	0.33	n/a
Isoproturon	1.99×10^{-2}	1.10	101
Naphthalene	1.55×10^{-4}	10.17	8
Phosphate	3.63	5.63	312
Cadmium	6.13×10^{-2}	0.31	n/a
Lead	0.68	2.79	36556
Diclofenac	5.12×10^{-2}	0.41	n/a
Metoprolol	1.25×10^{-4}	1.24	185

In this case study, the quality of the irrigation water is thus insufficient for long-term irrigation. Either further treatment of the wastewater used for irrigation or an alternative irrigation regime is required. The sustainability indices comprehensibly indicate which contaminants harm the public health and the environment based on the irrigation water quality and site-specific parameters. This allows for the identification of problematic contaminants, such that these specific contaminants can be prioritized during wastewater treatment.

Sensitivity analysis

We show the sensitivity of the sustainability indices to the input parameters in Table 3.4. The input parameters which are expected to have the most uncertainty are the adsorption coefficient and the degradation rate constant (Dubus et al., 2003; Lammoglia et al., 2018). Additionally, there may also be significant uncertainty in the drainage, evapotranspiration, and irrigation rates (Dubus et al., 2003; Long et al., 2014).

The sensitivity of the sustainability indices to the input parameters differs for each contaminant, as it depends on factors such as the dominant transport process, the value

Table 3.4: The response of the critical sustainability factor F_c and critical sustainability time t_c in response to decreases and increases of 10% of the adsorption coefficient k, the degradation rate constant λ, the drainage rate q, and the evapotranspiration rate T. The critical sustainability time is only shown for contaminants whose standards are violated, as this parameter is otherwise undefined.

	k		λ		q		T		I	
F_c	-10%	+10%	-10%	+10%	-10%	+10%	-10%	+10%	-10%	+10%
Diuron	0.33	0.33	0.37	0.30	0.33	0.33	0.33	0.33	0.30	0.36
Isoproturon	1.22	1.01	1.23	1.01	1.10	1.10	1.11	1.10	0.99	1.22
Naphthalene	10.17	10.18	11.30	9.25	10.17	10.17	10.18	10.17	9.16	11.19
Phosphate	5.64	5.63	5.64	5.64	5.70	5.57	6.17	5.18	5.07	6.20
Cadmium	0.35	0.29	0.31	0.31	0.32	0.31	0.32	0.31	0.28	0.35
Lead	3.03	2.59	2.80	2.80	2.83	2.76	2.82	2.77	2.52	3.08
Diclofenac	0.41	0.41	0.46	0.38	0.41	0.41	0.41	0.41	0.37	0.46
Metoprolol	1.24	1.24	1.38	1.13	1.24	1.24	1.24	1.24	1.12	1.36
	k		λ		q		T		I	
t_c	-10%	+10%	-10%	+10%	-10%	+10%	-10%	+10%	-10%	+10%
Isoproturon	73	208	81	204	101	101	101	102	N/A	74
Naphthalene	8	8	8	9	8	8	8	8	9	8
Phosphate	281	342	312	312	311	312	309	315	350	281
Lead	32255	41046	36556	36556	36431	36682	36479	36633	41830	32478
Metoprolol	185	184	162	222	185	185	184	185	254	149

of the critical sustainability factor, and which environmental compartment controls the critical sustainability factor.

For most cases, the dominant transport process is the main factor that drives the sensitivity of the sustainability indices to the input parameters. For all contaminants that degrade, degradation is the dominant removal process. Therefore, all degrading contaminants are greatly sensitive to errors in the degradation rate constant. None of the contaminants in this case study are sensitive to the drainage rate, since leaching is a minor removal process compared to the other removal processes. Only phosphate is sensitive to the evapotranspiration, as this is the only contaminant where plant uptake is an important removal process. Removal by soil erosion is the dominant transport process for cadmium and lead, while degradation in the adsorbed phase for isoproturon. The sustainability indices of these contaminants are therefore sensitive to the adsorption coefficient.

However, not everything can be explained by the dominant transport processes when we look at the adsorption coefficient. For example, degradation in the adsorbed phase is the dominant removal process for diuron, naphthalene, diclofenac, and metoprolol. Nevertheless, these contaminants are not sensitive to the adsorption coefficient. The critical sustainability factors of these contaminants are all determined by the soil quality standard. On the one hand, adsorption enhances contaminant accumulation in the soil, and on the other hand there is increased removal by degradation in the adsorbed phase and soil erosion. These two opposing effects nearly cancel each other out.

Within our framework, irrigation water is the only source of contaminant input. The contaminant concentration in the root zone at steady state is therefore a linear function of the irrigation rate, as can be derived from Equation (3.6). Naturally, the sustainability indices are therefore very sensitive to the irrigation rate. However, the annual irrigation rate may be estimated with more certainty than the other parameters considered in the sensitivity analysis. While not shown here, the sensitivity of the sustainability indices to the input concentration (i.e., the concentration of contaminants in the irrigation water) is equal to its sensitivity to the irrigation rate.

Additionally, the value of the critical sustainability factor also plays a role for the sensitivity of the critical sustainability time to input parameters. When the critical sustainability factor is close to one, the critical sustainability time becomes more sensitive.

Keeping these mechanisms in mind, it becomes possible to identify what the key parameters are for each contaminant. These key parameters can then be prioritized to be determined with great precision. Even when there are errors in the input parameters, the key parameters can still be identified, as long as the erroneous input parameters are still on the same order of magnitude as the correct values.

3.4 Discussion and conclusions

In this study, we proposed a framework for the integrated sustainability assessment of wastewater irrigation based on the work of Moolenaar et al. (1997). At this point, it is worthwhile to mention that the overall framework would also be applicable to other situations, such as the application of (bio)sludges or bulk waste materials at the soil surface. However, in those cases, the processes involving changes to those sludges and materials such as the mineralization of organic matter and subsequent changes in soil bulk density, soil hydraulic properties and related effects, need to be accounted for also. Since these are modifications of the root zone, this complicates the framework, but do not alter its essence.

Currently, quality standards for the various environmental compartments have been developed and are often applied separately. However, the contaminant fluxes to each compartment are coupled. Therefore, the benefit of the developed framework is that we comprehensively integrate the quality standards of different environmental compartments. This framework is made operational by two sustainability indices, that give information on which contaminants will violate quality standards, which environmental compartments are at risk, and on what timescale standards will be exceeded.

The results of the case study show that the time scales at which problems occur varies tremendously between different contaminants. The different time scales to reach the maximum values illustrate that reactivity plays a central role in how fast deterioration occurs, and that exceedance of quality standards differs for different environmental compartments. This is of direct importance for the urgency to take measures for better sustainability management.

The uncertainty in the input parameters, especially the adsorption coefficient and degradation rate constant, can potentially significantly affect the results of the sustainability assessment. However, the sensitivity of the sustainability indices to these parameters differs per contaminant species, and mostly depends on the dominant transport process for the contaminant. It is therefore valuable to determine the dominant transport process beforehand. This can be estimated from the transport parameters, for example with the use of Damköhler numbers (Cornelissen et al., 2020).

The current framework is an extension to the work of Moolenaar et al. (1997), which focused on and illustrated the benefit of integrating compartments for heavy metals. By adding transport processes such as biodegradation, erosion, and volatilization, the framework is applicable to a much broader range of contaminants. Another difference with the work of Moolenaar et al. (1997) is that we de-valued the discrepancy factor. The discrepancy factor was originally meant to be a first indicator of potential problems, which could be estimated with relatively few assumptions and simple calculations. However, we have shown here that the discrepancy factor is an indicator that is appropriate for severe

violations of environmental standards, but mild violations of quality standards may be masked.

The core of the framework consists of comparing contaminant fluxes to quality standards of the relevant environmental compartments. However, in many countries, quality standards for the environmental compartments have not been defined, or have been defined despite recognized flaws. Moreover, quality standards are lacking at all for many CECs, as awareness of these contaminants is recent and quantification of their pathways in the environment is still limited (Lapworth et al., 2012). The framework cannot be applied in such cases, but these shortcomings do not invalidate its concept. Rather, a limited application to those compartments where constraints have been defined emphasizes where additional environmental quality standards are needed. In the example application, soil quality standards were not available for diclofenac and metoprolol. Therefore, we used the soil quality standard of permethrin instead, which is also a pharmaceutical. However, diclofenac is a non-steroidal anti-inflammatory drug, and metoprolol is a beta-blocker, while permethrin is an insecticide. Therefore, quality standards for diclofenac and metoprolol may be expected to be less toxic, and thus the quality standards in this example may be too strict. The same applies to the crop quality standard, for which no information was available for naphthalene, diclofenac, and metoprolol. Instead, we used the same quality standards as for the pesticides diuron and isoproturon, which might be more strict than necessary for the pharmaceuticals considered here. Naturally, with disputable quality standards as in our example, the framework will give a disputable outcome, but may help to identify gaps and weaknesses and give a rational basis for improvement.

Though our work aims to indicate how different standards of different environmental compartments as soil, crop, and groundwater may be used to assess sustainability of soil and water management in an integrated fashion, we already mentioned that this requires that such standards are available. The development of such standards and their foundation (whether (eco)toxicological or otherwise) is, of course, an active field of research (Lapworth et al., 2019). For instance, synergistic and antagonistic effects of contaminant mixtures on biota may affect the associated hazards (Barber et al., 2013). Particularly for treated wastewater, this may reflect on how quality standards for compartments such as soil or water should be adjusted to appropriately account for those hazards. Though relevant for this investigation, the development of environmental standards as such is not the aim of this paper. Rather, if appropriate standards have been agreed upon, we show how to harmonize them for different compartments. As we showed, also uncertainty of other model parameters affects the outcome. The involved uncertainty in our framework's results, as in other environmental assessments, remains a persistent and hard to tackle issue in environmental management. As current environmental standards reveal, management cannot wait until such issues are satisfactorily resolved.

Recognizing that absent or flawed environmental standards and uncertainty or bias in parameters affect the value of our integrated sustainability framework, as indeed environmental assessments in general, the framework has several benefits. It gives an integrated perspective to appreciate environmental contamination of different compartments and inspires where mitigating interventions might be most effective and have the highest priority. Where appropriate standards are missing or flawed, it may help to recognize how important that is, compared with the impacts on other compartments which can be quantified to satisfaction. Even so, the integrated framework is no panacea, but a useful ingredient to assessment of our management choices.

Chapter 4

Pressure development in charged porous media with heterogeneous pore sizes

This chapter is based on:

Cornelissen, P., Leijnse, A., Niasar, V., van der Zee, S. E. A. T. M., (2019). Pressure development in charged porous media with heterogeneous pore sizes. *Advances in Water Resources, 128*, 193-205.

Abstract

Upscaling the microscopic processes in charged porous media which are responsible for pore pressure evolution and swelling is a topic of ongoing research. Current theories assume homogeneous media with uniform pore sizes and the impact of microscopic heterogeneity is neglected. This is a preliminary study to determine the significance of such pore-scale heterogeneity on the pressure evolution in charged porous media, where we neglect deformation of the solid phase. We present a pore-network model to simulate salt transport and pressure evolution in a charged porous medium. Results show that, for pore radii following a log-normal distribution, the average pressure in heterogeneous networks are significantly lower than in homogeneous networks with the same mean pore size. This is expressed by lower average pressures, as well as lower streaming potentials and faster ion transport rates in heterogeneous networks. These results indicate that heterogeneity in charged porous media should be investigated further.

4.1 Introduction

Changes in salinity can affect the pressure in tight charged porous media, which leads to numerous problems. An example of a charged porous medium is clay, where changes in salinity affect the pressure. This causes the clay to expand or shrink. Such swelling processes cause problems in several different fields of study. For example, the use of poor quality irrigation water can lead to swell-shrink processes in agricultural soils, decreasing the growing conditions of crops (Quirk and Schofield, 1955; Shainberg and Letey, 1984). In petroleum engineering, the use of low-salinity water-based drilling fluids in shale leads to swelling and can cause wellbore instabilities (van Oort et al., 1996; Joekar-Niasar and Mahani, 2016). Furthermore, swelling increases the sealing capacity of clay barriers, preventing the migration of radionuclides when storing radioactive waste in the subsurface (Pusch, 1992). Understanding the pressure evolution in such materials is therefore of great importance.

The salinity and fluid pressure in such porous media are related because of the charged surfaces. The charge of the porous medium is balanced by a surplus of counter-ions near the charged surface (Bolt, 1982). The resulting ion distribution near the charged surface is often described by the diffuse double layer model. Here, the first layer consists of immobile cations which are strongly adsorbed to the charged surface, referred to as the Stern layer. The second layer consists of diffuse ions, which is the net result of electrostatic forces and thermal motion. The thickness of the double layer is inversely related to the ion valence and salt concentration. The presence of this diffuse layer and the corresponding electric field is what affects the pressure inside charged porous media.

The salt concentration affects the pressure through two processes (Barbour et al., 1992). The first process is osmotic water flow. Gradients in salinity drive osmotic flow, which alters the bulk pressure in the porous medium. The electric potential in the double layer promotes transport of counterions, while it hinders transport of coions. Thus, a net transport of charge occurs, which results in an electric potential, the so-called streaming potential or diffusion potential. This electric potential induces movement of ions through electrophoresis. The movement of the cations induces viscous drag on the fluid, and thus water also flows in response to the streaming potential. Such water flow is termed electro-osmosis. This water flow changes the bulk pressure, i.e. the pressure in the water that is not affected by the diffuse double layer. Secondly, the diffuse double layer influences the interparticle stresses as it changes the disjoining pressure. The disjoining pressure is the additional pressure between two surfaces. The diffuse double layer affects the electric component of the disjoining pressure. This component is the net result of the repulsive osmotic pressure and the attractive Maxwell stress. Both processes will be considered in this study. On the macroscopic scale, swelling of media is related to the swelling pressure. The macroscopic swelling pressure is defined as the external pressure that must be applied to a sample to keep it from expanding (Low, 1987). Under transient conditions, the

bulk pressure and disjoining pressure should both be considered to calculate the swelling pressure. Under no-flow conditions, the swelling pressure is simply the volume-averaged disjoining pressure (Derjaguin et al., 1987).

The swelling pressure has been estimated based on theoretical frameworks before. Most studies estimate the swelling pressure according to diffuse double layer theory, for both equilibrium conditions (Shainberg et al., 1971a; Madsen and Müller-Vonmoos, 1985) and transient conditions (Moyne and Murad, 2002; Horseman et al., 2007; Gonçalvès et al., 2010). These transient models included the combined effect of the bulk pressure and the disjoining pressure in the effective stress in the porous medium. The effect of salinity on the reduction of hydraulic conductivity due to swelling in soils based on double layer theory has also been investigated (e.g. Bresler et al. (1982); Russo (2013)). The aforementioned studies translated the relevant microscopic processes to larger scales. However, these studies omitted the impact of microscopic heterogeneity on the large-scale behaviour. These studies considered clay as the porous medium, and assumed that the microstructure is homogeneous, and consists of parallel particles. This allows for a simplification of the mathematical problem. However, most natural porous media have heterogeneous pore sizes (e.g. Kuila and Prasad (2013)). In most studies, the disjoining pressure is estimated based on a 'representative' interplatelet distance (Gonçalvès et al., 2010). However, a definition of such an interplatelet distance is lacking for heterogeneous media. To determine the importance of heterogeneity, we apply an alternative upscaling method.

Pore-network modelling is a useful approach for scaling up flow and transport processes in heterogeneous porous media. The effect of microscopic heterogeneities can be translated to large scale behaviour. In such models, the geometry of the pore space is simplified, and flow and transport between individual pores is simulated. Pore-network models were originally tools for upscaling multiphase flow in porous media (Fatt, 1956). Over time, these models have been applied to other topics such as dynamic multiphase flow (Joekar-Niasar et al., 2010a) and reactive transport (Acharya et al., 2005; Babaei and Joekar-Niasar, 2016). A pore-network model that includes electrokinetic transport has been developed before by Obliger et al. (2014). However, in this study, we use the framework developed by Joekar-Niasar et al. (2013), which gives a more accurate description of the ion distributions in charged channels.

The aim of this study is to determine the significance of heterogeneous pore sizes on the pressure evolution in charged porous media. This study is a first step in including heterogeneity, in which we neglect deformation of the solid structure. For this purpose, we developed a pore-network model that includes the effect of diffuse double layers in pores on water flow and ionic transport. The model considers both the evolution of the bulk pressure and the disjoining pressure. We find the swelling pressure by volume-averaging the sum of these pressure components. These computations will be done for both

homogeneous and heterogeneous pore networks, and the results are compared to determine the significance of heterogeneity.

4.2 Pore-network model

We developed a pore network model that includes electrokinetic effects on water flow and ionic transport to investigate the effect of heterogeneity on the swelling pressure. The model was used simulate the evolution of the pressure field, electric field, and salt concentration inside a pore network as a consequence of changes in ionic strength. This study was limited to homovalent electrolyte solutions, in particular 1:1 electrolyte solutions such as NaCl. We only considered scenarios where the pore network is fully saturated. Thus, only the effect of the electrolyte concentration on the swelling pressure was considered.

The pore space is discretized in pore bodies and pore throats. Storage of mass and charge occurs in pore bodies, while transport of these properties occurs in the pore throats. The shape of the pore bodies is spherical. The walls of the pore bodies are assumed to have no charge. The ion distribution inside the pore bodies can therefore be considered homogeneous. Thus, a single value for the cation concentration, anion concentration, fluid pressure and electric potential is assigned to each pore body. The potential in the pore bodies is the streaming potential, which develops as a result of electroneutrality. The pore throats have rectangular cross-sections. The geometry of the pore throat is characterized by its height h and the dimensionless width $\bar{w} = w/h$ (Figure 4.1). We consider only square cross sections ($\bar{w} = 1$) in this study, but this method can also be applied to different pore geometries. Contrary to pore bodies, walls of pore throats are charged. We employ the Gouy-Chapman model, and thus assume that the charge of the porous medium is completely compensated by the diffuse layer. There is no immobile Stern layer in our model. The no-slip surface for fluid flow is therefore located at the channel wall. Thus, the surface potential equals the zeta potential in this case. A uniform zeta potential is assigned to the channel walls. We consider a dimensionless zeta potential $\bar{\zeta}$, defined as $\bar{\zeta} = \frac{F\zeta}{RT}$. Here, ζ is the zeta potential [V], F is the Faraday constant [C/mol], R is the gas constant [J/(mol K)], and T is the absolute temperature [K]. The zeta potential can vary as a function of time. Since we assumed a uniform zeta potential, this implies that the surface charge density cannot be uniform across the channel walls, as the charge of adjacent walls interact with each other. Therefore, we apply a constant average surface charge density σ_ζ instead. This is explained in more detail in 4A. We assume that the ions are in local equilibrium, which allows for the use of the Poisson-Boltzmann equation in the pore throats.

Additionally, we assume that resistance to flow in pore bodies is negligible compared with that in pore throats. Thus, only the permeability of pore throats is of interest. Furthermore, we assume that the pore network is rigid and not deformable, and that

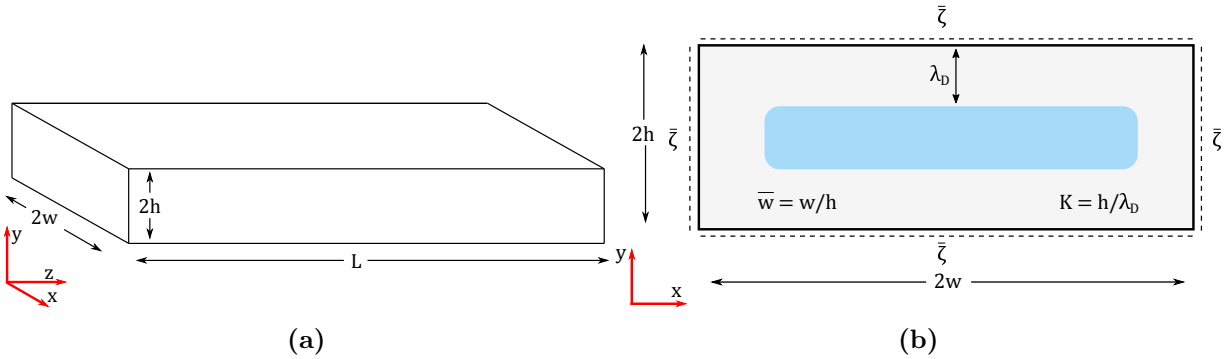

Figure 4.1: (a) Schematic representation of a pore throat. The pore throat geometry is characterized by its height h, width w and length L. (b) Cross-section of a pore throat. The pore throat is defined by the dimensionless width $\bar{w} = w/h$ and the dimensionless radius $K = h/\lambda_D$, which is the channel height scaled by the Debye length. All boundaries have a uniform zeta potential. Figure is adapted from Joekar-Niasar et al. (2013).

the temperature, dynamic viscosity and permittivity of water are constant. Finally, the effect of gravity on water flow is neglected, as it is not relevant to this study. Table 4.1 shows the values of material, fluid and transport properties used in the pore network modelling. Parametrisation was based on properties of montmorillonite, water, and electrolyte properties of NaCl. We use the same diffusion coefficient for both the cation and anion species, which for NaCl is reasonable. The next section presents the properties of the pore network itself.

Table 4.1: Fluid and transport properties used in the pore-network model.

Property	**Symbol**	**Value**
Electrokinetic surface charge density [C/m^2]	σ_ζ	5.00×10^{-4}
Dynamic viscosity [Pa s]	η	1.00×10^{-3}
Temperature [K]	T	298
Permittivity of water [C^2/(J m)]	ϵ	7.12×10^{-10}
Ion diffusion coefficient [m^2/s]	D	1×10^{-9}

4.2.1 Pore-network geometry and topology

The pore body radii and pore throat inscribed radii were generated from a truncated log-normal distribution, with no spatial correlation, as spatial autocorrelation data are not available. The pore size distribution f is described by:

$$f = \frac{\sqrt{2}\exp\left(-\frac{1}{2}\left(\frac{\ln\frac{R_i}{R_m}}{\sigma_{ps}}\right)^2\right)}{\sqrt{\pi\sigma_{ps}^2}R_i\left(\operatorname{erf}\left(\frac{\ln\frac{R_{max}}{R_m}}{\sqrt{2\sigma_{ps}^2}}\right)-\operatorname{erf}\left(\frac{\ln\frac{R_{min}}{R_m}}{\sqrt{2\sigma_{ps}^2}}\right)\right)} \tag{4.1}$$

where R_i is the radius of a pore, R_m is the mean pore body radius, R_{max} is the maximum pore radius, R_{min} is the minimum pore body radius and σ_{ps} is the standard deviation. The pore body radii were generated with a mean pore body size of 80 nm and standard deviation of 20 nm, based on experimental N_2 gas-adsorption data from Kuila and Prasad (2013). The minimum pore body radius was set to 10 nm and the maximum pore body radius was set to 150 nm. Since the pore throats have square cross-sections, we refer here to the inscribed radii. The inscribed pore throat radii were generated from a distribution with mean pore size of 20 nm and standard deviation of 10 nm, with a minimum radius of 10 nm and a maximum of 50 nm. These values are based on the experimental data of Kuila and Prasad (2013). Larger standard deviations have also been tested, which did not lead to different conclusions. We imposed the condition that the pore throat radius could not be larger than the radius of the adjacent pore bodies. When a pore throat radius was generated that did not meet this condition, a new pore throat radius was generated until this condition was met. The network used in this study was a cubic lattice. The pores have a coordination number of 6, except for boundary pores. The distance between two pore bodies was set to 1.8 μm, which resembles the upper limit of a clay particle size. The size of the network must be large enough to give a good representation of the pore size distribution. Therefore, several network sizes were tested to determine the appropriate network size.

4.2.2 Boundary and initial conditions

The pore network is connected to a salt reservoir at one end of the network. The salt concentration, fluid pressure and electric potential inside the reservoir are constant in time. Dirichlet-type boundary conditions are imposed on this boundary. At all other boundaries we imposed a zero flux for water, salt and charge. The fluid pressure and electric potential are set to zero. Thus, the pressure and electric potential we calculate are reference values. The solution in the reservoir is electrically neutral. The cation concentration is therefore equal to the anion concentration for a homovalent case. The initial condition is that the pressure and electric potential are equal to their boundary conditions, meaning there is no initial gradient in these properties. The initial salt concentration is set to 1.0×10^{-2} M, and the reservoir concentration is set to 1.5×10^{-4} M. We expose the pore network to a low-salinity reservoir to induce an increase in pressure. With these initial and boundary concentrations, the dimensionless radius $K = h/\lambda_D$ varies between 0.4 and 16, and the dimensionless zeta potential $\bar{\zeta}$ varies between 0.08 and 3.45.

4.2.3 Equations for water flow, ion transport and electric current

The expressions for water flow, ion transport and the electric current are based on the work of Joekar-Niasar et al. (2013), that derived the equations presented here. A minor difference with the equations from Joekar-Niasar et al. (2013) is that in this paper, the exponential term is approximated by a fourth-order polynomial series instead

of an even-degree second-order polynomial. This was done to obtain more convenient expressions for the flow and transport coefficients. In the following sections, the subscripts i and j denote variables defined in pore bodies i and j. The subscript ij denotes variables defined in the pore throat connecting pore bodies i and j.

Water flow

In charged porous media, water flow has a hydrodynamic, chemical-osmotic and electro-osmotic component (Lemaire et al., 2007). These water fluxes are driven by gradients in fluid pressure, salt concentration, and electric potential, respectively. The net water flux is the sum of these components. These water fluxes can be written as a pore throat permeability multiplied by the difference in pressure, salt concentration, and electric potential:

$$q_{ij} = K_{ij}^{h}(P_i^b - P_j^b) + K_{ij}^{c}(C_i^b - C_j^b) + K_{ij}^{e}(\phi_i^b - \phi_j^b) \tag{4.2}$$

where q_{ij} is the total volumetric water flux through pore throat ij [m^3/s], P^b is the bulk pressure in in pore bodies i and j [Pa], C^b is the bulk concentration in pore bodies i and j [mol/m^3], and ϕ^b is the streaming potential in pore bodies i and j [V]. K_{ij}^{h}, K_{ij}^{c} and K_{ij}^{e} are the hydrodynamic, chemical-osmotic and electro-osmotic permeability of pore throat ij, respectively. Expressions for these coefficients are given in Equations 4C.3, 4C.4, and 4C.7 in 4C.

Ion transport

Transport of ions in the presence of an electric field is described by the Nernst-Planck equation. The distribution of ions inside pore throats is influenced by the charge of the channel walls. This causes a discrepancy between transport of cations and anions. The average ion flux through a pore throat is given by:

$$J_{ij}^{\pm} = G_{ij}^{h\pm}(P_i^b - P_j^b) + G_{ij}^{c\pm}(C_i^b - C_j^b) + G_{ij}^{e\pm}(\phi_i^b - \phi_j^b) \tag{4.3}$$

where J_{ij}^{+} and J_{ij}^{-} are the cation and anion mass fluxes through pore throat ij [mol/s], respectively. The first term on the right-hand side of Equation 4.3, $G_{ij}^{h\pm}$, describes hydrodynamic advective transport. The second term, $G_{ij}^{c\pm}$, describes the combined transport by chemical-osmotic advection and diffusion. The last term, $G_{ij}^{e\pm}$, describes combined transport by electro-osmotic advection and electromigration. The expressions for all these terms are given in 4C.

Electric current

The electric current through a pore throat is defined as the difference between the mass flux of cations and the mass flux of anions through the pore throat, multiplied by Faraday's

constant and the ion charge. The resulting expression for the electric current through a pore throat is then:

$$I_{ij} = ZF(J_{ij}^{+} - J_{ij}^{-}) = M_{ij}^{h}(P_i^b - P_j^b) + M_{ij}^{c}(C_i^b - C_j^b) + M_{ij}^{e}(\phi_i^b - \phi_j^b) \tag{4.4}$$

where I_{ij} is the electric current through pore throat ij [C/s], M_{ij}^{h} is the hydrodynamic component of the electric current, M_{ij}^{c} is the electric current due to the combined effect of chemical-osmotic advection and diffusion, and M_{ij}^{e} is the electric current due to the combined effect of electro-osmotic advection and electromigration. The expressions for these terms are given in 4C. This equation is only valid for homovalent electrolyte solutions.

4.2.4 Disjoining pressure

The disjoining pressure is the difference between the bulk fluid pressure and the pressure between two charged surfaces. It consists of three components. In this study we will only consider the electric component, and thus neglect the structural component originating from the modified structure of water molecules near the charged solid surface, and the van der Waals' force. The neglected components are only significant at length scales smaller than 5 nm (McGuiggan and Pashley, 1988). Moreover, these components are constant in a rigid pore network, according to current theoretical expressions. The electric component of the disjoining pressure is the net result of the osmotic pressure and the Maxwell stress. An expression for the disjoining pressure in a two-dimensional channel is derived in 4B. The disjoining pressure in a two-dimensional channel is variable in space, unlike in the commonly used one-dimensional case. Since we are interested in the swelling pressure, we choose to calculate the average disjoining pressure at the channel walls. The average disjoining pressure is the same on every wall of a pore throat, since we consider square pore throats. We only look at the disjoining pressure normal to the pore surface. The average disjoining pressure in a pore throat is given by:

$$\langle \Pi_d \rangle = RTC^b \bar{\zeta}^2 - \frac{\epsilon}{2}\langle E_y \rangle^2 \tag{4.5}$$

where $\langle \Pi_d \rangle$ is the averaged disjoining pressure [Pa] in a pore throat and $\langle E_y \rangle$ is the average electric field at the channel wall [V/m]. The expression for $\langle E_y \rangle$ is provided in 4B. It should be noted that in our pore-network model, the bulk pressure is defined only in pore bodies, while the disjoining pressure is only defined in pore throats.

4.2.5 Computational procedure

Governing equations

The governing equations of the pore-network model are the conservation equations for fluid mass, salt mass and charge. These equations are used to calculate the unknown variables

of the system, which are fluid pressure P^b, salt concentration C^b and electric potential ϕ^b. The first conservation equation is the fluid mass balance. For an incompressible fluid under saturated conditions, the volume of water entering a pore body is equal to the volume of water leaving the pore body. The fluid mass balance then yields:

$$\sum_{m=1}^{N} q_{ij} = 0 \tag{4.6}$$

The expressions for flow (Equation 4.2) can be substituted in this equation, which yields:

$$\sum_{m=1}^{N} K_{ij}^{h}(P_i^b - P_j^b) + K_{ij}^{c}(C_i^b - C_j^b) + K_{ij}^{e}(\phi_i^b - \phi_j^b) = 0 \tag{4.7}$$

where N is the number of pores connected to pore i. Secondly, we use the steady-state charge conservation equation. The electric field is assumed to be in steady-state, as the time-scale of electric relaxation is much smaller than the time-scale of ionic transport, which prohibits separation of cations and anions. The conservation of charge equation then yields:

$$\sum_{m=1}^{N} I_{ij} = 0 \tag{4.8}$$

Substituting the expressions for the electric current from Equation 4.4, this equation can be written as:

$$\sum_{m=1}^{N} M_{ij}^{h}(P_i^b - P_j^b) + M_{ij}^{c}(C_i^b - C_j^b) + M_{ij}^{e}(\phi_i^b - \phi_j^b) = 0 \tag{4.9}$$

Finally, we use the mass balance equations for both the cation and anion species, which are given by:

$$V_i \frac{\Delta C_i^{\pm}}{\tau} = -\sum_{m=1}^{N} J_{ij}^{\pm} \tag{4.10}$$

where V_i is the volume of pore body i [m^3] and τ is the time step size [s]. Substituting the expression for the ion mass fluxes (Equation 4.3), the equation can be rewritten as:

$$V_i \frac{\Delta C_i^{\pm}}{\tau} = -\sum_{m=1}^{N} G_{ij}^{h\pm}(P_i^b - P_j^b) + G_{ij}^{c\pm}(C_i^b - C_j^b) + G_{ij}^{e\pm}(\phi_i^b - \phi_j^b) \tag{4.11}$$

Solver procedure

At the start of each time step, the concentration of the previous time step is used to calculate the electric potential in each pore throat, from which the flow and transport coefficients are calculated. Second, the charge balance equation (Equation 4.9) is solved using a semi-implicit scheme, using the pressure and the salt concentration of the previous

time step. This results in a linear system of equations. This system is solved to obtain the electric potential in each pore body for the current time step. Third, the fluid mass balance equation (Equation 4.7) is solved using a semi-implicit scheme for the pressure field. This results in a linear system of equations, which is solved to obtain the pressure in each pore body. Finally, the ion concentrations are then updated by solving the ion mass balance (Equation 4.11) using an explicit scheme. Since we imposed that there is no net change of the charge in a pore body, the cation and anion concentrations are equal. Therefore, Equation 4.11 has to be solved only once, either for cation or anion concentration. The systems of linear equations are solved by using the direct sparse solver from Intel MKL PARDISO (Intel, 2018).

Time stepping

The maximum time step size is limited by the ion mass fluxes through the pores to prevent numerical instabilities. The time step size is determined by the time it takes to fill or drain a pore to its maximum or minimum concentration, respectively. A local time step size is calculated for each pore body based on the ion fluxes. When there is a net inflow of salt in the pore body, the local time step is defined as the amount of time it takes to reach the maximum concentration, i.e. $\tau_i = (C_{max} - C_i)/\sum J_{ij}$. On the other hand, when there is a net outflow of salt in the pore body, the local time step is equal to the time it takes to reaches the minimum concentration: $\tau_i = \text{abs}((C_i - C_{min})/\sum J_{ij})$. Here, τ_i is the local time step size of pore i. The global time step size is then chosen as a fraction of the minimum local time step size:

$$\tau = 0.01 \times \min(\tau_i) \tag{4.12}$$

A truncation criterion of 10^{-3} is imposed when the concentration is close to C_{min} or C_{max}.

Averaging of parameters

Local parameters are averaged to obtain macroscopic parameters. Parameters defined in pore bodies, such as the bulk pressure, salt concentration and electric potential, are averaged over the pore body volume. For example, the average concentration is defined as:

$$\langle C \rangle = \frac{\sum V_i C_i}{\sum V_i} \tag{4.13}$$

Averaging of the disjoining pressure is more complicated. In swelling pressure measurements in clay, the pressure in the direction perpendicular to the clay bedding is often measured (Low, 1987). To mimic this, we want to know the average disjoining pressure in the vertical direction of the network. A complication is that the disjoining pressure is anisotropic, and thus the orientation of the pore throats must be taken into account. Therefore, we are interested only in the component of the disjoining pressure

that acts on the vertical direction of the pore network, which is defined as $\Pi_d^v = \Pi_d \cos\theta$. Here, Π_d^v is the vertical component of the disjoining pressure [Pa], and θ is the angle of the pore throat with respect to the longitudinal axis of the pore-network. We assumed that all pore throats are not rotated along its longitudinal axis, meaning that there is only one channel wall facing the vertical direction per pore throat. The average disjoining pressure in this study is therefore actually the average vertical disjoining pressure. The disjoining pressure is averaged over the pore surface on which it acts:

$$\langle \Pi_d^v \rangle = \frac{\sum A_{ij}^s \Pi_d^v}{\sum A_{ij}^s} \tag{4.14}$$

where A_{ij}^s is the surface area of the walls of pore throat ij.

4.3 Results and discussion

4.3.1 Network size

The pore network size needs to be sufficiently large to get a good representation of the pore size distribution. At the same time, we want it as small as possible to decrease computation time. Therefore, we tested various pore network sizes to determine the appropriate network size. We considered $n \times n \times n$ cubic lattices for the pore network, defined by the number of pore bodies in one direction n. A sufficient network size should result in a similar average pressures between different realisations. We found that this was the case for a network size of $n = 20$. A similar network size was reported by Obliger et al. (2014), who looked at macroscopic flow and transport coefficients in charged pore networks. The results below are all obtained from simulations with network size $n = 20$. The total network length is therefore 35 μm. The computation time for such networks was 12-16 hours on an Intel(R) Core(TM) i5-4690 CPU @ 3.50GHz with 8.00 GB RAM.

4.3.2 Evolution of the salt concentration

Salt transport is governed by diffusion (Figure 4.2). To assert the significance of diffusion compared to advection, the Péclet number was computed for each pore throat. The maximum Péclet number did not exceed 0.05, which indicates that diffusion is indeed the dominant process in salt transport. The discrepancy between homogeneous and heterogeneous networks becomes significant when the concentration drops below 0.001 M, when the effect of the diffuse double layers becomes more important. The salt concentration decreases in the whole network, until it reaches the boundary condition value. The concentration front moves faster in heterogeneous pore networks than in homogeneous pore networks (Figure 4.2). The time until steady-state is reached is therefore also shorter for heterogeneous networks. The time to reach steady-state for the homogeneous network was 3.5 s, while for heterogeneous networks it was around 2.5 s.

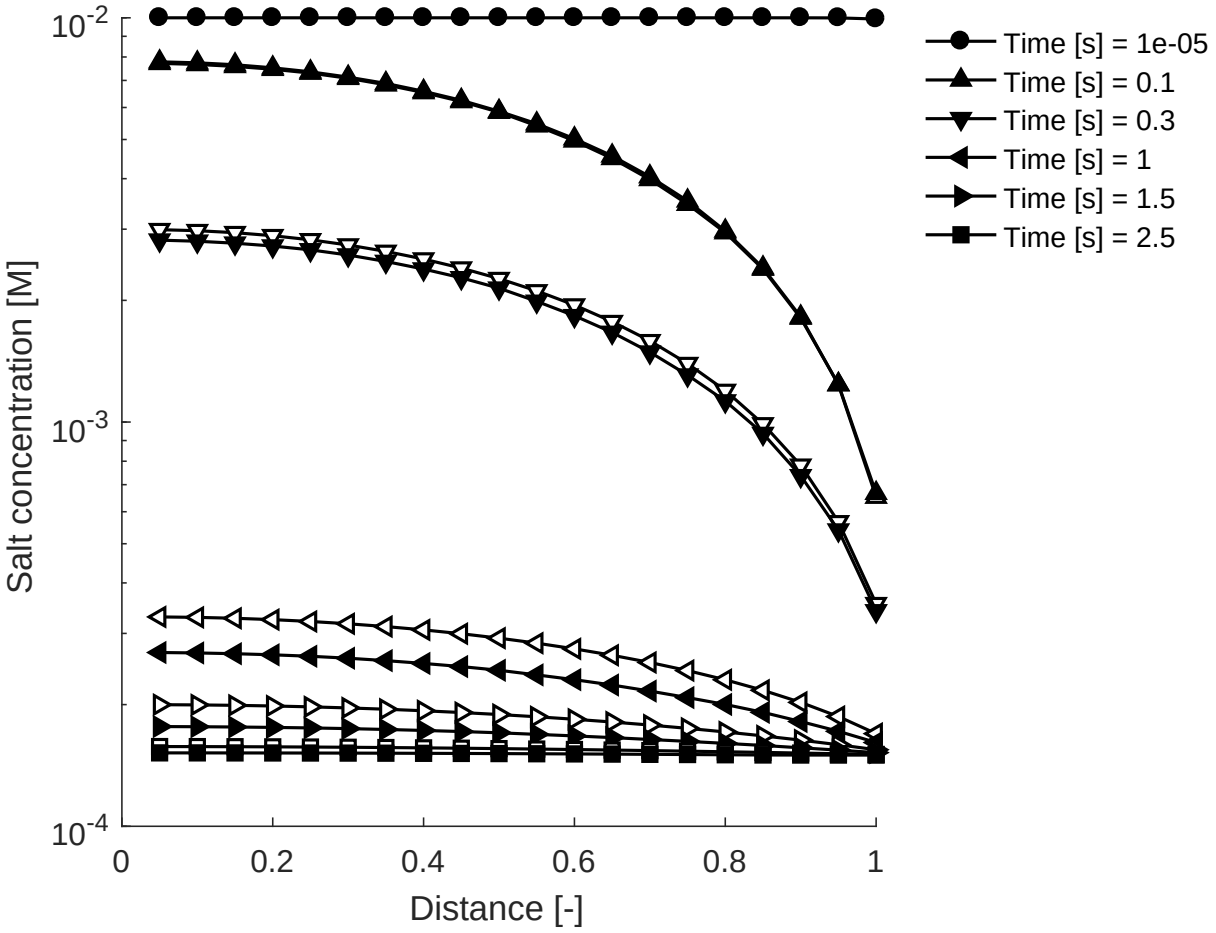

Figure 4.2: Salt concentration profile at various points in time for a homogeneous network (open markers) and a heterogeneous network (closed markers). The dimensionless distance is defined as the distance divided by the total network length.

4.3.3 Evolution of the streaming potential

The profile of the streaming potential at various points in time is shown in Figure 4.3. This is the electric potential that develops due to unequal transport of cations and anions. This is not the electric potential in the diffuse double layer. The streaming potential starts out at the reference value, which is zero. Ions diffuse into the reservoir at distance of 1.0, due to the lower salt concentration in the reservoir. Cations travel relatively faster through the network than anions, since anions are repelled from the negatively charged channel walls. To keep the bulk solution in the pore bodies electroneutral, the electric potential drops. As the salt concentration decreases, the diffuse double layers extend. This causes a stronger unequal transport between cations and anions. However, the salt concentration gradient becomes smaller over time, which reduces the ionic flux. However, the first process dominates, and the electric potential becomes more negative over time (see $t = 0.1$ s and $t = 0.3$ s in Figure 4.3). The situation reverses when the salt concentration becomes small, i.e. when the system approaches the steady-state situation.

During this phase, the electric potential increases back to its reference value ($t = 1$ s and $t = 1.5$ s in Figure 4.3). The final electric potential is not shown, as it is the same as the initial electric potential.

Figure 4.3 also shows the difference in electric potential for homogeneous and heterogeneous pore networks. The average electric potential in heterogeneous networks is significantly lower (less negative) than that in homogeneous networks. The streaming potential develops due to different transport rates of cations and anions in the negatively charged channels. This difference in ionic transport rates becomes more significant when the thickness of the double layer is thick compared to the pore radius. There is less overlapping of the diffuse double layers in the larger pores that exist in heterogeneous networks, which results in smaller streaming potentials (less negative) in such networks.

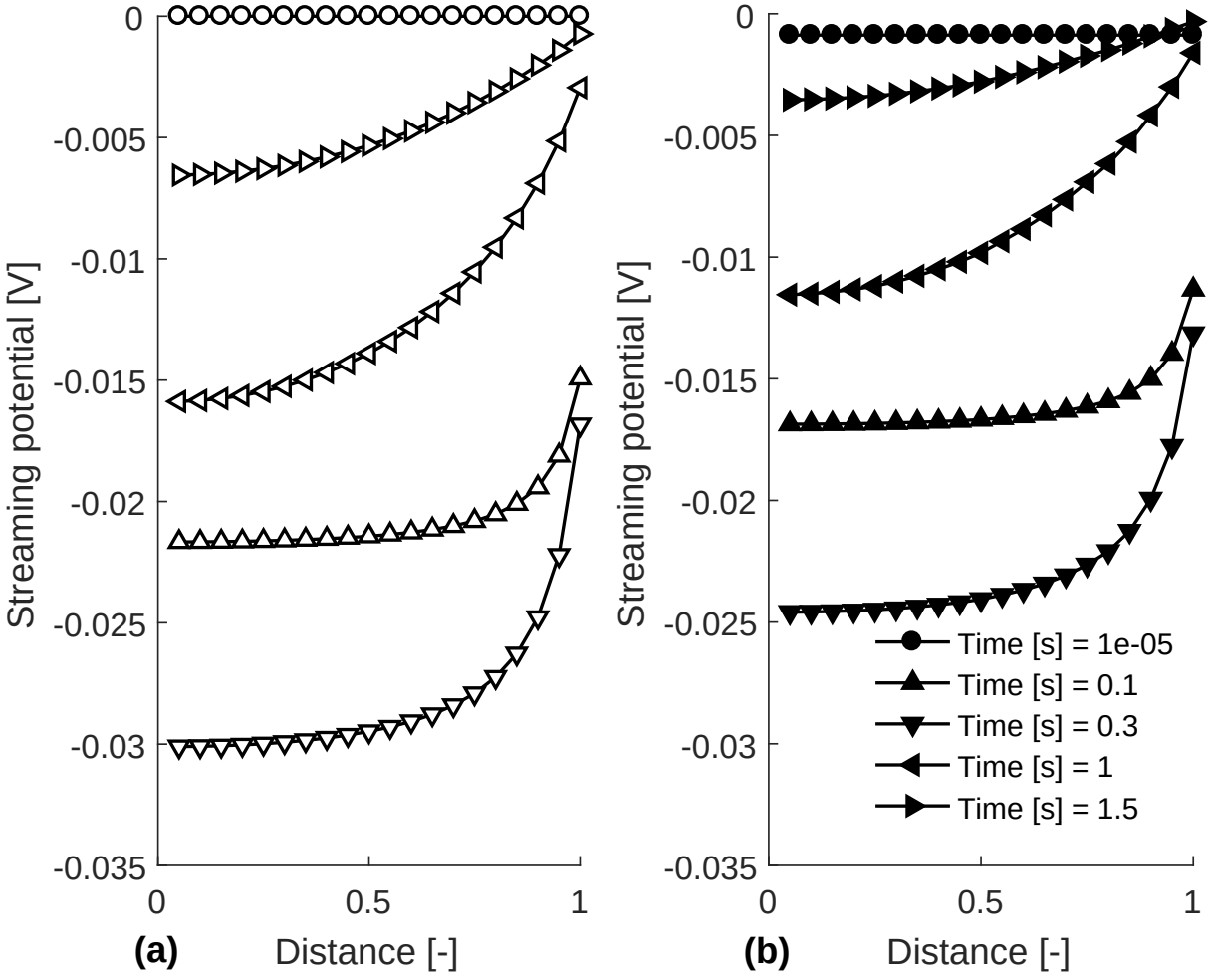

Figure 4.3: Profile of the streaming potential at various time steps, for (a) a homogeneous network (open markers) and for (b) a heterogeneous network (closed markers). The dimensionless distance is defined as the distance divided by the total network length.

4.3.4 Evolution of the pressure

Figure 4.4 shows the profile of the bulk pressure at various moments in time. The bulk pressure shows non-monotonic behaviour: at first it increases, then it drops. The development of the bulk pressure is closely related to the evolution of the streaming potential. As the electric potential in the pore network drops, water flows into the network by electro-osmosis. At the same time, chemical-osmotic flow drives water in the opposite direction, towards the reservoir. The increase of the bulk pressure suggests there is a net inflow of water. Thus, electro-osmotic flow dominates over chemical-osmotic flow. When the electric potential drops, the inflow of water decreases, and the pressure drops to its reference value.

The effect of heterogeneity on the bulk pressure is similar to its effect on the streaming potential. In our model, the streaming potential is the main driving force for water flow. Since lower streaming potentials are observed in heterogeneous networks, lower bulk pressures are also observed in such networks. The bulk pressure in a heterogeneous network was up to 46% smaller than that in a homogeneous network. The maximum pressure in homogeneous porous media was 1172 Pa, while in heterogeneous networks the maximum observed pressure was 650 Pa. Thus, the differences in average bulk pressure between homogeneous and heterogeneous networks are significant. This implies that the pressure evolution in heterogeneous networks cannot be approximated by a homogeneous network with the same mean pore radius. A second homogenous network was considered, where the median value of the pore size distribution was assigned to all pore throat radii. While this yielded results closer to the heterogeneous network, the pressure was still significantly overestimated.

The disjoining pressure increases monotonically over time, as the salt concentration drops (Figure 4.5). The disjoining pressure is higher near the reservoir (distance equal to 1.0), where the salt concentration is lower. At steady state, the disjoining pressure is the same over the whole network in the homogeneous system, because the pore radii and bulk concentration are identical for every pore. In the heterogeneous network, the bulk concentration is equal in each pore, but the pore radii are different. Therefore, the disjoining pressure is not equal in each pore. This causes the erratic pattern of the disjoining pressure in heterogeneous networks (Figure 4.5). This pattern would be smoother for larger pore networks, with more pores per cross-section. Additionally, Figure 4.5 shows that the average disjoining pressure in the heterogeneous network is significantly lower than that in the homogeneous network. The maximum average disjoining pressure in homogeneous systems is 1056 Pa, while for heterogeneous systems the maximum observed pressure is 882 Pa, which is 16% lower.

Although we used intrinsic average pressure in the previous sections, a clear definition of the average pressure in a porous medium is lacking. The pressure is often averaged as we did using the intrinsic phase average operator (e.g. Joekar-Niasar and

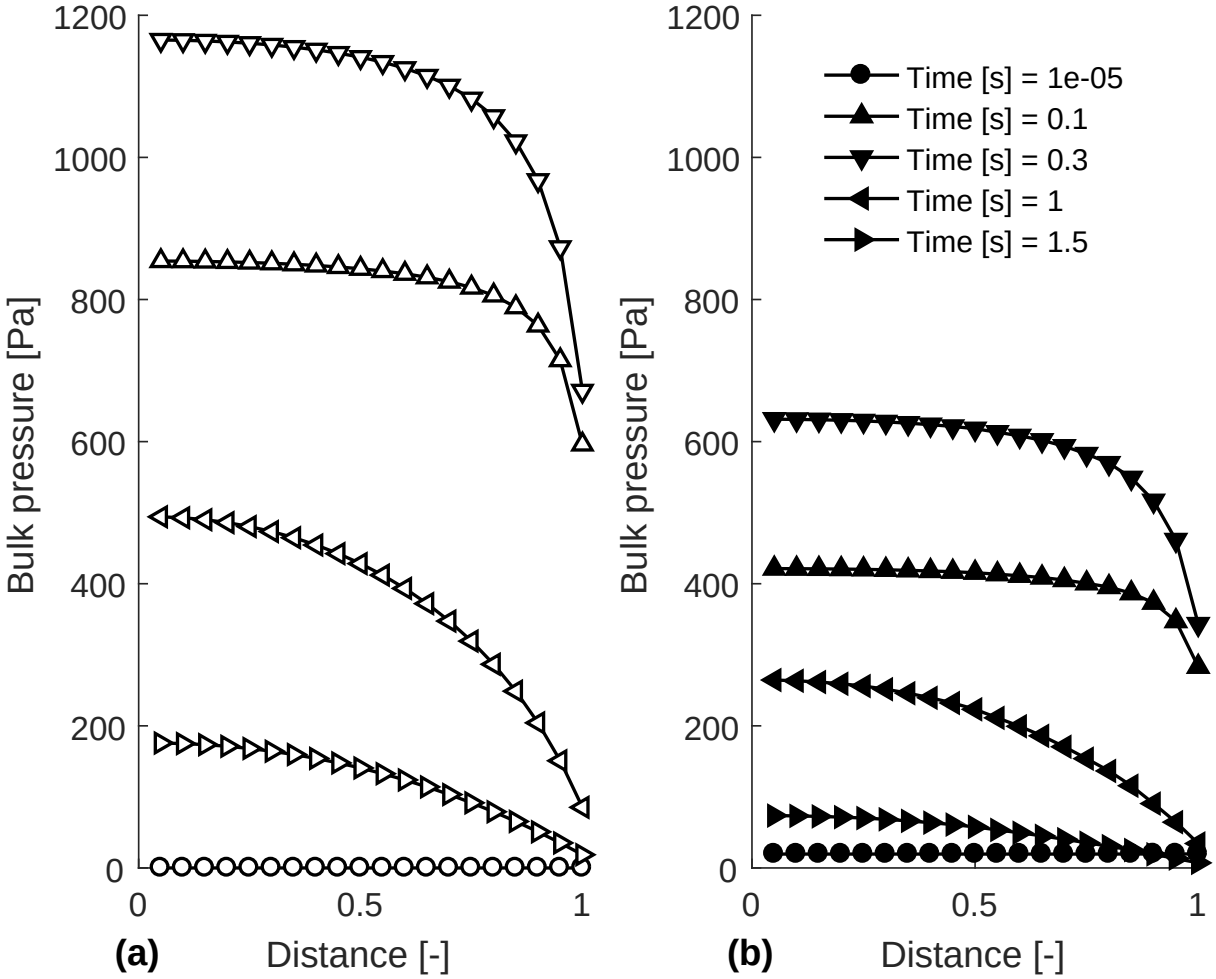

Figure 4.4: Profile of the bulk pressure in the pore network, for (a) a homogenous network (open markers) and for (b) a heterogeneous network (closed markers). The dimensionless distance is defined as the distance divided by the total network length.

Hassanizadeh (2011)). However, Nordbotten et al. (2007) showed that this can introduce averaging artefacts, and they proposed a centroid-corrected averaging operator instead. Nevertheless, the intrinsic phase average is still frequently used. The definition of the average pressure in a charged porous medium is even more complex, as the disjoining pressure is anisotropic. Gonçalvès et al. (2010) proposed to average the disjoining pressure over the surface area of the solid particles, as this is the surface on which the pressure acts. A similar method was used in this study. However, in a heterogeneous system, this averaged pressure does not reflect the swelling potential. The pressure in smaller pores is much larger than in the larger pores. For example, at steady-state, the pressure in the smallest pore is 4.2 kPa, while in the largest pore it is 0.6 kPa. The small pores would swell significantly more than the large pores, which is not captured by the volume-averaged pressure. This suggests that the volume-averaged pressure does not give a good indication on the effective swelling pressure in a heterogeneous network.

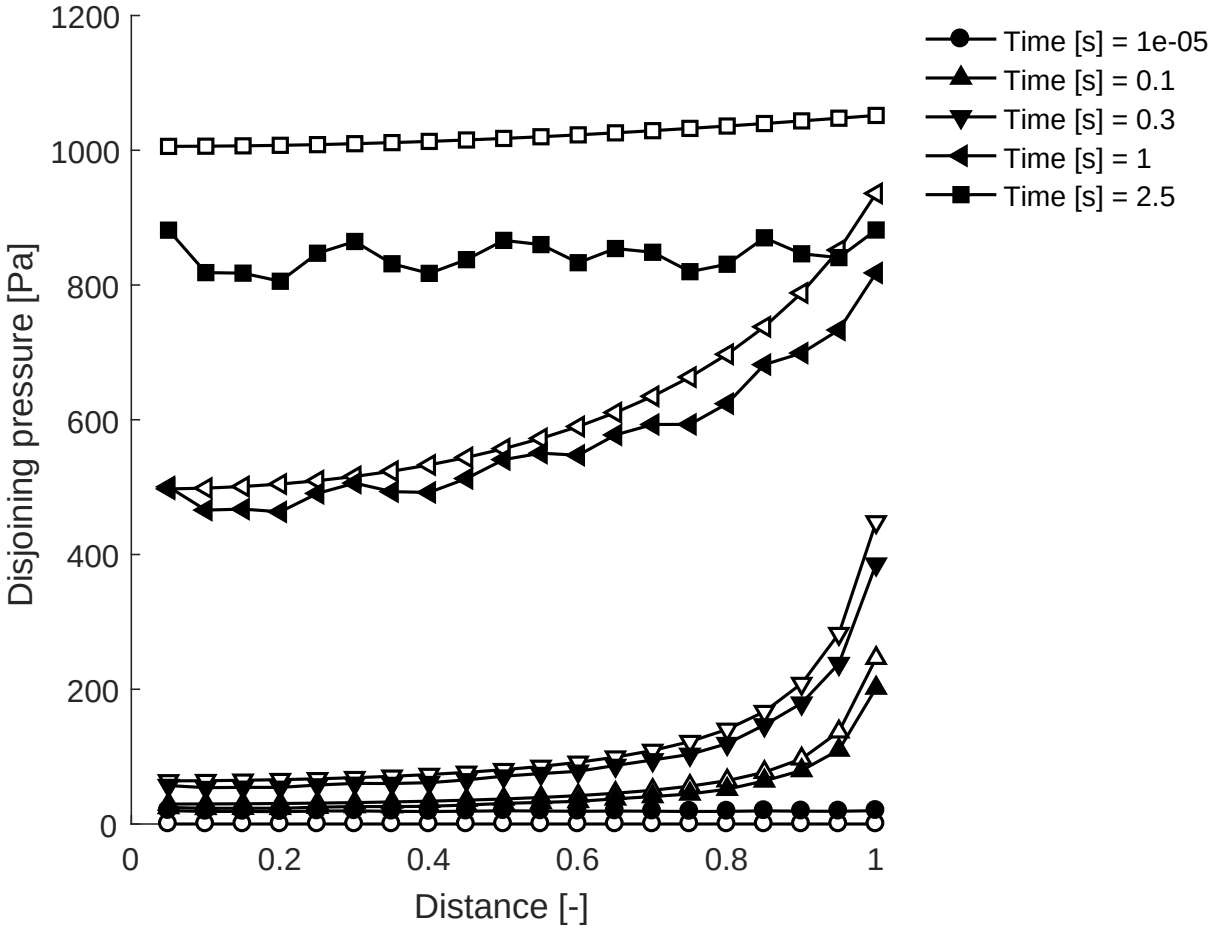

Figure 4.5: Profile of the average disjoining pressure in the network for a homogeneous network (open markers) and a heterogeneous network (closed markers). The dimensionless distance is defined as the distance divided by the total network length.

The pressure in this study is on the order of kPa, while most experimental studies in clays show pressures on the order of MPa. The reason for this is that the surface charge density of the solid phase used in the model was based on experimentally obtained data from Delgado et al. (1986) and Low (1987). These studies show that most of the charge of the clay is compensated by the Stern layer, which would yield low electric potentials in the diffuse double layer. For example, Low (1987) reports that only 2% of the charge of the clay is compensated by the diffuse layer, which results in disjoining pressures in the range as reported in this study. This discrepancy between diffuse double layer theory and experiments have been attributed to the structural component of the disjoining pressure by Low (1987), although theoretical development of this component is lacking. Alternatively, some studies neglect the charge of the Stern layer and assume that the full charge deficit of the clay is compensated by the diffuse double layer. Such situations result in high electric potentials and disjoining pressures comparable to experimental measurements. In the pore-network model, we chose to use small electric potentials, since it makes use of the

Debye-Hückel approximation, which is only accurate for small electric potentials. This approximation would overestimate the electric potential in the pore throats under high electric potential conditions. In such cases, the nonlinear Poisson-Boltzmann equation should be solved instead to obtain an accurate solution for the electric potential. However, for the message of this paper, the use of the Debye-Hückel approximation instead of the nonlinear Poisson-Boltzmann equation is not important.

4.4 Conclusions

We investigated the significance of heterogeneity on the pressure evolution in rigid charged porous media. For this purpose, we developed a pore-network model for simulating water flow and salt transport in such media. We simulated water flow and salt transport in homogeneous and heterogeneous pore networks. A log-normal pore size distribution was assumed for the heterogeneous networks, with a mean pore size equal to the homogeneous networks' pore size. We compared the evolution of the pressure between both cases. Of course, for homogeneous networks at steady-state, the averaged swelling pressure was equal to the microscopic disjoining pressure, which is in agreement with Derjaguin et al. (1987). In the heterogeneous networks, the average pressure was much lower than in the homogeneous network, while local pressures could be much higher. This raises the question if the volume-averaged pressure represents the swelling potential of heterogeneous systems. This also makes it difficult to estimate the swelling pressure based on diffuse double layer theory, as a definition of a representative pore size is not clear. As expected, large pores dominate electrokinetic processes in heterogeneous networks. This effect is seen in both the lower average bulk pressure and the lower average disjoining pressure, and is also reflected in the lower streaming potential and higher ion transport rates compared to the homogeneous network. The results indicate that heterogeneity in charged porous media should be investigated further, as these insights can have implications for practical purposes such as the management of agricultural soils.

The pore-network model presented in this study can be extended in future work. The nonlinear Poisson-Boltzmann equation could be included in the model to make it applicable to high electric potentials, which allows for a better comparison with experimental data. However, no analytical solution exists for the nonlinear Poisson-Boltzmann equation in rectangular or cylindrical domains. Therefore, the Poisson-Boltzmann equation has to be solved numerically for each pore, or approximated semi-analytically similar to the work of Oyanader and Arce (2005). This would drastically increase the computational demand, but makes the model applicable to a wider range of situations. Additionally, the Gouy-Chapman model could be extended for more realistic descriptions of the diffuse double layer. Possibilities are including the Stern layer, cation exchange, or ion-ion correlation. Finally, including deformation of the pore network in response to the swelling pressure could give valuable information on the evolution of the

hydraulic properties in swelling soils.

Appendix

4A Electric potential in a charged rectangular channel

We consider the Gouy-Chapman model, and thus neglect the Stern layer. The zeta potential is equal to the surface potential in this case. The ions in the diffuse layer can move due to external gradients, like pressure, concentration or electric potential. The ion concentration profiles in the diffuse layer under equilibrium conditions can be described by the Boltzmann distribution, which for a homovalent electrolyte is given by:

$$C^{\pm} = C^{b} \exp(\mp Z\bar{\psi}) \tag{4A.1}$$

where $C^{\pm}$ is the ion concentration of species in a pore throat [mol/m^3], C^b is the concentration in the bulk solution, Z is the ion valence of the electrolyte species [-], and $\bar{\psi}$ is the dimensionless electric potential in the electric double layer [-]. The dimensionless electric potential is defined as: $\bar{\psi} = \frac{F\psi}{RT}$, where ψ is the electric potential [V]. The electric field in a channel is given by the solution to the Poisson-Boltzmann equation. To obtain an analytical solution for the Poisson-Boltzmann equation in a rectangular channel, we have to make use of the Debye-Hückel approximation to linearise the Poisson-Boltzmann. This is done by using the approximation $\sinh\bar{\psi} \approx \bar{\psi}$, which is a valid approximation for small electric potentials. While strictly speaking this is a valid approximation only for zeta potentials of less than 25 mV, it is still a good approximation for zeta potentials up to 75 mV (Masliyah and Bhattacharjee, 2005). The linearised Poisson-Boltzmann equation is given by:

$$\nabla^2\bar{\psi} = \frac{1}{\lambda_D^2}\bar{\psi} \tag{4A.2}$$

where λ_D is the Debye length [m], which for a homovalent electrolyte is defined as $\lambda_D = \sqrt{\frac{\epsilon RT}{2Z^2F^2C^b}}$. Before this equation can be solved, appropriate boundary conditions should be applied. Montmorillonite is assumed to have a constant surface charge density (van Olphen, 1963; Lehikoinen, 1999; Sperry and Peirce, 1999; Tournassat et al., 2011). This boundary condition implies that the zeta potential is a function of the salt concentration. However, we use the analytical expressions for flow and transport through rectangular charged channels by Joekar-Niasar et al. (2013), which are based on a constant zeta potential at the channel walls. The solution to the linear Poisson-Boltzmann equation in a rectangular channel with a constant zeta potential is given by:

$$\bar{\psi} = \bar{\zeta}\left(\frac{\cosh(K\bar{y})}{\cosh(K)} + \sum_{m=1}^{\infty} A_m \cos\left(\frac{(2m-1)\pi\bar{y}}{2}\right)\cosh(\Re_m\bar{x})\right) \tag{4A.3}$$

where ζ is the zeta potential, $\Re_m = \sqrt{\frac{(2m-1)^2\pi^2}{4} + K^2}$, $A_m = \frac{4(-1)^{m+1}K^2}{(2m-1)\pi\Re_m^2\cosh(\Re_m\bar{w})}$ and the dimensionless coordinates $\bar{x} = x/h$ and $\bar{y} = y/h$ (Joekar-Niasar et al., 2013; Ng and Qi, 2015). We truncate the infinite series to two terms. To include such a dynamic zeta potential, but still make use of the expression for the electric potential in Equation 4A.3, we derive a relationship between the surface charge density and the zeta potential. The solution for the electric potential can be used to find a relationship between the surface charge density and the zeta potential, since $\sigma_\zeta/\epsilon = -\nabla\psi \cdot \mathbf{n}$. Integrating this over the channel walls yields the average surface charge density. For this expression for the electric potential, the following relationship between the average surface charge density and the zeta potential is obtained:

$$\sigma_\zeta = \frac{\epsilon\zeta}{h}\left(K\tanh(K) - \sum_{m=1}^{\infty} A_m(-1)^{m+1}\frac{(2m-1)\pi}{\Re_m}\sinh(\Re_m\bar{w})\right) \tag{4A.4}$$

where σ_ζ is the average electrokinetic surface charge density [C/m^2]. The above expression for the electric potential was used to derive expressions for the ion concentration profiles. This expression is only valid for pore throats with square cross-sections.

4B Disjoining pressure in a charged rectangular channel

The disjoining pressure in a two-dimensional situation is different than in one-dimensional case. In a two-dimensional case, the disjoining pressure is not constant across the whole channel. We choose to calculate the normal component of the disjoining stress tensor at the channel walls. Since we have rectangular channel cross-sections, this component is equal at each wall of the channel. Therefore, it is arbitrary which channel wall is chosen. We chose the wall perpendicular to the y-axis at $\bar{y} = 1$, Since we look only at the normal component on one of the channel walls, we consider only a single element of the disjoining pressure stress tensor. This component is given by:

$$\Pi_d = \Pi + \frac{\epsilon}{2}\left(E_x^2 - E_y^2\right) \tag{4B.1}$$

where Π is the osmotic pressure [Pa], and E_x and E_y are the x- and y-components of the electric field. The x-component of the electric field (the tangential component) is zero at this wall, since the electric potential is constant and equal to the zeta potential over the whole length of the wall. The expression for the disjoining pressure then reduces to:

$$\Pi_d = \Pi - \frac{\epsilon}{2}E_y^2 \tag{4B.2}$$

Since we have a constant zeta potential at the channel walls, the electric field directed normal from the wall is variable in space. Therefore, we calculate the average disjoining

pressure on the surface as:

$$\langle \Pi_d \rangle = \langle \Pi \rangle - \frac{\epsilon}{2} \langle E_y^2 \rangle \tag{4B.3}$$

The electric field is related to the electric potential through the relation $E_y = -\partial\psi/\partial y$. The average electric field $\langle E^2 \rangle$ can then be calculated using our expression for the electric potential. This yields:

$$\begin{aligned}\langle E_y^2 \rangle = \left(\frac{RT\bar{\zeta}}{hF}\right)^2 \Bigg(& K^2 \tanh^2(K) + \frac{A_1^2\pi^2}{8}\left(1 + \frac{\sinh(2\Re_1\bar{w})}{2\bar{w}\Re_1}\right) + \frac{9A_2^2\pi^2}{8}\left(1 + \frac{\sinh(2\Re_2\bar{w})}{2\bar{w}\Re_2}\right) \\ & - \frac{K\tanh(K)A_1\pi\sinh(\Re_1\bar{w})}{2\bar{w}\Re_2} + \frac{3K\tanh(K)A_2\pi\sinh(\Re_1\bar{w})}{\bar{w}\Re_2} \\ & - \frac{3A_1A_2\pi^2\big(\Re_1\sinh(\Re_1\bar{w})\cosh(\Re_2\bar{w}) - \Re_2\cosh(\Re_1\bar{w})\sinh(\Re_2\bar{w})\big)}{2\bar{w}(\Re_1^2 - \Re_2^2)} \Bigg)\end{aligned} \tag{4B.4}$$

An expression for the osmotic pressure Π can be obtained assuming a Boltzmann distribution for the ions. For low electric potentials, this yields:

$$\Pi = RTC^b\bar{\zeta}^2 \tag{4B.5}$$

The osmotic pressure is constant across the length of the channel wall, because the zeta potential is constant. The expression for the osmotic pressure is therefore the same as for the average osmotic pressure: $\langle \Pi \rangle = \Pi$. Equations 4B.4 and 4B.5 are substituted into Equation 4B.3 to calculate the disjoining pressure at each time step.

4C Expressions for flow and transport

The equations for transport of water, salt and electric charge are based on the work of Joekar-Niasar et al. (2013). A brief summary is given here.

The water flow velocity is obtained from the modified Stokes equation. The flow velocity can be divided into three components: the hydrodynamic velocity u_h (driven by gradients in fluid pressure), the chemical-osmotic velocity u_c (driven by gradients in salt concentration), and the electro-osmotic velocity u_e (driven by gradients in electric potential):

$$\eta\left(\frac{\partial^2 u_h}{\partial x^2} + \frac{\partial^2 u_h}{\partial y^2}\right) = \frac{\partial P^b}{\partial z} \tag{4C.1a}$$

$$\eta\left(\frac{\partial^2 u_c}{\partial x^2} + \frac{\partial^2 u_c}{\partial y^2}\right) = 2RT(\cosh(\bar{\psi}) - 1)\frac{\partial C^b}{\partial z} \tag{4C.1b}$$

$$\eta\left(\frac{\partial^2 u_e}{\partial x^2} + \frac{\partial^2 u_e}{\partial y^2}\right) = \epsilon\left(\frac{\partial^2 \psi}{\partial x^2} + \frac{\partial^2 \psi}{\partial y^2}\right)\frac{\partial \phi^b}{\partial z} \tag{4C.1c}$$

where η is the dynamic viscosity of water [Pa s]. These equations are solved analytically for u_h, u_c, and u_e in a rectangular domain. The solutions are not shown here, but can be found in Joekar-Niasar et al. (2013). The gradient, e.g. $\frac{\partial P^b}{\partial z}$ between two pore bodies is discretized as $\frac{P_i^b - P_j^b}{L}$, where L is the length of pore throat ij [m]. For the pore-network model, we require average fluxes for each pore throat. Therefore, the local fluxes are averaged over the cross-sectional area of the pore throat to obtain coefficients for flow and transport. For example, the average hydrodynamic flow velocity is given by:

$$\langle u_h \rangle = \frac{1}{4\bar{w}} \int_{-1}^{1} \int_{-\bar{w}}^{\bar{w}} u_h \, d\bar{x} d\bar{y} \tag{4C.2}$$

The volumetric water flux through a pore throat is then simply the average flow rate multiplied by the cross sectional area of the pore throat. For example, the hydrodynamic water flux is given by: $q_{ij}^h = A\langle u_h \rangle = K_{ij}^h (P_i^b - P_j^b)$, where A is the cross-sectional area of the pore throat [m^2], and K_{ij}^h is the hydrodynamic permeability of pore throat ij. The expression for the hydrodynamic permeability is then given by:

$$K_{ij}^h = -\frac{32h^2}{\eta \pi^5 \bar{w} L} A \left(\pi \bar{w} - 2 \tanh\left(\frac{\pi \bar{w}}{2}\right) \right) \tag{4C.3}$$

The same methodology is used to obtain the coefficients for chemico-osmotic and electro-osmotic flow. The chemical-osmotic permeability of pore throat ij is given by:

$$K_{ij}^c = -\frac{32RT\bar{w}h^2}{\eta \pi^4 L} A\big((a_0 - 1)\Omega_0 + a_1\Omega_1 + a_2\Omega_2 + a_3\Omega_3 + a_4\Omega_4\big) \tag{4C.4}$$

where the coefficients Ω^n are given by:

$$\Omega_0 = \frac{\delta_0^{11}}{1+\bar{w}^2} + \frac{\delta_0^{12}}{3(9+\bar{w}^2)} + \frac{\delta_0^{21}}{3(1+9\bar{w}^2)} + \frac{\delta_0^{22}}{81(1+\bar{w}^2)} \tag{4C.5a}$$

$$\Omega_1 = \frac{\delta_1^{11}}{1+\bar{w}^2} + \frac{\delta_1^{12}}{3(9+\bar{w}^2)} + \frac{\delta_1^{21}}{3(1+9\bar{w}^2)} + \frac{\delta_1^{22}}{81(1+\bar{w}^2)} \tag{4C.5b}$$

$$\Omega_2 = \frac{\delta_2^{11}}{1+\bar{w}^2} + \frac{\delta_2^{12}}{3(9+\bar{w}^2)} + \frac{\delta_2^{21}}{3(1+9\bar{w}^2)} + \frac{\delta_2^{22}}{81(1+\bar{w}^2)} \tag{4C.5c}$$

$$\Omega_3 = \frac{\delta_3^{11}}{1+\bar{w}^2} + \frac{\delta_3^{12}}{3(9+\bar{w}^2)} + \frac{\delta_3^{21}}{3(1+9\bar{w}^2)} + \frac{\delta_3^{22}}{81(1+\bar{w}^2)} \tag{4C.5d}$$

$$\Omega_4 = \frac{\delta_4^{11}}{1+\bar{w}^2} + \frac{\delta_4^{12}}{3(9+\bar{w}^2)} + \frac{\delta_4^{21}}{3(1+9\bar{w}^2)} + \frac{\delta_4^{22}}{81(1+\bar{w}^2)} \tag{4C.5e}$$

The coefficients δ_a^{pq} with p and $q = 1, 2$ are given in Table 4C.1. The coefficients a_i in Equation 4C.4 are constants, which originate from the fact that the solution for the

chemical-osmotic velocity was obtained by approximating the hyperbolic cosine by a polynomial function:

$$\cosh(\bar{\psi}) \approx a_0 + a_1\bar{\psi} + a_2\bar{\psi}^2 + a_3\bar{\psi}^3 + a_4\bar{\psi}^4 \tag{4C.6}$$

We fitted this function for the range $0 \leq \bar{\psi} \leq 3$, with an R^2 of 1. The values of the fitting coefficients were 1.0, -0.08858, 0.7524, -0.2172, and 0.1037 for the coefficients a_0, a_1, a_2, a_3, and a_4, respectively.

Finally, electro-osmosis is water flow driven by gradients in electric potential. The electro-osmotic permeability of pore throat ij is given by:

$$K_{ij}^{e} = -\frac{\epsilon RT}{\eta FL} A\big(\langle\bar{\psi}\rangle - \bar{\zeta}\big) \tag{4C.7}$$

where ϵ is the electric permittivity of water [C^2/(J m)], F is the Faraday constant [C/mol]. The zeta potential ζ denotes the electric potential at the shear plane inside the pore throat. We assume that it is located at the channel wall. The term $\langle\bar{\psi}\rangle$ is the average electric potential in the pore throat. The expression for this term is shown in Table 4C.2 in 4C.

Transport of ions is based on the Nernst-Planck equation. Assuming a monovalent electrolyte solution with a Boltzmann distribution, the average ion flux through pore throat ij for a monovalent electrolyte is given by:

$$\langle J_{ij}^{\pm}\rangle = \langle u_h \exp(\pm\bar{\psi})\rangle C^b + \langle u_c \exp \pm(\bar{\psi})\rangle C^b + \langle u_e \exp(\pm\bar{\psi})\rangle C^b - D\langle\exp(\pm\bar{\psi})\rangle \frac{\partial C^b}{\partial z} \mp D\langle\exp(\pm\bar{\psi})\rangle C^b \frac{\partial \bar{\phi}^b}{\partial z} \tag{4C.8}$$

where $\bar{\phi}^b = \frac{F\phi^b}{RT}$ is the dimensionless streaming potential [-], and C^b is the ion concentration of the upstream pore body. The averaging of the parameters occurs in the same manner as Equation 4C.2. The ion distribution is described by the exponential Boltzmann distribution, which we approximated by a polynomial function:

$$\exp(\pm\bar{\psi}) \approx b_0^{\pm} + b_1^{\pm}\bar{\psi} + b_2^{\pm}\bar{\psi}^2 + b_3^{\pm}\bar{\psi}^3 + b_4^{\pm}\bar{\psi}^4 \tag{4C.9}$$

We fitted this function for a range of $0 \leq \bar{\psi} \leq 3$, with an R^2 of 1. For the cations, we found values of 1.0, 0.8079, 1.055, -0.326, and 0.1965 for the coefficients b_0^+, b_1^+, b_2^+, b_3^+ and b_4^+, respectively. For the anions, we found values of 1.0, -0.9851, 0.4494, -0.1084, and 0.01097 for the coefficients b_0^-, b_1^-, b_2^-, b_3^- and b_4^-, respectively.

The pressure-driven salt transport through pore throat ij only consists of hydrodynamic advection:

$$G_{ij}^{h\pm} = \frac{A}{L}\langle u_h \exp(\pm\bar{\psi})\rangle C^b \tag{4C.10}$$

The average hydrodynamic advective flux can be written by making use of the polynomial approximation:

$$\langle u_h \exp(\pm\bar{\psi})\rangle = b_0^{\pm}\langle u_h\rangle + b_1^{\pm}\langle u_h\bar{\psi}\rangle + b_2^{\pm}\langle u_h\bar{\psi}^2\rangle + b_3^{\pm}\langle u_h\bar{\psi}^3\rangle + b_4^{\pm}\langle u_h\bar{\psi}^4\rangle \tag{4C.11}$$

These terms are shown in Table 4C.3.

Gradients in salt concentration cause ionic transport through pore throat ij via both chemical-osmotic advection and diffusion:

$$G_{ij}^{c\pm} = A\langle u_c \exp(\pm\bar{\psi})\rangle C^b - \frac{DA}{L}\langle \exp(\pm\bar{\psi})\rangle \tag{4C.12}$$

where D is the ion diffusion coefficient [m^2/s], which we set equal for both cations and anions in this study. The average chemical-osmotic advection can be written as:

$$\langle u_c \exp(\pm\bar{\psi})\rangle = b_0^{\pm}\langle u_c\rangle + b_1^{\pm}\langle u_c\bar{\psi}\rangle + b_2^{\pm}\langle u_c\bar{\psi}^2\rangle + b_3^{\pm}\langle u_c\bar{\psi}^3\rangle + b_4^{\pm}\langle u_c\bar{\psi}^4\rangle \tag{4C.13}$$

These coefficients are shown in Table 4C.4. The average ion distribution is given by:

$$\langle \exp(\pm\bar{\psi})\rangle = b_0^{\pm} + b_1^{\pm}\langle\bar{\psi}\rangle + b_2^{\pm}\langle\bar{\psi}^2\rangle + b_3^{\pm}\langle\bar{\psi}^3\rangle + b_4^{\pm}\langle\bar{\psi}^4\rangle \tag{4C.14}$$

These coefficients are shown in Table 4C.2.

Gradients in electric potential cause ionic transport through electro-osmotic advection and electromigration:

$$G_{ij}^{e\pm} = \frac{A}{L}\langle u_e \exp(\pm\bar{\psi})\rangle C^b \mp \frac{DA}{L}\langle \exp(\mp\bar{\psi})\rangle C^b \tag{4C.15}$$

The term $\langle \exp(\pm\bar{\psi})\rangle$ is already written out in Equation 4C.14 and the components are shown in Table 4C.2. The average electro-osmotic advection can be written as:

$$\langle u_e \exp(\pm\bar{\psi})\rangle = b_0^{\pm}\langle u_e\rangle + b_1^{\pm}\langle u_e\bar{\psi}\rangle + b_2^{\pm}\langle u_e\bar{\psi}^2\rangle + b_3^{\pm}\langle u_e\bar{\psi}^3\rangle + b_4^{\pm}\langle u_e\bar{\psi}^4\rangle \tag{4C.16}$$

These terms are shown in Table 4C.5.

Since we only consider homovalent electrolyte solutions, the electric current through pore throat ij is given by:

$$I_{ij} = ZF\big(\langle J_{ij}^{+}\rangle - \langle J_{ij}^{-}\rangle\big) \tag{4C.17}$$

Thus, the coefficients for charge transport through pore throat ij can be written in terms of the coefficients for salt transport:

$$M_{ij}^{h} = ZF(G_{ij}^{h+} - G_{ij}^{h-}) \tag{4C.18a}$$

$$M_{ij}^{c} = ZF(G_{ij}^{c+} - G_{ij}^{c-}) \tag{4C.18b}$$

$$M_{ij}^{e} = ZF(G_{ij}^{e+} - G_{ij}^{e-}) \tag{4C.18c}$$

No new expressions are therefore required for the transport of charge.

Table 4C.1: Expressions for chemical-osmotic advection

$$
\begin{aligned}
\delta_1^{11} &= \bar{\zeta}\left(\frac{16\bar{w}}{4K^2+\pi^2}+\frac{4\pi\bar{w}A_1\cosh(\Re_1\bar{w})}{4\Re_1^2\bar{w}^2+\pi^2}\right)\\
\delta_1^{12} &= \bar{\zeta}\left(\frac{48\bar{w}}{4K^2+9\pi^2}+\frac{4\pi\bar{w}A_2\cosh(\Re_2\bar{w})}{4\Re_2^2\bar{w}^2+\pi^2}\right)\\
\delta_1^{21} &= \bar{\zeta}\left(\frac{16\bar{w}}{3(4K^2+\pi^2)}+\frac{12\pi\bar{w}A_1\cosh(\Re_1\bar{w})}{4\Re_1^2\bar{w}^2+9\pi^2}\right)\\
\delta_1^{22} &= \bar{\zeta}\left(\frac{16\bar{w}}{4K^2+9\pi^2}+\frac{12\pi\bar{w}A_2\cosh(\Re_2\bar{w})}{4\Re_2^2\bar{w}^2+9\pi^2}\right)\\
\delta_2^{11} &= \bar{\zeta}^2\Bigg(\frac{8}{105}\bar{w}\Bigg(105\left(\frac{1}{\pi^2}+\frac{\cosh[2K]}{16K^2+\pi^2}\right)\operatorname{sech}(K)^2+70A_1^2\left(\frac{1}{\pi^2}+\frac{\cosh(2\bar{w}\Re_1)}{\pi^2+16\bar{w}^2\Re_1^2}\right)\\
&\quad +54A_2^2\left(\frac{1}{\pi^2}+\frac{\cosh(2\bar{w}\Re_2)}{\pi^2+16\bar{w}^2\Re_2^2}\right)+28A_1A_2\left(\frac{\cosh(\bar{w}(\Re_1-\Re_2)}{\pi^2+4\bar{w}^2(\Re_1-\Re_2)^2}+\frac{\cosh(\bar{w}(\Re_1+\Re_2))}{\pi^2+4\bar{w}^2(\Re_1+\Re_2)^2}\right)\\
&\quad +\frac{105\pi^3\cosh(\bar{w}\Re_1)A_1\tanh(K)}{(K^3+K\pi^2)(\pi^2+4\bar{w}^2\Re_1^2)}-\frac{315K\pi^3\cosh(\bar{w}\Re_2)A_2\tanh(K)}{(K^4+5K^2\pi^2+4\pi^4)(\pi^2+4\bar{w}^2\Re_2^2)}\Bigg)\Bigg)\\
\delta_2^{12} &= \bar{\zeta}^2\Bigg(\frac{8}{315}\bar{w}\Bigg(210\frac{(\pi^2+8K^2\operatorname{sech}(K)^2)}{16K^2\pi^2+\pi^4}+70A_1^2\left(\frac{1}{\pi^2}+\frac{9\cosh(2\bar{w}\Re_1)}{9\pi^2+16\bar{w}^2\Re_1^2}\right)\\
&\quad +54A_2^2\left(\frac{1}{\pi^2}+\frac{9\cosh(2\bar{w}\Re_2)}{9\pi^2+16\bar{w}^2\Re_2^2}\right)+504A_1A_2\left(\frac{\cosh(\bar{w}(\Re_1-\Re_2))}{9\pi^2+4\bar{w}^2(\Re_1-\Re_2)^2}+\frac{\cosh(\bar{w}(\Re_1+\Re_2))}{9\pi^2+4\bar{w}^2(\Re_1+\Re_2)^2}\right)\\
&\quad +\frac{945\pi^3\cosh(\bar{w}\Re_1)A_1\tanh(K)}{(K^3+K\pi^2)(9\pi^2+4\bar{w}^2\Re_1^2)}-\frac{2835K\pi^3\cosh(\bar{w}\Re_2)A_2\tanh(K)}{(K^4+5K^2\pi^2+4\pi^4)(9\pi^2+4\bar{w}^2\Re_2^2)}\Bigg)\Bigg)\\
\delta_2^{21} &= \bar{\zeta}^2\Bigg(\frac{8}{315}\bar{w}\Bigg(105\left(\frac{1}{\pi^2}+\frac{9\cosh(2K)}{16K^2+9\pi^2}\right)\operatorname{sech}(K)^2+42A_1^2\left(-\frac{1}{\pi^2}-\frac{\cosh(2\bar{w}\Re_1)}{\pi^2+16\bar{w}^2\Re_1^2}\right)\\
&\quad +70A_2^2\left(\frac{1}{\pi^2}+\frac{\cosh(2\bar{w}\Re_2)}{\pi^2+16\bar{w}^2\Re_2^2}\right)-324A_1A_2\left(\frac{\cosh(\bar{w}(\Re_1-\Re_2))}{\pi^2+4\bar{w}^2(\Re_1-\Re_2)^2}+\frac{\cosh(\bar{w}(\Re_1+\Re_2))}{\pi^2+4\bar{w}^2(\Re_1+\Re_2)^2}\right)\\
&\quad +\frac{945K\pi^3\cosh(\bar{w}\Re_1)A_1\tanh(K)}{(K^4+5K^2\pi^2+4\pi^4)(\pi^2+4\bar{w}^2\Re_1^2)}-\frac{2835\pi^3\cosh(\bar{w}\Re_2)A_2\tanh(K)}{(K^3+9K\pi^2)(\pi^2+4\bar{w}^2\Re_2^2)}\Bigg)\Bigg)\\
\delta_2^{22} &= \bar{\zeta}^2\Bigg(\frac{8}{945}\bar{w}\Bigg(105\left(\frac{1}{\pi^2}+\frac{9\cosh(2K)}{16K^2+9\pi^2}\right)\operatorname{sech}(K)^2+42A_1^2\left(-\frac{1}{\pi^2}-\frac{9\cosh(2\bar{w}\Re_1)}{9\pi^2+16\bar{w}^2\Re_1^2}\right)\\
&\quad +70A_2^2\left(\frac{1}{\pi^2}+\frac{9\cosh(2\bar{w}\Re_2)}{9\pi^2+16\bar{w}^2\Re_2^2}\right)-2916A_1A_2\left(\frac{\cosh(\bar{w}(\Re_1-\Re_2))}{9\pi^2+4\bar{w}^2(\Re_1-\Re_2)^2}+\frac{\cosh(\bar{w}(\Re_1+\Re_2))}{9\pi^2+4\bar{w}^2(\Re_1+\Re_2)^2}\right)\\
&\quad +\frac{8505K\pi^3\cosh(\bar{w}\Re_1)A_1\tanh(K)}{(K^4+5K^2\pi^2+4\pi^4)(9\pi^2+4\bar{w}^2\Re_1^2)}-\frac{25515\pi^3\cosh(\bar{w}\Re_2)A_2\tanh(K)}{(K^3+9K\pi^2)(9\pi^2+4\bar{w}^2\Re_2^2)}\Bigg)\Bigg)\\
\delta_3^{11} &= \bar{\zeta}^3\Bigg(\Bigg(\frac{4\bar{w}}{\pi}\left(\frac{3\pi\cosh(K)}{4K^2+\pi^2}+\frac{\pi\cosh(3K)}{36K^2+\pi^2}\right)\operatorname{sech}^3(K)+\frac{12A_1\pi\bar{w}\cosh(\Re_1\bar{w})}{16\Re_1^2\bar{w}^2+4\pi^2}\operatorname{sech}^2(K)\\
&\quad \times\left(\frac{\pi^2\sinh(2K)}{4K^3+K\pi^2}+2\right)+\frac{72A_1^2\pi^3}{16K^4+40K^2\pi^2+9\pi^4}\left(\frac{2\bar{w}}{\pi}+\frac{2\pi\bar{w}\cosh(2\Re_1\bar{w})}{16\Re_1^2\bar{w}^2+\pi^2}\right)\\
&\quad +\frac{3A_1^3}{4}\left(\frac{3\bar{w}\pi\cosh(\Re_1\bar{w})}{4\Re_1^2\bar{w}^2+\pi^2}+\frac{\pi\bar{w}\cosh(3\Re_1\bar{w})}{36\Re_1^2\bar{w}^2+\pi^2}\right)\Bigg)\Bigg)\\
\delta_3^{12} &= \bar{\zeta}^3\Bigg(\Bigg(\frac{4\bar{w}}{\pi}\left(\frac{9\pi\cosh(K)}{4K^2+9\pi^2}+\frac{\pi\cosh(3K)}{12K^2+3\pi^2}\right)\operatorname{sech}^3(K)+\frac{12A_1\pi\bar{w}\cosh(\Re_1\bar{w})}{16\Re_1^2\bar{w}^2+4\pi^2}\operatorname{sech}^2(K)\\
&\quad \times\left(\frac{3\pi^2K\sinh(2K)}{4K^4+5\pi^2K^2+\pi^4}\right)+\frac{72A_1^2\pi^3(12K^2-5\pi^2)}{64K^6+560K^4\pi^2+1036\pi^4K^2+225\pi^6}\left(\frac{2\bar{w}}{\pi}+\frac{2\pi\bar{w}\cosh(2\Re_1\bar{w})}{16\Re_1^2\bar{w}^2+\pi^2}\right)\\
&\quad -\frac{A_1^3}{4}\left(\frac{3\bar{w}\pi\cosh(\Re_1\bar{w})}{4\Re_1^2\bar{w}^2+\pi^2}+\frac{\pi\bar{w}\cosh(3\Re_1\bar{w})}{36\Re_1^2\bar{w}^2+\pi^2}\right)\Bigg)\Bigg)
\end{aligned}
$$

Table 4C.1: (continued)

$$
\begin{aligned}
\delta_3^{21} = \;& \bar{\zeta}^3\Bigg(\Bigg(\frac{4\bar{w}}{3\pi}\left(\frac{3\pi\cosh(K)}{4K^2+\pi^2}+\frac{\pi\cosh(3K)}{36K^2+\pi^2}\right)\operatorname{sech}^3(K)+\frac{36A_1\pi\bar{w}\cosh(\Re_1\bar{w})}{16\Re_1^2\bar{w}^2+4\pi^2}\operatorname{sech}^2(K)\\
&\times\left(\frac{\pi^2\sinh(2K)}{4K^3+K\pi^2}+2\right)+\frac{72A_1^2\pi^3}{16K^4+40K^2\pi^2+9\pi^4}\left(\frac{2\bar{w}}{3\pi}+\frac{6\pi\bar{w}\cosh(2\Re_1\bar{w})}{16\Re_1^2\bar{w}^2+9\pi^2}\right)\\
&+\frac{3A_1^3}{4}\left(\frac{9\bar{w}\pi\cosh(\Re_1\bar{w})}{4\Re_1^2\bar{w}^2+9\pi^2}+\frac{\pi\bar{w}\cosh(3\Re_1\bar{w})}{12\Re_1^2\bar{w}^2+3\pi^2}\right)\Bigg)\Bigg)\\
\delta_3^{22} = \;& \bar{\zeta}^3\Bigg(\Bigg(\frac{4\bar{w}}{3\pi}\left(\frac{9\pi\cosh(K)}{4K^2+9\pi^2}+\frac{\pi\cosh(3K)}{12K^2+3\pi^2}\right)\operatorname{sech}^3(K)+\frac{36A_1\pi\bar{w}\cosh(\Re_1\bar{w})}{16\Re_1^2\bar{w}^2+36\pi^2}\operatorname{sech}^2(K)\\
&\times\left(\frac{3\pi^2K\sinh(2K)}{4K^4+5\pi^2K^2+\pi^4}\right)+\frac{72A_1^2\pi^3(12K^2-5\pi^2)}{64K^6+560K^4\pi^2+1036\pi^4K^2+225\pi^6}\left(\frac{2\bar{w}}{3\pi}+\frac{6\pi\bar{w}\cosh(2\Re_1\bar{w})}{16\Re_1^2\bar{w}^2+9\pi^2}\right)\\
&-\frac{A_1^3}{4}\left(\frac{9\bar{w}\pi\cosh(\Re_1\bar{w})}{4\Re_1^2\bar{w}^2+9\pi^2}+\frac{\pi\bar{w}\cosh(3\Re_1\bar{w})}{12\Re_1^2\bar{w}^2+3\pi^2}\right)\Bigg)\Bigg)\\
\delta_4^{11} = \;& \bar{\zeta}^4\Bigg(\frac{2}{15}\bar{w}\Bigg(15\left(\frac{3}{\pi^2}+\frac{4\cosh(2K)}{16K^2+\pi^2}+\frac{\cosh(4K)}{64K^2+\pi^2}\right)\operatorname{sech}(K)^4\\
&+\frac{240(256K^4+160K^2\pi^2+9\pi^4+9\pi^4\cosh(2K))\operatorname{sech}(K)^2A_1^2(\pi^2\cosh(\bar{w}\Re_1)^2+8\bar{w}^2\Re_1^2)}{\pi^2(256K^4+160K^2\pi^2+9\pi^4)(\pi^2+16\bar{w}^2\Re_1^2)}\\
&+8A_1^4\left(\frac{3}{\pi^2}+\frac{4\cosh(2\bar{w}\Re_1)}{\pi^2+16\bar{w}^2\Re_1^2}+\frac{\cosh(4\bar{w}\Re_1)}{\pi^2+64\bar{w}^2\Re_1^2}\right)\\
&+\frac{20A_1\tanh(K)\pi^3(41K^2+5\pi^2+(K^2+\pi^2)\cosh(2K))\cosh(\bar{w}\Re_1)\operatorname{sech}(K)^2}{K(K^2+\pi^2)(9K^2+\pi^2)(\pi^2+4\bar{w}^2\Re_1^2)}\\
&+\frac{90\pi^5A_1^3\tanh(K)}{K(K^4+5K^2\pi^2+4\pi^4)}\left(\frac{3\cosh(\bar{w}\Re_1)}{\pi^2+4\bar{w}^2\Re_1^2}+\frac{\cosh(3\bar{w}\Re_1)}{\pi^2+36\bar{w}^2\Re_1^2}\right)\Bigg)\Bigg)\\
\delta_4^{12} = \;& \bar{\zeta}^4\Bigg(\frac{2}{15}\bar{w}\Bigg(5\left(\frac{3}{\pi^2}+\frac{4\cosh(2K)}{16K^2+\pi^2}+\frac{\cosh(4K)}{64K^2+\pi^2}\right)\operatorname{sech}(K)^4\\
&+\frac{80(256K^4+160K^2\pi^2+9\pi^4+9\pi^4\cosh(2K))\operatorname{sech}(K)^2A_1^2(9\pi^2\cosh(\bar{w}\Re_1\Big)^2+8\bar{w}^2\Re_1^2)}{\pi^2(256K^4+160K^2\pi^2+9\pi^4)(9\pi^2+16\bar{w}^2\Re_1^2)}\\
&+8A_1^4\left(\frac{1}{\pi^2}+\frac{12\cosh(2\bar{w}\Re_1)}{9\pi^2+16\bar{w}^2\Re_1^2}+\frac{3\cosh(4\bar{w}\Re_1)}{9\pi^2+64\bar{w}^2\Re_1^2}\right)\\
&+\frac{30A_1\pi^3\cosh(\bar{w}\Re_1)\operatorname{sech}(K)^3(9\sinh(K)(9K^2+\pi^2)+\sinh(3K)(K^2+\pi^2))}{K(K^2+\pi^2)(9K^2+\pi^2)(9\pi^2+4\bar{w}^2\Re_1^2)}\\
&+\frac{30\pi^5A_1^3\tanh(K)}{K(K^4+5K^2\pi^2+4\pi^4)}\left(\frac{27\cosh(\bar{w}\Re_1)}{9\pi^2+4\bar{w}^2\Re_1^2}+\frac{\cosh(3\bar{w}\Re_1)}{\pi^2+4\bar{w}^2\Re_1^2}\right)\Bigg)\Bigg)\\
\delta_4^{21} = \;& \bar{\zeta}^4\Bigg(\frac{2}{35}\bar{w}\Bigg(35\left(\frac{1}{\pi^2}+\frac{12\cosh(2K)}{16K^2+9\pi^2}+\frac{3\cosh(4K)}{64K^2+9\pi^2}\right)\operatorname{sech}(K)^4\\
&+\frac{630K\pi^3\cosh(\bar{w}\Re_1)\operatorname{sech}(K)^2A_1\left(\frac{\operatorname{sech}(K)\sinh(3K)}{81K^4+45K^2\pi^2+4\pi^4}+\frac{\tanh(K)}{K^4+5K^2\pi^2+4\pi^4}\right)}{\pi^2+4\bar{w}^2\Re_1^2}\\
&+A_1^4\left(-\frac{24}{\pi^2}-\frac{32\cosh(2\bar{w}\Re_1)}{\pi^2+16\bar{w}^2\Re_1^2}-\frac{8\cosh(4\bar{w}\Re_1)}{\pi^2+64\bar{w}^2\Re_1^2}\right)\\
&-1260\frac{\pi^5A_1^3(\pi^2-K^2)\tanh(K)}{K(K^2+\pi^2)(K^2+4\pi^2)(K^2+9\pi^2)}\left(\frac{3\cosh(\bar{w}\Re_1)}{\pi^2+4\bar{w}^2\Re_1^2}+\frac{\cosh(3\bar{w}\Re_1)}{\pi^2+36\bar{w}^2\Re_1^2}\right)\\
&-\big(112(4096K^6+8960K^4\pi^2+4144K^2\pi^4+225\pi^6+45\pi^4(-48K^2+5\pi^2)\\
&\times\cosh(2K))\operatorname{sech}(K)^2A_1^2(\pi^2\cosh(\bar{w}\Re_1)^2+8\bar{w}^2\Re_1^2)\big)/\big(\pi^2(16K^2+\pi^2)\\
&\times(16K^2+9\pi^2)(16K^2+25\pi^2)(\pi^2+16\bar{w}^2\Re_1^2)\big)\Bigg)\Bigg)
\end{aligned}
$$

Table 4C.1: (continued)

$$
\begin{aligned}
\delta_4^{22} = \; & \bar{\zeta}^4\Bigg(\frac{2}{105}\bar{w}\Bigg(35\Big(\frac{1}{\pi^2}+\frac{12\cosh(2K)}{16K^2+9\pi^2}+\frac{3\cosh(4K)}{64K^2+9\pi^2}\Big)\operatorname{sech}(K)^4 \\
& +\frac{5670K\pi^3\cosh(\bar{w}\Re_1)\operatorname{sech}(K)^3\Big(\frac{\sinh[K]}{K^4+5K^2\pi^2+4\pi^4}+\frac{\sinh[3K]}{81K^4+45K^2\pi^2+4\pi^4}\Big)A_1}{9\pi^2+4\bar{w}^2\Re_1^2} \\
& +24A_1^4\Big(-\frac{1}{\pi^2}-\frac{12\cosh(2\bar{w}\Re_1)}{9\pi^2+16\bar{w}^2\Re_1^2}-\frac{3\cosh(4\bar{w}\Re_1)}{9\pi^2+64\bar{w}^2\Re_1^2}\Big) \\
& -\big(112(4096K^6+8960K^4\pi^2+4144K^2\pi^4+225\pi^6+45\pi^4(-48K^2+5\pi^2) \\
& \times\cosh(2K))\operatorname{sech}(K)^2A_1^2(9\pi^2\cosh(\bar{w}\Re_1)^2+8\bar{w}^2\Re_1^2\big)/\big(\pi^2(16K^2+\pi^2) \\
& \times(16K^2+9\pi^2)(16K^2+25\pi^2)(9\pi^2+16\bar{w}^2\Re_1^2)\big) \\
& -\frac{630\pi^5A_1^3(\pi^2-K^2)\tanh(K)}{K(K^2+\pi^2)(K^2+4\pi^2)(K^2+9\pi^2)}\Big(\frac{\cosh(3\bar{w}\Re_1)}{\pi^2+4\bar{w}^2\Re_1^2}+\frac{27\cosh(\bar{w}\Re_1)}{9\pi^2+4\bar{w}^2\Re_1^2}\Big)\Big)\Bigg)
\end{aligned}
$$

Table 4C.2: Expressions for the ion distribution in pore throats

$$
\begin{aligned}
\langle\bar{\psi}\rangle = \; & \bar{\zeta}\Big(\frac{\tanh(K)}{K}+\frac{2A_1\sinh(\Re_1\bar{w})}{\pi\bar{w}\Re_1}-\frac{2A_2\sinh(\Re_2\bar{w})}{3\pi\bar{w}\Re_2}\Big) \\
\langle\bar{\psi}^2\rangle = \; & \bar{\zeta}^2\Bigg(\frac{1}{2}\Big(\operatorname{sech}(K)^2+\frac{\tanh(K)}{K}\Big)+\frac{A_1^2}{4}\Big(1+\frac{\sinh(2\bar{w}\Re_1)}{2\bar{w}\Re_1}\Big)+\frac{A_2^2}{4}\Big(1+\frac{\sinh(2\bar{w}\Re_2)}{2\bar{w}\Re_2}\Big) \\
& +\frac{4\pi A_1\sinh(\Re_1\bar{w})}{\bar{w}\Re_1(4K^2+\pi^2)}-\frac{12\pi A_2\sinh(\Re_2\bar{w})}{\bar{w}\Re_2(4K^2+9\pi^2)}\Bigg) \\
\langle\bar{\psi}^3\rangle = \; & \bar{\zeta}^3\Bigg(\operatorname{sech}(K)^3\frac{9\sinh(K)+\sinh(3K)}{12K}+\frac{4A_1^3(9\sinh(\Re_1\bar{w})+\sinh(3\Re_1\bar{w}))}{36\pi\bar{w}\Re_1} \\
& +\frac{3A_1(16K^2+\pi^2+\pi^2\cosh(2K))\operatorname{sech}(K)^2\sinh(\Re_1\bar{w})}{\pi(16K^2+\pi^2)\bar{w}\Re_1}+\frac{3A_1^2\pi^2\tanh(K)}{4K(K^2+\pi^2)}\Big(1+\frac{\sinh(2\Re_1\bar{w})}{2\bar{w}\Re_1}\Big) \\
& -\frac{A_2^3(9\sinh(\Re_2\bar{w})+\sinh(3\Re_2\bar{w}))}{27\pi\bar{w}\Re_2}-\frac{A_2(16K^2+9\pi^2+9\pi^2\cosh(2K))\operatorname{sech}(K)^2\sinh(\Re_2\bar{w})}{\pi(16K^2+9\pi^2)\bar{w}\Re_2} \\
& +\frac{27A_2^2\pi^2\tanh(K)}{4K(K^2+9\pi^2)}\Big(1+\frac{\sinh(2\Re_2\bar{w})}{2\bar{w}\Re_2}\Big)+\frac{A_1^2A_2}{5\pi\bar{w}}\Big(\frac{\sinh(\bar{w}(2\Re_1-\Re_2))}{2\Re_1-\Re_2}+\frac{\sinh(\bar{w}(2\Re_1+\Re_2))}{2\Re_1+\Re_2} \\
& +\frac{2\sinh(\Re_2\bar{w})}{\Re_2}\Big)+\frac{27A_1A_2^2}{35\pi\bar{w}}\Big(\frac{\sinh(\bar{w}(\Re_1-2\Re_2))}{\Re_1-2\Re_2}+\frac{\sinh(\bar{w}(\Re_1+\Re_2))}{\Re_1+2\Re_2}+\frac{2\sinh(\Re_1\bar{w})}{\Re_1}\Big) \\
& -\frac{9A_1A_2K\pi^2\tanh(K)(\Re_1\sinh(\Re_1\bar{w})\cosh(\Re_2\bar{w})-\Re_2\cosh(\Re_1\bar{w})\sinh(\Re_2\bar{w}))}{\bar{w}(K^4+5K^2\pi^2+4\pi^4)(\Re_1^2-\Re_2^2)}\Bigg) \\
\langle\bar{\psi}^4\rangle = \; & \bar{\zeta}^4\Bigg(\frac{4A_1\pi(52K^2+\pi^2+(4K^2+\pi^2)\cosh(2K))\operatorname{sech}^2(K)\sinh(\Re_1\bar{w})}{(4K^2+\pi^2)(36K^2+\pi^2\Re_1\bar{w})}+\frac{4A_1^3\pi^3(9\sinh(\Re_1\bar{w})+\sinh(3\Re_1\bar{w})}{(4K^2+\pi^2)(4K^2+9\pi^2)\Re_1\bar{w}} \\
& +\frac{3A_1^4(8\sinh(2\Re_1\bar{w})+\sinh(4\Re_1\bar{w})+12\Re_1\bar{w})}{256\Re_1\bar{w}}+\frac{\operatorname{sech}^4(K)(12K+8\sinh(2K)+\sinh(4K))}{32K} \\
& +\frac{3A_1^2(\sinh(2\Re_1\bar{w})+2\Re_1\bar{w})(K(4K^2+\pi^2)\operatorname{sech}^2(K)+\pi^2\tanh(K))}{8K(4K^2+\pi^2)\Re_1\bar{w}}\Bigg)
\end{aligned}
$$

Table 4C.2: (continued)

$$
\begin{aligned}
\langle\bar{\psi}^5\rangle = \;& \bar{\zeta}^5\Bigg(\frac{\operatorname{sech}(K)^5(150\sinh(K)+25\sinh(3K)+3\sinh(5K))}{240K} + \frac{5A_1\sinh(\Re_1\bar{w})\operatorname{sech}(K)^4}{4\pi\bar{w}\Re_1}\Bigg(\frac{4\pi^2\cosh(2K)}{16K^2+\pi^2} \\
& + \frac{\pi^2\cosh(4K)}{64K^2+\pi^2} + 3\Bigg) + \frac{10\pi^2A_1^2\operatorname{sech}(K)^3}{48\bar{w}}\Bigg(\frac{9\sinh(K)}{K^3+\pi^2K} + \frac{\sinh(3K)}{K(9K^2+\pi^2)}\Bigg) \\
& \times\Bigg(\bar{w} + \frac{\sinh(2\Re_1\bar{w})}{2\Re_1}\Bigg) + \frac{10A_1^3\operatorname{sech}(K)^2}{144\pi\bar{w}\Re_1}\Bigg(8 + \frac{72\pi\cosh(2K)}{(16K^2+\pi^2)(16K^2+9\pi^2)}\Bigg) \\
& \times\Big(9\sinh(\Re_1\bar{w}) + \sinh(3\Re_1\bar{w})\Big) \\
& + \frac{15A_1^4}{64\bar{w}\Re_1}\Bigg(\frac{(\pi^4(12\bar{w}\Re_1+8\sinh(2\Re_1\bar{w})+\sinh(4\Re_1\bar{w}))\tanh(K)}{K^5+5K^3\pi^2+4K\pi^4}\Bigg) \\
& + \frac{64A_1^5}{14400\pi\bar{w}\Re_1}\Big(150\sinh(\Re_1\bar{w}) + 25\sinh(3\Re_1\bar{w}) + 3\sinh(5\Re_1\bar{w})\Big)\Bigg)
\end{aligned}
$$

Table 4C.3: Expressions for hydrodynamic advection

$$
\begin{aligned}
\langle u_h\bar{\psi}\rangle = \;& \frac{16h^2}{\eta\pi^3}\bar{\zeta}\Bigg(\frac{2(\pi\bar{w}-2\tanh(\frac{\pi\bar{w}}{2}))}{\bar{w}(4K^2+\pi^2)} + \frac{A_1}{4\bar{w}}\Bigg(\frac{2\sinh(\Re_1\bar{w})}{\Re_1} - \frac{4\pi\tanh(\frac{\pi\bar{w}}{2})\cosh(\Re_1\bar{w})-8\Re_1\sinh(\Re_1\bar{w})}{\pi^2-4\Re_1^2}\Bigg)\Bigg) \\
\langle u_h\bar{\psi}^2\rangle = \;& \frac{16h^2}{\eta\pi^3}\bar{\zeta}^2\Bigg(\frac{(16K^2+\pi^2+\pi^2\cosh(2K))\operatorname{sech}^2(K)(\pi\bar{w}-2\tanh(\frac{\pi\bar{w}}{2}))}{(16K^2\pi^2+\pi^4)\bar{w}} + \frac{2A_1^2}{3\pi\bar{w}}\Bigg(\bar{w} + \frac{\sinh(2\Re_1\bar{w})}{2\Re_1} \\
& - \operatorname{sech}(\frac{\pi\bar{w}}{2})\Bigg(\frac{2\sinh(\frac{\pi\bar{w}}{2})}{\pi} + \frac{\sinh\left(\frac{\bar{w}(\pi-4\Re_1)}{2}\right)}{\pi-4\Re_1} + \frac{\sinh\left(\frac{\bar{w}(\pi+4\Re_1)}{2}\right)}{\pi+4\Re_1}\Bigg)\Bigg) + \frac{32A_1A_2}{4\bar{w}} \\
& \times\frac{(\cosh(\Re_2\bar{w})\sinh(\Re_1\bar{w})\Re_1-\cosh(\Re_1\bar{w})\sinh(\Re_2\bar{w})\Re_2)}{15\pi(\Re_1^2-\Re_2^2)} - \frac{16A_1A_2\operatorname{sech}(\frac{\pi\bar{w}}{2})}{15\pi}\Bigg(\frac{\sinh\left(\frac{\bar{w}(\pi-2\Re_1-2\Re_2)}{2}\right)}{\pi-2\Re_1-2\Re_2} \\
& + \frac{\sinh\left(\frac{\bar{w}(\pi+2\Re_1-2\Re_2)}{2}\right)}{\pi+2\Re_1-2\Re_2} + \frac{\sinh\left(\frac{\bar{w}(\pi-2\Re_1+2\Re_2)}{2}\right)}{\pi-2\Re_1+2\Re_2}\Bigg) + \frac{18A_2^2}{35\pi\bar{w}}\Bigg(\bar{w} + \frac{\sinh(2\Re_2\bar{w})}{2\Re_2} \\
& - \operatorname{sech}(\frac{\pi\bar{w}}{2})\Bigg(\frac{2\sinh(\frac{\pi\bar{w}}{2})}{\pi} + \frac{\sinh\left(\frac{\bar{w}(\pi-4\Re_2)}{2}\right)}{\pi-4\Re_2} + \frac{\sinh\left(\frac{\bar{w}(\pi+4\Re_2)}{2}\right)}{\pi+4\Re_2}\Bigg)\Bigg) \\
& + \frac{\pi^2A_1\tanh(K)}{\bar{w}}\Bigg(\frac{\sinh(\Re_1\bar{w})}{K^3\Re_1+K\pi^2\Re_1} - \frac{2(\pi\cosh(\Re_1\bar{w})\tanh(\frac{\pi\bar{w}}{2})-2\sinh(\Re_1\bar{w})\Re_1)}{K(K^2+\pi^2)(\pi^2-4\Re_1^2)}\Bigg) \\
& - \frac{3K\pi^2A_2(\pi^2\sinh(\Re_2\bar{w})-2\pi\cosh(\Re_2\bar{w})\tanh(\frac{\pi\bar{w}}{2}))}{(K^2+\pi^2)(K^2+4\pi^2)\Re_2\bar{w}(\pi^2-4\Re_2^2)}\Bigg) \\
\langle u_h\bar{\psi}^3\rangle = \;& \frac{16h^2}{\eta\pi^3}\bar{\zeta}^3\Bigg(\frac{\cosh(3K)\operatorname{sech}^3(K)(\pi\bar{w}-2\tanh(\frac{\pi\bar{w}}{2}))}{4\bar{w}(36K^2+\pi^2)} + \frac{A_1^3}{32\bar{w}}\Bigg(\frac{9\sinh(\Re_1\bar{w})+\sinh(3\Re_1\bar{w})}{\Re_1} \\
& - 3\operatorname{sech}(\frac{\pi\bar{w}}{2})\Bigg(\frac{\sinh\left(\frac{\bar{w}(\pi-6\Re_1)}{2}\right)}{\pi-6\Re_1} + \frac{3\sinh\left(\frac{\bar{w}(\pi-2\Re_1)}{2}\right)}{\pi-2\Re_1} + \frac{3\sinh\left(\frac{\bar{w}(\pi+2\Re_1)}{2}\right)}{\pi+2\Re_1} \\
& + \frac{\sinh\left(\frac{\bar{w}(\pi+6\Re_1)}{2}\right)}{\pi+6\Re_1}\Bigg)\Bigg) + \frac{3A_1}{8\bar{w}}\Bigg(\frac{\sinh(\Re_1\bar{w})}{\Re_1} - \frac{2\pi\tanh(\frac{\pi\bar{w}}{2})\cosh(\Re_1\bar{w})-4\Re_1\sinh(\Re_1\bar{w})}{(\pi^2-4\Re_1^2)}\Bigg) \\
& \times\operatorname{sech}(K)^2\Big(2 + \frac{\pi^2\sinh(2K)}{4K^3+\pi^2K}\Big) + \frac{18A_1^2\pi^3}{\bar{w}(16K^4+40\pi^2K^2+9\pi^4)}\Bigg(\bar{w} + \frac{\sinh(2\Re_1\bar{w})}{2\Re_1} \\
& - \operatorname{sech}(\frac{\pi\bar{w}}{2})\Bigg(\frac{2\sinh(\pi\bar{w}/2)}{\pi} + \frac{\sinh\left(\frac{\bar{w}(\pi-4\Re_1)}{2}\right)}{\pi-4\Re_1} + \frac{\sinh\left(\frac{\bar{w}(\pi+4\Re_1)}{2}\right)}{\pi+4\Re_1}\Bigg)\Bigg)\Bigg)
\end{aligned}
$$

Table 4C.3: (continued)

$$
\begin{aligned}
\langle u_h\bar{\psi}^4\rangle = \;& \tfrac{16h^2}{\eta\pi^3}\bar{\zeta}^4\Bigg(\big((4\pi^2(64K^2+\pi^2)\cosh(2K)+(16K^2+\pi^2)(3(64K^2+\pi^2)\\
&+\pi^2\cosh(4K)))\operatorname{sech}^4(K)(\pi\bar{w}-2\tanh(\tfrac{\pi\bar{w}}{2}))\big)/\big(4\pi^2(16K^2+\pi^2)\\
&(64K^2+\pi^2)\bar{w}\big)-\tfrac{2(256K^4+160K^2\pi^2+9\pi^4+9\pi^4\cosh(2K))\operatorname{sech}^2(K)A_1^2}{\bar{w}(256K^4\pi+160K^2\pi^3+9\pi^5)}\Bigg(-\bar{w}+\tfrac{2\tanh(\frac{\pi\bar{w}}{2})}{\pi}\\
&+\tfrac{\operatorname{sech}(\frac{\pi\bar{w}}{2})\sinh\left(\frac{\bar{w}(\pi-4\Re_1)}{2}\right)}{\pi-4\Re_1}-\tfrac{\sinh\left(2\Re_1\bar{w}\right)}{2\Re_1}+\tfrac{\operatorname{sech}(\frac{\pi\bar{w}}{2})\sinh\left(\frac{\bar{w}(\pi+4\Re_1)}{2}\right)}{\pi+4\Re_1}\Bigg)\\
&+\tfrac{A_1^4}{30\pi\bar{w}}\Bigg(\tfrac{8\sinh(2\Re_1\bar{w})+\sinh(4\Re_1\bar{w})+12\Re_1\bar{w}}{\Re_1}-4\operatorname{sech}(\tfrac{\pi\bar{w}}{2})\Bigg(\tfrac{6\sinh(\frac{\pi\bar{w}}{2})}{\pi}+\tfrac{\sinh\left(\frac{\bar{w}(\pi-8\Re_1)}{2}\right)}{\pi-8\Re_1}\\
&+\tfrac{4\sinh\left(\frac{\bar{w}(\pi-4\Re_1)}{2}\right)}{\pi-4\Re_1}+\tfrac{4\sinh\left(\frac{\bar{w}(\pi+4\Re_1)}{2}\right)}{\pi+4\Re_1}+\tfrac{\sinh\left(\frac{\bar{w}(\pi+8\Re_1)}{2}\right)}{\pi+8\Re_1}\Bigg)\Bigg)\\
&-\tfrac{\pi^2(41K^2+5\pi^2+(K^2+\pi^2)\cosh(2K))\operatorname{sech}^2(K)A_1\tanh(K)}{6K(K^2+\pi^2)(9K^2+\pi)\bar{w}}\\
&\times\Bigg(-\tfrac{2\sinh(\Re_1\bar{w})}{\Re_1}+\tfrac{4\pi\cosh(\Re_1\bar{w})\tanh(\frac{\pi\bar{w}}{2})}{\pi^2-4\Re_1^2}-\tfrac{8\sinh(\Re_1\bar{w})\Re_1}{\pi^2-4\Re_1^2}\Bigg)+\tfrac{\pi^4A_1^3\tanh(K)}{2(K^5+5K^3\pi^2+4K\pi^4)\bar{w}}\\
&\times\Bigg(9\sinh(\Re_1\bar{w})+\tfrac{\sinh(3\Re_1\bar{w})}{\Re_1}-3\operatorname{sech}(\tfrac{\pi\bar{w}}{2})\Bigg(\tfrac{\sinh\left(\frac{\bar{w}(\pi-6\Re_1)}{2}\right)}{\pi-6\Re_1}+\tfrac{3\sinh\left(\frac{\bar{w}(\pi-2\Re_1)}{2}\right)}{\pi-2\Re_1}\\
&+\tfrac{3\sinh\left(\frac{\bar{w}(\pi+2\Re_1)}{2}\right)}{\pi+2\Re_1}+\tfrac{\sinh\left(\frac{\bar{w}(\pi+6\Re_1)}{2}\right)}{\pi+6\Re_1}\Bigg)\Bigg)\Bigg)
\end{aligned}
$$

Table 4C.4: Expressions for chemical-osmotic advection.

$$
\begin{aligned}
\langle u_c\bar{\psi}\rangle = \;& \tfrac{2RT}{\eta}\tfrac{h^2}{\pi^2L}\Bigg(a_1\Bigg(\tfrac{\delta_1^{11}\delta_1^{11}}{1+\bar{w}^2}+\tfrac{\delta_1^{12}\delta_1^{12}}{9+\bar{w}^2}+\tfrac{\delta_1^{21}\delta_1^{21}}{1+9\bar{w}^2}+\tfrac{\delta_1^{22}\delta_1^{22}}{9(1+\bar{w}^2)}\Bigg)\\
&+a_2\Bigg(\tfrac{\delta_1^{11}\delta_2^{11}}{1+\bar{w}^2}+\tfrac{\delta_1^{12}\delta_2^{12}}{9+\bar{w}^2}+\tfrac{\delta_1^{21}\delta_2^{21}}{1+9\bar{w}^2}+\tfrac{\delta_1^{22}\delta_2^{22}}{9(1+\bar{w}^2)}\Bigg)+a_3\Bigg(\tfrac{\delta_1^{11}\delta_3^{11}}{1+\bar{w}^2}+\tfrac{\delta_1^{12}\delta_3^{12}}{9+\bar{w}^2}+\tfrac{\delta_1^{21}\delta_3^{21}}{1+9\bar{w}^2}+\tfrac{\delta_1^{22}\delta_3^{22}}{9(1+\bar{w}^2)}\Bigg)\\
&+a_4\Bigg(\tfrac{\delta_1^{11}\delta_4^{11}}{1+\bar{w}^2}+\tfrac{\delta_1^{12}\delta_4^{12}}{9+\bar{w}^2}+\tfrac{\delta_1^{21}\delta_4^{21}}{1+9\bar{w}^2}+\tfrac{\delta_1^{22}\delta_4^{22}}{9(1+\bar{w}^2)}\Bigg)\Bigg)\\
\langle u_c\bar{\psi}^2\rangle = \;& \tfrac{2RT}{\eta}\tfrac{h^2}{\pi^2L}\Bigg(a_1\Bigg(\tfrac{\delta_2^{11}\delta_1^{11}}{1+\bar{w}^2}+\tfrac{\delta_2^{12}\delta_1^{12}}{9+\bar{w}^2}+\tfrac{\delta_2^{21}\delta_1^{21}}{1+9\bar{w}^2}+\tfrac{\delta_2^{22}\delta_1^{22}}{9(1+\bar{w}^2)}\Bigg)\\
&+a_2\Bigg(\tfrac{\delta_2^{11}\delta_2^{11}}{1+\bar{w}^2}+\tfrac{\delta_2^{12}\delta_2^{12}}{9+\bar{w}^2}+\tfrac{\delta_2^{21}\delta_2^{21}}{1+9\bar{w}^2}+\tfrac{\delta_2^{22}\delta_2^{22}}{9(1+\bar{w}^2)}\Bigg)+a_3\Bigg(\tfrac{\delta_2^{11}\delta_3^{11}}{1+\bar{w}^2}+\tfrac{\delta_2^{12}\delta_3^{12}}{9+\bar{w}^2}+\tfrac{\delta_2^{21}\delta_3^{21}}{1+9\bar{w}^2}+\tfrac{\delta_2^{22}\delta_3^{22}}{9(1+\bar{w}^2)}\Bigg)\\
&+a_4\Bigg(\tfrac{\delta_2^{11}\delta_4^{11}}{1+\bar{w}^2}+\tfrac{\delta_2^{12}\delta_4^{12}}{9+\bar{w}^2}+\tfrac{\delta_2^{21}\delta_4^{21}}{1+9\bar{w}^2}+\tfrac{\delta_2^{22}\delta_4^{22}}{9(1+\bar{w}^2)}\Bigg)\Bigg)\\
\langle u_c\bar{\psi}^3\rangle = \;& \tfrac{2RT}{\eta}\tfrac{h^2}{\pi^2L}\Bigg(a_1\Bigg(\tfrac{\delta_3^{11}\delta_1^{11}}{1+\bar{w}^2}+\tfrac{\delta_3^{12}\delta_1^{12}}{9+\bar{w}^2}+\tfrac{\delta_3^{21}\delta_1^{21}}{1+9\bar{w}^2}+\tfrac{\delta_3^{22}\delta_1^{22}}{9(1+\bar{w}^2)}\Bigg)\\
&+a_2\Bigg(\tfrac{\delta_3^{11}\delta_2^{11}}{1+\bar{w}^2}+\tfrac{\delta_3^{12}\delta_2^{12}}{9+\bar{w}^2}+\tfrac{\delta_3^{21}\delta_2^{21}}{1+9\bar{w}^2}+\tfrac{\delta_3^{22}\delta_2^{22}}{9(1+\bar{w}^2)}\Bigg)+a_3\Bigg(\tfrac{\delta_3^{11}\delta_3^{11}}{1+\bar{w}^2}+\tfrac{\delta_3^{12}\delta_3^{12}}{9+\bar{w}^2}+\tfrac{\delta_3^{21}\delta_3^{21}}{1+9\bar{w}^2}+\tfrac{\delta_3^{22}\delta_3^{22}}{9(1+\bar{w}^2)}\Bigg)\\
&+a_4\Bigg(\tfrac{\delta_3^{11}\delta_4^{11}}{1+\bar{w}^2}+\tfrac{\delta_3^{12}\delta_4^{12}}{9+\bar{w}^2}+\tfrac{\delta_3^{21}\delta_4^{21}}{1+9\bar{w}^2}+\tfrac{\delta_3^{22}\delta_4^{22}}{9(1+\bar{w}^2)}\Bigg)\Bigg)
\end{aligned}
$$

Table 4C.4: (continued)

$$\begin{aligned}\langle u_c\bar{\psi}^4\rangle = \quad & \frac{2RT}{\eta}\frac{h^2}{\pi^2 L}\Bigg(a_1\left(\frac{\delta_4^{11}\delta_1^{11}}{1+\bar{w}^2}+\frac{\delta_4^{12}\delta_1^{12}}{9+\bar{w}^2}+\frac{\delta_4^{21}\delta_1^{21}}{1+9\bar{w}^2}+\frac{\delta_4^{22}\delta_1^{22}}{9(1+\bar{w}^2)}\right)\\ & +a_2\left(\frac{\delta_4^{11}\delta_2^{11}}{1+\bar{w}^2}+\frac{\delta_4^{12}\delta_2^{12}}{9+\bar{w}^2}+\frac{\delta_4^{21}\delta_2^{21}}{1+9\bar{w}^2}+\frac{\delta_4^{22}\delta_2^{22}}{9(1+\bar{w}^2)}\right)+a_3\left(\frac{\delta_4^{11}\delta_3^{11}}{1+\bar{w}^2}+\frac{\delta_4^{12}\delta_3^{12}}{9+\bar{w}^2}+\frac{\delta_4^{21}\delta_3^{21}}{1+9\bar{w}^2}+\frac{\delta_4^{22}\delta_3^{22}}{9(1+\bar{w}^2)}\right)\\ & +a_4\left(\frac{\delta_4^{11}\delta_4^{11}}{1+\bar{w}^2}+\frac{\delta_4^{12}\delta_4^{12}}{9+\bar{w}^2}+\frac{\delta_4^{21}\delta_4^{21}}{1+9\bar{w}^2}+\frac{\delta_4^{22}\delta_4^{22}}{9(1+\bar{w}^2)}\right)\Bigg)\end{aligned}$$

Table 4C.5: Expressions for electro-osmotic advection. The expressions for the averaged electric potentials are given in Table 4C.2.

$$\begin{aligned}\langle u_e\psi\rangle &= \frac{\epsilon RT}{\eta F}(\langle\bar{\psi}^2\rangle-\bar{\zeta}\langle\bar{\psi}\rangle)\\ \langle u_e\psi^2\rangle &= \frac{\epsilon RT}{\eta F}(\langle\bar{\psi}^3\rangle-\bar{\zeta}\langle\bar{\psi}^2\rangle)\\ \langle u_e\psi^3\rangle &= \frac{\epsilon RT}{\eta F}(\langle\bar{\psi}^4\rangle-\bar{\zeta}\langle\bar{\psi}^3\rangle)\\ \langle u_e\psi^4\rangle &= \frac{\epsilon RT}{\eta F}(\langle\bar{\psi}^5\rangle-\bar{\zeta}\langle\bar{\psi}^4\rangle)\end{aligned}$$

4D Nomenclature

Table 4D.1: Nomenclature.

Symbol	Definition [units]
a_m	Fitting coefficient for hyperbolic function [-]
A	Cross-sectional area of pore throat [m^2]
A_{ij}^s	Surface area of pore throat walls [m^2]
$b_m^{\pm}$	Fitting coefficient for cations and anions, respectively
C^b	Bulk concentration [mol m^{-3}]
C_i^b	Bulk concentration in pore body i [mol m^{-3}]
C_j^b	Bulk concentration in pore body j [mol m^{-3}]
C_{max}	Maximum possible bulk concentration [mol m^{-3}]
C_{min}	Minimum possible bulk concentration [mol m^{-3}]
$C^{\pm}$	Ion concentration in pore throat ij [mol m^{-3}]
D	Ion diffusion coefficient [m^2 s^{-1}]
E_x	x-component of electric field in pore throat [V m^{-1}]
E_y	y-component of electric field in pore throat [V m^{-1}]
f	Pore size distribution function
F	Faraday constant [C mol^{-1}]
$G_{ij}^{h\pm}$	Pressure-driven salt transport coefficient [mol s^{-1} Pa^{-1}]
$G_{ij}^{c\pm}$	Concentration-driven salt transport coefficient [m^3 s^{-1}]
$G_{ij}^{e\pm}$	Electric potential-driven salt transport coefficient [mol s^{-1} V^{-1}]
h	Pore throat height [m]
i	Pore body index
ij	Pore throat index
I_{ij}	Electric current throat pore throat ij [C s^{-1}]
j	Pore body index
$J_{ij}^{\pm}$	Salt mass flux through pore throat ij [mol s^{-1}]
J_{ij}^{+}	Cation mass flux through pore throat ij [mol s^{-1}]
J_{ij}^{-}	Anion mass flux through pore throat ij [mol s^{-1}]
K	Dimensionless pore throat height [-]
K_{ij}^h	Hydrodynamic permeability of pore throat ij [m^3 s^{-1} Pa^{-1}]
K_{ij}^c	Chemico-osmotic permeability of pore throat ij [m^6 s^{-1} mol^{-1}]
K_{ij}^e	Electro-osmotic permeability of pore throat ij [m^3 s^{-1} V^{-1}]
L	Pore throat length [m]
m	Counter
M_{ij}^h	Pressure-driven electric current coefficient [C s^{-1} Pa^{-1}]
M_{ij}^c	Concentration-driven electric current coefficient [C m^3 s^{-1} mol^{-1}]
M_{ij}^e	Electric potential-driven electric current coefficient [C s^{-1} V^{-1}]

Table 4D.1: (continued)

n	Number of pore bodies in network in each direction [-]
N	Number of pore throats connected to pore body i [-]
P^b	Bulk pressure in a pore body [Pa]
P_i^b	Bulk pressure in pore body i [Pa]
P_j^b	Bulk pressure in pore body j [Pa]
q_{ij}	Water flux through pore throat ij [m^3 s^{-1}]
R	Gas constant [J mol^{-1} K^{-1}]
R_i	Radius of pore body i [m]
R_m	Mean pore body radius [m]
R_{max}	Maximum pore body radius [m]
R_{min}	Minimum pore body radius [m]
T	Temperature [K]
u_c	Chemico-osmotic flow velocity in pore throat [m s^{-1}]
u_e	Electro-osmotic flow velocity in pore throat [m s^{-1}]
u_h	Hydrodynamic flow velocity in pore throat [m s^{-1}]
V_i	Volume of pore body i [m^3]
w	Pore throat width [m]
$\bar{w}$	Dimensionless pore throat width [-]
x	x-coordinate [m]
$\bar{x}$	Dimensionless x-coordinate [-]
y	y-coordinate [m]
$\bar{y}$	Dimensionless y-coordinate [-]
z	z-coordinate [m]
Z	Charge of ion species [-]
δ_m^{pq}	Coefficient for chemico-osmotic flow and transport [-]
ϵ	Electric permittivity of water [C^2 J^{-1} m^{-1}]
ζ	Zeta potential in pore throat [V]
$\bar{\zeta}$	Dimensionless zeta potential of pore throat [-]
η	Dynamic viscosity of water [Pa s]
λ_D	Debye length in pore throat [m^{-1}]
Π	Osmotic pressure [Pa]
Π_d	Disjoining pressure [Pa]
σ_ζ	Electrokinetic surface charge density [C m^{-2}]
σ_{ps}	Standard deviation of pore size distribution [m]
τ	Global time step size [s]
τ_i	Local time step size of pore body i [s]
ϕ^b	Bulk electric potential in a pore body [V]
ϕ_i^b	Bulk electric potential in pore body i [V]
ϕ_j^b	Bulk electric potential in pore body j [V]
ψ	Electric potential in double layer in pore throat [V]
$\bar{\psi}$	Dimensionless electric potential in double layer in pore throat [-]
Ω_m	Coefficient for chemico-osmotic advective transport [-]

Chapter 5

Pore-to-continuum upscaling of salinity and sodicity effects on soil hydraulic properties

This chapter is based on:

Cornelissen, P., van der Zee, S. E. A. T. M., Leijnse, A., Niasar, V., (2021). Pore-to-continuum upscaling of salinity and sodicity effects on soil hydraulic properties. *Submitted manuscript.*

Abstract

Soil sodicity may cause irreversible damage to the structure of clayey and loamy soils. In sodic soils, the micropores generally swell at the expense of macropores, reducing the soil permeability for air and water flow. However, there have been limited studies linking the microscopic scale swelling behaviours to the macroscopic soil hydraulic properties. Many studies use Poisson-Boltzmann theory to model the forces between clay particles, despite general awareness that not all observations can be explained by this theory. Therefore, we apply density functional theory (DFT) in this study instead to model the forces between clay particles at the microscopic scale. Furthermore, we use a pore-network model to link swelling of the micropores to changes in saturated and unsaturated hydraulic properties. The numerical results of the DFT model are in reasonable agreement with experimental observations. Almost no swelling is predicted when the exchangeable sodium percentage (ESP) is low, but significant swelling occurs once a threshold value is reached. We found that the threshold ESP ranges between 16 and 24% for salinities between 50 and 300 mol/m^3, with lower ESP threshold values corresponding to a lower pore water salinity. Swelling of the micropores resulted in a drastic reduction of the hydraulic conductivity and an increase of the air-entry pressure, while the relative permeability and the shape of the water retention curve remained unaffected.

5.1 Introduction

Soil sodicity refers to the relative accumulation of sodium in the cation exchange complex with respect to multivalent cations such as calcium and magnesium in clayey and loamy soils. Sodium may accumulate in soils due to irrigation with marginal water (Rengasamy and Olsson, 1993; Schacht and Marschner, 2015), or through capillary rise from saline groundwater (van der Zee et al., 2010b; van de Craats et al., 2020). Sodic soils experience significant structural degradation when coming into contact with low salinity water, which significantly restricts water flow, aeration, and plant root growth (Shainberg and Letey, 1984). Remediation of sodic soils is difficult, costly, and time-consuming (Lebron et al., 2002). Therefore, the focus should rather be on anticipation and prevention of soil sodification, which requires models that relate the pore water chemistry to soil deformation and degradation.

Soil structure degradation due to sodicity occurs at the microscopic scale. Swelling clay minerals such as montmorillonite generally have a negative surface charge, which is screened by cations in the interlamellar pore space (e.g., Bolt (1982); Bresler et al. (1982)). This screening is less effective at low ionic strength in water (e.g., low salinity or when sodium is the most prevalent cation). When the charge of the clay particles is insufficiently screened by the cations, a repulsive force develops between the clay particles, known as the disjoining pressure (Derjaguin et al., 1987). This causes swelling of the interlamellar pores, which often results in shrinking of the macropores (Musso et al., 2013). Additionally, the macropores may be clogged by dislodged clay particles (So and Aylmore, 1993). These changes to the pore size distribution may drastically alter the saturated soil hydraulic conductivity (Quirk and Schofield, 1955; McNeal and Coleman, 1966; Shainberg and Caiserman, 1971; Frenkel et al., 1978; Shainberg et al., 1981) and the soil water retention curve (Russo and Bresler, 1977; Siyag et al., 1983; Malik et al., 1992). These experimental studies conclude that the soil hydraulic properties cannot be specified independently of the pore water quality. Nevertheless, the coupling between pore water chemistry and hydraulic parameters is often neglected in soil-water models.

Theoretical research has focused mostly on the microscopic scale of individual clay lamella (Bolt, 1982; Bresler et al., 1982). Many of these studies on the microscopic scale worked with the Poisson-Boltzmann theory to calculate the electric field between two clay particles. The Poisson-Boltzmann theory treats the ions as point charges, which may predict unrealistically large ion concentrations (Quesada-Pérez et al., 2003), as well as being unable to predict the stability of montmorillonite under non-sodic conditions (Israelachvili, 1991; McBridge, 1997). The stability of calcium montmorillonite can be predicted by advanced theories that include ion-ion correlation, such as density functional theory or the hypernetted-chain equation. Such an approach has been pursued for a constant surface potential boundary condition (Kjellander et al., 1988), and more recently for the case of a constant surface charge density (Le et al., 2015; Rocha et al., 2016),

which is more appropriate for clay particles (Tournassat et al., 2011). However, to our knowledge, such models have not yet been used to predict swelling in the context of soil sodicity, and this is the key contribution of the present study.

Compared to microscopic models, the macroscopic response of soil hydraulic parameters to clay swelling has received little attention in theoretical studies. The UNSATCHEM model includes interaction between pore water chemistry and the soil's saturated hydraulic conductivity (Šimůnek et al., 2012), based on the empirical relationship of McNeal and Coleman (1966). However, changes to the soil water retention curve due to soil swelling are neglected. Porosity and permeability changes due to changing pore water chemistry have also been incorporated in macroscopic models using a homogenization approach (Barbour and Fredlund, 1989; Moyne and Murad, 2002, 2006; Murad and Moyne, 2008), and thus assume a homogenous soil structure. Russo (1988, 2013) developed a model to link pore water chemistry to saturated and unsaturated macroscopic hydraulic properties to sodic conditions by using a capillary bundle model, but made use of Poisson-Boltzmann theory. Tuller and Or (2003) developed a pore-scale model for the upscaling of hydraulic properties of macropores that shrink or swell in response to the shrinking and swelling of surrounding micropores. However, their approach is limited to this specific configuration of the micro- and macropores, and also used Poisson-Boltzmann theory.

Therefore, we propose an alternative approach to model the macroscopic response of soils to sodic conditions. First, we use density function theory instead of Poisson-Boltzmann theory to model the disjoining pressure between clay particles. This can be used to estimate swelling of clay at the microscopic scale. Then we link swelling of the micropores to shrinking of the macropores, and use a pore network to calculate the soil hydraulic conductivity and soil water retention curve. In pore-network modelling (PNM), the pore space is converted into a network of nodes and bonds with simplified geometries. Pore-network models have been used for upscaling various processes in porous media, such as multiphase flow (Joekar-Niasar et al., 2008, 2010b; An et al., 2020a), solute transport (Acharya et al., 2005; Babaei and Joekar-Niasar, 2016; An et al., 2020b), and electrokinetics (Cornelissen et al., 2019). However, to the best of our knowledge, PNM has not been used before for upscaling the effect of soil sodicity on the hydraulic properties. The aim of this study is then to determine the suitability of density functional theory for predicting swelling of sodic soils by comparing with experimental observations, and additionally upscaling the response of the macroscopic soil hydraulic properties with pore-network modelling.

5.2 Methods

To link the processes originating at the nanoscopic scale to macroscopic effects, we assumed a multiscale structure of soils as shown in Figure 5.1. We considered only montmorillonite, as this is the most common swelling clay mineral in sodic soils. On

the nanoscopic scale, clay consists of sheet-like particles, which are less than 1 nm thick and typically 100 nm long and wide. These sheets are often stacked together to form clay clusters or tactoids. Finally, tactoids may clump together in addition to other soil materials, such as quartz, calcite, and organic matter, to form aggregates. This three-scale structure gives rise to three levels of porosity: the intra-tactoid pores (0.9-10 nm), the inter-tactoid pores (10-70 nm) and the inter-aggregate pores (0.5-100 µm) (Kuila and Prasad, 2013; Musso et al., 2013). Changes in pore water chemistry alter the disjoining pressure between the clay particles in the intra-tactoid pores, which leads to swelling or shrinking of this pore class. Swelling of the intra-tactoid pores usually occurs at the expense of the macropores, which shrink as a result (Musso et al., 2013).

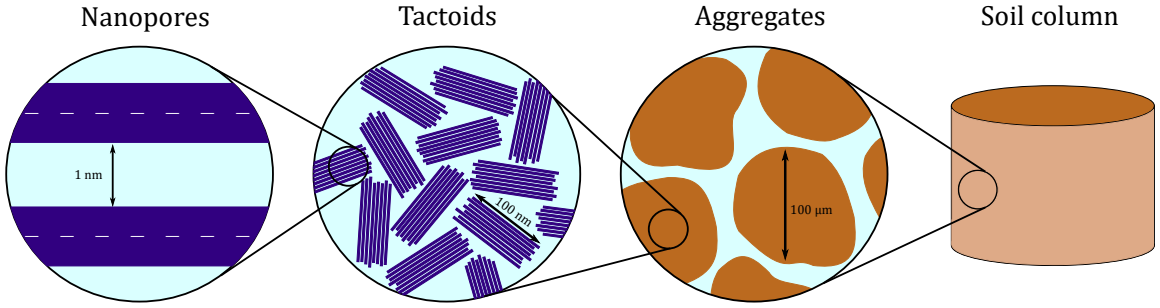

Figure 5.1: The multiscale structure of montmorillonite clay soils, based on Lemaire et al. (2007). On the nanoscopic scale, clay particles are separated by a distance of 0.9 to 4 nm. Clay particles are generally stacked in a parallel arrangement to form so-called tactoids. These tactoids may clump together with other materials such as organic matter, calcite, or quartz to form aggregates.

In this study, we limit our focus to systems containing only sodium, calcium, and chloride ions. While more ionic species are present in the pore water under natural conditions, the ionic species chosen here are the most common ones. We assume that the bulk solution (i.e., the pore water unaffected by the electric field around the clay particles) is electroneutral. In that case, the ionic concentrations in the bulk solution are related through

$$C = [Cl^-] = [Na^+] + 2[Ca^{2+}], \tag{5.1}$$

where $[Cl^-]$, $[Na^+]$, and $[Ca^{2+}]$ are the chloride, sodium, and calcium concentrations [mol/m^3] in the bulk solution, respectively. In essence, this implies equivalence of positive and negative mole-charges.

In practice, soil sodification is quantified by the exchangeable sodium percentage (Richards et al., 1954). The exchangeable sodium percentage (ESP) is defined as the percentage of the cation exchange capacity that is occupied by adsorbed sodium. Generally, a critical ESP value of 15% is used as a threshold above which significant soil deterioration occurs

(Shainberg and Letey, 1984), although in reality this threshold value may range from 5 to 20% based on many factors, such as the salinity of the pore water and soil type (Sumner, 1993). Measuring the ESP is relatively laborious, and therefore the sodium adsorption ratio (SAR) of the solution is often used instead, which in absence of other cations is given by

$$\mathrm{SAR} = \frac{[Na^{+}]}{\sqrt{[Ca^{2+}]}}, \tag{5.2}$$

where the ionic concentrations are in mmol/l (which is equivalent to mol/m^3). Since the values of SAR and ESP are similar for ESP < 15, a critical SAR value of 15 mmol$^{0.5}$/l$^{0.5}$ has been suggested (Bresler et al., 1982). We can calculate the sodium and calcium concentrations for any given combination of C and SAR using Equations 5.1 and 5.2.

We first present the nanoscopic model to calculate the disjoining pressure in the intra-tactoid pores. Then, we present the method to link the nanoscopic model to the pore-network model to predict the macroscopic hydraulic properties. In this study, we will limit our focus to equilibrium situations, and neglect the time-dependent salt transport and disjoining pressure. Swelling and shrinking of the clay due to osmotic flow is therefore also neglected.

5.2.1 Nanoscopic scale: density functional theory

Ion distribution between charged clay particles

We assume that the clay platelets in the tactoids are stacked in parallel orientation, separated by a distance $2H$. Additionally, we assume that the electric field between the clay particles is one-dimensional and varies only in the direction normal of the orientation of the clay platelets (Figure 5.2).

To calculate the disjoining pressure between the clay particles, we need the ion distribution in the nanopores. For this purpose, we follow the approach of Le et al. (2016) and Rocha et al. (2016), and use the density functional theory (DFT) framework. This approach is based on minimization of the thermodynamic potential, where the free energy is described with a functional relation of the ionic concentrations. The mean spherical approximation (MSA) is used as a closure relation. The ions are treated as hard spheres with a specified diameter d. Following Le et al. (2016) and Rocha et al. (2016), we used a value of 4.25×10^{-10} m for the ion diameter, which falls within the range of values reported in the literature (Kiriukhin and Collins, 2002; Yang et al., 2002). An expression for the ion distribution has been derived by combining the DFT and MSA approach which yields

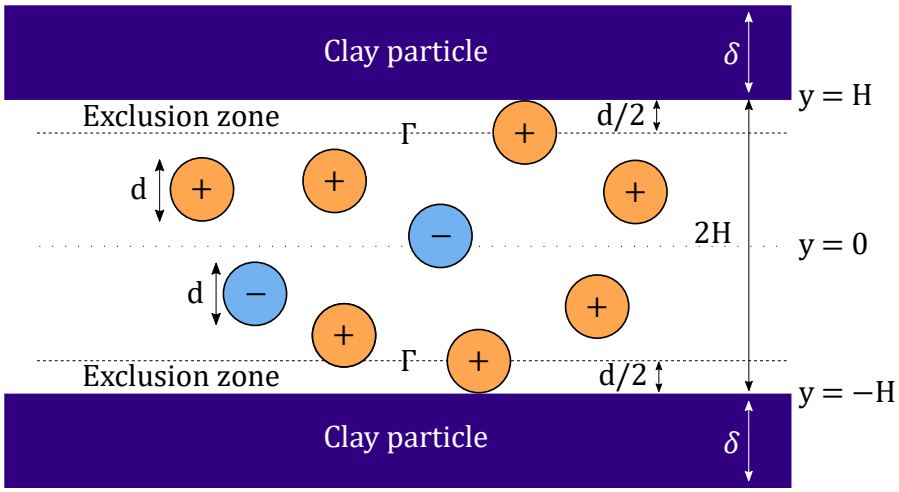

Figure 5.2: Schematic representation of the pore space between two clay particles of thickness δ which are separated by a distance $2H$. The ions are represented as hard spheres with diameter d. The exclusion zone is defined as the region near the clay surface where the ionic concentrations vanish, since the ions cannot approach the clay surface closer than the ion radius (i.e., at a distance of $d/2$ from the clay surface). The boundary between the exclusion zone and the fluid domain is denoted by Γ.

$$g_i(y) = \exp\left(- z_i\bar{\psi}(y) + \sum_{m=1}^{3} n_A C_{b_m} \int \tilde{c}_{im}(|y - y'|)h_m(y')dy' \right), \tag{5.3}$$

where g_i is the ion distribution function of ionic species i [-], z_i is the charge number of the ionic species [-], $\bar{\psi}$ is the dimensionless electric potential, defined as $\bar{\psi} = \frac{F\psi}{RT}$, with F the Faraday constant [C/mol], ψ the electric potential [V], R is the gas constant [J/mol/K], T is the absolute temperature [K], n_A is Avogadro's constant, C_{b_m} is the bulk concentration [mol/m^3] of ionic species m. The ion-ion correlation forces between ionic species i and m are denoted by $\tilde{c}_{im}$, and $h_m = g_m - 1$.

The expression for the ion distribution in Equation 5.3 is combined with Gauss' law to calculate the electric field through

$$\nabla^2\bar{\psi} = \frac{F^2}{\epsilon RT} \sum_{i=1}^{3} z_i C_{b_i} g_i, \tag{5.4}$$

where ϵ is the permittivity of the fluid [C^2/J/m]. It should be noted that the Poisson-Boltzmann problem is obtained when the second term in the exponential term of Equation 5.3 vanishes (i.e., when ion correlation forces are neglected). We opt to use the complete form of Equation 5.3 as we are interested in mixed sodium-calcium systems in which ion-ion correlations play an important role.

As a boundary condition, we assume a constant surface charge density, which is appropriate for clay minerals which owe their negative charge to isomorphous substitution (Tournassat et al., 2011). This boundary condition can be expressed as

$$\nabla\bar{\psi} \cdot \mathbf{n} = -\frac{F\sigma}{\epsilon RT} \quad \text{on } \Gamma, \tag{5.5}$$

where σ is the surface charge density of the clay mineral [C/m^2]. Additionally, the ion concentrations in the bulk solution are required as a boundary condition. In our case, we derive the bulk concentrations by specifying C and the SAR. To solve the Equations 5.3-5.5, we follow the approach of Le et al. (2016) and Rocha et al. (2016), which is summarized in 5A.

Once the electric field and the ion distribution are known, the ESP can be calculated. The ESP is defined as the total charge of the sodium ions divided by total negative charge (i.e., the sum of charge of the clay particles and the chloride ions) expressed as percentage. The total ionic charges are obtained by integrating the volumetric charge density over the pore size (Bolt, 1955). Here, we integrate only over the thickness of the double layer h, which is defined as the distance from the clay surface where the ionic concentrations are equal to their concentration in the bulk solution (i.e., where $g_i = 1$). This is done because the charge deficit of the clay particle is screened completely by cations within this distance. For overlapping double layers, this is the same as integrating over the whole interplatelet distance (i.e., $h = H$). For non-overlapping double layers, integrating over the whole interplatelet distance means partly integrating over the bulk solution, which would affect the calculated ESP. Denoting the indices $i = 1$ for chloride and $i = 2$ for sodium, this yields the following expression for the ESP

$$\text{ESP} = \frac{[Na^+]F\int_0^h g_2(y)dy}{\sigma + [Cl^-]F\int_0^h g_1(y)dy} \times 100\% \tag{5.6}$$

Disjoining pressure and mechanical equilibrium

Once the electric potential and ion distribution are known, we can compute the disjoining pressure at the clay mineral surface. The pressure in a nanopore is given by the sum of the osmotic pressure and the Maxwell stress. Here, we use an alternative expression for the disjoining pressure given by Rocha et al. (2016). The disjoining pressure is obtained by subtracting the osmotic pressure for the case of a single particle (i.e., $H = \infty$)) from the osmotic pressure calculated for the desired H, both calculated at the exclusion zone interface (i.e., at a distance $d/2$ of the clay surface) and with the same surface charge density σ. This yields

$$\Pi_d = RT \sum_{i=1}^{3} C_{b_i} g_i - RT \sum_{i=1}^{3} C_{b_i} g_i \Big|_{H \to \infty} \quad \text{on } \Gamma, \tag{5.7}$$

where Π_d is the component of the disjoining pressure [Pa] normal to the clay surface, and Γ is the exclusion zone interface, located at a distance of $d/2$ from the clay surface. In this study, we used $H = 10^{-7}$ m to approximate the osmotic pressure for a single particle.

We assume that the clay platelets are stacked in parallel arrangement to form tactoids. We simplify the situation by making the assumption that clay platelets can only be displaced in the direction normal to their orientation. Changes in intra-tactoid porosity are therefore directly related to changes in the interlamellar spacing. In a parallel particle arrangement, the clay particles are never in contact with each other. Therefore, the effective stress, which describes the stresses transmitted between the clay particles at contact points, vanishes (Le, 2013). The condition of mechanical equilibrium then reduces to

$$P = \Pi_d, \tag{5.8}$$

where P is the external or overburden pressure (Le et al., 2015, 2016). This allows us to compute the interlamellar spacing at equilibrium for a given external pressure and electrolyte composition. We assume a constant overburden pressure for all micropores, which results in a homogeneous pore size for the micropores.

5.2.2 Pore-network modelling of soil swelling

To link swelling of the intra-tactoid pores to changes in the macroscopic soil hydraulic properties, we use a pore-network model. In these models, the pore space is discretized into pore bodies (nodes) and pore throats (bonds). We assume spherical and cylindrical geometry for the pore bodies and throats, respectively. We generated 40.000 pore bodies at random locations within a cubic domain of 1.0 × 1.0 × 1.0 cm. Connections between the pore throats were created based on Delaunay triangulation. Pore throats were then randomly removed until the average connections for each pore body equals 4 to achieve the average coordination number for granular materials and soils (Ioannidis and Chatzis, 2000; Rabbani et al., 2016). The initial pore body and throat radii are randomly generated from a truncated lognormal distribution f, given by

$$f(R_i, \sigma_{ps}) = \frac{\sqrt{2} \exp\left(-\frac{1}{2} \left(\frac{\ln(\frac{R_i}{R_m})}{\sigma_{ps}} \right)^2 \right)}{R_i \sqrt{\pi \sigma_{ps}^2} \left(\operatorname{erf}\left(\frac{\ln(\frac{R_{max}}{R_m})}{\sqrt{2\sigma_{ps}^2}} \right) - \operatorname{erf}\left(\frac{\ln(\frac{R_{min}}{R_m})}{\sqrt{2\sigma_{ps}^2}} \right) \right)}, \tag{5.9}$$

where R_i is the pore radius, σ_{ps} is the standard deviation of the pore radius, and R_{max}, R_{min}, and R_m are the maximum, minimum, and mean radius, respectively (Joekar-Niasar et al., 2010b).

Shrinking of macropores

We consider a soil sample of which the total volume is constrained. Since the volume occupied by the soil particles does not change due to swelling, the total porosity must also be constant. Therefore, swelling of the micropores must come at the expense of the macropore volume. We therefore have

$$\phi = \phi_{macro} + \phi_{micro}, \tag{5.10}$$

where ϕ is the total porosity, ϕ_{macro} is the macroporosity, and ϕ_{micro} is the microporosity. The initial macroporosity is calculated from the pore bodies and throats generated from the pore size distribution (Equation 5.9). The microporosity is given by

$$\phi_{micro} = \frac{\phi_{tactoid}}{1 - \phi_{tactoid}} f_c, \tag{5.11}$$

where f_c is the volumetric clay fraction, and $\phi_{tactoid}$ is the porosity of a single tactoid, given by

$$\phi_{tactoid} = \frac{2H}{2H + \delta} \tag{5.12}$$

This expression is derived for parallelly oriented particles of thickness δ (Murad and Moyne, 2008). Thus, changes in the pore water chemistry or overburden pressure affect the tactoid porosity (Equations 5.8 and 5.12), which in turn affects the microporosity (Equation 5.11) and macroporosity (Equation 5.10). The pore body and pore throat radii are calculated from the macropore volume. The volume fraction of the macroporosity that is occupied by each pore throat and body is calculated for the initial situation. It is assumed that this volume fraction remains constant during swelling and shrinking, which allows calculating of the pore throat and body volumes after changes in macroporosity. The pore body and throat radii can easily be obtained from their volume, as we assumed spherical and cylindrical shapes for the pore bodies and throats.

Saturated hydraulic conductivity

To calculate the hydraulic conductivity of the pore network, we need to solve the pressure in each pore. We assume that the fluid is incompressible, and therefore the water mass balance for each pore body reads

$$\sum q_{ij} = 0, \tag{5.13}$$

where q_{ij} is the volumetric water flux [m^3/s] between two pore bodies i and j. We assume laminar and unidirectional water flow in the pore throats. Therefore, the volumetric water flux through a pore throat is then given by the Hagen-Poiseuille equation for cylindrical pore throats

$$q_{ij} = \frac{\pi}{8\mu L_{ij}} r_{ij}^4 (P_i - P_j), \tag{5.14}$$

where μ is the dynamic viscosity of water [Pa s], L_{ij} and r_{ij} are the length [m] and radius [m] of the pore throat connecting pore bodies pore bodies i and j, respectively. Finally, P_i and P_j [Pa] denote the fluid pressure in pore bodies i and j, respectively. Combining Equations 5.13 and 5.14 yields a system of linear equations. For a fixed pressure at specified boundaries of the pore-network, this set of equations can be solved implicitly to obtain the fluid pressure in each pore body. Once the pressure field is known, the saturated hydraulic conductivity can be calculated by rearranging Darcy's law

$$K_s = \frac{QL\rho_w g}{A\Delta P}, \tag{5.15}$$

where K_s [m/s] is the saturated hydraulic conductivity, Q [m^3/s] is the volumetric water flux measured at the outlet of the pore network, L [m] is the length of the pore network from inlet to outlet, ρ_w [kg/m^3] is the density of water, g [m/s^2] is the acceleration due to gravity, A [m^2] is the cross-sectional area of the pore network, and ΔP [Pa] is the prescribed pressure difference between the inlet and outlet. Naturally, the shift to smaller macropore sizes due to swelling of the intra-tactoid pores affects the soil hydraulic properties. The saturated hydraulic conductivity decreases as the intra-tactoid porosity increases. The reduction factor r is defined as

$$K_s(SAR, C) = r(SAR, C) K_{ref}, \tag{5.16}$$

where K_{ref} is the saturated hydraulic conductivity [m/s] as calculated by the pore-network model for a given reference scenario.

Unsaturated hydraulic properties

Next, we calculate the equilibrium soil water retention curve for the primary drainage curve, although this approach can also be applied to imbibition and scanning curves. At one boundary of the pore-network, the pore network is connected to a reservoir of the non-wetting phase, in this case air. The opposite boundary is connected to a water

reservoir. The air pressure in the reservoir is increased stepwise. When the air pressure exceeds the air-entry pressure of a pore throat, the pore throat and connected pore bodies are drained. The entry pressure for each pore throat, which is the capillary pressure at which air is able to invade the pore throat. This is given by Young-Laplace equation, which for cylindrical pore throats yields

$$P^c_{ij,entry} = \frac{2\sigma_{aw}\cos(\theta_{aw})}{r_{ij}}, \tag{5.17}$$

where σ_{aw} is the interfacial tension [N/m], and θ_{aw} is the air-water contact angle [°]. Since pore bodies are much larger than pore throats, the entry pressure of pore bodies is much smaller than that of pore throats. Therefore, we can assume that pore bodies are invaded once an adjacent pore throat is invaded. Once a pore body or throat is invaded, the air pressure inside is set equal to the air pressure in the reservoir. For each invaded pore, the invasion criteria for all connected pore throats are checked. This process is iterated until no change in the total number of invaded pores occurs, which indicates that the equilibrium state is reached. For a given capillary pressure, we can then calculate the saturation by the ratio of the volume of saturated pores to the total volume of pores:

$$s = \frac{\sum_i V_i^w}{\sum_i V_i}, \tag{5.18}$$

where V_i [m^3] is the volume of pore body i. The superscript w denotes the pore bodies that are saturated with water. Plotting the saturation versus the capillary pressure yields the soil water retention curve. The resulting soil water retention curves are fitted to the van Genuchten function (van Genuchten, 1980), given by

$$s = \frac{\theta - \theta_r}{\theta_s - \theta_r} = \left(1 + (\alpha P_c)^n\right)^{-(1-1/n)}, \tag{5.19}$$

where θ is the volumetric water content [-], θ_r is the residual water content [-], here defined as the water stored in the micropores, θ_s is the water content at saturation [-], which equals the sum of the micro- and macroporosity. Additionally, α is the inverse of the air-entry pressure [1/Pa], and n is a parameter that describes the pore size distribution [-].

The nanopores in clay soils may also swell due to hydration. The saturation state may therefore also affect the degree of swelling. The capillary pressure range that we consider here is chosen such that the macropores are completely drained. The micro- and nanopores are not invaded within this capillary pressure range, since these pores are smaller than the macropores by several orders of magnitude. We therefore neglect swelling effects due to water uptake.

5.3 Results and discussion

We first present the results of the DFT-MSA model for the microscopic scale. Afterwards, we present the response of the macroscopic soil hydraulic properties. The input parameters used in this study for both the DFT-MSA model and the pore-network model are listed in Table B.1 of 5B.

5.3.1 Clay swelling at the microscopic scale

We show the disjoining pressure as a function of the interplatelet distance in Figure 5.3, which is plotted for a fixed total salinity of 10 mol/m^3 and various SAR values. For most interplatelet distances, the disjoining pressure between two clay particles is repulsive, as indicated by a positive value. However, at low SAR, the disjoining pressure is negative for interplatelet distances of 0.8 to 1 nm. A negative pressure indicates that the net force between two adjacent clay particles is attractive. This attractive regime agrees well with experimental observations that clay particles are separated by a distance of approximately 0.9 nm when calcium is the dominant cation, i.e., at low SAR (Kjellander et al., 1988). As the SAR increases, the interplatelet distance range at which the disjoining pressure is negative shrinks, until the disjoining pressure becomes purely repulsive, which indicates that tactoids start to swell. The threshold at which this happens is governed by both the SAR and the total salinity C.

Swelling of clay tactoids can thus be explained by the transition from a negative to a positive disjoining pressure. However, the negative disjoining pressure cannot be predicted by Poisson-Boltzmann theory. The disjoining pressure is negative when the attractive Maxwell component dominates over the repulsive osmotic component. The use of the Poisson-Boltzmann equation may lead to unrealistically high cation concentrations near the mineral surface. Therefore, the osmotic pressure always exceeds the Maxwell stress, resulting in a repulsive disjoining pressure. However, when ion-ion correlation effects are included (such as in the DFT-MSA framework used here), the counterion concentration near the clay surface is limited by the size of the ions. This results in a smaller osmotic pressure, which allows the Maxwell stress to dominate in particular cases. This highlights that advanced models that include ion-ion correlations are critical for making predictions on the stability of clays (Kjellander et al., 1988; Quirk, 2001; Rocha et al., 2016).

The transition from an attractive to a repulsive disjoining pressure leads to an abrupt change of the interplatelet distance at mechanical equilibrium (Figure 5.4). At low SAR, the interplatelet distance shows only slight sensitivity to the SAR and salinity. However, once the SAR exceeds a certain threshold, major swelling occurs as the interplatelet distance rapidly increases. The SAR at which this strong swelling occurs depends on the total salt concentration; swelling occurs at a SAR of 18 for a salinity of 100 mol/m^3, while at a concentration of 500 mol/m^3 a SAR of 42 is required. Additionally, the interplatelet

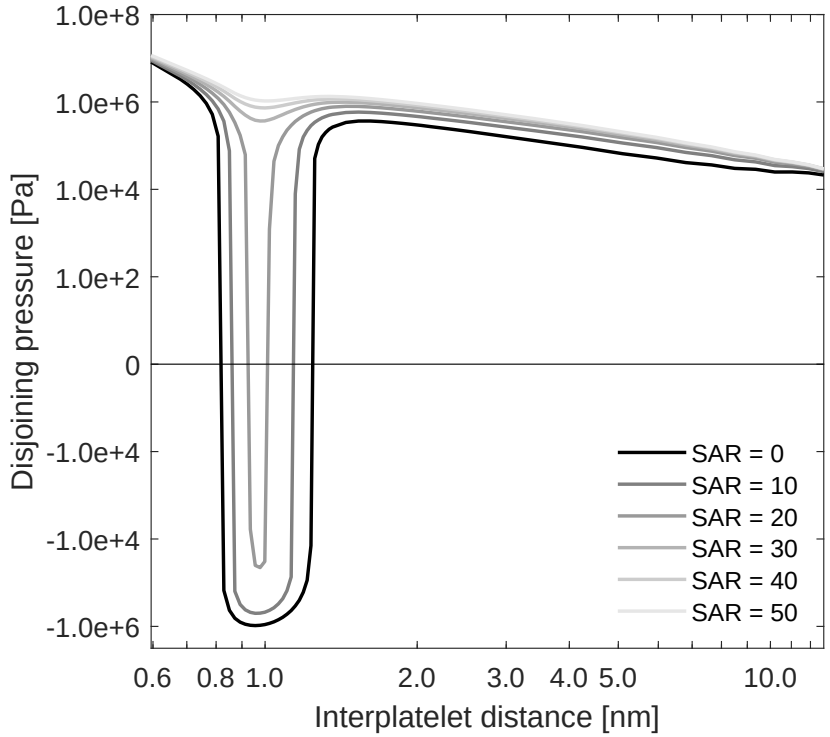

Figure 5.3: The disjoining pressure as a function of the interplatelet distance $2H$ for various SAR values and a fixed total salinity of 10 mol/m^3.

distance is larger after swelling at low salt concentrations.

In Figure 5.4, we plotted the results as a function of the SAR, since it is a natural boundary condition for the DFT-MSA model. However, in practice, the SAR is only used as a proxy for the ESP. While the SAR depends only on the pore water chemistry, the ESP also depends on soil properties such as the pore size distribution and the surface charge density of the clay minerals. The ESP is thus not a boundary condition of the model, but can be obtained through post-processing. We show the same equilibrium interplatelet distance, but then plotted as a function of ESP instead in Figure 5.5. When the ESP is low, it has little effect on the interplatelet distance. A sudden increase in interplatelet distance is seen once the ESP reaches a certain threshold, which depends on the salt concentration. For a salinity of 100 mol/m^3, swelling starts at an ESP of 16%, while for a salinity of 300 mol/m^3, swelling starts at an ESP of 24%. Swelling is also more significant at lower salt concentrations, indicated by a larger interplatelet distance. This is in agreement with the results from Quirk and Schofield (1955), who found that for a given ESP, adequate soil permeability may be maintained by increasing the salinity.

The ESP is partly governed by the strength of the electric field between clay particles. Therefore, the pore size plays an important role. In small pores, the electric field is stronger which results in stronger attraction of calcium over sodium ions. Small pores

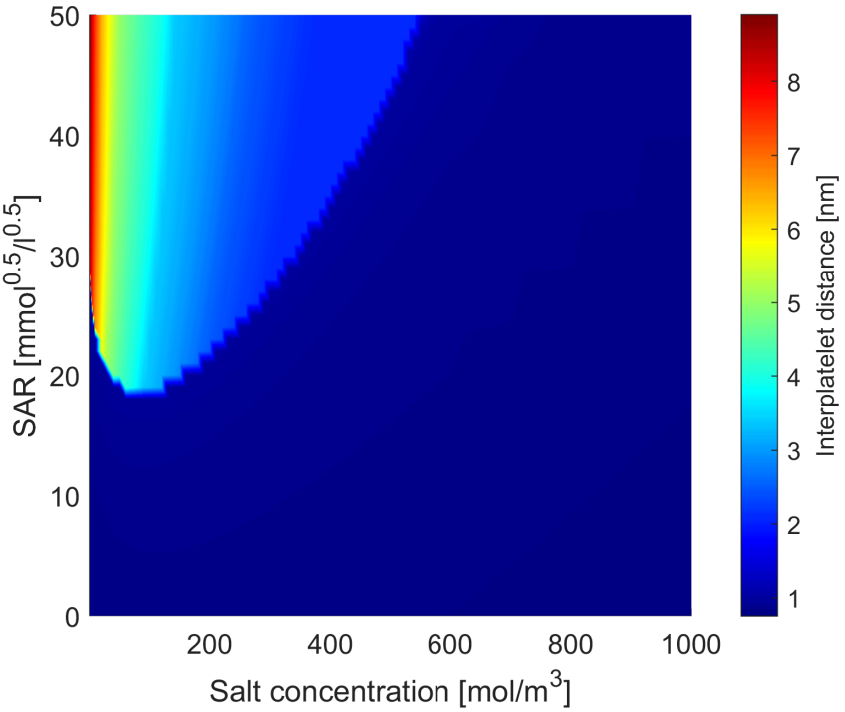

Figure 5.4: Interplatelet distance calculated from Equation 5.8, for various combinations of sodium and calcium concentrations and an external pressure of $P = 10^5$ Pa.

therefore have a lower ESP than large pores. From Figure 5.3, we can see that for a given overburden pressure, several values of H satisfy mechanical equilibrium (Equation 5.8). This means that both internal pores (around 0.9 nm) and external pores (> 2 nm) may exist simultaneously. As the SAR increases, the internal pores may disappear, indicating the disintegration of tactoids and increasing the water retention of the clay. On the other hand, a higher overburden pressure may prevent disintegration of tactoids. The ESP in Figure 5.5 was calculated from the minimum interplatelet distance at mechanical equilibrium, which corresponds to the intra-tactoid pores. However, the larger inter-tactoid pores would have a higher ESP. The ESP values obtained from experiments are an average of both intra-tactoid and inter-tactoid pores, and are therefore expected to be higher than the values reported here.

We now apply the DFT-MSA model to the experimental data of Shainberg et al. (1971b). They measured the water retention of clay pastes for several combinations of pore water chemistry and overburden pressure. The six different ion solutions are listed in Table 1. Additionally, they attempted to model this with Poisson-Boltzmann theory. They recognized that at low SAR, the clay particles clump together to form tactoids, and that these tactoids break down once a certain threshold SAR is reached. However, Poisson-Boltzmann theory is only applicable at the external surfaces of the tactoids,

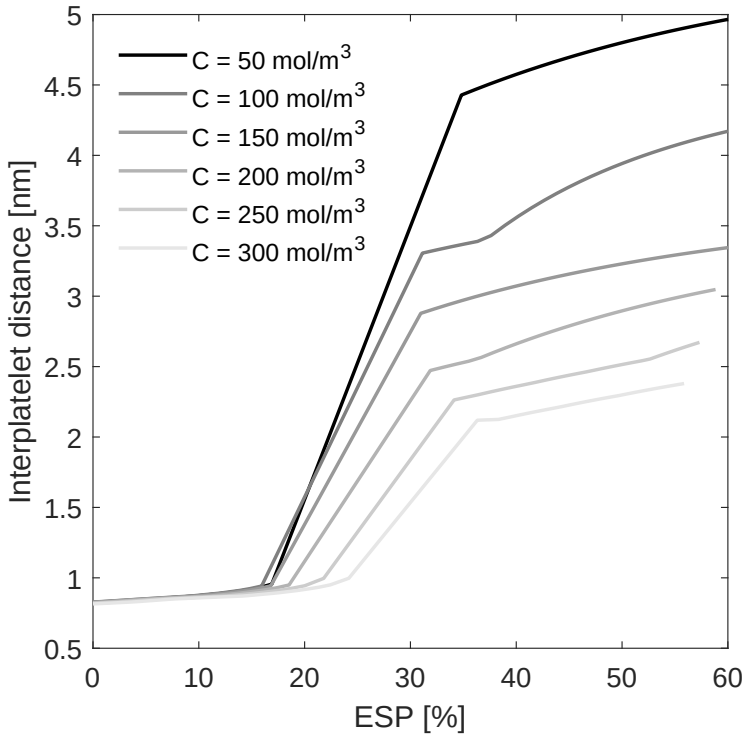

Figure 5.5: The interplatelet distance calculated from mechanical equilibrium, plotted as a function of ESP for various levels of salinity.

not the internal surfaces. Therefore, they defined only the external surface area of the tactoids as the active surface area. They calculated the active surface area using the number of clay particles per tactoid as a fitting parameter. Reasonable agreement between experimental and numerical values were obtained for Na-montmorillonite (SAR= ∞), but not for Ca-montmorillonite (SAR= 0).

Table 5.1: Combinations of sodium and calcium concentrations used by Shainberg et al. (1971b).

SAR [mmol$^{0.5}$/l$^{0.5}$]	$[Na^+]$ [mol/m^3]	$[Ca^{2+}]$ [mol/m^3]
0	0.00	1.00
7	10.00	2.00
14.2	10.00	0.50
32	10.00	0.10
100	10.00	0.01
∞	10.00	0.00

From Shainberg et al. (1971b), we take the total specific surface area of montmorillonite to be 8.0×10^6 cm^2/g. For Ca-montmorillonite, we require an estimate of the surface area of the internal pores and the external pores. We found that assigning a fraction of 55% of the

total clay surface area to the internal pores yielded the best match between experimental and numerical observations (Figure 5.6a). For the pure sodium solution, there is only one pore size at the respective overburden pressure, which means that the tactoids have disintegrated. Using Poisson-Boltzmann theory, Shainberg et al. (1971b) could not obtain a good fit between numerical and experimental results for Ca-montmorillonite. They attempted to use the number of clay particles per tactoid as a fitting parameter to obtain better agreement between experimental and model results. However, they found that the number of particles per tactoid is also dependent on the overburden pressure, and is therefore not constant for a given SAR. While the DFT-MSA approach still requires fitting to experimental values to obtain the surface area of the internal pores at low SAR, this method is able to describe the change in clay water content due to varying overburden pressure.

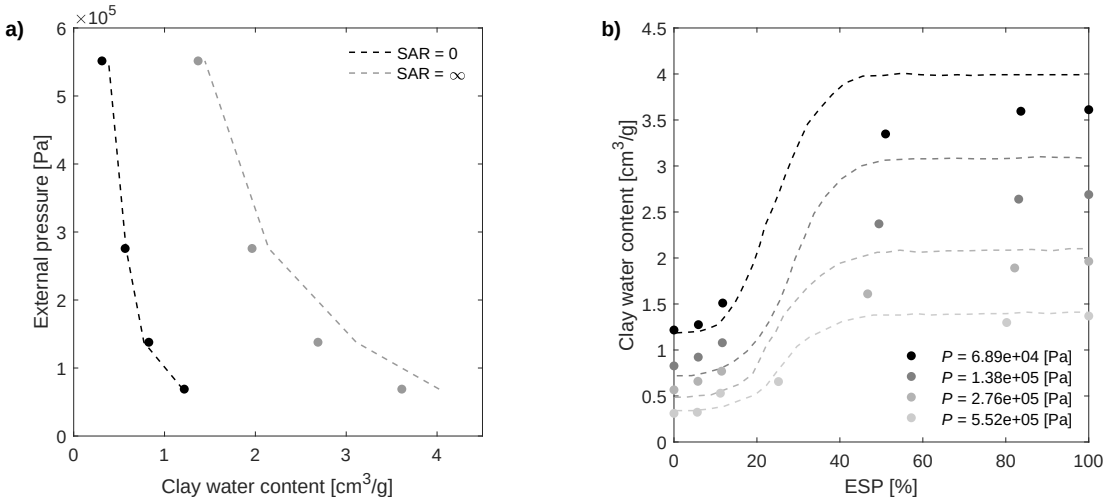

Figure 5.6: Comparison between the experimental results of Shainberg et al. (1971b) (dashed lines) and the DFT-MSA model results of this study (dots). a) The clay water content versus the overburden pressure for Ca-montmorillonite (SAR= 0) and Na-montmorillonite (SAR= ∞). b) The water content in clay sample plotted as a function of the ESP for various overburden pressures.

In Figure 5.6b, we show the clay water content as a function of the ESP for both our DFT-MSA model and the experimental results of Shainberg et al. (1971b). The experimental and numerical values show reasonable agreement at low ESP. Shainberg et al. (1971b) were not able to reproduce reasonable results at low ESP, because they only considered the external pores. This leads to an overestimation of the clay water content, and a high sensitivity to the overburden pressure. On the other hand, if we assumed all pores to be internal pores, the clay water content is underestimated, and the effect of the overburden pressure is negligible. To obtain a good fit with experimental results, both internal and external pores should be included in the model. In Figure 5.6b, we again assumed that the internal surface area occupied 55% of the total surface area,

which yields reasonable results at low ESP.

Nevertheless, the water retention at high ESP is underestimated by the model, particularly at low overburden pressures. The Poisson-Boltzmann approach of Shainberg et al. (1971b) also underestimated the water content at high ESP. The model assumes that clay particles are aligned in parallel orientation. This assumption is more likely to hold at high overburden pressures than at low pressures. This may explain the smaller discrepancy between experimental and numerical values for higher overburden pressures. The advantage of the DFT-MSA approach over the Poisson-Boltzmann approach is that it becomes possible to predict at what combination of pore water chemistry and overburden pressure the clay tactoids start to disintegrate.

5.3.2 Change in soil hydraulic parameters due to clay swelling

Since swelling of the intra-tactoid pores results in shrinking of the macropores, the response of the interplatelet distance to SAR and C directly affects the macroscopic response. In Figure 5.7, we show the distribution of the pore throat radii for several SAR values at a salinity of 50 mol/m^3. As the SAR increases, the pore throat distribution shifts to smaller values. However, this shift is small as long as the SAR remains below its threshold value. Therefore, there is almost no impact on the pore size distribution when the SAR ranges between 0 and 10 mmol$^{0.5}$/l$^{0.5}$, but the pores shrink significantly once the SAR is increased further. However, the shape of the pore size distribution does not change noticeably due to swelling. This is due to the fact that the volume fraction of the macroporosity occupied by each pore throat and body remains constant. Thus, the largest macropores will remain the largest, while the smallest pores will remain the smallest, and the shape of the pore size distribution does not change.

Obviously, the shift in pore sizes has a strong impact on the hydraulic conductivity. We show the reduction factor of the hydraulic conductivity (defined in Equation 5.16) in Figure 5.8. The evolution of the hydraulic conductivity is closely related to that of the interplatelet distance: the reduction in hydraulic conductivity is small at low ESP, until a critical value of 16 to 24% (depending on the salinity) is reached, after which the hydraulic conductivity is drastically reduced. The discontinuity between high and low reduction factors appears due to the sudden increase in interplatelet distance, which is accompanied with a jump in ESP. In Figure 5.8, we have also plotted the experimental results of (Shainberg and Caiserman, 1971), which were obtained for a salinity of 10 mol/m^3. The model and experimental results agree qualitatively in the sense that there is little reduction at low ESP, but significant reduction in hydraulic conductivity occurs once an ESP of 15-20% has been reached. Additionally, we have compared our results with the empirical expressions for the reduction factor from McNeal and Coleman (1966) and Ezlit (2009). However, the ESP at which soil degradation occurs is significantly lower in our model compared to the parametrization given by these studies and are therefore

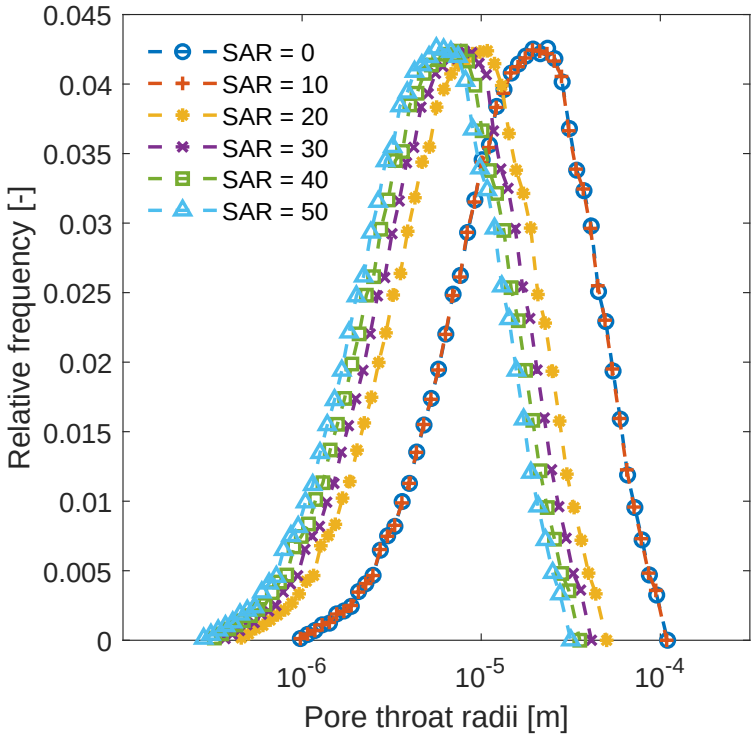

Figure 5.7: Distribution of the macropore throat radii for various values of the SAR, and a salinity of 50 mol/m^3.

not shown here.

Since the macropores shrink due to clay swelling, a larger capillary pressure is required for air to invade the pore network. This results in smaller values for the inverse air-entry pressure α in the van Genuchten equation (Figure 5.9). However, the shape of the soil water retention curves does not change due to swelling (not shown here). Similarly, the relative permeability does not change significantly as a function of SAR. While the pore sizes shrink due to clay swelling, the shape of the pore size distributions is not affected significantly. The relative permeability is strongly dependent on the shape of the pore size distribution and the connectivity of the pore network. In our approach, swelling does not affect the connectivity of the network, but only affects the pore sizes. This insensitivity of the relative permeability and shape of the soil water retention curve to swelling is indicated by an almost constant value for the pore size distribution index n in the van Genuchten equation. While the shape of the water retention curve is not affected by swelling, the residual water content is affected, as was already shown in Figure 5.6.

Within the DFT-MSA model, we treat the ions as hard spheres with a diameter of 0.425 nm for all ionic species. In reality, ions do not have a sharp boundary, and therefore the ionic radius is not clearly defined. Therefore, the values for ion radii reported in the literature may vary significantly depending on the chosen model (Kiriukhin and Collins,

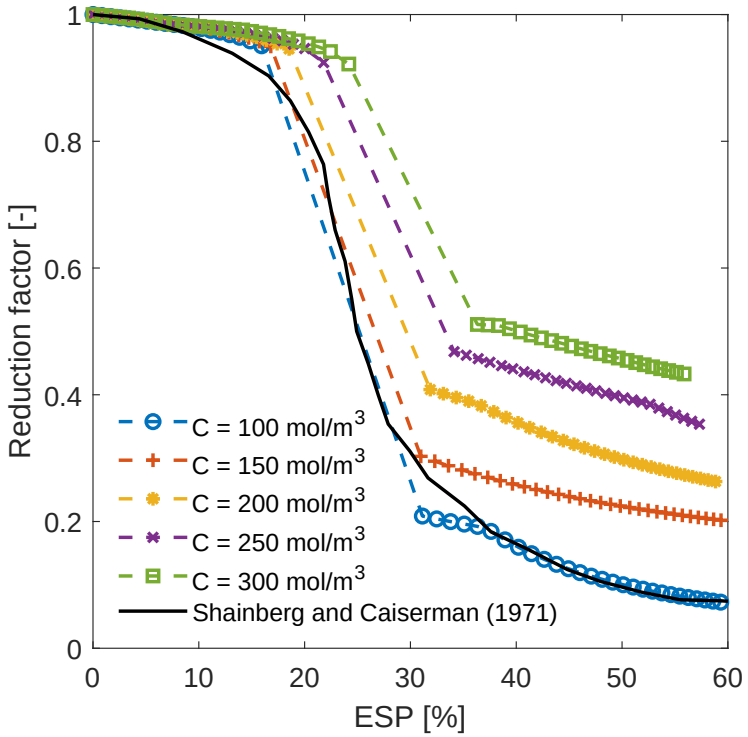

Figure 5.8: Reduction factor for the hydraulic conductivity as a function of the ESP for various salinities. The black line shows the experimental results of Shainberg and Caiserman (1971) for a total salt concentration of 10 mol/m^3.

2002; Yang et al., 2002; Hussain et al., 2006). Additionally, the ion sizes of sodium, calcium, and chloride are different. Nevertheless, the ion diameter significantly affects the outcome of the DFT-MSA model. When the ion diameter is small, the accumulation of cations near the clay surface will not be restricted as much by ion-ion correlation. It is then more likely that the osmotic pressure dominates over the Maxwell stress, resulting in repulsive disjoining pressures. On the other hand, when the ion diameter is large, the accumulation of cations near the clay surface is restricted due to ion-ion correlations. This allows the Maxwell stress to dominate more over the osmotic pressure, leading to a more negative disjoining pressure instead. We made additional simulations with an ion diameter 10% larger than in the reference simulations. This resulted in the critical SAR value to be increased by approximately 10 mmol$^{0.5}$/l$^{0.5}$, and the critical ESP is increased then lies at 23 to 31% for salinities of 100 to 300 mol/m^3. Thus, the chosen value for the ion diameter significantly affects the predicted threshold values above which sodic soils start to swell.

In this study, we have considered swelling of clay tactoids (i.e., the increase of the interplatelet distance) as the only mechanism that affects the pore size distribution. However, when the clay particles move apart, they may be dislodged entirely from the

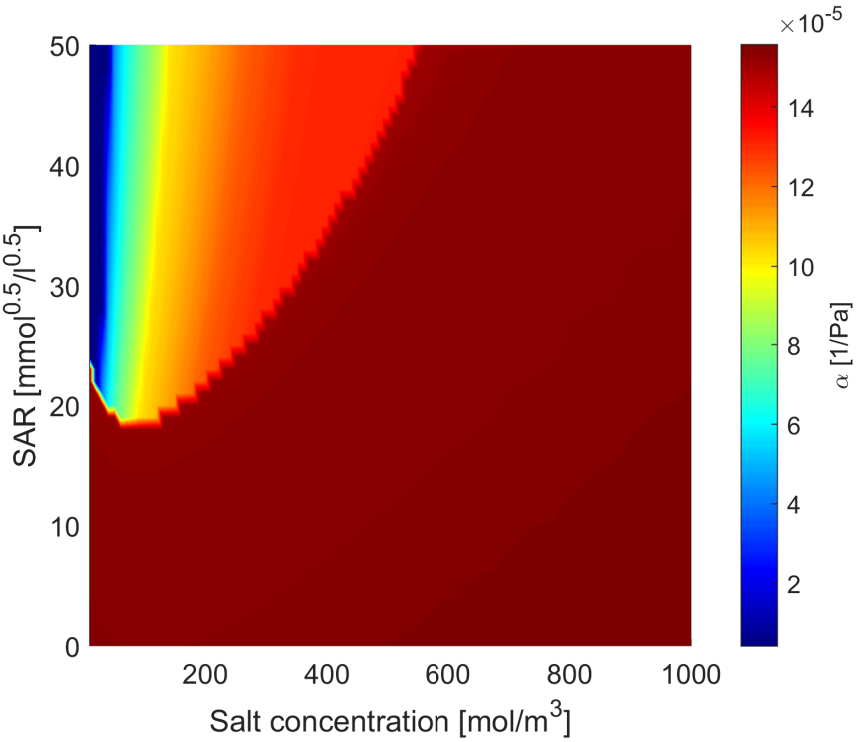

Figure 5.9: The inverse air-entry pressure α of the van Genuchten function plotted as a function of the salt concentration and SAR.

tactoid, which is termed clay dispersion. These loose particles may be transported with the water flow and plug pores, which further decreases the hydraulic conductivity of the soil. Since we did not consider dispersion, the predicted change in soil hydraulic properties is a conservative estimate.

We have used a simple method to adjust the macropore size distribution due to swelling of the micropores. More accurate results may be obtained when using more complex models. Nevertheless, there is a vast scale difference between the clay platelets, which initiate swelling, and the macropores, which contribute significantly to the soil hydraulic properties. However, modelling these two scales simultaneously is too computationally demanding. Therefore, these scales have to considered separately, and linked through some upscaling method.

An example of more advanced models is the discrete element method (DEM), where the soil is modelled as individual particles. In such models, soil particle rearrangement is calculated based on the forces between the particles using Newton's second law. Such models have been used for the nanoscopic scale to model the movement of individual clay platelets (Pagano et al., 2020). However, these models did not include the complex physics required to model the interaction between clay particles and pore water chemistry, such as DFT-MSA or the hypernetted chain approximation. Including these advanced models in

DEM, where clay particles may not be parallelly oriented, is a significant computational challenge. On the macroscopic scale, DEM can also be used. For example, Sweijen et al. (2016) used DEM coupled with a pore-network model to calculate the change in hydraulic properties due to swelling of super adsorbent polymer particles. However, this cannot easily be translated to clay aggregates, which are plastic and porous, while DEM particles are generally non-deformable and solid. Linking the swelling of micropores to changes in the macroscopic hydraulic parameters therefore remains challenging. The approach used in this study is therefore only a first step to bridge this gap.

5.4 Conclusions

In this study, we applied the DFT-MSA framework to calculate the interaction between clay particles in the context of soil sodicity. In previous studies, Poisson-Boltzmann theory was frequently used to determine the forces between clay particles, even though it neglects the ion-ion correlation forces which are crucial for the stable configuration of clay particles under non-sodic conditions. While the DFT-MSA framework has been used previously to explain the stability of Ca-montmorillonite, the framework has not yet been applied to predict soil sodicity impacts (e.g., to determine the required sodium concentration for montmorillonite soils to structurally break down). The numerical results of the DFT-MSA model agreed well with experimental observations. The model predicts that almost no swelling occurs at low ESP, but significant swelling occurs once a threshold ESP value has been reached. The critical ESP ranged from 16 to 24% in the salinity range of 50 to 300 mol/m^3, with lower thresholds for lower salinities. This study shows that advanced theory such as DFT-MSA are crucial for modelling soil sodicity on the microscopic scale. These models should therefore be used over the prevalent Poisson-Boltzmann models, despite being much more complex.

Furthermore, we made a first step to translate the swelling of micropores to changes in the macroscopic soil hydraulic properties. The shrinking of the macropores is controlled by swelling of the micropores. Therefore, a strong reduction in hydraulic conductivity is seen once the ESP exceeds its threshold value. The hydraulic conductivity and air-entry pressure are significantly altered due to clay swelling. However, since the shape of the pore size distribution and the pore network connectivity do not change in our approach, swelling had no impact on the relative permeability and the shape of the soil water retention curve, indicated by an almost constant pore size distribution index in the van Genuchten function.

In this study, we have limited ourselves to the equilibrium state for a given salt solution. Transient effects have been neglected, which may also affect the soil hydraulic properties. For example, a gradient in pore water salinity may result in osmotic water flow into or out of the clay sample, which may lead to additional swelling or shrinking. These effects are disregarded when looking only at the steady-state situation. Thus, the present study

can be extended in future to include the transient swelling behaviour. Additionally, we made several simplifying assumptions to translate swelling of the micropores to shrinking of the macropores. Using a more advanced soil mechanical model for this step will likely yield better results, especially for the shape of the water retention curve and the relative permeability.

Appendix

5A Numerical procedure for solving the Poisson problem

5A.1 Equations

Solving Equations 5.3-5.5 to obtain the ion distribution and electric potential inside a nanopore requires a complex numerical procedure. We followed the approach proposed by Le et al. (2016) and Rocha et al. (2016). Readers are referred there for a detailed derivation of the governing equations and numerical procedure. In the current section, we will present a summary of the equations that are solved to allow reproduction of our results.

The main idea behind the numerical procedure is to split the ion distribution g_i into an electrostatic component $\exp(-z_i\bar{\psi})$ and an ion-ion correlation component $\tilde{g}_i$, yielding

$$g_i(y) = \tilde{g}_i(y)\exp\big(-z_i\bar{\psi}(y)\big), \tag{5A.1}$$

where the expression for $\tilde{g}_i$ simply follows from Equation 5.3

$$\tilde{g}_i(y) = \exp\left(n_A\sum_{j=1}^{3}C_{b_j}\int\tilde{c}_{ij}(|y-y'|)h_j(y')dy'\right) \tag{5A.2}$$

While $\exp\left(-z_i\bar{\psi}\right)$ is computed from the current iteration, $\tilde{g}_i$ is computed from the previous iteration. Thus, for a certain iteration k, the Poisson problem (Equation 5.4) is solved as

$$\nabla^2\bar{\psi}^{k+1} = \frac{F^2}{\epsilon RT}\sum_{i=1}^{3}z_iC_{b_i}\tilde{g}_i^k\exp(-z_i\bar{\psi}^{k+1}) \tag{5A.3}$$

The Poisson problem is solved for the one-dimensional case, and linearized using the Newton-Raphson method as follows

$$\exp(-z_i\bar{\psi}^{k,s+1}) \approx \exp(-z_i\bar{\psi}^{k,s}) - z_i\exp(-z_i\bar{\psi}^{k,s})(\bar{\psi}^{k,s+1} - \bar{\psi}^{k,s}), \tag{5A.4}$$

and solved until convergence in s is achieved. A constant surface charge boundary condition is assumed, as stated in Equation 5.5.

Solving the Fredholm integral (Equation 5.3) is more complex. Following Lozada-Cassou and Díaz-Herrera (1990), the integral can be simplified for the particular case of parallel clay particles, which yields

$$\tilde{g}_i^k = \exp\left(\sum_{j=1}^{3}\int_0^{H-d/2} K_{ij}(y,y')h_j^k(y')dy' + J(y)\right), \tag{5A.5}$$

where expressions for K_{ij} and J are given in Section A.3, and $h_j = g_j - 1$. We approximate the integral using the trapezoidal rule to obtain

$$\tilde{g}_i^k \approx \exp\left(\sum_{j=1}^{3}\sum_{q=1}^{n} w_q K_{ij}(y,y_q)h_j^k(y_q) + J(y)\right), \tag{5A.6}$$

where w_q are the weights associated with the discretization of the integral. By denoting the ionic species i and j as (1) chloride, (2) sodium, and (3) calcium, we can simplify the problem to only five expressions for the kernels as follows

$$\begin{aligned} K_1 &= \tfrac{1}{[Cl^-]}K_{11} = \tfrac{1}{[Na^+]}K_{22} \\ K_2 &= \tfrac{1}{[Na^+]}K_{12} = \tfrac{1}{[Cl^-]}K_{21} \\ K_3 &= \tfrac{1}{[Ca^{2+}]}K_{13} = \tfrac{1}{[Cl^-]}K_{31} \\ K_4 &= \tfrac{1}{[Ca^{2+}]}K_{23} = \tfrac{1}{[Na^+]}K_{32} \\ K_5 &= \tfrac{1}{[Ca^{2+}]}K_{33} \end{aligned} \tag{5A.7}$$

The numerical procedure proposed by Le et al. (2016) and Rocha et al. (2016) consists of using the collocation method and writing the ion distribution coefficients $h_i^k(y)$ for each ionic species as eigenfunction expansions at specified collocation points y_p, with $p = 1, ..., n$. The approximate ion distribution coefficient at the collocation points $H_i^k(y_p) \approx h_i^k(y_p)$ can thus be written as

$$
\begin{aligned}
H_1^k(y_p) &= \sum_{v=1}^{n} a_1^{v,k} U_1^v(y_p) = \sum_{v=1}^{n} a_2^{v,k} U_2^v(y_p) = \sum_{v=1}^{n} a_3^{v,k} U_3^v(y_p) \\
H_2^k(y_p) &= \sum_{v=1}^{n} b_1^{v,k} U_1^v(y_p) = \sum_{v=1}^{n} b_2^{v,k} U_2^v(y_p) = \sum_{v=1}^{n} b_4^{v,k} U_4^v(y_p) \\
H_3^k(y_p) &= \sum_{v=1}^{n} c_3^{v,k} U_3^v(y_p) = \sum_{v=1}^{n} c_4^{v,k} U_4^v(y_p) = \sum_{v=1}^{n} c_5^{v,k} U_5^v(y_p)
\end{aligned}
\tag{5A.8}
$$

where a_i, b_i, and c_i are expansion coefficients which have to be computed. The eigenfunctions follow from the eigenvalue problem

$$
\sum_{q=1}^{n} w_q K_m(y_p, y_q) U_m^v(y_q) = \Lambda_m^v U_m^v(y_p) \quad m = 1, ..., 5 \tag{5A.9}
$$

where Λ_m^v and U_m^v are the approximate eigenvalues and eigenfunctions, respectively, with $v = 1, ..., n$. The eigenvalue problem is thus solved for five sets of eigenpairs, corresponding to the five possible combinations of ions. For ease of notation, we write the eigenfunction in matrix form $\mathbf{U}_i$ with $(\mathbf{U}_i)_{pv} = U_i^v(y_p)$ for $p, v = 1, ..., n$, and use the following vector notation

$$
H_i = \begin{bmatrix} H_i(y_1) \\ ... \\ H_i(y_n) \end{bmatrix}, \; G_i = \begin{bmatrix} G_i(y_1) \\ ... \\ G_i(y_n), \end{bmatrix} \bar{\psi} = \begin{bmatrix} \bar{\psi}(y_1) \\ ... \\ \bar{\psi}(y_n) \end{bmatrix}, \; J = \begin{bmatrix} J(y_1) \\ ... \\ J(y_n) \end{bmatrix}, \; \Lambda_m = \begin{bmatrix} \Lambda_m(y_1) \\ ... \\ \Lambda_m(y_n) \end{bmatrix},
$$

$$
a_i = \begin{bmatrix} a_{i_1} \\ ... \\ a_{i_n} \end{bmatrix}, \; b_i = \begin{bmatrix} b_{i_1} \\ ... \\ b_{i_n} \end{bmatrix}, \; c_i = \begin{bmatrix} c_{i_1} \\ ... \\ c_{i_n} \end{bmatrix} \tag{5A.10}
$$

By using Equations 5A.5-5A.9, using $H_i^k = G_i^k - 1$, with $G_i^k \approx g_i^k$ at the collocation points, and applying rotation matrices to transform the eigenfunction expansions to reduce the problem to only the coefficients a_1, b_1, and c_1, we can rewrite Equation 5.3 as

$$
\begin{aligned}
\mathbf{U}_1 a_1^{k+1} = \exp\Bigg(\bar{\psi}^k + [Cl^-]\mathbf{U}_1(a_1^k \circ \Lambda_1) + [Na^+]\mathbf{U}_2\Big((\mathbf{U}_2^{-1}\mathbf{U}_1 b_1^k) \circ \Lambda_2\Big) \\
+ [Ca^{2+}]\mathbf{U}_3\Big((\mathbf{U}_3^{-1}\mathbf{U}_1 c_1^k) \circ \Lambda_3\Big) + J\Bigg) - 1
\end{aligned}
\tag{5A.11a}
$$

$$\mathbf{U}_1 b_1^{k+1} = \exp\Bigg(-\bar{\psi}^k + [Cl^-]\mathbf{U}_2\Big((\mathbf{U}_2^{-1}\mathbf{U}_1 a_1^k)\circ\Lambda_2) + [Na^+]\mathbf{U}_1(b_1^k\circ\Lambda_1) + [Ca^{2+}]\mathbf{U}_4\Big((\mathbf{U}_4^{-1}\mathbf{U}_1 c_1^k)\circ\Lambda_4\Big) + J\Big) - 1 \quad \text{(5A.11b)}$$

$$\mathbf{U}_1 c_1^{k+1} = \exp\Bigg(-2\bar{\psi}^k + [Cl^-]\mathbf{U}_3\Big((\mathbf{U}_3^{-1}\mathbf{U}_1 a_1^k)\circ\Lambda_3) + [Na^+]\mathbf{U}_4\Big((\mathbf{U}_4^{-1}\mathbf{U}_1 b_1^k)\circ\Lambda_4\Big) + [Ca^{2+}]\mathbf{U}_5\Big((\mathbf{U}_5^{-1}\mathbf{U}_1 c_1^k)\circ\Lambda_5\Big) + J\Big) - 1 \quad \text{(5A.11c)}$$

Here, $\circ$ denotes the Hadamard product between two vectors. This is a nonlinear system of equations which needs to be solved for the coefficients a_1, b_1, and c_1. As we show in Equation 5A.11, we use a Picard iteration scheme to solve this set of equations, meaning that the coefficients on the right-hand side are computed from the previous iteration. Once the coefficients a_1, b_1, and c_1 are known, the ion-ion correlation functions $\tilde{g}_i$ can be updated from

$$\tilde{g}_1^k = \exp\Bigg([Cl^-]\mathbf{U}_1(a_1^k\circ\Lambda_1) + [Na^+]\mathbf{U}_2\Big((\mathbf{U}_2^{-1}\mathbf{U}_1 b_1^k)\circ\Lambda_2\Big) + [Ca^{2+}]\mathbf{U}_3\Big((\mathbf{U}_3^{-1}\mathbf{U}_1 c_1^k)\circ\Lambda_3\Big) + J\Big) \quad \text{(5A.12a)}$$

$$\tilde{g}_2^k = \exp\Bigg([Cl^-]\mathbf{U}_2\Big((\mathbf{U}_2^{-1}\mathbf{U}_1 a_1^k)\circ\Lambda_2) + [Na^+]\mathbf{U}_1(b_1^k\circ\Lambda_1) + [Ca^{2+}]\mathbf{U}_4\Big((\mathbf{U}_4^{-1}\mathbf{U}_1 c_1^k)\circ\Lambda_4\Big) + J\Big) \quad \text{(5A.12b)}$$

$$\tilde{g}_3^k = \exp\Bigg([Cl^-]\mathbf{U}_3\Big((\mathbf{U}_3^{-1}\mathbf{U}_1 a_1^k)\circ\Lambda_3) + [Na^+]\mathbf{U}_4\Big((\mathbf{U}_4^{-1}\mathbf{U}_1 b_1^k)\circ\Lambda_4\Big) + [Ca^{2+}]\mathbf{U}_5\Big((\mathbf{U}_5^{-1}\mathbf{U}_1 c_1^k)\circ\Lambda_5\Big) + J\Big) \quad \text{(5A.12c)}$$

with

$$\tilde{g}_i^k = \begin{bmatrix} \tilde{g}_i^k(y_1) \\ ... \\ \tilde{g}_i^k(y_n) \end{bmatrix} \quad \text{(5A.13)}$$

This ion-ion correlation term can then be inserted in the Poisson equation (Equation 5A.3).

5A.2 Numerical procedure

We now present the numerical procedure to solve the system of equations given in the previous section, as given by Le et al. (2016) and Rocha et al. (2016).

1. First, the eigenproblem (Equation 5A.9) is solved to obtain the eigenvalues and eigenfunctions Λ_m^v and U_m^v at the collocation points for $m = 1, ..., 5$ and $v = 1, ..., n$. Since the eigenfunctions and eigenvalues are independent of the iteration over k, these only need to be computed once.

2. For the first iteration $k = 0$, we choose $\tilde{g}_i = 1$ as an initial estimate of the ion correlation term. This means that we neglect ion-ion correlation and hence solve the Poisson-Boltzmann problem to obtain a first estimate of the electric potential profile.

3. Next, we iterate over k in a loop from $k = 1, 2, ...$

    a. Equation 5A.11 is solved to with a Picard iteration scheme to obtain the coefficients a_1^{k+1}, b_1^{k+1}, and c_1^{k+1} based on their values in the previous iteration, a_1^k, b_1^k, and c_1^k.

    b. With the computed a_1^{k+1}, b_1^{k+1}, and c_1^{k+1} from step 3.a., the ion-correlation term $\tilde{g}_i^{k+1}$ is updated through Equation 5A.12.

    c. The new value for $\tilde{g}_i^k$ is inserted in the Poisson problem (Equation 5A.3) and is solved for $\bar{\psi}^{k+1}$.

    d. Return to step 3.a. until $|\bar{\psi}^{k+1} - \bar{\psi}^k|$ is smaller than a specified tolerance and the algorithm has converged.

5A.3 Expressions for coefficients

Finally, we state the expressions for the variables stated in Section A.1. The expressions for the kernels are given by

$$K_{ij}(y, y') = \begin{cases} n_A C_{b_j} \left(M_1(y, y') + \frac{z_i z_j}{2\epsilon k_B T d} L_1(y, y') \right) & \text{if } \; y < d \;\; \text{and} \;\; y + y' < d \\ n_A C_{b_j} \left(M_2(y, y') + \frac{z_i z_j}{2\epsilon k_B T d} L_2(y, y') \right) & \text{if } \; y - d < y' < y + d \end{cases} \tag{5A.14}$$

and zero otherwise, where k_B is the Boltzmann constant. These terms represent the ion-ion correlation forces within the pore domain. The hard sphere component of the ion-particle correlation is incorporated in M_1 and M_2, with

$$\begin{aligned} M_1(y,y') &= 2\pi\left(a_1\left(\frac{d^2}{2}-\frac{(y+y')^2}{2}\right)+\frac{a_2}{d}\left(\frac{d^3}{3}-\frac{(y+y')^3}{3}\right)+\frac{a_3}{d^3}\left(\frac{d^5}{5}-\frac{(y+y')^5}{5}\right)\right) \\ M_2(y,y') &= 2\pi\left(a_1\left(\frac{d^2}{2}-\frac{(y-y')^2}{2}\right)+\frac{a_2}{d}\left(\frac{d^3}{3}-\frac{(y-y')^3}{3}\right)+\frac{a_3}{d^3}\left(\frac{d^5}{5}-\frac{(y-y')^5}{5}\right)\right) \end{aligned} \tag{5A.15}$$

with $a_1 = -\frac{(1+2\eta)^2}{(1-\eta)^4}$, $a_2 = 6\eta\frac{(1+\eta/2)^2}{(1-\eta)^4}$, $a_3 = \frac{\eta}{2}a_1$, and $\eta = \frac{\pi d^3 n_A}{6}\sum_{j=1}^{3} C_{b_j}$. The short-range correction of the Coulomb term is incorporated in L_1 and L_2, given by

$$\begin{aligned} L_1(y,y') &= d\big(d-(y+y')\big)-B\big(d^2-(y+y')^2\big)+\frac{B^2}{3d}\big(d^3-(y+y')^3\big) \\ L_2(y,y') &= d\big(d-(y-y')\big)-B\big(d^2-(y-y')^2\big)+\frac{B^2}{3d}\big(d^3-(y-y')^3\big) \end{aligned} \tag{5A.16}$$

with $B = \frac{\kappa^2 d^2+\kappa d-\kappa d\sqrt{1+2\kappa d}}{\kappa^2 d^2}$ and $\kappa = \frac{F^2}{\epsilon RT}\sum_{i=1}^{3} z_i^2 C_{b_i}$ is the inverse Debye length. Finally, the function $J(y)$ comprises of the hard sphere component within the exclusion zone, which is given by

$$J(y) = -\sum_{j=1}^{3} n_A C_{b_j}\int_{H-d/2}^{H+d/2}\big(M_1(y,y')+M_2(y,y')\big)dy' \tag{5A.17}$$

5B Table of input parameters

Table 5B.1: Values for the input parameters used in this study for the DFT-MSA and PNM model.

Parameter	Symbol	Value
Gas constant [J/mol/K]	R	8.31
Faraday constant [C/mol]	F	9.65×10^{4}
Boltzman constant [J/K]	k_B	1.38×10^{-23}
Permittivity of water [C^2/J/m]	ϵ	6.95×10^{-10}
Absolute temperature [K]	T	298
Surface charge density [C/m^2]	σ	-0.10
Ion diameter [m]	d	4.25×10^{-10}
Clay particle thickness [m]	δ	1.00×10^{-9}
Minimum pore body radius [m]	R_{min}	1.00×10^{-5}
Mean pore body radius [m]	R_m	1.00×10^{-4}
Maximum pore body radius [m]	R_{max}	3.00×10^{-4}
Standard deviation pore bodies [m]	σ_{pb}	5.33×10^{-5}
Minimum pore throat radius [m]	r_{min}	1.00×10^{-6}
Mean pore throat radius [m]	r_m	2.00×10^{-5}
Maximum pore throat radius [m]	r_{max}	1.00×10^{-4}
Standard deviation pore throats [m]	σ_{pt}	2.62×10^{-5}
Density of water [kg/m^3]	ρ_w	1.00×10^{3}
Gravitational acceleration [m/s^2]	g	9.81
Dynamic viscosity water [Pa s]	μ	1.00×10^{-3}
Interfacial tension (air-water) [N/m]	σ_{aw}	7.25×10^{-2}
Contact angle (air-water) [°]	θ_{aw}	0.00
Volumetric clay fraction [-]	f_c	0.10
Initial macroporosity [-]	ϕ_{macro}	0.46

Chapter 6

Synthesis

6.1 Introduction

Wastewater irrigation is practiced worldwide to alleviate the pressure on freshwater resources. However, the numerous contaminants that may be present in wastewater can threaten the public health and the environment, as these contaminants may accumulate in the soil, crops, or groundwater. Several challenges related to wastewater irrigation have been investigated in this thesis. Due to the large number of contaminants that may be present in wastewater, it is not realistic to treat each contaminant individually in this thesis. Instead, the thesis is split in two general directions (Figure 6.1). The first part of the thesis is spent on general analyses applicable to a large range of contaminants which adsorb and degrade, including many contaminants of emerging concern. In the second part of the thesis, specific attention has been given to the negative impacts of sodium on the soil structure (i.e., soil sodification). In this final chapter, we summarize the main findings of this thesis, place them into context, and discuss their relation to previous studies. Finally, we go over the implications of our results and give recommendations for future research directions.

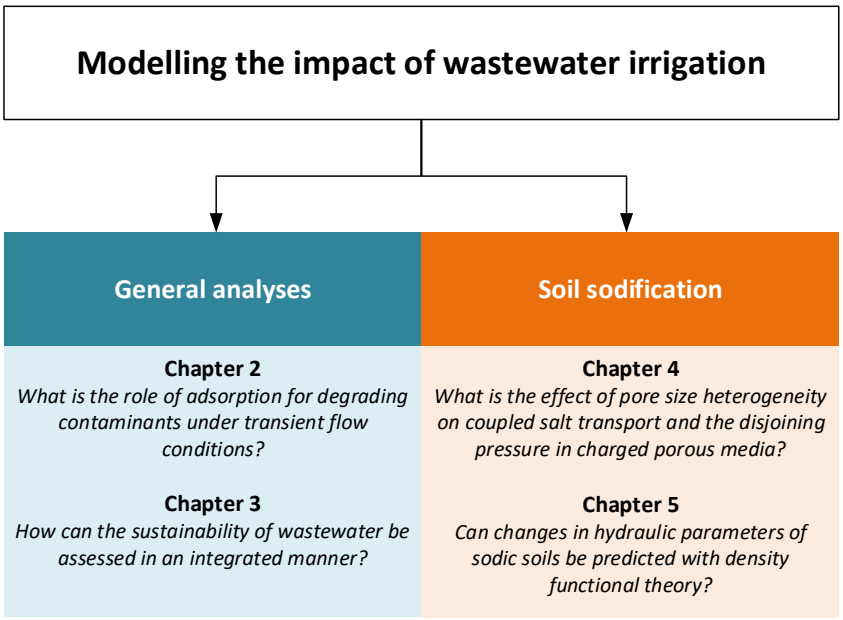

Figure 6.1: This thesis is divided in two main research directions. The first part of the thesis focuses on more general analyses, applicable to many contaminants which adsorb and degrade, which includes many contaminants of emerging concern. The second part of the thesis focuses on the detrimental effect of sodium on the structure of clay soils.

6.2 General discussion

6.2.1 Contaminant adsorption and degradation

Many contaminants of emerging concern, such as pharmaceuticals and personal care products, experience adsorption and degradation to a certain degree. Adsorbed contaminants may or may not be available for degradation (e.g., Ogram et al. (1985); Park et al. (2003)), but this distinction is not always made in experimental studies where the degradation rate is measured. Nevertheless, Beltman et al. (2008) found that these degradation concepts determine the role that adsorption plays on a contaminants fate for single pulse inputs under steady flow conditions.

This was investigated further in Chapter 2 for transient flow conditions, which is more realistic for wastewater irrigation. When contaminants do not degrade in the adsorbed phase, adsorption does not impact the long-term average contaminant concentration in the root zone. Nevertheless, the temporal fluctuations in the contaminant concentration, associated with temporal variations in rainfall and irrigation, are still affected by adsorption. When contaminants do degrade in the adsorbed phase, similar results were obtained in case of linear adsorption. However, adsorption does influence the long-term average contaminant concentration and fluxes in case of nonlinear adsorption. Thus, assuming an incorrect degradation concept for nonlinearly adsorption contaminants leads to erroneous predictions.

There are two major differences between the study of Beltman et al. (2008) and the analysis in Chapter 2. First, we considered multiple contaminant input pulses, while Beltman et al. (2008) considered only a single contaminant input pulse. Second, Beltman et al. (2008) looked only at the effect of the degradation concepts on the contaminant mass leached to the groundwater, while we concerned ourselves with the contaminant concentration in the root zone and the contaminant fluxes between various environmental compartments. Nevertheless, the findings of this thesis agree with the results of Beltman et al. (2008) in the sense that when a contaminant only degrades in the solution phase, adsorption only affects the time when the contaminant concentration plateau is reached, but not the value of the concentration and fluxes.

Furthermore, we investigated when temporal fluctuations of the contaminant concentration and fluxes are negligible compared to their long-term average values. When neglecting these temporal variations in irrigation and rainfall, it is possible to predict the average concentration and fluxes using analytical solutions. For most cases, the results of the analytical model are close to the results of the fluctuating model. The concentration and fluxes can be predicted with errors up to 10%, although this is dependent on the contaminant properties and climate.

The analytical model thus yields a reasonable estimate of the long-term average

contaminant concentration and fluxes under the conditions considered in this thesis. However, when temporal fluctuations are significant (e.g., under strong seasonal climate or for weakly adsorbing contaminants), the concentration at any point in time may strongly deviate from its average value. Quality standards for contaminants in the environment are often defined in two ways, defining either acute health risks for short-term exposure, or long-term risks associated with chronic exposure. The yearly-averaged contaminant concentration is relevant for chronic exposure, which can be estimated reasonably well with the analytical model. However, when there are large temporal concentration fluctuations, the short-term exposure standards may be exceeded. The analytical model can therefore not be used to predict all risks to the public health and the environment.

6.2.2 Sustainability assessment of wastewater irrigation

While regulations for irrigation water quality already exist with respect to several traditional contaminants (WHO, 2006; USEPA, 2012; European Council, 2019), such regulations are still missing for many contaminants of emerging concern and other chemical hazards (Rizzo et al., 2018). To determine regulations and guidelines for these contaminants, a framework is necessary to assess the sustainability of wastewater irrigation. This framework should assess the sustainability in an integrated manner by considering all potential contaminant pathways and environmental compartments, as sustainability should be defined for all environmental compartments simultaneously.

We have developed such a framework in Chapter 3. All environmental compartments are considered in an integrated manner. Previous risk assessments of contaminants of emerging concern were often limited to one or two environmental compartments or contaminant exposure routes (e.g., Weber et al. (2006); Troldborg et al. (2017); Delli Compagni et al. (2020)), while our framework considers all relevant compartments. By comparing existing quality standards with the predicted contaminant concentration and fluxes, a prediction of the sustainability of a wastewater irrigation practice can be made. This framework is built on the results of Chapter 2, and makes use of analytical solutions to predict the long-term contaminant concentration and fluxes. For each contaminant, the outcome of the sustainability assessment is given in a comprehensible manner using two sustainability indices. The first index is the critical sustainability factor, which gives information on which environmental compartment is threatened the most, and how severe the quality standards are exceeded. The second index is the critical sustainability time. If quality standards are exceeded, this index gives information on what timescale these problems are expected to occur.

The framework is based on the assumption that quality standards exist for all the contaminants present in wastewater. If such quality standards are not available, the sustainability assessment cannot be carried out. After all, it is not possible to assess the dangers of a contaminant when its effects on the public health and the environment

are unknown. The long-term health risks are not yet known for many contaminants of emerging concern, and quality standards are often not developed yet for many of these contaminants. In such cases, the framework still proves useful for identifying gaps in knowledge and data, which allows for prioritization of contaminant properties which require further investigation.

6.2.3 Upscaling sodicity effects in soils

Wastewater of either municipal or industrial origin often contains large amounts of sodium. Therefore, wastewater irrigation puts the soil at risk of sodification. Under certain conditions, the micropores in sodic soils may swell at the expense of the macropores (Musso et al., 2013). This change in soil structure hinders plant root growth, water flow, and aeration of the soil (Shainberg and Letey, 1984). Models are required to anticipate soil structure degradation induced by sodicity.

In Chapter 4, we focused on the upscaling salt transport and water flow in charged porous media with heterogeneous pore sizes such as clay. We developed a pore-network model that includes diffuse double layer theory and its effects on salt transport (e.g., electromigration) and water flow (e.g., osmosis). A pore-network model including electrokinetic effects was already developed by Obliger et al. (2014), but their analysis was limited to steady-state situation, while in Chapter 4 we also investigate transient effects (e.g., the timescale on which the salt concentration and fluid pressure change). Salt transport, osmotic water flow, and clay swelling are all driven by the strength of the electric field inside the pores, which is stronger in narrow pores compared to large pores. However, the majority of the salt and water transport takes place in the larger pores, where the electric field is weaker. This reduces the importance of electrokinetic effects on salt and water flow in heterogeneous porous media.

The stronger electric field in narrow pores also leads to a larger disjoining pressure here. On the macroscopic scale, the swelling pressure is defined as the pressure required to prevent a soil sample from swelling. The swelling pressure has also been defined as the volume-averaged disjoining pressure (Derjaguin et al., 1987). However, this definition leads to some problems in heterogeneous media. First, the average pressure is not a well-defined physical concept and is debated in the literature (Nordbotten et al., 2007). Often, the average pressure is obtained using some form of volume-averaging (e.g., Joekar-Niasar and Hassanizadeh (2011)). Contrarily, Gonçalvès et al. (2010) proposed to average over the surface area on which the disjoining pressure acts. We compared both a volume-averaging and a surface-averaging approach for the disjoining pressure, which yielded similar results. Averaging the disjoining pressure in heterogeneous media yields a relatively low swelling pressure, as the average pressure is dominated by the larger pores. This does not have to mean that there is no deformation in the clay sample, as the large disjoining pressure in the small pores may cause local clay swelling.

While the pore-network model is suitable for upscaling flow and transport processes, deformation of the solid phase (i.e., clay swelling) is disregarded in the model. Nevertheless, deformation is a crucial aspect of sodic soils. Other upscaling techniques, such as the homogenization approach (e.g., Moyne and Murad (2002, 2006); Murad and Moyne (2008)) do include soil deformation, but are limited to homogeneous soils. Salt transport, water flow, and deformation are coupled in swelling clays, and can therefore not be considered separately. The results of Chapter 4 are therefore valid for general charged porous media, but may not be applicable to clay without further extensions to the pore-network model.

6.2.4 Impact of sodicity on soil hydraulic properties

In Chapter 5, we focus on the structural degradation of clay soils due to sodicity. Most models for the interaction between clay particles on the microscopic scale use simplifications for the electric field around a clay particle. Often, the Poisson-Boltzmann theory is used within the DLVO framework (Derjaguin and Landau, 1941; Verwey and Overbeek, 1948). The ions size is neglected in this framework (i.e., the ions are assumed to be infinitely small), which may result in unrealistically large predictions for the cation concentrations near clay mineral surfaces. These models are also not able to explain the stable configuration of montmorillonite clay under non-sodic conditions. To overcome these limitations, we made use of density functional theory in combination with the mean sphere approximation (DFT-MSA), which takes the finite size of the ions and the associated ion-ion correlations into account.

Previous studies already pointed out that ion-ion correlation forces are required to explain the stability of calcium-montmorillonite (Kjellander et al., 1988; Rocha et al., 2016). In Chapter 5, we expanded on their work to investigate whether the critical sodium content (expressed as SAR or ESP) at which soil structure degradation occurs can be predicted with this theory. The critical sodium content at which the clay structure breaks down obtained with the DFT-MSA model matches with experimental observations.

Additionally, we translated swelling at the microscopic scale to changes in the macroscopic hydraulic properties, namely the hydraulic conductivity and the soil water retention curve. Using the DFT-MSA model for the microscopic scale, we linked swelling of the micropores to shrinking of the macropores, under the assumption that the total porosity (i.e., the sum of the micro- and macroporosity) remains constant during swelling. The hydraulic properties were computed using pore-network modelling. Naturally, the shrinking of macropores leads to a significant reduction in the hydraulic conductivity, and an increase in the air-entry pressure. These predicted changes in soil hydraulic properties were also in reasonable agreement with experimental results.

The analysis in this chapter was limited by a simple upscaling model to translate swelling of micropores to shrinking of macropores. The assumptions in this model lead to a

constant shape for the pore size distribution (i.e., the pore size distribution shifts to smaller values due to shrinking, but its shape is not altered). This leads to artificial effects, such as that the shape factor of the water retention curve and the relative permeability curve are unaffected by clay swelling. This can be improved by including a more realistic soil mechanical model.

6.3 Implications

6.3.1 Predicting contaminant fate in the environment

In Chapter 2, we showed that the degradation concept plays an important for the contaminant fate for nonlinearly adsorbing contaminants. When making predictions for the fate of contaminants in the environment, a choice must be made whether or not contaminants are available for degradation in the adsorbed phase. When this degradation concept is incorrectly chosen, the contaminant concentrations and fluxes may be under- or overestimated. This is important for environmental risk assessment studies, as erroneous predictions may lead to harmful situation being falsely predicted as safe.

Thus, this has implications for scientists that are concerned with measuring the environmental behaviour of contaminants. Currently, studies which measured the degradation rate do not always report whether degradation takes place in the solution phase, the adsorption phase, or both. Nevertheless, this information is crucial for contaminant transport models which are required to make predictions on the environmental fate of contaminants. Therefore, it is important to know whether or not a contaminant degrades in the adsorbed phase. When this is the case, it is also important to measure the adsorption parameters together with the degradation rate. Additionally, for nonlinearly adsorbing contaminants that degrade, the contaminant concentration at which the degradation experiment was carried out should be reported, as the contaminant concentration influences the strength of adsorption under nonlinear sorption.

The result that the simplified model often yields reasonable estimates of the long-term contaminant concentration and the fluxes is of practical value. This simplified model uses analytical solutions and thus does not make use of complex numerical models. The analytical models also require relatively few input parameters. Therefore, this model is practical to use to obtain a quick estimate of the long-term behaviour of contaminants in the environment. These analytical models can therefore be used to carry out a preliminary sustainability assessment to prioritize which contaminants or parameters need further investigation. Of course, more complex models are still valuable for more detailed analyses.

The framework developed in Chapter 3 can serve as a tool to aid in the development of regulations for irrigation water quality. These regulations are still missing for many

contaminants, including contaminants of emerging concern. The framework may be used to assess whether environmental quality standards are likely to be exceeded, based on case-specific variables such as irrigation water quality, climate, irrigation management, and soil type. When environmental quality standards are missing, the framework may instead highlight missing information. In this case, the framework cannot give a definite answer to the question whether irrigation with wastewater is sustainable, but does aid in prioritizing further data collection. Since the framework in Chapter 3 makes use of the aforementioned analytical model, only the long-term average situation is considered, while temporal fluctuations are neglected. The sustainability assessment should therefore be seen as a first assessment, which can aid in prioritizing further, more detailed, investigations.

6.3.2 Anticipating soil sodification

The pore-network model presented in Chapter 4 is a tool for upscaling water flow and salt transport in charged porous media such as clay. The motivation to develop this model stems from the fact that previous upscaling methods often assume a degree of homogeneity for the pore sizes on the microscopic scale (e.g., Tuller and Or (2003); Murad and Moyne (2008)). Heterogeneity is an important characteristic of soils, and in Chapter 4 we showed the importance of heterogeneous pore sizes on the timescale at which salt transport and water flow occur in charged porous media. Therefore, it is critical to include pore size heterogeneity when upscaling electrokinetic transport processes. However, the pore-network model is only the first step in upscaling electrokinetic transport processes in soils. While the pore-network model approach is promising, further extensions are required before the model is applicable to clay soils.

The results of Chapter 5 are important for modelling soil structure damage due to sodicity. We showed that the stability and breakdown of sodic soils is modelled well with DFT-MSA theory, while this is not the case for Poisson-Boltzmann theory. The reason behind this is that ion-ion correlations play an important role for the stability of non-sodic soils. Therefore, theories which include ion-ion correlation such as DFT-MSA are required to accurately model soil structure damage due to sodicity. However, including ion-ion correlation results in a much larger numerical complexity, which is why ion-ion correlation is often still neglected in clay particle interaction models. The Poisson-Boltzmann model is easier to solve numerically, and in many cases even analytical approximations exist. To encourage the use of ion-ion correlation in clay particle interaction models, we have published the code to solve the DFT-MSA equations. This makes the DFT-MSA framework more accessible for researchers to incorporate the DFT-MSA framework in their own work.

6.4 Challenges and recommendations

There are still many questions related to contaminant transport in context of wastewater irrigation which need to be answered. In order to make predictions about the fate of contaminants in the environment, we require adequate knowledge of the behaviour of all contaminants that may be present in wastewater, in addition to all (eco)toxicological effects. Especially for contaminants of emerging concern, the risks of chronic exposure are not yet known. Since these contaminants have started being observed in the environment relatively recently, the threat they pose to the public health and the environment is uncertain. In many cases, no environmental quality standards have yet been proposed for these contaminants. Thus, further experimental research on these contaminants is urgently required to determine their toxicity to humans and other organisms, and their behaviour in the environment.

Within this thesis, we presented a framework to assess the sustainability of wastewater irrigation on the farm-level. However, contaminants may travel significant distances from the irrigated fields through the ground- or surface water, especially when considering large timescales. This may be a problem when contaminants reach areas where stricter quality standards are required, for example near drinking water production wells or nature reserves. Thus, the sustainability of wastewater irrigation should also be investigated on the regional scale, for example with regional hydrological models.

There are also many challenges remaining in the field of soil sodicity. The pore-network model developed in Chapter 4 can be extended further such that it is applicable to a broader range of boundary conditions. The pore-network model made use of the linearized Poisson-Boltzmann equation, which limits its applicability to low electric potentials only (e.g., low surface charge density and/or high salinity conditions). Therefore, either the nonlinear Poisson-Boltzmann equation or DFT-MSA model should be solved instead to determine the electric field and ion distribution within the pores. The DFT-MSA model should definitely be used in the narrow intra-tactoid pores, as our results indicated that Poisson-Boltzmann theory is not sufficient to describe the physics there. In the larger inter-tactoid pores, ion-ion correlations are not as significant, and nonlinear Poisson-Boltzmann theory may be sufficient. However, no analytical solutions are available for the nonlinear Poisson-Boltzmann equation and the DFT-MSA model. Solving these equations numerically for each pore significantly increases the computational demand, and thus nullify a major advantage of pore-network models. A possible alternative is to use lookup table instead, which would sacrifice some accuracy to gain computation speed.

More importantly, it is necessary to include deformation of the pore-network in response to swelling and shrinking of the pores due to varying salt concentration and composition. While the pore-network model presented in Chapter 4 can calculate the evolution of

the fluid pressure and disjoining pressure, its effect on the soil structure was not included. When considering soil structure degradation due to sodicity, deformation of the pore-network is a vital step which is still missing. Adding soil deformation to the pore-network model is not an easy task, as these models were developed under the assumption of a rigid solid phase. Nevertheless, behind soil sodicity lies a complex coupled system, where the salt transport, water flow, the electric field, and soil deformation are all coupled (Figure 6.2). These processes therefore cannot be considered separately. The model presented in Chapter 5 did include soil deformation, but this process was included in a simplified manner. Additionally, this model was limited to equilibrium conditions, despite that transient pressure changes may also lead to soil deformation. Thus, the sodicity models presented in this thesis can be extended by including more advanced soil mechanical models.

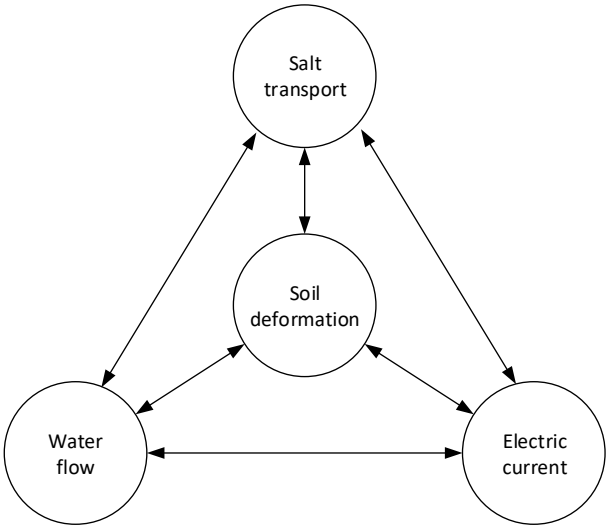

Figure 6.2: Behind clay soils lies a complex coupled system, as salt transport, water flow, the electric field all impact soil mechanics, and vice versa. For example, water flow affects salt transport through advection and the electric field through the streaming potential, and the electric field affects salt transport by electromigration and water flow by electro-osmosis. The bulk fluid pressure (water flow) and disjoining pressure (salt concentration and electric field) impact soil deformation. The resulting changes in porosity and permeability affect the transport rates of salt, water, and electric charge.

A potential solution is to follow a hybrid-model approach. For example, Sweijen et al. (2016) combined a discrete element method for the soil mechanical part with a pore-network model for calculating water flow. The discrete element method is used for modelling granular materials such as soils on the particle-scale. This method has also been applied to clays (e.g., Pagano et al. (2020)), but not in the context of soil sodicity. For this purpose, the disjoining pressure must be included in the discrete element model. However, this also poses a computational challenge. In Chapter 5, the soil structure was

simplified by assuming that all clay particles lay in parallel orientation. This drastically simplifies the mathematical problem to calculate the ion distribution, electric potential, and disjoining pressure between the clay platelets. In reality, there is more randomness in the orientation of clay particles. This is a challenge especially when using advanced theory such as DFT-MSA, as solving these equations in randomly oriented particle packings poses a significant computational challenge. Nevertheless, these advanced theories are crucial for the interaction between clay particles.

An additional difficulty is the large difference in scales at which the processes occur. The processes governing clay swelling occur on the scale of several nanometres, while the soil hydraulic properties are governed by larger pores on the scale of 1-100 micrometres. Therefore, at least two models are likely to be required: one model for the swelling of clay on the microscopic scale, and a second model for calculating the effect on the soil hydraulic properties. These models need to be linked through adequate upscaling techniques.

6.5 Concluding remarks

Whether wastewater irrigation is sustainable may change over time. Many factors that affect the sustainability of wastewater irrigation may change in the future. For example, climate change may increase irrigation demands, pollution may further decrease the quality of wastewater, while on the other hand wastewater treatment technologies may improve. The uncertainties surrounding the harmful effects of chronic exposure to many contaminants of emerging concern may also play a role. Therefore, it is important to keep evaluating whether wastewater irrigation practices are sustainable. All these predictions of sustainability are based on models, which are a simplification of reality. In practice, the accumulation of contaminants in the environment should be continuously monitored to ensure that no harm is done to the public health and environment.

This thesis was limited to the risks that wastewater irrigation poses to the public health and the environment. However, these risks are not the only challenges that may prevent the successful implementation of wastewater irrigation. Other aspects should also be considered, such as the presence of adequate infrastructure for wastewater transport, or the issue of social acceptance, as people might not be willing to consume produce which has been irrigated with wastewater, despite it being deemed safe by scientists and authorities. The successful implementation of wastewater irrigation thus poses a challenge for multiple scientific disciplines.

References

Acharya, R. C., van der Zee, S. E. A. T. M., and Leijnse, A. (2005). Transport modeling of nonlinearly adsorbing solutes in physically heterogeneous pore networks. *Water Resources Research*, *41*, W02020. doi: https://doi.org/10.1029/2004wr003500.

Al-Nakshabandi, G. A., Saqqar, M. M., Shatanawi, M. R., Fayyad, M., and Al-Horani, H. (1997). Some environmental problems associated with the use of treated wastewater for irrigation in Jordan. *Agricultural Water Management*, *34*, 81 – 94. doi: https://doi.org/10.1016/S0378-3774(96)01287-5.

Ali, A. M., Shafiee, M. E., and Berglund, E. Z. (2017). Agent-based modeling to simulate the dynamics of urban water supply: Climate, population growth, and water shortages. *Sustainable Cities and Society*, *28*, 420 – 434. doi: https://doi.org/10.1016/j.scs.2016.10.001.

Allen, R. G., Pereira, L. S., Raes, D., and Smith, M. (1998). Crop evapotranspiration – Guidelines for computing crop water requirements. *FAO Irrigation and Drainage Paper*, *56*.

An, S., Erfani, H., Godinez-Brizuela, O. E., and Niasar, V. (2020a). Transition from viscous fingering to capillary fingering: Application of GPU-based fully implicit dynamic pore network modeling. *Water Resources Research*, *56*, e2020WR028149. doi: https://doi.org/10.1029/2020WR028149.

An, S., Hasan, S., Erfani, H., Babaei, M., and Niasar, V. (2020b). Unravelling effects of the pore-size correlation length on the two-phase flow and solute transport properties: GPU-based pore-network modeling. *Water Resources Research*, *56*, e2020WR027403. doi: https://doi.org/10.1029/2020WR027403.

Babaei, M., and Joekar-Niasar, V. (2016). A transport phase diagram for pore-level correlated porous media. *Advances in Water Resources*, *92*, 23–29. doi: https://doi.org/10.1016/j.advwatres.2016.03.014.

Bahri, A. (1998). Wastewater reclamation and reuse in Tunisia. In T. Asano (Ed.), *Wastewater reclamation and reuse* (pp. 877–916). CRC Press.

Barber, L. B., Keefe, S. H., Brown, G. K., Furlong, E. T., Gray, J. L., Kolpin, D. W., Meyer, M. T., Sandstrom, M. W., and Zaugg, S. D. (2013).

Persistence and potential effects of complex organic contaminant mixtures in wastewater-impacted streams. *Environmental Science & Technology*, *47*, 2177–2188. doi: https://doi.org/10.1021/es303720g.

Barbour, S. L., and Fredlund, D. G. (1989). Mechanisms of osmotic flow and volume change in clay soils. *Canadian Geotechnical Journal*, *26*, 551–562. doi: https://doi.org/10.1139/t89-068.

Barbour, S. L., Fredlund, D. G., and Pufahl, D. E. (1992). The Osmotic Role in the behavior of Swelling Clay Soils. In *Mechanics of Swelling* (pp. 97–139). Springer Berlin Heidelberg. doi: https://doi.org/10.1007/978-3-642-84619-9_5.

Beltman, W. H. J., Boesten, J. J. T. I., and van der Zee, S. E. A. T. M. (2008). Spatial moment analysis of transport of nonlinearly adsorbing pesticides using analytical approximations. *Water Resources Research*, *44*. doi: https://doi.org/10.1029/2007wr006436.

Bixio, D., Thoeye, C., de Koning, J., Joksimovic, D., Savic, D., Wintgens, T., and Melin, T. (2006). Wastewater reuse in Europe. *Desalination*, *187*, 89–101. doi: https://doi.org/10.1016/j.desal.2005.04.070.

Boekhold, A. E., and van der Zee, S. E. A. T. M. (1991). Long-term effects of soil heterogeneity on cadmium behaviour in soil. *Journal of Contaminant Hydrology*, *7*, 371–390. doi: https://doi.org/10.1016/0169-7722(91)90003-J.

Boivin, A., Cherrier, R., and Schiavon, M. (2005). A comparison of five pesticides adsorption and desorption processes in thirteen contrasting field soils. *Chemosphere*, *61*, 668 – 676. doi: https://doi.org/10.1016/j.chemosphere.2005.03.024.

Bolt, G. H. (1955). Ion adsorption by clays. *Soil Science*, *79*, 267–276. doi: https://doi.org/10.1097/00010694-195504000-00004.

Bolt, G. H. (1982). The ionic distribution in the diffuse double layer. In G. Bolt (Ed.), *Soil Chemistry B. Physico-Chemical Models* chapter 1. (p. 1–25). Elsevier volume 5 of *Developments in Soil Science*. doi: https://doi.org/10.1016/S0166-2481(08)70656-1.

BOM (2019). Climate data online. Bureau of Meteorology, Government of Australia. Available online: http://www.bom.gov.au/climate/data/. Last accessed: 22-05-2019.

Botter, G., Daly, E., Porporato, A., Rodriguez-Iturbe, I., and Rinaldo, A. (2008). Probabilistic dynamics of soil nitrate: coupling of ecohydrological and biogeochemical processes. *Journal of Colloid and Interface Science*, *44*. doi: https://doi.org/10.1029/2007wr006108.

Bouwer, H., and Idelovitch, E. (1987). Quality requirements for irrigation with sewage water. *Journal of Irrigation and Drainage Engineering*, *113*, 516–535. doi: https://doi.org/10.1061/(ASCE)0733-9437(1987)113:4(516).

Bradl, H. B. (2004). Adsorption of heavy metal ions on soils and soil

constituents. *Journal of Colloid and Interface Science*, *277*, 1–18. doi: https://doi.org/10.1016/j.jcis.2004.04.005.

Bresler, E., McNeal, B. L., and Carter, D. L. (1982). *Saline and Sodic Soils: Principles-Dynamics-Modeling*. Berlin Heidelberg: Springer-Verlag. doi: https://doi.org/10.1007/978-3-642-68324-4.

Briggs, G. G., Bromilow, R. H., and Evans, A. A. (1982). Relationships between lipophilicity and root uptake and translocation of non-ionised chemicals by barley. *Pesticide Science*, *13*, 495–504. doi: https://doi.org/10.1002/ps.2780130506.

Candela, L., Fabregat, S., Josa, A., Suriol, J., Vigués, N., and Mas, J. (2007). Assessment of soil and groundwater impacts by treated urban wastewater reuse. A case study: Application in a golf course (Girona, Spain). *Science of the Total Environment*, *374*, 26 – 35. doi: https://doi.org/10.1016/j.scitotenv.2006.12.028.

Carmo, A. M., Hundal, L. S., and Thompson, M. L. (2000). Sorption of Hydrophobic Organic Compounds by Soil Materials: Application of Unit Equivalent Freundlich Coefficients. *Environmental Science & Technology*, *34*, 4363–4369. doi: https://doi.org/10.1021/es000968v.

Chen, C., Li, J., Chen, P., Ding, R., Zhang, P., and Li, X. (2014). Occurrence of antibiotics and antibiotic resistances in soils from wastewater irrigation areas in Beijing and Tianjin, China. *Environmental Pollution*, *193*, 94 – 101. doi: https://doi.org/10.1016/j.envpol.2014.06.005.

Chiou, C. T., Sheng, G., and Manes, M. (2001). A Partition-Limited Model for the Plant Uptake of Organic Contaminants from Soil and Water. *Environmental Science & Technology*, *35*, 1437–1444. doi: https://doi.org/10.1021/es0017561.

Cirkel, D. G., van der Zee, S. E. A. T. M., and Meeussen, J. C. L. (2015). Front spreading with nonlinear sorption for oscillating flow. *Water Resources Research*, *51*, 2986–2993. doi: https://doi.org/10.1002/2014WR015847.

Cornelissen, P., Leijnse, A., Joekar-Niasar, V., and van der Zee, S. E. A. T. M. (2019). Pressure development in charged porous media with heterogeneous pore sizes. *Advances in Water Resources*, *128*, 193–205. doi: https://doi.org/10.1016/j.advwatres.2019.05.001.

Cornelissen, P., van der Zee, S. E. A. T. M., and Leijnse, A. (2020). Role of degradation concepts for adsorbing contaminants in context of wastewater irrigation. *Vadose Zone Journal*, *19*, e20064. doi: https://doi.org/10.1002/vzj2.20064.

Debicka, M., Kocowicz, A., Weber, J., and Jamroz, E. (2016). Organic matter effects on phosphorus sorption in sandy soils. *Archives of Agronomy and Soil Science*, *62*, 840–855. doi: https://doi.org/10.1080/03650340.2015.1083981.

Delgado, A., Gonzalez-Caballero, F., and Bruque, J. M. (1986). On the zeta

potential and surface charge density of montmorillonite in aqueous electrolyte solutions. *Journal of Colloid and Interface Science*, *113*, 203–211. doi: https://doi.org/10.1016/0021-9797(86)90220-1.

Delli Compagni, R., Gabrielli, M., Polesel, F., Turolla, A., Trapp, S., Vezzaro, L., and Antonelli, M. (2020). Risk assessment of contaminants of emerging concern in the context of wastewater reuse for irrigation: an integrated modelling approach. *Chemosphere*, *242*, 125185. doi: https://doi.org/10.1016/j.chemosphere.2019.125185.

Derjaguin, B., and Landau, L. (1941). Theory of the stability of strongly charged lyophobic sols and of the adhesion of strongly charged particles in solutions of electrolytes. *Acta Physico Chimica UR*, *14*, 633–662.

Derjaguin, B. V., Churaev, N. V., Muller, V. M., and Kitchener, J. A. (1987). *Surface Forces*. Boston, Massachusetts, United States of America: Springer. doi: https://doi.org/10.1007/978-1-4757-6639-4.

Dietz, A. C., and Schnoor, J. L. (2001). Advances in phytoremediation. *Environmental Health Perspectives*, *109*, 163–168. doi: https://doi.org/10.1289/ehp.01109s1163.

Drillia, P., Stamatelatou, K., and Lyberatos, G. (2005). Fate and mobility of pharmaceuticals in solid matrices. *Chemosphere*, *60*, 1034–1044. doi: https://doi.org/10.1016/j.chemosphere.2005.01.032.

Dubus, I. G., Brown, C. D., and Beulke, S. (2003). Sensitivity analyses for four pesticide leaching models. *Pest Management Science*, *59*, 962–982. doi: https://doi.org/10.1002/ps.723.

Eagleson, P. S. (1978). Climate, soil and vegetation: 3. A simplified model of soil moisture movemennt in the liquid phase. *Water Resources Research*, *14*, 722–730. doi: https://doi.org/10.1029/WR014i005p00722.

Ebeling, D., van den Ende, D., and Mugele, F. (2011). Electrostatic interaction forces in aqueous salt solutions of variable concentration and valency. *Nanotechnology*, *22*, 305706. doi: https://doi.org/10.1088/0957-4484/22/30/305706.

European Commission (2011). Proposal for a Directive of the European Parliament and of the Council amending Directives 2000/60/EC and 2008/105/EC as regards priority substances in the field of water policy. Available online: https://op.europa.eu/en/publication-detail/-/publication/859825c3-d7c7-424b-96dd-84eb700ef0bf.

European Commission (2015). *Technical Guidance Document on Risk Assessment, Part II*. Technical Report EUR 20418 EN/2, European Commission, Joint Research Centre.

European Council (2005). On maximum residue levels of pesticides in or on food and feed of plant and animal origin and amending Council Directive 91/414/EEC. Available online:

https://eur-lex.europa.eu/legal-content/EN/ALL/?uri=CELEX%3A32005R0396.

European Council (2006). Regulation (EC) No 1907/2006 of the European Parliament and of the Council. Available online: https://eur-lex.europa.eu/legal-content/EN/TXT/?uri=CELEX%3A02006R1907-20140410.

European Council (2019). Regulation of the European Parliament and of the Council on minimum requirements for water reuse. Available online: https://www.consilium.europa.eu/en/press/press-releases/2020/04/07/water-reuse-for-agricultural-irrigation-council-adopts-new-rules/.

Ezlit, Y. D. (2009). *Modelling the change in conductivity of soil associated with the application of saline-sodic water*. Ph.D. thesis University of Southern Queensland Toowoomba, Queensland, Australia.

Famiglietti, J. S. (2014). The global groundwater crisis. *Nature Climate Change*, *4*, 945–948. doi: https://doi.org/10.1038/nclimate2425.

FAO (2010). AQUASTAT Database. Food and Agriculture Organization of the United Nations. Available online: www.fao.org/nr/water/aquastat/data/query/index.html?lang=en. Last accessed: 24-08-2021.

Farahat, E., and Linderholm, H. W. (2015). The effect of long-term wastewater irrigation on accumulation and transfer of heavy metals in Cupressus sempervirens leaves and adjacent soils. *Science of the Total Environment*, *512-513*, 1 – 7. doi: https://doi.org/10.1016/j.scitotenv.2015.01.032.

Fatt, I. (1956). *The Network Model of Porous Media*. Technical Report SPE-574-G, Society of Petroleum Engineers.

Feigin, A., Ravina, I., and J., S. (1978). Effect of irrigation with treated sewage effluent on soil, plant and environment. *Water Resources Research*, *14*, 722–730. doi: https://doi.org/10.1029/WR014i005p00722.

Frenkel, H., Goertzen, J. O., and Rhoades, J. D. (1978). Effects of clay type and content, exchangeable sodium percentage, and electrolyte concentration on clay dispersion and hydraulic conductivity. *Soil Science Society of America Journal*, *42*, 32–39. doi: https://doi.org/10.2136/sssaj1978.03615995004200010008x.

Gallegos, E., Warren, A., Robles, E., Campoy, E., Calderon, A., Sainz, M. G., Bonilla, P., and Escolero, O. (1999). The effects of wastewater irrigation on groundwater quality in Mexico. *Water Science and Technology*, *40*, 45–52. doi: https://doi.org/10.1016/S0273-1223(99)00429-1.

Geissen, V., Mol, H., Klumpp, E., Umlauf, G., Nadal, M., van der Ploeg, M., van der Zee, S. E. A. T. M., and Ritsema, C. J. (2015). Emerging pollutants in the environment: a

challenge for water resource management. *International Soil and Water Conservation Research*, *3*, 57–65. doi: https://doi.org/10.1016/j.iswcr.2015.03.002.

Gonçalvès, J., Rousseau-Gueutin, P., de Marsily, G., Cosenza, P., and Violette, S. C. W. (2010). What is the significance of pore pressure in a saturated shale layer? *Water Resources Research*, *46*, W04514. doi: https://doi.org/10.1029/2009wr008090.

Guo, L., Jury, W. A., Wagenet, R. J., and Flury, M. (2000). Dependence of pesticide degradation on sorption: nonequilibrium model and application to soil reactors. *Journal of Contaminant Hydrology*, *43*, 45–62. doi: https://doi.org/10.1016/S0169-7722(99)00097-2.

Hamilton, A. J., Boland, A. M., Stevens, D., Kelly, J., Radcliffe, J., Ziehrl, A., Dillon, P., and Paulin, B. (2005). Position of the Australian horticultural industry with respect to the use of reclaimed water. *Agricultural Water Management*, *71*, 181–209. doi: https://doi.org/10.1016/j.agwat.2004.11.001.

Hamilton, A. J., Stagnitti, F., Xiong, X., Kreidl, S. L., Benke, K. K., and Maher, P. (2007). Wastewater Irrigation: The State of Play. *Vadose Zone Journal*, *6*, 823–840. doi: https://doi.org/10.2136/vzj2007.0026.

Horseman, S. T., Harrington, J. F., and Noy, D. J. (2007). Swelling and osmotic flow in a potential host rock. *Physics and Chemistry of the Earth, Parts A/B/C*, *32*, 408–420. doi: https://doi.org/10.1016/j.pce.2006.05.003.

Hussain, A. A., Abashar, E. E., and Al-Mutaz, I. S. (2006). Effect of ion sizes on separation characteristics of nanofiltration membrane systems. *Journal of King Saud University - Engineering Sciences*, *19*, 1–18. doi: https://doi.org/10.1016/S1018-3639(18)30844-4.

Intel (2018). Developer Reference for Intel Math Kernel Library. Available online: https://software.intel.com/en-us/mkl-developer-reference-fortran.

Ioannidis, M. A., and Chatzis, I. (2000). On the geometry and topology of 3D stochastic porous media. *Journal of Colloid and Interface Science*, *229*, 323–334. doi: https://doi.org/10.1006/jcis.2000.7055.

Israelachvili, F. (1991). *Intermolecular and Surface Forces*. (2nd ed.). New York, New York, United States of America: Academic Press.

Jalali, M., Merikhpour, H., Kaledhonkar, M., and van der Zee, S. E. A. T. M. (2008). Effects of wastewater irrigation on soil sodicity and nutrient leaching in calcareous soils. *Agricultural Water Management*, *95*, 143 – 153. doi: https://doi.org/10.1016/j.agwat.2007.09.010.

Jaramillo, M. F., and Restrepo, I. (2017). Wastewater reuse in agriculture: a review about its limitations and benefits. *Sustainability*, *9*, 1734. doi: https://doi.org/10.3390/su9101734.

Jjemba, P. K. (2002). The effect of chloroquine, quinacrine, and metronidazole on

both soybean plants and soil microbiota. *Chemosphere*, *46*, 1019 – 1025. doi: https://doi.org/10.1016/S0045-6535(01)00139-4.

Joekar-Niasar, V., and Hassanizadeh, S. M. (2011). Specific interfacial area: The missing state variable in two-phase flow equations? *Water Resources Research*, *47*. doi: https://doi.org/10.1029/2010WR009291.

Joekar-Niasar, V., Hassanizadeh, S. M., and Dahle, H. K. (2010a). Non-equilibrium effects in capillarity and interfacial area in two-phase flow: dynamic pore-network modelling. *Journal of Fluid Mechanics*, *655*, 38–71. doi: https://doi.org/10.1017/s0022112010000704.

Joekar-Niasar, V., Hassanizadeh, S. M., and Dahle, H. K. (2010b). Non-equilibrium effects in capillarity and interfacial area in two-phase flow: dynamic pore-network modelling. *Journal of Fluid Mechanics*, *655*, 38–71. doi: https://doi.org/10.1017/s0022112010000704.

Joekar-Niasar, V., Hassanizadeh, S. M., and Leijnse, A. (2008). Insights into the relationships among capillary pressure, saturation, interfacial area and relative permeability using pore-network modeling. *Transport in Porous Media*, *74*, 201–219. doi: https://doi.org/10.1007/s11242-007-9191-7.

Joekar-Niasar, V., and Mahani, H. (2016). Nonmonotonic pressure field induced by ionic diffusion in charged thin films. *Industrial & Engineering Research*, *55*, 6227–6235. doi: https://doi.org/10.102/acs.iecr.6b00842.

Joekar-Niasar, V., Schotting, R., and Leijnse, A. (2013). Analytical solution of electrohydrodynamic flow and transport in rectangular channels: inclusion of double layer effects. *Computational Geosciences*, *17*, 497–513. doi: https://doi.org/10.1007/s10596-012-9337-8.

Jury, W. A., Russo, D., Streile, G., and El Abd, H. (1990). Evaluation of volatilization by organic chemicals residing below the soil surface. *Water Resources Research*, *26*, 13–20. doi: https://doi.org/10.1029/WR026i001p00013.

Kim, S., Chen, J., Cheng, T., Gindulyte, A., He, J., He, S., Li, B. A., Q.and Shoemaker, Thiessen, P. A., Yu, B., Zaslavsky, L., Zhang, J., and Bolton, E. E. (2019). PubChem 2019 update: improved access to chemical data. *Nucleic Acids Research*, *47*, D1102–D1109.

Kim, S., Chu, K. H., Al-Hamadani, Y. A., Park, C. M., Jang, M., Kim, D.-H., Yu, M., Heo, J., and Yoon, Y. (2018). Removal of contaminants of emerging concern by membranes in water and wastewater: A review. *Chemical Engineering Journal*, *335*, 896 – 914. doi: https://doi.org/10.1016/j.cej.2017.11.044.

Kiriukhin, M. Y., and Collins, K. D. (2002). Dynamic hydration numbers for biologically important ions. *Biophysical Chemistry*, *99*, 155–168. doi: https://doi.org/10.1016/S0301-4622(02)00153-9.

Kjellander, R., Marcelja, S., and Quirk, J. P. (1988). Attractive double-layer interactions between calcium clay particles. *Journal of Colloid and Interface Science*, *126*, 194–211. doi: https://doi.org/10.1016/0021-9797(88)90113-0.

KNMI (2019). Dagwaarden neerslagstations. Royal Netherlands Meteorological Institute. Available online: https://www.knmi.nl/nederland-nu/klimatologie/monv/reeksen. Last accessed: 22-05-2019.

KNMI (2020). Overzicht van de neerslag en verdamping in Nederland. Royal Dutch Meteorological Institute. Available online: https://www.knmi.nl/nederland-nu/klimatologie/gegevens/monv.

Kodešová, R., Kočárek, M., Klement, A., Golovko, O., Koba, O., Fér, M., Nikodem, A., Vondráčková, L., Jakšík, O., and Grabic, R. (2016). An analysis of the dissipation of pharmaceuticals under thirteen different soil conditions. *Science of the Total Environment*, *544*, 369 – 381. doi: https://doi.org/10.1016/j.scitotenv.2015.11.085.

Kodešová, R., Grabic, R., Kočárek, M., Klement, A., Golovko, O., Fér, M., Nikodem, A., and Jakšík, O. (2015). Pharmaceuticals' sorptions relative to properties of thirteen different soils. *Science of the Total Environment*, *511*, 435 – 443. doi: https://doi.org/10.1016/j.scitotenv.2014.12.088.

Kuila, U., and Prasad, M. (2013). Specific surface area and pore-size distribution in clays and shales. *Geophysical Prospecting*, *61*, 341–362. doi: https://doi.org/10.1111/1365-2478.12028.

Kuntz, D., and Grathwohl, P. (2009). Comparison of steady-state and transient flow conditions on reactive transport of contaminants in the vadose soil zone. *Journal of Hydrology*, *396*, 225–233. doi: https://doi.org/10.1016/j.jhydrol.2009.02.006.

Kwaad, F. J. P. M. (1991). Summer and winter regimes of runoff generation and soil erosion on cultivated loess soils (The Netherlands). *Earth Surface Processes and Landforms*, *16*, 653–662. doi: https://doi.org/10.1002/esp.3290160709.

Laio, F., Porporato, A., Ridolfi, L., and Rodriguez-Iturbe, I. (2001). Plants in water-controlled ecosystems: active role in hydrologic processes and respone to water stress: II. Probabilistic soil moisture dynamics. *Advances in Water Resources*, *24*, 707–723. doi: https://doi.org/10.1016/S0309-1708(01)00005-7.

Lammoglia, S.-K., Brun, F., Quemar, T., Moeys, J., Barriuso, E., Gabrielle, B., and Mamy, L. (2018). Modelling pesticides leaching in cropping systems: Effect of uncertainties in climate, agricultural practices, soil and pesticide properties. *Environmental Modelling & Software*, *109*, 342 – 352. doi: https://doi.org/10.1016/j.envsoft.2018.08.007.

Lapworth, D., Baran, N., Stuart, M., and Ward, R. (2012). Emerging organic contaminants in groundwater: A review of sources, fate and occurrence. *Environmental Pollution*, *163*, 287 – 303. doi: https://doi.org/10.1016/j.envpol.2011.12.034.

Lapworth, D. J., Lopez, B., Laabs, V., Kozel, R., Wolter, R., Ward, R., Amelin, E. V., Besien, T., Claessens, J., Delloy, F., Ferretti, E., and Grath, J. (2019). Developing a groundwater watch list for substances of emerging concern. *Environmental Research Letters*, *14*, 035004. doi: https://doi.org/10.1088/1748-9326/aaf4d7.

Lawhon, P., and Schwartz, M. (2001). Linking environmental and economic sustainability in establishing standards for wastewater re-use in Israel. *Water Science & Technology*, *53*, 203–212. doi: https://doi.org/10.2166/wst.2006.262.

Le, T. D. (2013). *Mécanique et transport dans les milieux poreux déformables: prise en compte des corrélations ion-ion et application aux argiles smectiques*. Ph.D. thesis Université de Lorraine Nancy, France. In French.

Le, T. D., Moyne, C., and Murad, M. A. (2015). A three-scale model for ionic solute transport in swelling clays incorporating ion-ion correlation effects. *Advances in Water Resources*, *75*, 31–52. doi: https://doi.org/10.1016/j.advwatres.2014.10.005.

Le, T. D., Rocha, A. C., Murad, M. A., Moyne, C., and Oliveira, S. P. (2016). Multiscale contaminant transport in swelling clays incorporating ion-ion correlation effects. In J. H. Cushman, and D. M. Tartakovsky (Eds.), *Handbook of Groundwater Engineering* chapter 14. CRC Press, Taylor & Francis Group. (3rd ed.). doi: https://doi.org/10.1201/9781315371801.

Lebron, I., Suarez, D. L., and Yoshida, T. (2002). Gypsum effect on the aggregate size and geometry of three sodic soils under reclamation. *Soil Science Society of America Journal*, *66*, 92–98. doi: https://doi.org/10.2136/sssaj2002.9200.

Lee, S. Z., Allen, H. E., P., H. C., Sparks, D. L., Sanders, P. F., and Peijnenburg, W. J. G. M. (1996). Predicting soil-water partition coefficients for cadmium. *Environmental Science & Technology*, *30*, 3418–3424. doi: https://doi.org/10.1021/es9507933.

Lee, S. Z., L., C., Yang, H. H., M., C. C., and C., L. M. (1998). Adsorption characteristics of lead onto soils. *Journal of Hazardous Materials*, *63*, 37–49. doi: https://doi.org/10.1016/S0304-3894(98)00203-9.

Lehikoinen, J. (1999). *Ion diffusion in compacted bentonite*. Posiva Report.

Lemaire, T., Moyne, C., and Stemmelen, D. (2007). Modelling of electro-osmosis in clayey materials including pH effects. *Physics and Chemistry of the Earth, Parts A/B/C*, *32*, 441–452. doi: https://doi.org/10.1016/j.pce.2006.05.004.

Liu, Y., Xu, Z., Wu, X., Gui, W., and Zhu, G. (2010). Adsorption and desorption behavior of herbicide diuron on various Chinese cultivated soils. *Journal of Hazardous Materials*, *178*, 462 – 468. doi: https://doi.org/10.1016/j.jhazmat.2010.01.105.

Long, D., Longuevergne, L., and Scanlon, B. R. (2014). Uncertainty in evapotranspiration from land surface modeling, remote sensing, and GRACE satellites. *Water Resources Research*, *50*, 1131–1151. doi: https://doi.org/10.1002/2013WR014581.

Low, P. F. (1987). Structural component of the swelling pressure of clays. *Langmuir*, *3*, 18–25. doi: https://doi.org/10.1021/la00073a004.

Lozada-Cassou, M., and Díaz-Herrera, E. (1990). Three point extension for hypernetted chain and other integral equation theories: numerical results. *The Journal of Chemical Physics*, *92*, 1194–1210. doi: https://doi.org/10.1063/1.458128.

Madsen, F. T., and Müller-Vonmoos, M. (1985). Swelling Pressure Calculated from Mineralogical Properties of a Jurassic Opalinum Shale, Switzerland. *Clays and Clay Minerals*, *33*, 501–509. doi: https://doi.org/10.1346/CCMN.1985.0330604.

Malik, M., Mustafa, M. A., and Letey, J. (1992). Effect of mixed Na/Ca solutions on swelling, dispersion and transient water flow in unsaturated montmorillonitic soils. *Geoderma*, *52*, 17–28. doi: https://doi.org/10.1016/0016-7061(92)90072-F.

Manzoni, S., and Porporato, A. (2009). Soil carbon and nitrogen mineralization: theory and models across scales. *Soil Biology and Biochemistry*, *41*, 1355–1379. doi: https://doi.org/10.1016/j.soilbio.2009.02.031.

Mapanda, F., Mangwayana, E., Nyamangara, J., and Giller, K. (2005). The effect of long-term irrigation using wastewater on heavy metal contents of soils under vegetables in Harare, Zimbabwe. *Agriculture, Ecosystems & Environment*, *107*, 151 – 165. doi: https://doi.org/10.1016/j.agee.2004.11.005.

Masliyah, J. H., and Bhattacharjee, S. (2005). Electric Double Layer. In *Electrokinetic and Colloid Transport Phenomena* chapter 5. (pp. 105–178). John Wiley & Sons, Inc. doi: https://doi.org/10.1002/0471799742.ch5.

Mathur, S. (2004). Modeling phytoremediation of soils. *Practice Periodical of Hazardous, Toxic, and Radioactive Waste Management*, *8*, 286–297. doi: https://doi.org/10.1061/(ASCE)1090-025X(2004)8:4(286).

McBridge, M. B. (1997). A critique of diffuse double alyer models applied to colloid and surface chemistry. *Clays and Clay Minerals*, *45*, 598–608. doi: https://doi.org/10.1346/CCMN.1997.0450412.

McGuiggan, P. M., and Pashley, R. M. (1988). Molecular layering in thin aqueous films. *The Journal of Physical Chemistry*, *92*, 1235–1239. doi: https://doi.org/10.1021/j100316a045.

McNeal, B. L., and Coleman, N. T. (1966). Effect of solution composition on soil hydraulic conductivity. *Soil Science Society of America Journal*, *30*, 308–312. doi: https://doi.org/10.2136/sssaj1966.03615995003000030007x.

Mekonnen, M. M., and Hoekstra, A. Y. (2016). Four billion people facing severe water scarcity. *Science Advances*, *2*, e1500323. doi: https://doi.org/10.1126/sciadv.1500323.

Menneer, J. C., McLay, C. D. A., and Lee, R. (2001). Effects of sodium-contaminated wastewater on soil permeability of two New Zealand soils. *Australian Journal of Soil*

Research, *39*, 877–891. doi: https://doi.org/10.1071/SR99082.

Metcalf, L., Harrison, P. E., and Tchobanoglous, G. (2004). *Wastewater Engineering: Treatment, Disposal, and Reuse* volume 4. New York, NY, USA: McGraw-Hill.

Minasny, B., and McBratney, A. B. (2002). The efficiency of various approaches to obtaining estimates of soil hydraulic properties. *Geoderma*, *107*, 55–70. doi: https://doi.org/10.1016/S0016-7061(01)00138-0.

Moolenaar, S. W., van der Zee, S. E. A. T. M., and Lexmond, T. M. (1997). Indicators of the sustainability of heavy-metal management in agro-ecosystems. *Science of the Total Environment*, *201*, 155 – 169. doi: https://doi.org/10.1016/S0048-9697(97)00123-X.

Moyne, C., and Murad, M. A. (2002). Electro-chemo-mechanical couplings in swelling clays derived from a micro/macro-homogenization procedure. *International Journal of Solids and Structures*, *39*, 6159–6190. doi: https://doi.org/10.1016/S0020-7683(02)00461-4.

Moyne, C., and Murad, M. A. (2006). A two-scale model for coupled electro-chemo-mechanical phenomena and Onsager's reciprocity relations in expansive clays: I. Homogenization analysis. *Transport in Porous Media*, *62*, 333–380. doi: https://doi.org/10.1007/s11242-005-1290-8.

Mrozik, W., and Stefanńska, J. (2014). Adsorption and biodegradation of antidiabetic pharmaceuticals in soils. *Chemosphere*, *95*, 281–288. doi: https://doi.org/10.1016/j.chemosphere.2013.09.012.

Muñoz, I., Gómez-Ramos, M. J., Agüera, A., Fernández-Alba, A. R., García-Reyes, J. F., and Molina-Díaz, A. (2009). Chemical evaluation of contaminants in wastewater effluents and the environmental risk of reusing effluents in agriculture. *TrAC Trends in Analytical Chemistry*, *28*, 676 – 694. doi: https://doi.org/10.1016/j.trac.2009.03.007.

Murad, M. A., and Moyne, C. (2008). A dual-porosity model for ionic solute transport in expansive clays. *Computional Geosciences*, *12*. doi: https://doi.org/10.1007/s10596-007-9060-z.

Musso, G., Romero, E., and Della Vecchia, G. (2013). Double-structure effects on the chemo-hydro-mechanical behaviour of a compacted active clay. *Géotechnique*, *63*, 206–220. doi: https://doi.org/10.1680/geot.SIP13.P.011.

Muyen, Z., Moore, G. A., and Wrigley, R. J. (2011). Soil salinity and sodicity effects of wastewater irrigation in South East Australia. *Agricultural Water Management*, *99*, 33 – 41. doi: https://doi.org/10.1016/j.agwat.2011.07.021.

Ng, C.-O., and Qi, C. (2015). Electro-osmotic flow in a rotating rectangular microchannel. *Proceedings. Mathematical, Physical, and Engineering Sciences / The Royal Society*, *471*, 20150200. doi: https://doi.org/10.1098/rspa.2015.0200.

Nordbotten, J. M., Celia, M. A., Dahle, H. K., and Hassanizadeh, S. M. (2007).

Interpretation of macroscale variables in Darcy's law. *Water Resources Research*, *43*. doi: https://doi.org/10.1029/2006wr005018.

NVWA (1999). Warenwetregeling Verontreinigingen in levensmiddelen. *Staatscourant*, *30*.

Obliger, A., Jardat, M., Coelho, D., Bekri, S., and Rotenberg, B. (2014). Pore network model of electrokinetic transport through charged porous media. *Physiocal Review E*, *89*, 043013. doi: https://doi.org/10.1103/PhysRevE.89.043013.

Ogram, A. V., Jessup, R. E., Ou, L. T., and Rao, P. S. (1985). Effects of sorption on biological degradation rates of (2,4-dichlorophenox) acetic acid in soils. *Applied and Environmental Microbiology*, *49*, 582–587. doi: https://doi.org/10.1128/AEM.49.3.582-587.1985.

Oyanader, M., and Arce, P. (2005). A new and simpler approach for the solution of the electrostatic potential differential equation. Enhanced solution for planar, cylindrical and annular geometries. *Journal of Colloid and Interface Science*, *284*, 315–322. doi: https://doi.org/10.1016/j.jcis.2004.10.035.

Pagano, A. G., Magnanimo, V., Weinhart, T., and Tarantino, A. (2020). Exploring the micromechanics of non-active clays by way of virtual DEM experiments. *Géotechnique*, *70*, 303–316. doi: https://doi.org/10.1680/jgeot.18.P.060.

Park, J. H., Feng, Y., Ji, P., Voice, T. C., and Boyd, S. A. (2003). Assessment of bioavailability of soil-sorbed atrazine. *Applied and Environmental Microbiology*, *69*, 3288–3298. doi: https://doi.org/10.1128/aem.69.6.3288-3298.2003.

Paruch, A. M. (2014). The impact of wastewater irrigation on the chemical quality of groundwater. *Water and Environment Journal*, *28*, 502–508. doi: https://doi.org/10.1111/wej.12064.

Pedersen, J. A., Soliman, M., and Suffet, I. H. M. (2005). Human Pharmaceuticals, Hormones, and Personal Care Product Ingredients in Runoff from Agricultural Fields Irrigated with Treated Wastewater. *Journal of Agricultural and Food Chemistry*, *53*, 1625–1632. doi: https://doi.org/10.1021/jf049228m.

Pedrero, F., and Alarcón, J. J. (2009). Effects of treated wastewater irrigation on lemon trees. *Desalination*, *246*, 631 – 639. doi: https://doi.org/10.1016/j.desal.2008.07.017.

Pereira, B. F. F., He, Z., Stoffella, P. J., Montes, C. R., Melfi, A. J., and Baligar, V. C. (2012). Nutrients and Nonessential Elements in Soil after 11 Years of Wastewater Irrigation. *Journal of Environmental Quality*, *41*, 920–927. doi: https://doi.org/10.2134/jeq2011.0047.

Petrović, M., Gonzalez, S., and Barceló, D. (2003). Analysis and removal of emerging contaminants in wastewater and drinking water. *TrAC Trends in Analytical Chemistry*, *22*, 685 – 696. doi: https://doi.org/10.1016/S0165-9936(03)01105-1.

Porporato, A., Laio, F., Ridolfi, L., and Rodriguez-Iturbe, I. (2001). Plants in water-controlled ecosystems: active role in hydrologic processes and response to water stress: III. Vegetation water stress. *Advances in Water Resources*, *24*, 725–744. doi: https://doi.org/10.1016/S0309-1708(01)00006-9.

Pusch, R. (1992). Use of bentonite for isolation of radioactive waste products. *Clay Minerals*, *27*, 353–361. doi: https://doi.org/10.1180/claymin.1992.027.3.08.

Qian, Y. L., and Mecham, B. (2005). Long-Term Effects of Recycled Wastewater Irrigation on Soil Chemical Properties on Golf Course Fairways. *Agronomy Journal*, *97*, 717–721. doi: https://doi.org/10.2134/agronj2004.0140.

Quesada-Pérez, M., González-Tovar, E., Martín-Molina, A., Lozada-Cassou, M., and Hidalgo-Álvarez, R. (2003). Overcharging in colloids: beyond the Poisson-Boltzmann approach. *ChemPhysChem*, *4*, 234–248. doi: https://doi.org/10.1002/cphc.200390040.

Quirk, J. P. (2001). The significance of the threshold and turbidity concentrations in relation to sodicity and microstructure. *Australian Journal of Soil Research*, *39*, 1185–1217. doi: https://doi.org/10.1071/SR00050.

Quirk, J. P., and Schofield, R. K. (1955). The effect of electrolyte concentration on soil permeability. *Journal of Soil Science*, *6*, 163–178. doi: https://doi.org/10.1111/j.1365-2389.1955.tb00841.x.

Rabbani, A., Ayatollahi, S., Kharrat, R., and Dashti, N. (2016). Estimation of 3-D pore network coordination number of rocks from watershed segmentation of a single 2-D image. *Advances in Water Resources*, *94*, 264–277. doi: https://doi.org/0.1016/j.advwatres.2016.05.020.

Radcliffe, J. C. (2004). *Water Recycling in Australia*. Parkville, Australia: Australian Academy of Technological Sciences and Engineering.

Razzaghi, S., Khodaverdiloo, H., and Dashtaki, S. G. (2016). Effects of long-term wastewater irrigation on soil physical properties and performance of selected infiltration models in a semi-arid region. *Hydrological Sciences Journal*, *61*, 1778–1790. doi: https://doi.org/10.1080/02626667.2015.1051981.

Recycled Water Taskforce (2003). *Water recycling 2030: recommendations of California's Recycled Water Taskforce*. Technical Report, California Department of Water Resources Sacramento, California, USA.

Rengasamy, P., and Olsson, K. A. (1993). Irrigation and sodicity. *Australian Journal of Soil Research*, *31*, 821–837. doi: https://doi.org/10.1071/SR9930821.

Rezapour, S., and Samadi, A. (2011). Soil quality response to long-term wastewater irrigation in Inceptisols from a semi-arid environment. *Nutrient Cycling in Agroecosystems*, *91*, 269–280. doi: https://doi.org/10.1007/s10705-011-9460-2.

Rezapour, S., Samadi, A., and Khodaverdiloo, H. (2011). An Investigation

of the Soil Property Changes and Heavy Metal Accumulation in Relation to Long-term Wastewater Irrigation in the Semi-arid Region of Iran. *Soil and Sediment Contamination: An International Journal*, *20*, 841–856. doi: https://doi.org/10.1080/15320383.2011.609202.

Richards, L. A., Allison, L. E., Bernstein, L., Bower, C. A., Brown, J. W., Fireman, M., Hatcher, J. T., Hayward, H. E., Pearson, G. A., Reeve, R. C., and Wilcox, L. V. (1954). Diagnosis and Improvement of Saline and Alkali Soils. In *Agriculture Handbook* (p. 159). Washington D.C., United States of America: U.S. Government Printing Office volume 60.

Riding, M. J., Doick, K. J., Martin, F. L., Jones, K. C., and Semple, K. T. (2013). Chemical measures of bioavailability/bioaccessibility of PAHs in soil: fundamentals to application. *Journal of Hazardous Materials*, *261*, 687–700. doi: https://doi.org/10.1016/j.jhazmat.2013.03.033.

RIVM (2020). Zoeksysteem Risico's van stoffen. Dutch National Institute for Public Health and the Environment. Available online: https://rvszoeksysteem.rivm.nl/stoffen.

Rizzo, L., Krätke, R., Linders, J., Scott, M., Vighi, M., and de Voogt, P. (2018). Proposed EU minimum quality requirements for water reuse in agricultural irrigation and aquifer recharge: SCHEER scientific advice. *Current Opinion in Environmental Science & Health*, *2*, 7 – 11. doi: https://doi.org/10.1016/j.coesh.2017.12.004.

Rocha, A. C., Murad, M. A., Moyne, C., Oliveira, S. P., and Le, T. D. (2016). A new methodology for computing ionic profiles and disjoining pressure in swelling porous media. *Computational Geosciences*, *20*, 975–996. doi: https://doi.org/10.1007/s10596-016-9572-5.

Rodgriguez-Iturbe, I., Porporato, A., Ridolfi, L., Isham, V., and Coxi, D. R. (1999). Probabilistic modelling of water balance at a point: the role of climate, soil and vegetation. *Proceedings of the Royal Society of London. Series A: Mathematical, Physical and Engineering Sciences*, *455*, 3789–3805. doi: https://doi.org/10.1098/rspa.1999.0477.

Rodriguez-Iturbe, I., and Porporato, A. (2005). *Ecohydrology of water-controlled ecosystems: soil moisture and plant dynamics*. Cambridge: Cambridge University Press. doi: https://doi.org/10.1017/CBO9780511535727.

Rouchaud, J., Neus, O., Bulcke, R., Cools, K., Eelen, H., and Dekkers, T. (2000). Soil Dissipation of Diuron, Chlorotoluron, Simazine, Propyzamide, and Diflufenican Herbicides After Repeated Applications in Fruit Tree Orchards. *Archives of Environmental Contamination and Toxicology*, *39*, 60–65. doi: https://doi.org/10.1007/s002440010080.

Russo, D. (1988). Numerical analysis of the nonsteady transport of interacting solutes through unsaturated soil. 1. Homogeneous systems. *Water Resources Research*, *24*,

271–284. doi: https://doi.org/10.1029/WR024i002p00271.

Russo, D. (2013). Consequences of salinity-induced-time-dependent soil hydraulic properties on flow and transport in salt-affected soils. *Procedia Environmental Sciences*, *19*, 623–632. doi: https://doi.org/10.1016/j.proenv.2013.06.071.

Russo, D., and Bresler, E. (1977). Effect of mixed Na/Ca solutions on the hydraulic properties of unsaturated soils. *Soil Science Society of America Journal*, *41*, 713–717. doi: https://doi.org/10.2136/sssaj1977.03615995004100040019x.

Sander, R. (2015). Compilation of Henry's law constants (version 4.0) for water as solvent. *Atmospheric Chemistry and Physics*, *15*, 4399–4981. doi: https://doi.org/10.5194/acp-15-4399-2015.

Sarhadi, A., Burn, D. H., Johnson, F., Mehrotra, R., and Sharma, A. (2016). Water resources climate change projections using supervised nonlinear and multivariate soft computing techniques. *Journal of Hydrology*, *536*, 119 – 132. doi: https://doi.org/10.1016/j.jhydrol.2016.02.040.

Schacht, K., and Marschner, B. (2015). Treated wastewater irrigation effects on soil hydraulic conductivity and aggregate stability of loamy soils in Israel. *Journal of Hydrology and Hydromechanics*, *63*, 47–54. doi: https://doi.org/10.1515/johh-2015-0010.

Segad, M., Jönsson, B., Åkesson, T., and Cabane, B. (2010). Ca/Na montmorillonite: structure, forces and swelling properties. *Langmuir*, *26*, 5782–5790. doi: https://doi.org/10.1021/la9036293.

Shah, S. H. H., Vervoort, R. W., Suweis, S., Guswa, A. J., Rinaldo, A., and der Zee, S. E. A. T. M. (2011). Stochastic modeling of salt accumulation in the root zone due to capillary flux from brackish groundwater. *Water Resources Research*, *47*. doi: https://doi.org/10.1029/2010wr009790.

Shainberg, I., Bresler, E., and Klausner, Y. (1971a). Studies on Na/Ca Montmorillonite systems 1. The swelling pressure. *Soil Science*, *111*, 214–219.

Shainberg, I., Bresler, E., and Klausner, Y. (1971b). Studies on Na/Ca montmorillonite systems 1. The swelling pressure. *Soil Science*, *111*, 214–219. doi: https://doi.org/10.1097/00010694-197104000-00002.

Shainberg, I., and Caiserman, A. (1971). Studies on Na/Ca montmorillonite systems 2. The hydraulic conductivity. *Soil Science*, *111*, 276–281. doi: https://doi.org/10.1097/00010694-197105000-00002.

Shainberg, I., and Letey, J. (1984). Response of soils to sodic and saline conditions. *Hilgardia*, *52*, 1–57. doi: https://doi.org/10.3733/hilg.v52n02p057.

Shainberg, I., Rhoades, J. D., Suarez, D. L., and Prather, R. J. (1981). Effect of low electrolyte concentration on clay dispersion and hydraulic conductivity

of sodic soils. *Soil Science Society of America Journal*, *45*, 287–291. doi: https://doi.org/10.2136/sssaj1981.03615995004500020009x.

Shetty, S. (2004). Treated wastewater use in Tunisia: lessons learned and the road ahead. In C. A. Scott, N. I. Faruqui, and L. Raschid-Sally (Eds.), *Wastewater use in irrigated agriculture: confronting the livelihood and environmental realities*. Wallingford, United Kingdom: CAB International.

Šimůnek, J., Šejna, M., and van Genuchten, M. T. (2012). *The UNSATCHEM Module for HYDRUS (2D/3D) Simulating Two-Dimensional Movement of and Reactions Between Major Ions in Soils*. Prague, Czech Republic: PC Progress. Version 1.0.

Siyag, R. S., Pal, R., Poonia, S. R., and Baruah, T. C. (1983). Effect of mixed cation solutions on hydraulic soil properties. *Agricultural Water Management*, *6*, 15–25. doi: https://doi.org/10.1016/0378-3774(83)90022-7.

So, H. B., and Aylmore, L. A. G. (1993). How do sodic soils behave? The effects of sodicity on soil physical behaviour. *Australian Journal of Soil Research*, *31*, 761–777. doi: https://doi.org/10.1071/SR9930761.

Sperry, J. M., and Peirce, J. J. (1999). Ion Exchange and Surface Charge on Montmorillonite Clay. *Water Environment Research*, *71*, 316–322. doi: https://doi.org/10.2175/106143098X121798.

Stamatelatou, K., Frouda, C., Fountoulakis, M. S., Drillia, P., Kornaros, M., and Lyberatos, G. (2003). Pharmaceuticals and health care products in wastewater effluents: the example of carbamazepine. *Water Supply*, *3*, 131–137. doi: https://doi.org/10.2166/ws.2003.0054.

Sumner, M. E. (1993). Sodic soils: new perspectives. *Australian Journal of Soil Research*, *31*, 683–750. doi: https://doi.org/10.1071/SR9930683.

Suweis, S., Rinaldo, A., van der Zee, S. E. A. T. M., Daly, E., Maritan, A., and Porporato, A. (2010). Stochastic modeling of soil salinity. *Geophysical Research Letters*, *37*. doi: https://doi.org/10.1029/2010gl042495.

Sweijen, T., Nikooee, E., Hassanizadeh, S. M., and Chareyre, B. (2016). The effects of swelling and porosity change on capillarity: DEM coupled with a pore-unit assembly method. *Transport in Porous Media*, *113*, 207–226. doi: https://doi.org/10.1007/s11242-016-0689-8.

Tang, C., Chen, J., Shindo, S., Sakura, Y., Zhang, W., and Shen, Y. (2004). Assessment of groundwater contamination by nitrates associated with wastewater irrigation: A case study in Shijiazhuang region, China. *Hydrological Processes*, *18*, 2303–2312. doi: https://doi.org/10.1002/hyp.5531.

Teuling, A. J., and Troch, P. A. (2005). Improved understanding of soil moisture variability dynamics. *Geophysical Research Letters*, *32*. doi:

https://doi.org/10.1029/2004gl021935.

Thiele-Bruhn, S., and Brümmer, G. W. (2005). Kinetics of Polycyclic Aromatic Hydrocarbon (PAH) Degradation in Long-term Polluted Soils during Bioremediation. *Plant and Soil*, *275*, 31–42. doi: https://doi.org/10.1007/s11104-004-0265-9.

Tournassat, C., Bizi, M., Braibant, G., and Crouzet, C. (2011). Influence of montmorillonite tactoid size on Na–Ca cation exchange reactions. *Journal of Colloid and Interface Science*, *364*, 443–454. doi: https://doi.org/10.1016/j.jcis.2011.07.039.

Toze, S. (2006). Reuse of effluent water — benefits and risks. *Agricultural Water Management*, *80*, 147 – 159. doi: https://doi.org/10.1016/j.agwat.2005.07.010.

Troldborg, M., Duckett, D., Allan, R., Hastings, E., and Hough, R. L. (2017). A risk-based approach for developing standards for irrigation with reclaimed water. *Water Research*, *126*, 372 – 384. doi: https://doi.org/10.1016/j.watres.2017.09.041.

Tuller, M., and Or, D. (2003). Hydraulic functions for swelling soils: pore scale considerations. *Journal of Hydrology*, *272*, 50–71. doi: https://doi.org/10.1016/S0022-1694(02)00254-8.

Tunc, T., and Sahin, U. (2015). The changes in the physical and hydraulic properties of a loamy soil under irrigation with simpler-reclaimed wastewaters. *Agricultural Water Management*, *158*, 213 – 224. doi: https://doi.org/10.1016/j.agwat.2015.05.012.

UNDP (2006). *Beyond scarcity: power, poverty and the global water crisis*. Technical Report, United Nations Development Programme.

UNESCO-WWAP (2003). *1st UN World Water Development Report: Water for People, Water for Life*. New York: UNESCO and Berghahn Books.

USDA (2014). Soil bulk density/moisture/aeration. United States Department of Agriculture, Natural Resources Conservation Service (USDA NRCS). Available online: https://www.nrcs.usda.gov/Internet/FSE_DOCUMENTS/nrcs142p2_053260.pdf.

USEPA (2004). *Guidelines for Water Reuse*. Technical Report EPA/625/R-04/108, United States Environmental Protection Agency Washington D. C., USA.

USEPA (2012). *Guidelines for Water Reuse*. Technical Report EPA/600/R-12/618, United States Environmental Protection Agency Washington D. C., USA.

USEPA (2014). Technical Appendix B, Physico-chemical Properties for TRI Chemicals and Chemical Categories. United States Environmental Protection Agency. Available online: https://www.epa.gov/sites/production/files/2014-03/documents/tech_app_b_v215.pdf.

van de Craats, D., van der Zee, S. E. A. T. M., Sui, C., van Asten, P. J. A., Cornelissen, P., and Leijnse, A. (2020). Soil sodicity originating from marginal groundwater. *Vadose Zone Journal*, *19*, e20010. doi: https://doi.org/10.1002/vzj2.20010.

van der Meer, R. W. (2020). *Watergebruik in de land- en tuinbouw 2017 en 2018*. Technical Report Nota 2020-030, Wageningen Economic Research Wageningen.

van der Zee, S. E. A. T. M., and Boesten, J. J. T. I. (1991). Effects of soil heterogeneity on pesticide leaching to groundwater. *Water Resources Research*, *27*, 3051–3063. doi: https://doi.org/10.1029/91WR01990.

van der Zee, S. E. A. T. M., Shah, S. H. H., van Uffelen, C. G. R., Raats, P. A. C., and dal Ferro, N. (2010a). Effects of soil heterogeneity on pesticide leaching to groundwater. *Agricultural Water Management*, *97*, 41–49. doi: https://doi.org/10.1016/j.agwat.2009.08.009.

van der Zee, S. E. A. T. M., Shah, S. H. H., van Uffelen, C. G. R., Raats, P. A. C., and Dal Ferro, N. (2010b). Soil sodicity as a result of periodical drought. *Agricultural Water Management*, *97*, 41–49. doi: https://doi.org/10.1016/j.agwat.2009.08.009.

van der Zee, S. E. A. T. M., Shah, S. H. H., and Vervoort, R. W. (2014). Root zone salinity and sodicity under seasonal rainfall due to feedback of decreasing hydraulic conductivity. *Water Resources Research*, *50*, 9432–9446. doi: https://doi.org/10.1002/2013wr015208.

van Duijn, C. J., and van der Zee, S. E. A. T. M. (2018). Large time behaviour of oscillatory nonlinear solute transport in porous media. *Chemical Engineering Science*, *183*, 86–94. doi: https://doi.org/10.1016/j.ces.2018.02.045.

van Duijvenbooden, W., Breeuwsma, A., and Boumans, L. J. M. (1987). *Kwetsbaarheid van het grondwater: kartering van kenmerken van de Nederlandse bodem in relatie tot de kwetsbaarheid van het grondwater voor verontreiniging*. Bilthoven: RIVM.

van Genuchten, M. T. (1980). A closed-form equation for predicting the hydraulic conductivity of unsaturated soils. *Soil Science Society of America Journal*, *44*, 892–898. doi: https://doi.org/10.2136/sssaj1980.03615995004400050002x.

van Olphen, H. (1963). *An Introduction to Clay Colloid Chemistry*. New York: Interscience Publishers, Div. of John Wiley & Sons. doi: https://doi.org/10.1002/jps.2600530238.

van Olphen, H. (1977). *An Introduction to Clay Colloid Chemistry*. (2nd ed.). John Wiley & Sons, New York.

van Oort, E., Hale, A. H., Mody, F. K., and Roy, S. (1996). Transport in Shales and the Design of Improved Water-Based Shale Drilling Fluids. *Society of Petroleum Engineers*, *SPE-28309-PA*. doi: https://doi.org/10.2118/28309-pa.

Vervoort, R. W., and van der Zee, S. E. A. T. M. (2008). Simulating the effect of capillary flux on the soil water balance in a stochastic ecohydrological framework. *Water Resources Research*, *44*. doi: https://doi.org/10.1029/2008wr006889.

Verwey, E. J. W., and Overbeek, J. T. G. (1948). Theory of the stability of lyophobic

colloids. *The Journal of Physical and Colloid Chemistry*, *51*, 631–636.

Virto, I., Bescansa, P., Imaz, M., and Enrique, A. (2006). Soil quality under food-processing wastewater irrigation in semi-arid land, northern Spain: Aggregation and organic matter fractions. *Journal of Soil and Water Conservation*, *61*, 398–407.

Vörösmarty, C. J., Green, P., Salisbury, J., and Lammers, R. B. (2000). Global water resources: vulnerability from climate change and population growth. *Science*, *289*, 284–288. doi: https://doi.org/10.1126/science.289.5477.284.

VTA (2019). Opbrengst uien 2019. Verenigde Telers Akkerbouw. Available online: https://www.vtanederland.nl/.

Walker, A., Jurado-Exposito, M., Bending, G., and Smith, V. (2001). Spatial variability in the degradation rate of isoproturon in soil. *Environmental Pollution*, *111*, 407 – 415. doi: https://doi.org/10.1016/S0269-7491(00)00092-0.

Walter, T., Ederer, H. J., Först, C., and Stieglitz, L. (2000). Sorption of selected polycyclic aromatic hydrocarbons on soils in oil-contaminated sytems. *Chemosphere*, *41*, 387–397. doi: https://doi.org/10.1016/S0045-6535(99)00328-8.

Wang, S., Wu, W., Liu, F., Yin, S., Bao, Z., and Liu, H. (2015). Spatial distribution and migration of nonylphenol in groundwater following long-term wastewater irrigation. *Journal of Contaminant Hydrology*, *177-178*, 85 – 92. doi: https://doi.org/10.1016/j.jconhyd.2015.03.013.

Weber, S., Khan, S., and Hollender, J. (2006). Human risk assessment of organic contaminants in reclaimed wastewater used for irrigation. *Desalination*, *187*, 53 – 64. doi: https://doi.org/10.1016/j.desal.2005.04.067.

Whitehead, D., and Beadle, C. L. (2004). Physiological regulation of productivity and water use in Eucalyptus: a review. *Forest Ecology and Management*, *193*, 113–140. doi: https://doi.org/10.1016/j.foreco.2004.01.026.

WHO (2006). *Guidelines for the safe use of wastewater, excreta and greywater*. Technical Report Vol. 4, World Health Organization Geneva, Switzerland. Available online: https://www.who.int/water_sanitation_health/publications/gsuweg4/en/.

Wildenschild, D., and Jensen, K. H. (1999). Numerical modeling of observed effective flow behavior in unsaturated heterogeneous sands. *Water Resources Research*, *35*, 29–42. doi: https://doi.org/10.1029/98WR01959.

Woodward, E. E., Andrews, D. M., Williams, C. F., and Watson, J. E. (2014). Vadose Zone Transport of Natural and Synthetic Estrogen Hormones at Penn State's "Living Filter" Wastewater Irrigation Site. *Journal of Environmental Quality*, *43*, 1933–1941. doi: https://doi.org/10.2134/jeq2014.04.0153.

Xu, J., Wu, L., and Chang, A. C. (2009). Degradation and adsorption of selected pharmaceuticals and personal care products

(PPCPs) in agricultural soils. *Chemosphere*, *77*, 1299 – 1305. doi: https://doi.org/10.1016/j.chemosphere.2009.09.063.

Xu, J., Wu, L., Chang, A. C., and Zhang, Y. (2010). Impact of long-term reclaimed wastewater irrigation on agricultural soils: A preliminary assessment. *Journal of Hazardous Materials*, *183*, 780 – 786. doi: https://doi.org/10.1016/j.jhazmat.2010.07.094.

Yang, K. L., Yiacoumi, S., and Tsouris, C. (2002). Monte Carlo simulations of electrical double-layer formation in nanopores. *The Journal of Chemical Physics*, *117*, 8499–8507. doi: https://doi.org/10.1063/1.1511726.

Zhang, T., Wu, B., Sun, N., Ye, Y., and Chen, H. (2013). Sorption and degradation of wastewater-associated pharmaceuticals and personal care products in agricultural soils and sediment. *Water Science and Technology*, *68*, 991–998. doi: https://doi.org/10.2166/wst.2013.326.

English summary

Freshwater resources worldwide are currently under pressure, while the water demand is expected to increase further due to climate change, urbanization, and the growing world population. Therefore, alternative water sources need to be considered when possible. Treated wastewater may be of insufficient quality for drinking water, but may be sufficient for irrigation in agriculture. This may significantly alleviate the pressure on existing freshwater resources, since agriculture is responsible for 70% of the global freshwater withdrawals. Wastewater irrigation has already been practiced for many years in arid and semi-arid regions around the world. In recent years, wastewater irrigation is also receiving increased attention in temperate climates. First, more extreme weather events are expected to occur under climate change, which puts pressure on conventional water sources. Second, treated wastewater is currently discharged directly into surface water in these countries. Wastewater irrigation may therefore be a more environmentally friendly alternative, as a portion of the contaminants may be filtered out by the soil.

However, the large number of contaminants that may be present in wastewater can pose a risk to the public health and the environment. While regulations exist for several traditional contaminant groups (e.g., heavy metals, several indicator-bacteria), these regulations are still missing for many contaminants, including contaminants of emerging concern such as pharmaceuticals and personal care products. Within this thesis, we considered several challenges that the contaminants in wastewater pose to the public health and the environment. This thesis is split into two parts. Within the first part, we focus on general analyses that are applicable to many adsorbing and degrading contaminants, including many contaminants of emerging concern. The second part of this thesis covers several aspects related to soil sodicity. This topic was chosen specifically because sodium is often present in high concentrations in wastewater, and accumulation of sodium in clay soils may lead to irreversible damage to the soil structure.

Many adsorbing and degrading contaminants, including contaminants of emerging concern, may or may not be available for biodegradation while adsorbed to the soil. This concept of whether degradation occurs in the adsorbed phase is an important factor for the fate of contaminants in the environment under steady flow conditions. In Chapter 2, we extended this analysis to transient flow conditions, as this is more realistic in the

case of irrigation. When contaminants are not degraded in the adsorbed phase, the long-term average contaminant concentration and fluxes are insensitive to the extent and (non-)linearity of adsorption. Nevertheless, adsorption does affect the temporal fluctuations in contaminant concentration and fluxes, as well as the time required to reach periodical steady state. When contaminants do degrade in the adsorbed phase, similar results are found for linear adsorption. However, in case of nonlinear adsorption, the contaminant concentration and fluxes are significantly impacted by adsorption, due to the interaction between contaminant concentration and adsorption in this case. Therefore, the degradation concept is an important factor that should be determined from degradation experiments.

Regulations for many contaminants of emerging concern in irrigation water are still missing. In Chapter 3, we developed a framework to assess the sustainability of wastewater irrigation, which may aid in developing such regulations. Frameworks for the sustainability assessment of wastewater irrigation have been previously developed, but considered only a limited number of environmental compartments and contaminant exposure routes. For a thorough sustainability assessment, all potential pathways that contaminants may follow must be considered. These environmental compartments are also coupled. For example, the contaminant mass that is available to leach to the groundwater is also dependent on the contaminant mass which is taken up by plants. Therefore, all these processes need to be considered simultaneously for a thorough sustainability assessment of wastewater irrigation. The framework in Chapter 3 makes use of analytical solutions and requires relatively few input parameters and is therefore suitable for practical applications. The output is given in a comprehensible manner by making use of two sustainability indices, which give information which environmental compartments are at risk and on what timescale problems will occur for each contaminant. However, the framework is based on the assumption that environmental quality standards exist for all contaminants and that all contaminant transport properties are known. This may not be the case for many contaminants of emerging concern. While this leads to flawed assessments, the framework may then still help determine whether the missing information is important relative to other fluxes and compartments. In this case, the framework also highlights where additional environmental quality standards are needed.

When wastewater is rich in sodium, wastewater irrigation may put the soil at risk of sodification. Soil sodicity refers to the relative accumulation of sodium on the cation exchange complex relative to other cations. When sodic soils are exposed to low salinity water, the soil structure may be severely degraded. This reduces soil water flow, aeration, and plant root growth, and negatively impacts agricultural productivity. Remediation of sodic soils is difficult and time-consuming once severe degradation has occurred. Therefore, the focus should instead be on anticipation and prevention of soil sodicity. Thus, models that relate soil sodicity to soil structure damage are needed. The link between sodium content and soil structure originates at the microscopic scale, from the

electric field between the negatively charged clay particles. Changes in salt concentration and composition alter the strength of the electric field and therefore also the pressure between the clay particles. In the case of sodicity, the pressure increases and the clay particles are pushed apart, which results in clay swelling and dispersion. Swelling of these microscopic pores generally occurs at the expense of the larger pores. This reduces the soil hydraulic conductivity and also impacts the unsaturated soil hydraulic properties. Upscaling techniques are required to translate swelling on the microscopic scale to the response of the macroscopic soil hydraulic properties.

In Chapter 4, we developed a pore-network model to compute the coupled system of salt concentration, fluid pressure, and electric potential. Pore-network models are a useful tool for upscaling pore-scale processes, while including pore-scale heterogeneities. Previous studies used upscaling techniques which assume a certain degree of homogeneity. However, soils are heterogeneous by nature. Pore size heterogeneity is especially important in clay soils, as the pore size strongly impacts the strength of the electrokinetic processes. The results of the pore-network model show that heterogeneity does indeed significantly impact the rate of salt transport and water flow. This model was only a first step in including heterogeneity in upscaling the microscopic electrokinetic effects in porous media. Deformation of the pore network, induced by swelling and shrinking of the pores, was neglected. While challenging to implement, this should be included in future studies to make the model better applicable to clay soils.

The electric field and force between clay particles is commonly computed with the Poisson-Boltzmann equation. However, this theory neglects ion-ion correlations, despite being critical for the stability of non-sodic soils. Therefore, advanced theories that include ion-ion correlation should be used instead of Poisson-Boltzmann theory, such as the hypernetted chain approximation or density functional theory. In Chapter 5, we have applied density functional theory in the context of soil sodicity, and found that the critical sodium content, above which severe soil degradation occurs, could be predicted well. Thus, it is necessary to use advanced theories which include ion-ion correlation when modelling sodicity-induced soil structure damage, despite the large increase in numerical complexity.

Additionally, we modelled the response of the soil hydraulic properties to sodicity. Making use of the aforementioned density functional theory, reasonable agreement was found between experimental and model results. The link between swelling of the micropores and shrinking of the macropores was represented in a simplified manner in this study. Further advances in soil sodicity modelling can be made by including more advanced soil mechanical models.

Nederlandse samenvatting

Conventionele zoetwaterbronnen staan onder druk, terwijl de vraag naar zoetwater naar verwachting verder zal toenemen door klimaatverandering, verstedelijking en bevolkingsgroei. Daarom is het gebruik van alternatieve waterbronnen noodzakelijk. Gereinigd afvalwater voldoet misschien niet aan de kwaliteitseisen voor drinkwater, maar kan mogelijk wel gebruikt worden voor irrigatie in de landbouw. Dit kan een groot deel van de druk op bestaande zoetwaterbronnen wegnemen, aangezien de landbouw verantwoordelijk is voor 70% van het watergebruik wereldwijd. In droge gebieden in de wereld wordt al jaren geïrrigeerd met afvalwater. Recentelijk is er ook meer aandacht voor irrigatie met afvalwater in landen met een meer gematigd klimaat. Ten eerste, omdat er meer extreme weerspatronen worden verwacht in de toekomst met het oog op klimaatverandering. Daarnaast wordt gereinigd afvalwater in deze landen nu direct geloosd in oppervlaktewateren. Irrigatie met afvalwater kan daarom een milieuvriendelijker alternatief zijn, omdat een deel van de verontreinigingen uit het water worden gefilterd door de bodem.

Echter kleven er ook nadelen aan het hergebruik van afvalwater voor irrigatie. De verontreinigingen in het afvalwater kunnen schade toebrengen aan de volksgezondheid en het milieu. Hoewel er normen bestaan voor enkele traditionele verontreinigingsgroepen (bijvoorbeeld zware metalen of bepaalde bacteriën), is dit niet het geval voor veel andere verontreinigingen, waaronder de zogenaamde opkomende stoffen als geneesmiddelen en verzorgingsproducten. In dit proefschrift worden meerdere uitdagingen beschouwd die gerelateerd zijn aan de verontreinigingen in afvalwater en hun schadelijke effecten op de volksgezondheid en het milieu. Dit proefschrift is opgebouwd uit twee delen. In het eerste deel focussen we op algemene analyses die toepasbaar zijn op vele adsorberende en afbreekbare verontreinigingen, zoals veel opkomende stoffen. Het tweede deel van het proefschrift richt zich op bodemsodiciteit. Het laatstgenoemde onderwerp is gekozen omdat natrium vaak in hoge concentraties aanwezig is in afvalwater, en wanneer natrium in kleibodems accumuleert, kan dit leiden tot onomkeerbare schade aan de bodemstructuur.

Veel adsorberende en afbrekende verontreinigingen, waaronder opkomende stoffen, zijn wel of niet afbreekbaar wanneer ze zijn geadsorbeerd aan de bodemdeeltjes. Het is

al bekend dat dit onderscheid tussen afbraakconcepten in de geadsorbeerde fase een belangrijke rol speelt in het lot van verontreinigingen in het milieu onder stationaire stroming. In Hoofdstuk 2 hebben we deze analyse uitgebreid naar niet-stationaire stroming, wat realistischer is in het geval van irrigatie. Wanneer verontreinigingen niet worden afgebroken in de geadsorbeerde fase, zijn de gemiddelde concentratie en fluxen op lange termijn niet gevoelig voor de mate en lineariteit van adsorptie. Desalniettemin beïnvloedt adsorptie wel de tijdsafhankelijke fluctuaties van de concentratie en fluxen, en ook de benodigde tijd om de periodieke evenwichtssituatie te bereiken. Wanneer verontreinigingen wel afbreken in de geadsorbeerde fase, vinden we dezelfde resultaten in het geval van lineaire adsorptie. Echter, in het geval van niet-lineaire adsorptie worden de concentratie en fluxen wel sterk beïnvloedt door adsorptie, vanwege de interactie tussen de mate van adsorptie en de concentratie. Het daarom van groot belang dat van elke stof het juiste afbraakconcept wordt bepaald in experimenten.

Voor veel verontreinigingen in afvalwater is nog geen regelgeving met betrekking tot de waterkwaliteit voor irrigatie. In Hoofdstuk 3 hebben we een kader ontwikkeld om de duurzaamheid van afvalwaterirrigatie te beoordelen. Soortgelijke kaders zijn eerder ontwikkeld, maar waren gelimiteerd omdat maar enkele milieucompartimenten werden beschouwd. Voor een volledige beoordeling van de duurzaamheid is het nodig om alle compartimenten en alle routes waardoor verontreinigingen schade kunnen brengen aan mens en milieu tegelijkertijd te beschouwen. Deze milieucompartimenten zijn ook allemaal aan elkaar gekoppeld. Zo is bijvoorbeeld de hoeveelheid stof die uitspoelt naar het grondwater ook afhankelijk van de hoeveelheid stof die wordt opgenomen door het gewas. Daarom is het belangrijk dat al deze processen tegelijkertijd worden beschouwd om tot een goede beoordeling van de duurzaamheid van afvalwaterirrigatie te komen. Het kader uit Hoofdstuk 3 is gebaseerd op analytische oplossingen en heeft relatief weinig parameters nodig, waardoor het bruikbaar is voor praktische toepassingen. De output wordt op een overzichtelijke manier gegeven door gebruik te maken van twee duurzaamheidsindicatoren, die informatie geven over welke milieucompartimenten worden bedreigd en op wat voor tijdschaal problemen ontstaan voor elke verontreiniging. Dit kader is gebaseerd op de aanname dat milieunormen bestaan voor elke verontreiniging en dat alle transportparameters bekend zijn. Voor veel opkomende stoffen zijn deze data onbekend. Hoewel dit kan leiden tot foutieve beoordelingen van de duurzaamheid, geeft dit ook aan waar nog informatie mist en waar dus extra onderzoek moet worden gedaan.

Wanneer afvalwater rijk is aan natrium, kan irrigatie met dit water leiden tot sodificatie van de bodem. Dit betekent dat er relatief veel natrium bindt aan het kationenadsorptiecomplex ten opzichte van andere kationen. Wanneer zulke sodische bodems worden blootgesteld aan water met een laag zoutgehalte, kan er hevige schade aan de bodemstructuur ontstaan. Dit leidt tot een vermindering in stroming van water en lucht in de bodem, alsook problemen met de wortelgroei van planten, en heeft dus een negatief effect of de landbouwproductiviteit. Het herstellen van sodische bodems is

moeilijk en tijdrovend. Daarom is het belangrijk om te richten op het anticiperen en voorkomen van bodemsodiciteit. Daarvoor zijn modellen nodig die het natriumgehalte in de bodem koppelen aan de bodemstructuur. Om de koppeling tussen de bodemstructuur en het natriumgehalte te begrijpen, moeten we kijken naar de microscopische schaal, naar het elektrische veld tussen de negatief-geladen kleideeltjes. Veranderingen in de zoutconcentratie en compositie leiden tot veranderingen in de sterkte van het elektrische veld en beïnvloeden daardoor de kracht tussen de kleideeltjes. In het geval van bodemsodiciteit wordt de kracht tussen twee kleideeltjes groter, waardoor de kleideeltjes elkaar afstoten en de bodem zal opzwellen. Het zwellen van deze microscopische poriën gaat vaak ten koste van de grotere poriën. Dit leidt tot een lagere doorlaatbaarheid van de bodem en beïnvloedt ook de onverzadigde hydraulische bodemparameters. Om dit zwellen op de microscopische schaal te vertalen naar veranderingen in bodemparameters op grotere schaal zijn opschalingstechnieken nodig.

In Hoofdstuk 4 hebben we een porie-netwerk model ontwikkeld om de wisselwerking tussen zouttransport, waterstroming, en het elektrische veld uit te rekenen. Porie-netwerk modellen zijn een nuttig gereedschap om porie-schaal processen op te schalen, maar wel de effecten van porie-schaal heterogeniteit mee te nemen. Voorgaande studies hebben opschalingstechnieken gebruikt waarbij een zekere mate van homogeniteit moet worden aangenomen. Echter is heterogeniteit een karakteristieke eigenschap van bodems. Vooral in kleibodems is heterogeniteit van belang, want de poriegrootte heeft een grote invloed op de sterkte van de elektrokinetische processen. De resultaten van het porie-netwerk model laten zien dat heterogeniteit inderdaad een grote invloed heeft op de snelheid van zouttransport en waterstroming. Dit model was een eerste stap om heterogeniteit mee te nemen bij het opschalen van microscopische elektrokinetische effecten in poreuze media. Deformatie van het porie-netwerk door het zwellen en krimpen van poriën was niet meegenomen. Hoewel dit proces niet eenvoudig is te modelleren, zou dit wel moeten worden toegevoegd in vervolgstudies om het model beter toepasbaar op kleibodems te maken.

Het elektrische veld en de kracht tussen twee kleideeltjes wordt vaak berekend met behulp van de Poisson-Boltzmann vergelijking. Deze theorie verwaarloost echter de ion-ion correlaties, terwijl het bekend is dat deze van cruciaal belang zijn voor de stabiliteit van niet-sodische bodems. Daarom moeten geavanceerdere theorieën die ion-ion correlaties meenemen worden gebruikt in plaats van de Poisson-Boltzmann theorie. Een voorbeeld hiervan is de dichtheidsintegraaltheorie, die we in Hoofdstuk 5 hebben toegepast in de context van bodemsodiciteit. Met behulp van dichtheidsintegraaltheorie kunnen goede schattingen van het kritieke natriumgehalte waarboven hevige bodemdegradatie plaatsvindt worden gemaakt. Het is daarom van groot belang dat zulke geavanceerde theorieën worden gebruikt om bodemstructuurschade te modelleren, ook al gaat dit gepaard met complexere numerieke modellen. Daarnaast hebben we ook de verandering in hydraulische bodemparameters gemodelleerd in relatie tot het natriumgehalte.

Gebruikmakend van de voorgenoemde dichtheidsintegraaltheorie vonden we een goede overeenkomst tussen het numerieke model en experimentele resultaten. In dit hoofdstuk was de stap van de microscopische schaal naar de macroscopische schaal versimpeld. Daarom kan deze stap worden verbeterd door het gebruik van modellen waarbij de bodemmechanica nauwkeuriger wordt beschreven.

Acknowledgements

Here, I would like to thank the people who supported me throughout obtaining a PhD and made the journey more pleasant.

First and foremost, I would like to thank my supervision team. Many thanks to my promotor, Sjoerd, for giving me the opportunity to do this PhD research, as well as steering my research project in the right direction and for allowing me the freedom to pursue my own research interests. Thanks to my co-promotor Toon, I really appreciate all the discussions we had regarding the physics and numerical issues we have faced during this research. I really enjoyed the atmosphere of our weekly Tuesday-morning meetings together with Sjoerd. Finally, I would like to thank my other co-promotor, Vahid, for his valuable insight regarding the part of the thesis concerned with electrokinetics, as well as your enthusiasm and optimism. Many thanks for your hospitality during my visit to Manchester. It is a shame that I could not come for another visit due to the corona pandemic.

Then, I would like to thank Coen Ritsema not only for being the substitute promotor at my defence, but also for the positivity he brings to the SLM group. I would also like to thank the secretaries of our group, Marnella and Rianne, for their help in solving all the administrative issues that popped up during the PhD project.

Next, I want to thank my office mates in Gaia for the occasional scientific discussions. Darrell, I liked seeing your unique view on things in our discussions, and of course I also enjoyed the ping-pong sessions. Daniël, it was nice to have someone to complain to about the struggles of a researcher. As the saying goes, 'gedeelde smart is halve smart'.

Meng, I value the many conversations we have had in the coffee room, and of course enjoyed the many dinners you have prepared for me. Pop, having your relaxed, care-free nature around made the PhD work much lighter. Hao, I enjoyed having you around for all the activities we did together. Of course, I would also like to thank the Pokémon team, consisting of Lingtong, Yueling, and Pop, for having the utmost confidence in my leadership abilities. Our walks around campus were a welcome break to the work life. Xiaomei, thank you for your support and efforts to keep me at SLM. Vera, your comments helped put the struggles of a PhD student into perspective. Nikola, thank you

for your involvement with finding options for my post-PhD career. Many thanks to the other colleagues from SLM, namely Karrar, Carlos, Fabio, Ricardo, Sija, Coleen, Corjan, Róger, Nicolas, Ke, Qian, Jiaoyang, Miao, Meindert, Jinfeng, Mirzokhid, Raoul, Hui, Yonghui, Rozita, and others that I may have forgotten to mention, for all the dinners, trips, sports, and other activities did together.

Outside of SLM, I would like to thank Pieter for the many nature-walks we undertook, where I could take my mind off work, and Maurits for initiating the occasional football nights. I also want to thank other friends that provided occasional distractions, including Enno, Ludo, and Tom. Of course, I would also like to thank my parents, siblings, and other family for their support throughout the PhD.

Last but definitely not least, I would like to thank my dear Katharina for her continuous love and support throughout my PhD research. Not only was your emotional support valuable to me, you also helped by proofreading my writings and letting me bounce ideas off you. Kitty, your softness and fluffiness proved a nice distraction from work.

About the author

Pavan Cornelissen was born on 19 February 1993 in Wageningen, the Netherlands. He obtained a bachelor's degree in Earth Sciences at Utrecht University in 2014. Developing an interest in groundwater flow and porous media, he obtained his master's degree in Earth Surface and Water (Hydrology) in 2016, also at Utrecht University. During his master's thesis research, he visited the Institute for Modelling Hydraulics and Environmental Systems at the University of Stuttgart (Germany) for three months. He also worked on a modelling project commissioned by the Geological Survey of the Netherlands (TNO). In 2016, Pavan started as a PhD candidate at the Soil Physics and Land Management Group of Wageningen University. During his PhD research, he gave presentations at several conferences, supervised BSc and MSc students, and assisted with computer practicals for BSc and MSc courses. Pavan currently works as a post-doctoral researcher at the Reservoir Engineering Group of Delft University of Technology.

Permanent e-mail address: pavancornelissen@gmail.com

Netherlands Research School for the
Socio-Economic and Natural Sciences of the Environment

D I P L O M A

for specialised PhD training

The Netherlands research school for the
Socio-Economic and Natural Sciences of the Environment
(SENSE) declares that

Pavan Cornelissen

born on February 19th 1993 in Wageningen, The Netherlands

has successfully fulfilled all requirements of the
educational PhD programme of SENSE.

Wageningen, April 1st 2022

Chair of the SENSE board

Prof. dr. Martin Wassen

The SENSE Director

Prof. Philipp Pattberg

The SENSE Research School has been accredited by the Royal Netherlands Academy of Arts and Sciences (KNAW)

KONINKLIJKE NEDERLANDSE
AKADEMIE VAN WETENSCHAPPEN

The SENSE Research School declares that **Pavan Cornelissen** has successfully fulfilled all requirements of the educational PhD programme of SENSE with a work load of 37.1 EC, including the following activities:

SENSE PhD Courses

- Environmental research in context (2017)
- Research in context activity: 'Co-organizing WIMEK-SENSE Symposium on: Soil contamination - Scope, Advances and Challenges (Wageningen, 1 September 2017)'

Other PhD and Advanced MSc Courses

- Summer School for flow and transport in terrestrial systems, TU Clausthal (2017)
- Basic statistics, PE&RC and SENSE (2017)
- Essentials of scientific writing and presenting, Wageningen Graduate Schools (2018)
- Scientific writing, Wageningen Graduate Schools (2018)
- Presenting with impact, Wageningen Graduate Schools (2018)
- Presenting for a non-scientific audience, Environmental Technology, Wageningen University (2018)
- Scientific publishing, Wageningen Graduate Schools (2018)

Management and Didactic Skills Training

- Supervision of MSc thesis titled 'Simulation of the sodic subsoil development in root zone using HYDRUS' (2017)
- Supervision of BSc thesis titled 'Transport of bacteria and viruses through the vadose zone after re-use of wastewater in irrigated agriculture' (2018)
- Supervision of BSc thesis titled 'Upscaling complex flow patterns in clay soils using a pore network model' (2020)
- Assisting computer practicals of the MSc course 'Advanced Hydrological Systems Analysis' (2017)
- Assisting computer practicals of the BSc course 'Hydrogeology' (2018-2020)

Oral Presentations

- *Salt diffusion in charged porous media*. EGU General Assembly, 4-8 May 2020, Online
- *Osmosis in groundwater*. Boussinesq Lecture, 18 October 2018, Utrecht, The Netherlands.

SENSE coordinator PhD education

Dr. ir. Peter Vermeulen

Colophon

The research described in this thesis was financially supported by the Netherlands Organisation for Scientific Research (NWO) under NWO contract 14299, which is partly funded by the Ministry of Economic Affairs and Climate Policy, and co-financed by the Netherlands Ministry of Infrastructure and Water Management and partners of the Dutch Water Nexus consortium.

Cover design by Pavan Cornelissen

Printed by Digiforce | www.proefschriftmaken.nl